Miniature Broadband-NIRS System to Measure CNS Tissue Oxygenation and Metabolism in Preclinical Research

Pardis Kaynezhad

A thesis submitted to University College London

For the Degree of Doctor of Philosophy (Ph.D)

Department of Medical Physics and Biomedical Engineering

University College London

2018

Declaration

I, Pardis Kaynezhad confirm that the work presented in this thesis is my own. Where information has been derived from other sources, I confirm that this has been indicated in the thesis.

Abstract

In-vivo measurement of CNS tissue oxygenation and metabolism is critical in health and disease. Broadband-near infrared spectroscopy is a non-invasive optical technique which measures tissue oxygenation, haemodynamics and metabolism through in-vivo quantification of concentration changes of oxy- and deoxy-haemoglobin ($\Delta[HbO_2]$ and $\Delta[HHb]$) and oxidised cytochrome-c-oxidase ($\Delta[oxCCO]$). Current commercially available NIRS systems only use a few wavelengths to measure concentration change that fails to provide accurate $\Delta[oxCCO]$ measurement. Broadband-NIRS instruments however, use more than 100 wavelengths which enables quantification of change in [oxCCO], an important marker of cellular oxidative metabolism. These systems tend to be bulky, requiring extensive calibrations and trained staff to operate them; making them less versatile and difficult to be adapted in the clinical environment. Furthermore, existing broadband-NIRS systems quantify chromophore concentration changes assuming a fixed optical pathlength across all the subjects using a previously measured DPF (differential pathlength factor) with time or frequency domain systems.

This thesis describes the development of a portable broadband-NIRS system called mini-CYRIL "CYtochrome Research Instrument and appLication", based on easily sourced components. A miniature white light source (HL-2000-HP) and miniature spectrometers (QE65pro and Ventana VIS-NIR) by Ocean Optics were customised for measuring CNS tissue oxygenation and metabolism. While having the features of commercially available NIRS systems in terms of portability, ease of use and no need for wavelength calibration, in terms of performance mini-CYRIL is comparable to broadband-NIRS instruments providing reliable $\Delta[oxCCO]$ measurements that have been validated and assessed through in-vivo tissue studies in (a) preclinical model of: (i) neonatal hypoxic-ischaemic (HI) encephalopathy, (ii) multiple sclerosis (MS) and (iii) low-light level therapy in the aged retina; (b) infants during brain functional activation.

Mini-CYRIL is furthermore novel in offering calculation of absolute change in the concentration of chromophores based on real-time measurement of the optical path of light traversing the tissue. None of the current NIRS systems offer this feature which is crucial in case of changing pathology following an injury.

Mini-CYRIL demonstrated that Δ[oxCCO] drops significantly during the HI insult in piglets and these observations were comparable to previous results with a standard broadband-NIRS system. In the MS studies, the Δ[oxCCO] as measured with mini-CYRIL on the inflamed spinal cord of rats during brief hyperoxia was significantly larger when compared to control animals; suggesting suppression of mitochondrial metabolism in MS due to tissue hypoxia. In the aged retina of rats, exposure to 670 nm caused a large increase in Δ[oxCCO] as measured by mini-CYRIL, an observation not seen at light exposure of 420 nm; suggesting enhanced retinal mitochondrial respiration by the red light.

We have demonstrated that it is possible to measure oxygenation and metabolism in the brain, spinal cord and the retina of the eye in pre-clinical studies with a highly portable, easy to operate and relatively cheap miniaturised broadband-NIRS device.

Impact Statement

The work done in this thesis will contribute knowledge in the research field of the pathophysiology of injury and disorder in brain and other parts of the central nervous system (CNS). Mini-CYRIL, a miniature broadband-near infrared spectroscopy (NIRS) system developed in this thesis, provides in-vivo measurement of tissue oxygenation, haemodynmics and metabolism non-invasively in real time. Our measurements will allow us to investigate the physiological mechanisms controlling the CNS tissue haemodynamic\oxygenation\metabolic regulation which are of critical importance, and highly active area of research in life sciences, neuroscience and clinical science.

Translational Research: Mini-CYRIL will benefit the broad neuroscience community. Being compact, portable and easy to use with an intuitive user interface, mini-CYRIL is a cross-platform instrument that can be operated by non-experts at any environment including the lab and the clinic; for a variety of applications preclinical and clinical; on different organs of the CNS; at multiple timescales from short-term minutes to long-term days measurements. In this thesis, I have demonstrated the use of the system in the following areas:

- Preclinical research developing neuroprotection therapies for acute hypoxic-ischaemic (HI) brain injuries. These researchers require brain monitoring instruments that are non-invasive, cheap and easy to operate.
- Investigating the functional haemodynamic response and oxidative metabolism of the developing human brain, potentially looking at neurovascular coupling as well as metabolism both in physiology and pathology.
- Furthermore, two new applications have been introduced to the field of broadband-NIRS including real-time monitoring of spinal cord tissue in preclinical models of Multiple Sclerosis as well as monitoring the retina in preclinical models of Age-related Macular Degeneration (AMD). Currently there is no simple physiological metric to indicate declining function that may lead to AMD and the methodology that was used in this study represents a step towards this, while providing new opportunities for further studies in both broadband-NIRS and retina research.

Long-term Impacts : The methodology and results produced in this research will benefit a wide group of people at risk of certain CNS disorders including babies, children and adults at risk of hypoxic-ischaemic brain injury leading to devastating neurological outcomes and death in severe cases; people between the age of 20-50 who are at risk of developing multiple sclerosis leading to paralysis and premature death in severe cases; and people 65 years and over who are at high risk of developing AMD resulting in blindness.

Collaborations: We have ongoing collaborations not only with optical industries (Ocean Optics, UK; Wasatch Photonics, USA; and LOPTEK, Germany), but also with:

1. Clinicians and neuroscientists at the UCL Institute of Neurology investigating perinatal hypoxia-ischaemia in piglets, where mini-CYRIL has replaced Magnetic Resonance Spectroscopy (MRS) during hypoxic-ischaemic (HI) insult and can be expanded for use in this patient population.
2. Neuroscientists at the Centre for Brain and Cognitive Development, Birkbeck College, investigating functional haemodynamic response and oxidative metabolism of the brain in physiology and pathology.
3. Neuroscientists at the Neuroinflammation Centre at the Institute of Neurology to assist with further understanding of the role of hypoxia and inflammation in Multiple Sclerosis.
4. And potentially, with neuroscientists at the Institute of Ophthalmology to establish a predictive biomarker for retina aging and AMD.

Journals: Due to the multidisciplinary nature of this research, publications were made in a wide range of journals and disciplines, including Nature Scientific Reports, Experimental Eye Research and Electro Optics Magazine.

Education: Mini-CYRIL can be easily deployed in the classroom environment as it is safe and can be used to demonstrate light tissue interactions and its application in medicine/medical research.

Public Engagement: Mini-CYRIL was exhibited recently at MetaboLight launch event by Dr Tachtsidis and his group. MetaboLight (http://metabolight.org/) is a web public engagement platform to inform on the use of light to monitor brain physiology.

Acknowledgements

I would like to acknowledge and extend my heartfelt gratitude towards the following people who have had a massive impact on the completion of this Ph.D. thesis.

Firstly, I would like to express my sincere gratitude and appreciation to my supervisor Dr Ilias Tachtsidis for his continuous support and guidance and for patiently leading me through all the ups and downs during the course of this Ph.D.

Also, thanks to my second supervisor, Dr Terence Leung who has helped me explore new ideas through the discussions we had.

I would like to thank all my wonderful friends and colleagues in the Multimodal Spectroscopy Group, especially Gemma, Fred, Phong and Izzy who have always been there for me and my special thanks to Izzy for kindly proofreading some of my chapters. Also, thanks to Cornelius for his great help in data collection.

Thanks to all the wonderful neuroscientists and clinicians at the Institute of Neurology, Queen Square; Neuroinflammation Centre; and the Institute of Ophthalmology for assisting me on the experiments which played a major role in the content of my report. Specifically, I would like to thank Andrew and Roshni for the useful discussions we had through which I learnt many new concepts and great ideas.

My special thanks to Professor Glen Jeffery who has been a wonderful source of wisdom in dealing with complicated biological topics and for giving me inspiration and encouragement to handle the uncertainties during the experiments.

I would like to specifically thank Mr Amin Rouzbahani for his incredible support in developing Mini-CYRIL's software.

I would like to thank all my family in Iran and here who have been incredibly supportive in every aspect, from babysitting to encouraging me during the difficult times. Thank you to my amazing aunt Mehrnoush and cousins with special thanks to Raha for proofreading parts of this thesis while on holiday!

Finally, I would like to thank my little family, Afsheen and Amirreza. My special thanks to my kind loving husband Afsheen, without whom I would never be able to complete this Ph.D. Thank you for your amazing support and patience during my studies and thank you my brilliant son Amirreza for being such a good hardworking boy, so I didn't have to worry about your school work while writing in your room!

Publications Resulting from this Work

Peer-Reviewed Journal Papers

- M. F. Siddiqui, S. Lloyd-Fox, **P. Kaynezhad**, I. Tachtsidis, M. H. Johnson, and C. E. Elwell, "Non-invasive measurement of a metabolic marker of infant brain function," *Scientific Reports*, vol. 7, no. 1, pp 1330, 2017.
- **P. Kaynezhad**, I. Tachtsidis, and G. Jeffery, "Optical monitoring of retinal respiration in real time: 670 nm light increases the redox state of mitochondria," *Experimental Eye Research*, vol. 152, pp. 88-93,2016.

Magazines

- **P. Kaynezhad**, I. De Roever, G. Bale, and I. Tachtsidis, "Optical monitoring of neonatal brain injury: towards the development of compact clinical systems," *Electro Optics*, London, pp. 18–19, Mar-2016.

Conference Presentations

- **Poster Presentation: Kaynezhad,P**., & Tachtsidis,I. "Miniature broadband NIRS system for in-vivo measurement of tissue oxygenation and metabolism." Annual Meeting of Functional Near-Infrared Spectroscopy (fNIRS). Paris, France (2016).
- **Oral Presentation: Kaynezhad,P.,** & Tachtsidis,I. "Miniature broadband NIRS system for in-vivo tissue oxygenation and metabolism." 44th Annual Meeting of the International Society on Oxygen Transport to Tissue (ISOTT). Chicago, USA (2016).
- **Oral Presentation: Kaynezhad,P**., Davies,A.L., Desai, R.A., Smith,K.J., & Tachtsidis,I. " Optical monitoring of spinal cord tissue oxygenation and metabolism during hyperoxia in a preclinical model of Multiple Sclerosis." 44th Annual Meeting of the International Society on Oxygen Transport to Tissue (ISOTT). Chicago, USA (2016).
- **Oral Presentation: Kaynezhad,P**., Davies,A.L., Desai, R.A., Smith,K.J., & Tachtsidis,I. "Optical Monitoring of Spinal Cord Tissue Oxygenation and Metabolism during Hyperoxia in a Preclinical Model of Multiple

Sclerosis." 34th British Medical Laser Association Annual Conference (BMLA), Darlington, UK (2016).

- **Poster Presentation**: **Kaynezhad,P.,** Davies,A.L., Desai, R.A., Smith,K.J., & Tachtsidis,I. "Optical Monitoring of Spinal Cord Tissue Oxygenation and Metabolism during Hyperoxia in a Preclinical Model of Multiple Sclerosis." Annual Photonex Conference (PHOTONEX), Imperial College London, UK (2016).
- **Poster Presentation: Kaynezhad,P.,** Bainbridge, A., Price, A., Kawano, G., Ezzati, M., Rostami, J., Broad, K.D., Beichert, L., Rocha Ferreira, E., Fierens, I., Taylor, A.O., Golay, X., Robertson, N.J., and Tachtsidis, I. "Optical Monitoring of Brain Tissue Oxygenation and Metabolism in Hypoxia-Ischaemia in the Preclinical Neonatal Model." Institute of physics (IOP), Optics in Clinical Practice Conference III. Nottingham, UK (2015).
- **Oral Presentation: Kaynezhad,P.**, Bainbridge, A., Price, A., Kawano, G., Ezzati, M., Rostami, J., Broad, K.D., Beichert, L., Rocha Ferreira, E., Fierens, I., Taylor, A.O., Golay, X., Robertson, N.J., and Tachtsidis, I. "Investigation of the association of the early recovery of cytochrome-c-oxidase redox state with injury severity following hypoxic-ischaemia in the neonatal pig." XXVIIth International Symposium on Cerebral Blood Flow, Metabolism and Function (Brain2015) Vancouver, Canada (2015).
- **Oral Presentation: Kaynezhad,P.,** Bainbridge, A., Price, A., Kawano, G., Ezzati, M., Rostami, J., Broad, K.D., Beichert, L., Rocha Ferreira, E., Fierens, I., Taylor, A.O., Golay, X., Robertson, N.J., and Tachtsidis, I. "Optical Monitoring of Brain Tissue Oxygenation and Metabolism in Hypoxia-Ischaemia in the Preclinical Neonatal Model." 33rd Annual Scientific Meeting of the British Medical Laser Association (BMLA), Brighton, UK (2015).

Awards

- **Winner of Best Poster:** The "Popular Choice Research Poster Award" at the PHOTONEX 2016 conference, Imperial College London, London, UK.
- **Winner of Best Presentation:** The "Photodiagnostics and Photodynamic Therapy Award", sponsored by Elsevier at 33rd Annual Scientific Meeting of the British Medical Laser Association (BMLA 2015), Brighton, UK.

Table of Contents

List of Figures

List of Tables

Abbreviations

A&E	Accident and emergency
ADP	Adenosine diphosphate
AMD	Age-related macular degeneration
APD	Avalanche photodiode
ATP	Adenosine triphosphate
AUTC	Area under the curve
MBLL	Modified Beer Lambert law
CCD	Charged coupled device
CCO	Cytochrome c oxidase
CNS	Central nervous system
CW	Continuous wave
CYRIL	Cytochrome research instrument and application
DCS	Diffuse correlation spectroscopy
DP	Differential pathlength
DPF	Differential pathlength factor
EAE	Encephalomyelitis

EEG	Electroencephalogram
EPP	Exchangeable phosphate pool
ETC	Electron transport chain
$FADH_2$	Flavin adenine dinucleotide
FiO_2	Fractional inspired oxygen
fNIRS	Functional near-infrared spectroscopy
HbO_2	Oxyhaemoglobin
HbDiff	Haemoglobin difference
HbT	Total haemoglobin
HHb	Deoxyhaemoglobin
HI	Hypoxia ischaemia
HIE	Hypoxic ischaemic encephalopathy
HR	Heart rate
ICU	Intensive care unit
LD	Laser diode
LED	Light emitting diode
MBLL	Modified Beer-Lambert law
MBP	Mean arterial blood pressure

Mini-CYRIL	Miniature-Cytochrome research instrument and application
MRI	Magnetic resonance imaging
MRO_2	Metabolic rate of oxygen
MRS	Magnetic resonance spectroscopy
MS	Multiple sclerosis
μ_a	Absorption coefficient
μ_s	Scattering coefficient
μ_s'	Reduced scattering coefficient
NA	Numerical aperture
NAD+	Nicotinamide adenine dinucleotide
NADH	Nicotinamide adenine dinucleotide hydride
NIR	Near-infrared
NIRS	Near-infrared spectroscopy
NMR	Nuclear magnetic resonance
NTP	Total nucleotide triphosphate
OCT	Optical coherence tomography
oxCCO	Oxidised-cytochrome c oxidase
PCr	Phosphocreatine

PD	Photodiode
PDA	Photodiode array
PET	Positron emission tomography
Pi	Inorganic phosphate
PMT	Photomultiplier tube
PNS	Peripheral nervous system
RF	Recovery fraction
SNR	Signal to noise ratio
SpO_2	Arterial oxygen saturation
UCL1	The first broadband-NIRS system developed at UCL
UCLn	UCL algorithm with n wavelengths

Chapter 1. Introduction

This chapter introduces the motivations behind this thesis and outlines its key features. The main motivation comes from the urgent need for a portable and easily deployable optical system that can be used at the patient bedside in order to measure tissue oxygen metabolism non-invasively. This is specifically vital for tissues of the central nervous system (CNS) such as brain due to their high energy demands and high metabolic rate.

Damages and injuries to the CNS tissues as a result of metabolic dysfunction usually lead to devastating and irreversible outcomes, as most neurones in the central nervous system cannot repair or renew. Near-infrared spectroscopy (NIRS) is a bedside technique that is typically known for the in-vivo measurement of tissue oxygenation and haemodynamics. Most portable commercial NIRS systems employ 2-4 wavelengths to quantify changes in oxygenated (HbO_2) and deoxygenated (HHb) haemoglobin and they are mainly deployed for the investigation of oxygen transport to tissue in clinical and preclinical settings. However, the measurement of how the transported oxygen is consumed at cellular level for energy production essential for cells' survival is missing in these systems.

Broadband-NIRS is a non-invasive optical technique that employs more than 100 wavelengths, which as well as oxygenation measurement enables the in-vivo measurement of metabolism through measuring oxidation state of cytochrome-c-oxidase, a valuable marker of cellular oxygen metabolism. Cytochrome-c-oxidase (or CCO or COX) is advantageous over the measurement of MRO_2 (metabolic rate of oxygen), since it is directly linked to tissue energetics and provides an insight into the function of mitochondria, the powerhouse of cells.

This chapter gives an overview of the importance of measuring tissue metabolism in-vivo, then summarises the key characteristics of a portable broadband NIRS that has been developed to quantify CCO. Next, the limitations of current broadband NIRS systems which hinder them from being utilised in clinical and preclinical settings as an established tool for in-vivo measurement of metabolism will be discussed, followed by an overview of how these problems are addressed in this

thesis. The final sections give a summary of the rest of the chapters and outline my part in the work.

1.1 Introduction to Optical Techniques for Measuring Metabolism

Energy required for tissue viability and function is expressed in units of ATP (adenosine triphosphate). ATP is primarily and most efficiently synthesised through aerobic or oxidative metabolism in the mitochondria that are known as the power house of cells. Oxidative metabolism which is also called aerobic respiration or cell respiration is a chemical process in which oxygen is utilised to produce energy from glucose through a series of oxidation reduction procedures. A very small amount of ATP ~2 out of around 30 per one molecule of glucose is generated in the absence of oxygen via anaerobic metabolism. ATP generation is highly crucial in maintaining normal function in nervous tissues.

Nerve cells or neurones depend almost entirely on aerobic metabolism for their energy supply. For instance, in a highly energy demanding organ such as brain in the central nervous system (CNS), in case of severe states such as cardiac arrest or stroke, a decrease in blood flow and oxygen below a certain level can lead to a 90% drop in ATP levels within 5 minutes. This could eventually lead to cell death that is often irreversible. Unlike the peripheral nervous system that has an intrinsic capability to regenerate and repair, most part of the CNS is incapable of regeneration and repair, therefore, monitoring tissue metabolism in the CNS is crucial. Several CNS injuries and disorders have been associated with abnormal tissue oxidative metabolism, most commonly as a result of disruption of the oxygen supply following a significant reduction in blood flow, or other origins such as inflammation or degeneration [1]. Whether the reason behind mitochondrial dysfunction in the nervous tissue is oxygen deficiency (hypoxia) or inflammation in general, the outcome is always devastating and as mentioned above often irreversible.

In this thesis, I investigate the development and application of a miniature optical system for the measurement of metabolism in three main parts of the CNS including brain, spinal cord and the retina in which mitochondrial dysfunction and neuronal death leads to permanent neurological disorders. These conditions include neonatal hypoxia-ischaemia (HI) usually following birth asphyxia, multiple sclerosis (MS), a neuro-inflammatory disease which usually affects people between 20-50 years

old and leads to limb paralysis and eventually premature death, as well as age-related macular degeneration (AMD), a common eye condition which is a leading cause of vision loss in people age 50 and over ultimately leading to loss of central vision. What all these diverse conditions have in common, is the permanent damage to the tissue because of impaired metabolism, which makes them necessary to be further investigated and studied. Techniques such as PET (positron emission tomography) and MRI/MRS (magnetic resonance imaging/spectroscopy) are gold standard methods in the clinic for the in-vivo measurement of metabolism. These techniques usually assess one or more contributing factors involved in ATP production to investigate tissue metabolism. The main parameters that are studied using these techniques include blood flow, tissue glucose uptake and metabolic rate of oxygen. Metabolic rate of oxygen (MRO_2) is known as the most reliable measure for the evaluation of oxygen metabolism in tissues which is estimated from three other parameters including blood oxygen saturation, total haemoglobin concentration and blood flow. MRO_2 can be also measured through optical techniques such as OCT (optical coherence tomography) and DCS (diffuse correlation spectroscopy). Optical techniques for in-vivo measurement of metabolism are advantageous to both PET and MRS, as these techniques are expensive equipment and involve ionising radiations, radio isotopes and large magnetic fields. These characteristics make PET and MRS impractical for bedside measurements, specifically for children, neonates and patients in intensive care units (ICU). Even though the measurement of MRO_2 is very useful in understanding tissue oxygen delivery and uptake, it fails to provide a direct measurement of tissue energetics at cellular level and simply relies on blood oxygenation measurements.

Broadband-NIRS is a unique optical technique in providing metabolism measurement at cellular level. It is based on the relative transparency of biological tissues specifically bones to NIR light (650-900 nm). It is also advantageous to other optical methods as it provides a ‘mitochondria-specific’ marker independent of haemoglobin oxygenation measurements and enables direct measurement of oxidative metabolism at cellular level. This marker is cytochrome-c-oxidase (CCO or COX), a key enzyme in the electron transport chain of the mitochondria which is responsible for over 95% of tissue oxidative metabolism. Like haemoglobin, which has an oxygenation dependent absorption spectrum in the NIR region (arterial blood

appearing bright red and venous blood appearing dark red), CCO has also a broad absorption band in the NIR that is redox dependent. Therefore, NIRS provides continuous non-invasive measurement of tissue oxygenation, haemodynamics and metabolism without the need for radioisotopes or contrast agents. The diagnostic potential of Broadband-NIRS was established after 1977, when Jobsis demonstrated a continuous measurement of brain tissue concentration of oxygenated and deoxygenated haemoglobin as well as CCO in anesthetised cats [2].

Continuous-wave (CW)-NIRS systems that are in the scope of this thesis and simply relate changes in light intensity to changes in relative concentration of haemoglobin, are relatively simple cost-effective instruments. CW-NIRS systems mainly include a light source emitting light at a constant frequency and amplitude for tissue illumination and a detector to measure light that has traversed the tissue either through reflection or transmission mode. The measured change in the attenuation of light through the tissue is simply converted to the change in the concentration of the NIR absorbing biomolecules (called chromophores) using the modified Beer-Lambert Law, which will be discussed in more details in chapter 3.

Most commercial CW-NIRS systems use 2-4 discrete wavelengths to quantify changes in oxygenation and haemodynamics and are incapable of providing CCO measurement, as its concentration in-vivo is one order of magnitude smaller than that of haemoglobin. Therefore, it is most likely that the resulting CCO signal be just a cross-talk artefact of the larger haemoglobin signal produced by the measurement algorithms. Broadband-NIRS systems however provide reliable measurement of CCO through utilising more than 100 wavelengths in the measurement algorithm hence minimising the cross-talk artefacts. A typical broadband NIRS system consists of a broadband light source (mainly white light source based on halogen-tungsten bulbs), broadband spectrometer (comprising a spectrograph and a CCD detector) to measure all the wavelengths across the spectrum and optical fibre cables to direct the light to/from the tissue. Since biological tissues are highly scattering media (because of the large refractive index mismatch among cells and tissues), the optical fibres in CW-broadband-NIRS systems are usually designed with large surface area and high numerical aperture (NA), to maximise light collection from tissue surface.

1.2 Motivations

So far three Broadband-NIRS systems have been developed at UCL, dedicated for the study of brain oxygenation, haemodynamics and metabolism in babies, adults and piglets. All the systems have Oriel radiometric fibre optic illuminator by Newport (77501) as their light source with different detection units. The first system which is the first broadband system developed at UCL in 1995 (UCL1) and has been used in this project as a gold standard, is a single channel system, with one source and one detector fibre which includes a mirror-based spectrograph with Wrights Instrument CCD. This system has been used in the preclinical study of Neonatal Hypoxia-Ischaemia at the UCL Institute of Neurology for about 20 years [3]. The second system is a four-channel system called (pHOS), which was developed in 2007 and has been used at the National Hospital for Neurology and Neurosurgery. pHOS includes a custom-built lens spectrograph with Princeton Instrument CCD and is used for brain oxygenation and metabolism measurement in adults with traumatic brain injury (TBI) [4]. The third system, called CYRIL developed in 2014, includes a lens based spectrograph with Princeton Instrument CCD, and is used at UCLH for the study of hypoxic-ischaemic encephalopathy (HIE), following birth asphyxia or other pregnancy complications, in new-born infants [5]. Recently (in 2016), another variation of the pHOS system has been developed with the capacity to do imaging [6]. All the systems have been shown to provide reliable measurements of changes in the oxidation state of CCO (Δ[oxCCO]) in clinical and preclinical studies.

Despite being simple, non-invasive, cost-effective and providing an independent marker of oxygen metabolism at cellular level, broadband-NIRS has remained mostly as a research tool rather than a clinical system. There are three main areas hindering broadband NIRS from being established as a bedside clinical instrument for metabolism measurement and the motivation of this project is built on these limitations:

1- Lack of clear understanding about the information that CCO measurement delivers: The physiological information that the measurement of CCO can provide for the clinicians is still unclear and somehow controversial. That is mainly because the relationship between the broadband-NIRS measurement of CCO

with other metabolic markers for brain injury that are measured with gold standard techniques, such as MRI/MRS or PET is not widely investigated.

2- **Bulkiness and complex daily calibrations:** While easy transportation and application are two important features of a bedside clinical system, current Broadband-NIRS systems are bulky and heavy hence difficult to handle in demanding environments such as intensive care unit (ICU) or accident and emergency (A&E), where many other monitoring equipment is used. Such systems typically occupy big trolleys and require calibration on a daily basis, which needs to be done by a trained physicist or clinician and is in contrast with a bedside clinical instrument.

3- **Absence of extensive research on other CNS tissues**: Despite PET and MRS that are applicable to a broad range of tissue metabolism measurements, most research in the broadband-NIRS and the measurement of CCO as a marker for metabolism has been extensively focused on brain (due to its high importance) and to a small extent on muscle studies. There are however other tissues in the CNS, also highly dependent on aerobic metabolism, including spinal cord and the retina (the neural tissue of the eye with a very high metabolic rate). While the in-vivo measurement of oxidative metabolism in such tissues could be valuable in studying many diseases where impaired metabolism is involved, there is very little or no research in broadband-NIRS studies of other CNS tissues.

There is therefore, a need for a compact portable system that can be easily deployed by non-physicists/engineers across various clinical and preclinical settings for in-vivo assessment of oxygenation and metabolism at bedside.

1.1 Aims and Objectives

A mentioned in the previous section, historically broadband-NIRS instruments for measuring in-vivo cytochrome-c-oxidase concentration changes, have been bulky, requiring large trolleys to transport them and occupied significant space within the experimental environment either laboratory or the hospital. These issues hinder their use and acceptance among experimentalist and clinicians. These early broadband-NIRS instruments required extensive calibration routines before measurements and their operation required some training and physics knowledge. In addition, there was a lack of knowledge in understanding the significance of the broadband-NIRS measurement of cytochrome-c-oxidase and its relationship with other brain tissue biochemistry markers of brain tissue injury.

The aims of this PhD are (1) to develop a novel portable broadband-NIRS instrument based on easily sourced components, which can be deployed in a variety of preclinical and clinical settings for the in-vivo measurement of tissue oxygenation (haemoglobin concentration changes) and metabolism (cytochrome-c-oxidase concentration changes) without the need for a physicist or engineer to collect and interpret the data; (2) and to demonstrate the relationship of the broadband-NIRS measurement of cytochrome-c-oxidase with the Magnetic Resonance Spectroscopy (or MRS) metabolic markers during and following hypoxic-ischaemic brain injury.

Not only miniaturised in size, which significantly enhances the portability and integration of the broadband-NIRS system in demanding pre-clinical and clinical settings, the proposed system will be advantageous to previously used systems in terms of ease of application with no daily wavelengths calibration required and the software which is easily operated by non-physicists and will be able to calculate absolute changes in the concentration of chromophores using the real-time changes in the optical pathlength measurement and display that is missing in all the existing systems. Existing NIRS systems (both commercial and broadband systems) quantify chromophore concentration changes assuming a fixed optical pathlength across all the subjects and for all source-detector spacings. The real-time display of optical pathlength that is also missing in the originally developed system enables monitoring changes in the scattering features that could possibly occur because of changing pathology following an injury.

To achieve the above aims the following objectives need to be completed:

1- Further investigation of the physiological information that the measurement of Δ[oxCCO] can deliver as a marker for CNS tissue metabolism and its correlation with measurements of mitochondrial energetics provided by MRS as a gold standard. To pursue this objective, the following steps were taken:

a. Exploring the relationship between Δ[oxCCO] as a mitochondrial marker with a gold standard clinical marker for tissue oxidative metabolism. In this project, the correlation between Δ[oxCCO] measurement has been investigated with the phosphorus (^{31}P)-MRS metabolite measurements as an established method for assessing brain status during and after induced hypoxia-ischaemia in an animal model, which is discussed in chapter 4.

b. Investigating the establishment of a quantifiable Δ[oxCCO] measure that can be easily interpreted and used by clinicians to monitor the HI or direct clinical manoeuvres when necessary.

Note: Objective 1 is the major part of this project and is investigated in all other sections (including spinal cord, retinal and functional activation studies).

2- To develop a novel compact broadband-NIRS system based on Ocean Optics light source and spectrometers, with a user-friendly interface allowing clinicians to collect and analyse the data. To pursue this objective, the following steps should be taken:

a. To investigate whether off-the-shelf miniature spectrometers with interesting advantages compared to custom-built units, such as low-cost, small footprint, light weight, use of high performance integrated CCDs and wide availability, can be used or modified to develop a portable clinical broadband-NIRS system for in-vivo measurements with a comparable performance to the current custom-built typical spectrometers.

b. To develop or utilise a compact white light source suitable for broadband-NIRS measurement.

c. To develop user-friendly software based on MATLAB which can be easily run and modified by other users. The software should continuously collect the NIRS spectral data and process the intensity data for the calculation and display of the concentrations of chromophores in real time.

3- To validate the miniature system primarily through standard cuff occlusion measurement and via comparing its performance with the gold standard custom-built system, UCL1, that has been used in the preclinical study of HI.

4- To explore and investigate new in-vivo applications for broadband-NIRS, oxCCO measurement using the developed miniature system (to investigate the feasibility of CCO measurement as a potential marker for other CNS tissue, toward the establishment of CCO as a bedside clinical marker). To pursue this objective, the potential of the Δ[oxCCO] measurement as a valuable marker for cellular oxidative metabolism will be examined in other CNS tissues with high energy demand such as spinal cord and the retina, where there is a large density of mitochondria and in-vivo measurement of CCO could be feasible.

1.3 Thesis Outline

This thesis has 8 subsequent chapters. The next two chapters include the background to the work followed by two methods chapters. The first one focuses on developing methods to understand the physiological information that CCO measurement delivers through investigating its correlation with ^{31}P-MRS markers for brain injury in new-born pigs. The next chapter which is the main scope this project, explains the development of two miniature broadband-NIRS systems with their specific challenges. Results are described in three following chapters each describing utilisation of the miniature broadband-NIRS system for the first time in preclinical studies.

Note: While all 3 results are presented to show the applicability of the miniature system in various in-vivo CNS tissue measurements, due to the multidisciplinary nature of this PhD thesis and the diversity of the applications of the miniature systems, each result chapter includes its brief background and physiological motives (that are the important aspect of this thesis).

The thesis ends with a discussion chapter that summarises the work done and describes the future work.

Background: This section includes two chapters. Chapter 2 covers the physiology background with a specific focus on the importance and techniques of measuring oxidative metabolism within the CNS. The chapter ends with the advantages of optical techniques for the in-vivo measurement of metabolism with a specific focus on NIRS offering CCO measurement as a useful marker for metabolism at cellular level.

Chapter 3 describes the background to tissue optics and the principles behind NIRS, and advantages of CW systems for in-vivo measurement of metabolism. The chapter follows with demonstrating some challenges associated with in-vivo measurement of CCO and how broadband NIRS overcomes these challenges. This chapter ends with a review about current broadband-NIRS systems and their application with an emphasis on the broadband-NIRS systems developed at UCL.

Methods: There are two chapters in the methods section:

Chapter 4 describes a study that was carried out as part of the software development and focuses on investigating the correlation between the CCO measurement that UCL1 provides with the ^{31}P-MRS markers for brain injury in piglets. An algorithm has been developed that offers a quantifiable measure that can be used by clinicians as a surrogate marker to determine the severity of piglets' brain damage following a hypoxic ischaemic brain injury. The algorithm has been developed based on the results that I acquired from UCL1 developed by Roger Springett [7] and has been used in the preclinical study of Hypoxia-Ischaemia (HI) in the neonatal pigs for measuring oxygenation and more specifically metabolism through CCO measurement [3]. This system has been used as a gold standard in this thesis due to its robust performance for many years. The results of this work were also presented in two international conferences [11]. The algorithm is implemented in the latest version of the software to assist the clinicians with inducing and monitoring HI in piglets.

Chapter 5 discusses the experimental work done towards the development of two compact portable clinical system using Ocean Optics miniature light source and spectrometers. The system is called mini-CYRIL, as a reference to the original broadband system CYRIL (CYtochrome Research Instrument and appLication) that was developed by Bale et al. [5]. The challenges and limitations for each system named as mini-CYRIL1 (mini-CYRIL, version 1) and mini-CYRIL2 (mini-CYRIL version 2) are investigated and the proposed solutions and upgrades are discussed in detail. The chapter ends with some cuff-occlusion measurements (as a standard technique to validate novel NIRS systems in the literature) to evaluate the performance of mini-CYRIL in vivo. The results of this work were presented in two international conferences [12].

Results: This section has three chapters including the results from utilising mini-CYRIL1 and mini-CYRIL2 in three different studies where in two of them CCO measurement has been introduced for the first time.

The use of Mini-CYRIL2 in monitoring new-born pigs in the animal study of HI (explained in chapter 4) is presented in chapter 6. In this chapter, the results from the original system developed by Springett, et al [3], [7] is compared with the results from mini-CYRIL2. Development of mini-CYRIL2 has been reported in the Electro Optics magazine [8].

Chapter 7 explains the use of mini-CYRIL1 to investigate the role of hypoxia in an animal model of multiple sclerosis, through in-vivo measurement of change in oxygenation and metabolism in the spinal cord of adult rats for the first time. The results of this work were also presented in three international conferences [13].

Chapter 8 depicts a novel application for the broadband-NIRS. It explains how mini-CYRIL1 for the first time was used to measure changes in retinal metabolism in real time using broadband-NIRS. This chapter explains the experimental design for in-vivo measurement of the retina of adult rats. The results were validated using residual analysis during treatment with red light which has shown to increase cells' respiration and ATP production. The results from this study have been published in Experimental Eye Research [9].

Discussion and Future Work: The final chapter (chapter 9) includes a summary and discussion of the results presented in this thesis and is followed by brief description of future work, which include system upgrades and new applications. The chapter ends with conclusion, a short summary of the whole thesis.

1.4 Personal Statement

The work presented in this thesis can be separated into five parts:

1- The analysis of multimodal data (MRS and NIRS data) to understand the CCO signal in relation to brain injury severity following the induction of hypoxia ischaemia in the neonatal pig and to develop an algorithm with a quantifiable measure of CCO that can be used to predict the degree of brain injury in piglets following HI.

2- The development of two miniature broadband-NIRS systems for real-time measurement of metabolism and oxygenation, high sensitivity mini-CYRIL1 applicable for reflection mode NIRS and exposed tissue studies as well as large throughput mini-CYRIL2 applicable in any measurement including brain transmission mode NIRS in the neonatal pig.

3- Application of mini-CYRIL2 and its measurement of CCO in the preclinical study of HI. The measurement of CCO produced by mini-CYRIL2 has been used to monitor the hypoxic-ischaemic insult in piglets' brain which led to inducing relatively similar brain injuries in all piglets.

4- Application of mini-CYRIL1 and the measurement of CCO to investigate the role of hypoxia in an animal model of multiple sclerosis (MS). Mini-CYRIL1 was used to measure real-time changes in spinal cord oxygenation and cellular respiration during transient hyperoxia (100% oxygen) in naïve rats and rats affected with experimental autoimmune encephalomyelitis (EAE) which is an animal model for MS.

5- Application of mini-CYRIL1 and the measurement of CCO in the first NIRS measurement of retina and the first in-vivo measurement of retinal metabolism. CCO measurement produced by mini-CYRIL1 was used to monitor the dynamics of change in oxygenation and retinal oxidative metabolism during transient exposure to low-power 670 nm light, which has shown to have therapeutic effects due to improving cellular respiration, ATP upregulation and reducing inflammation.

Remark: Mini-CYRIL2 and the measurement of CCO has also been used for the first time in the functional activation study (fNIRS) of developing human

brain [10]. The miniature system was used to monitor brain metabolic changes during visual auditory stimulation in 4-6-month-old infants.

As a multidisciplinary project, some of the work in this thesis is a result of collaboration by a number of individuals; therefore, it is important to acknowledge those involved and to highlight the work I carried out, which was done by the guidance of my supervisor Dr. Ilias Tachtsidis.

- The first part was mainly done by me. This includes system calibration, data collection and multimodal data analysis. Piglet preparation before inducing HI including surgery, setting up for systemic data monitoring, etc. was performed by the clinical team from the Preclinical Neonatal Neuroprotection group and MRS data collection was performed by MR physicists; Dr Alan Bainbridge and Dr David Price. The script for synchronising the NIRS data with the MRS and systemic data was written by Dr Aaron Oliver Taylor.
- The second part which is the development of the miniature system was carried out by me with the help of industry partners. This involved the selection and modification of optical components, the design and fabrication of optical fibres, the development of MATLAB software and preliminary testing and characterisation of the system. The system couldn't have been developed without the guidance from Dr Nick Barnett from Prolite UK, who was a great help in component selection and modification, and Dr. Margarethe Kampling from LOPTEK, Germany who assisted with optical fibres' design and fabrication.
- Data acquisition in the preclinical study of HI using mini-CYRIL2, was performed by myself and the clinical team, mainly Ingran and Kathryn as well as Adnan, Chris and Sara. MSc students Miss Melody Lun (whom I supervised) and Mr Cornelius Bauer were also responsible for data acquisition during their MSc projects. Data synchronisation script was originally written by Melody and the data analysis and script modification was done by me. I was also responsible for system maintenance and regular upgrades, ensuring good quality optical data collection, evaluation of optical data, synchronising the NIRS and systemic data, and saving backups of the data securely.

- In the preclinical MS study, I was responsible for the initial experimental setup including the selection of suitable optical fibres and data acquisition was primarily carried out by me. In later stage, data was collected by Dr Andrew Davies and Dr Roshni Desai at the Neuroinflammation Centre of the UCL Institute of Neurology, with my support ensuring good quality optical data is acquired. The data analysis was carried out by me.
- The retina study using mini-CYRIL1 was mostly carried out by me with great support from Professor Glen Jeffery at the UCL Institute of Ophthalmology. The experimental design, including design of optical fibres and part of the hypothesis in this study was developed by me. I also carried out the data analysis with guidance of my supervisor and Professor Jeffery. The results from this study have been published in the Experimental Eye Research journal [9].
- Applying mini-CYRIL2 in the fNIRS baby study and data analysis was done by Miss Maheen Siddiqui at Birkbeck baby lab. I was responsible for developing another mini-CYRIL2 system with different optical fibres, system maintenance, ensuring good quality optical data collection, evaluation of optical data and residual analysis. The results from this study have been published in Nature Scientific Reports [10].

Bibliography

[1] P. Liu, L. F. Chalak, and H. Lu, "Non-invasive assessment of neonatal brain oxygen metabolism: A review of newly available techniques," *Early Hum. Dev.*, vol. 90, no. 10, pp. 695–701, 2014.

[2] F. F. F. Jobsis, "Noninvasive, Infrared Monitoring of Cerebral and Myocardial Oxygen Sufficiency and Circulatory Parameters," *Science (80-.).*, vol. 198, no. 4323, pp. 1264–1267, 1977.

[3] C. E. Cooper and R. Springett, "Measurement of cytochrome oxidase and mitochondrial energetics by near-infrared spectroscopy.," *Philos. Trans. R. Soc. Lond. B. Biol. Sci.*, vol. 352, no. 1354, pp. 669–676, 1997.

[4] I. Tachtsidis, L. Gao, T. S. Leung, M. Kohl-Bareis, C. E. Cooper, and C. E. Elwell, "A hybrid multi-distance phase and broadband spatially resolved spectrometer and algorithm for resolving absolute concentrations of chromophores in the near-infrared light spectrum.," *Adv. Exp. Med. Biol.*, vol. 662, pp. 169–75, 2010.

[5] G. Bale, S. Mitra, J. Meek, N. Robertson, and I. Tachtsidis, "A new broadband near-infrared spectroscopy system for in-vivo measurements of cerebral cytochrome-c-oxidase changes in neonatal brain injury.," *Biomed. Opt. Express*, vol. 5, no. 10, pp. 3450–66, 2014.

[6] P. Phan, D. Highton, J. Lai, M. Smith, C. Elwell, and I. Tachtsidis, "Multi-channel multi-distance broadband near-infrared spectroscopy system to measure the spatial response of cellular oxygen metabolism and tissue oxygenation," *Biomed. Opt. Express*, vol. 7, no. 11, p. 4424, Nov. 2016.

[7] R. Springett, M. Wylezinska, E. B. Cady, M. Cope, and D. T. Delpy, "Oxygen dependency of cerebral oxidative phosphorylation in newborn piglets.," *J. Cereb. Blood Flow Metab.*, vol. 20, no. 2, pp. 280–9, 2000.

[8] P. Kaynezhad, I. De Roever, G. Bale, and I. Tachtsidis, "Optical monitoring of neonatal brain injury: towards the development of compact clinical systems," *Electro Optics*, London, pp. 18–19, Mar-2016.

[9] P. Kaynezhad, I. Tachtsidis, and G. Jeffery, "Optical monitoring of retinal respiration in real time: 670 nm light increases the redox state of mitochondria," *Exp. Eye Res.*, vol. 152, pp. 88–93, 2016.

[10] M. F. Siddiqui, S. Lloyd-Fox, P. Kaynezhad, I. Tachtsidis, M. H. Johnson, and C. E. Elwell, "Non-invasive measurement of a metabolic marker of infant brain function," *Sci. Rep.*, vol. 7, no. 1, p. 1330, 2017.

[11] Kaynezhad,P., Bainbridge, A., Price, A., Kawano, G., Ezzati, M., Rostami, J., Broad, K.D., Beichert, L., Rocha Ferreira, E., Fierens, I., Taylor, A.O., Golay, X., Robertson, N.J., and Tachtsidis, I. "Investigation of the association of the early recovery of cytochrome-c-oxidase redox state with injury severity following hypoxic-ischaemia in the neonatal pig." XXVIIth International Symposium on Cerebral Blood Flow, Metabolism and Function (Brain2015) Vancouver, Canada (2015) and 33rd Annual Scientific Meeting of the British Medical Laser Association (BMLA), Brighton, UK (2015).

[12] Kaynezhad,P., & Tachtsidis,I. "Miniature broadband NIRS system for in-vivo measurement of tissue oxygenation and metabolism." Annual Meeting of Functional Near-Infrared Spectroscopy (fNIRS). Paris, France (2016) and 44th Annual Meeting of the International Society on Oxygen Transport to Tissue (ISOTT). Chicago, USA (2016)

[13] Kaynezhad,P., Davies,A.L., Desai, R.A., Smith,K.J., & Tachtsidis,I. " Optical monitoring of spinal cord tissue oxygenation and metabolism during hyperoxia in a preclinical model of Multiple Sclerosis." 44th Annual Meeting of the International Society on Oxygen Transport to Tissue (ISOTT). Chicago, USA (2016), 34th British Medical Laser Association Annual Conference (BMLA), Darlington, UK (2016) and Annual Photonex Conference (PHOTONEX), Imperial College London, UK (2016)

Chapter 2. In-Vivo Measurement of Oxygen Metabolism in the Central Nervous System: Towards Establishing a Bedside Marker

In-vivo measurement of tissue metabolism is crucial in health and disease. This is of specific importance for tissues in the central nervous system (CNS) as nerve cells (neurones) in the CNS seldom repair or regenerate in case of damage. CNS neurones have a very high metabolic rate to meet their large energy demand hence are extremely susceptible to impaired metabolism and energy deficiency. Therefore, real-time measurement of CNS tissue energetics is enlightening in a broad range of preclinical and clinical research, as understanding tissue metabolism and how it is governed in different tissues enables building strategies for diagnosis, treatment, and prevention of disease.

In order to realise the importance of in-vivo measurement of metabolism, this chapter starts with an introduction to tissue metabolism and its different pathways, which is essential for the function and survival of biological tissues. It then proceeds with the significance of in-vivo measurement of metabolism in the CNS. Next, the techniques and recognised markers for measuring metabolism are discussed focusing on PET and MRI/MRS as gold standard diagnostic tools. Then the need for identifying a bedside marker for tissue respiration and the advantages of optical techniques in providing this marker for oxygen metabolism is discussed. The chapter proceeds with introducing cytochrome-c-oxidase (CCO) as a promising 'mitochondria-specific' marker for tissue metabolism and Near-Infrared Spectroscopy as a non-invasive optical technique for measuring CCO, which will be described in full details in the next chapter. The chapter finally ends with an introduction to the use of animal studies in understanding the physiology and resolving the optical issues surrounding the CCO measurement which is one of the aims of this thesis.

2.1 Metabolism and ATP Production in Living Cells

Cells are the building blocks of any living organism including the human body. There are many different types of cells with their own characteristic types and shapes

such as red blood cells with a spherical shape and having a diameter of 6-8 μm, in contrast with tree-like nerve cells comprising a body, that varies in size from 4-100 μm diameter, and a long fibre with varying length from a fraction of an inch to several feet. Figure 2.1 illustrates a simplified cell structure with its different compartments, called organelles that carry out specific cellular functions. Each cell has a membrane called cell membrane or plasma membrane which separates the watery phase inside the cell, cytoplasm, from that outside the cell, extracellular fluid [1]. The nucleus is the largest organelle in the cell, which includes the hereditary material DNA in which the ribosomes are synthesised before they migrate to the cytoplasm where they play an essential part in protein synthesis. The cytoplasm contains different compartments including mitochondria that are the powerhouse of the cell. Energy in cells is stored in large biomolecules called adenosine triphosphate (ATP). ATP is broken down to form ADP (adenosine diphosphate) and releases a large amount of energy**.** The majority of the ATP required for cellular function and survival is produced in the mitochondria. The chemical process through which energy is held in form of ATP in cells is called cellular respiration or metabolism. This includes all the breakdown and synthesis reactions, to produce ATP by oxidising carbohydrates, fatty acids, protein, lactate and ketones. Human nerve cells and muscle cells have more mitochondria and higher metabolic rate to meet their high energy demand.

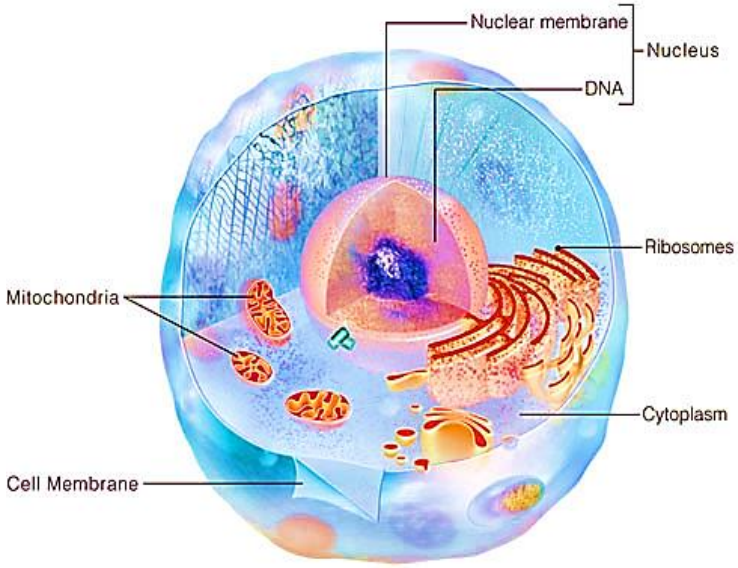

Figure 2.1: Simplified structure of a mammalian cell. Image taken from http://www.d.umn.edu/cla/faculty/troufs/anth1602/images/dna_0302_500.jpg

The most common fuel for ATP production in cells is glucose, which is the breakdown product of more complex molecules, carbohydrates. Fats and proteins are also broken down to simple molecules in the form of fatty acids and amino acids, which can be used for ATP production. However, in this thesis I will only focus on ATP production from the metabolism of glucose ($C_6H_{12}O_6$), as glucose is the main fuel for ATP production in the central nervous system. ATP generation is driven by oxidative phosphorylation, which occurs in the mitochondria of the cell. Oxidative phosphorylation starts with oxidation of NADH and is completed by addition of a phosphate group to ADP to form ATP. Cellular respiration can be summarised in the following equation [2].

$$\underbrace{C_6H_{12}O_6 + 6O_2}_{\text{Substrates}} \rightarrow \underbrace{6CO_2 + 6H_2O + 38ATP}_{\text{Products}} \quad (2.1)$$

2.2 ATP Production Pathways

ATP is a large energy-rich biomolecule often referred to as the currency of energy or the energy store in biological systems. ATP can be synthesised in two ways; anaerobic and aerobic respiration, summarised in Figure **2.2**. Anaerobic metabolism of glucose, also called glycolysis is a process in which glucose is broken down to form pyruvate. Glycolysis takes place in the cytoplasm, outside the mitochondria and does not need the presence of oxygen. Aerobic metabolism or respiration happens in the mitochondria and requires molecular oxygen to complete. It is the efficient pathway of ATP production and includes the complete oxidation of one molecule of glucose to carbon dioxide and water, which harvests about 36 molecules of ATP compared to only 2 molecules of ATP generated via anaerobic metabolism. The rest of this section describes ATP production pathways in more details.

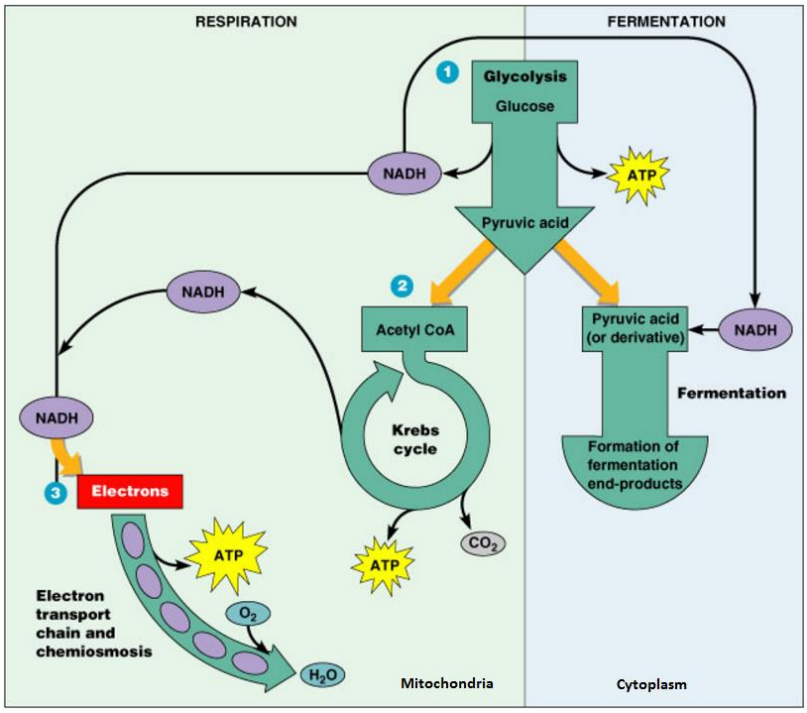

Figure 2.2: Simplified diagram of ATP production pathways through glucose metabolism ©2004 Pearson Education, Inc., Publishing as Benjamin Cummings. Image taken from http://classes.midlandstech.edu/carterp/Courses/bio225/chap05/ss4.htm

2.2.1 Anaerobic Metabolism (Glycolysis)

The first stage in the generation of ATP is glycolysis, which is simply the breakdown of glucose. It is an anaerobic process occurring in the cytoplasm of the cell during which glucose ($C_6H_{12}O_6$) as the substrates are converted into two pyruvate molecules ($C_3H_4O_3$), two NADH molecules, and two molecules of ATP. NADH (nicotinamide adenine dinucleotide) is an energy carrier or coenzyme, which temporarily holds the energy to be used in stage three. The two molecules of pyruvates are then transferred into the mitochondria where the 2nd and 3rd stages of respiration happen.

$$C_6H_{12}O_6 \longrightarrow 2\,(C_3H_4O_3) + 2\,NADH_2 + 2ATP \qquad (2.2)$$

2.2.2 Aerobic Metabolism

Aerobic energy metabolism occurs in the mitochondria of cells and in the presence of oxygen. It involves two procedures; the Krebs cycle and the electron transport chain, which are described below.

2.2.2.1 Krebs (Citric Acid) Cycle

In the Krebs cycle, also called citric acid or tricarboxylic acid (TCA) cycle, the energy in pyruvate molecules is transferred into two energy carriers NADH and $FADH_2$. During this process, the pyruvate molecules, as substrates, are oxidised and converted to 2 acetyl sugars. The acetyl sugars then react with water molecules and produce 2 ATP molecules as well as 6 NADH, 2 $FADH_2$ and 4 carbon dioxide molecules, which is a waste product. Like $NADH_2$, $FADH_2$ is also a coenzyme and assists with ATP production in stage 3 which is the electron transport chain (ETC).

$$2 \text{ Pyruvate sugars} + 2 \text{ NAD} + \longrightarrow 2 \text{ Acetyl sugar-CoA} + 2CO_2 + 2NADH_2 \quad (2.3)$$

$$2 \text{ Acetyl-CoA} + 6 H_2O \longrightarrow 4 CO_2 + 6 NADH_2 + 2 FADH_2 + 2 \text{ ATP} \quad (2.4)$$

2.2.2.2 Oxidative Phosphorylation

Oxidative phosphorylation is the main pathway through which cells produce ATP and is responsible for the production of the majority of ATP molecules per one molecule of glucose (theoretically between 30-34 out of the total 38 ATP molecules per one molecule of glucose. However, this is likely less than 30 due to other processes such as uncoupling and mitochondrial ROS production which are not in the scope of this thesis). Oxidative phosphorylation occurs in the inner mitochondria membrane, and can be broken down into two parts: oxidation of NADH and $FADH_2$ via protein complexes (known as I-IV, as shown in Figure 2.3) in the ETC, including a system of complex molecules and mobile carriers, and phosphorylation, the production of ATP at complex V (known as ATP synthase). Oxidative phosphorylation starts with the arrival of free electron carriers NAD and FAD at the Kerbs cycle which transfer electrons to complex I and II. These electrons are then passed through other complex molecules and electron carriers until they reach oxygen, the final electron acceptor,

where oxygen is reduced to water. The process of oxidation at each of the complexes I, III and IV results in the pumping of protons across the membrane from the matrix to the inner-membrane space, which creates an electrochemical gradient across the membrane. The proton gradient powers the ATP synthase, which is an enzyme capable of producing high amounts of ATP by adding a phosphate molecule (inorganic phosphate, Pi) to ADP.

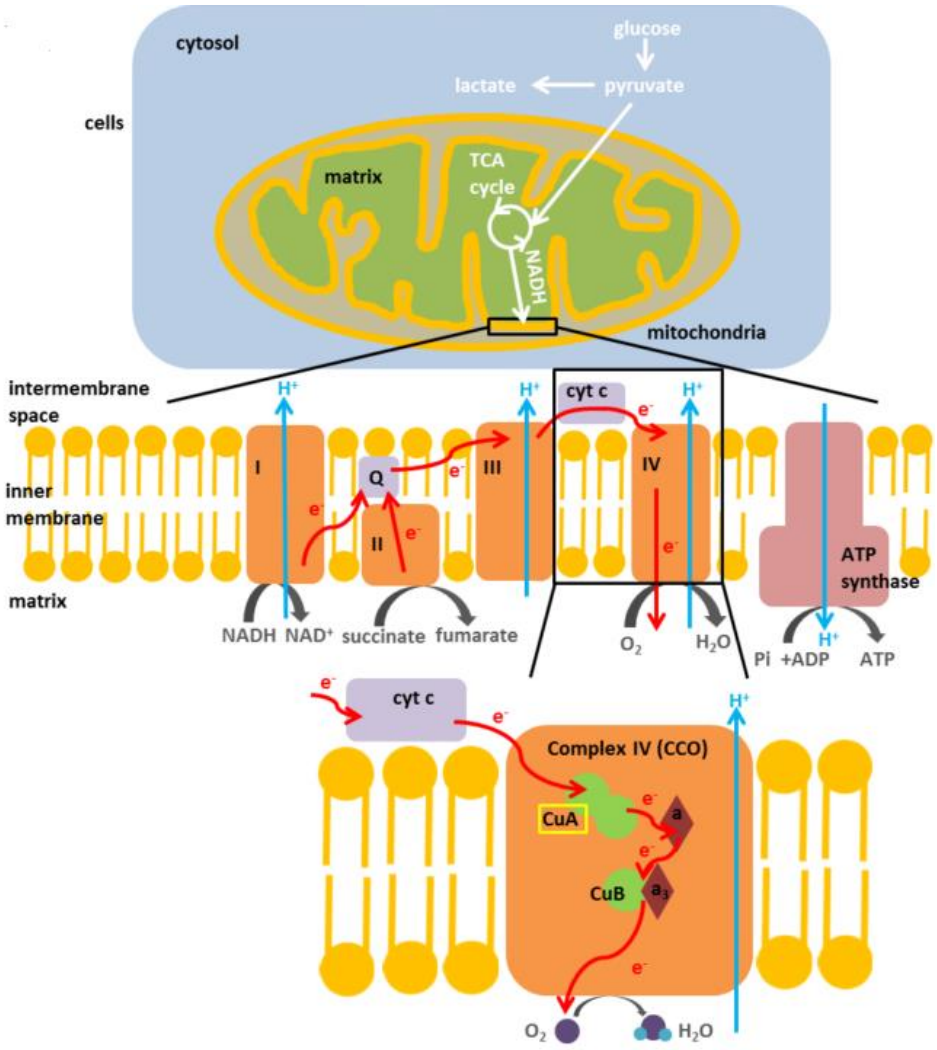

Figure 2.3: Schematic of cellular metabolism with the electron transport chain and CCO expanded. CCO is represented as complex IV. This diagram is limited to the carbohydrate metabolism (from glucose); fat metabolism, also aerobic, is ignored. Chromophores. Image taken from [3].

During ATP decomposition, the high-energy phosphate bond is broken and a large amount of energy is released which can be consumed in cells. The ETC is

completed when the electrons are transferred to molecular oxygen as the final electron acceptor. Cytochrome c oxidase (CCO) is the final enzyme in the ETC and oversees transferring the electrons to reduce molecular oxygen to water. CCO is responsible for more than 95% of aerobic energy metabolism in the cells. Therefore, the oxidation and reduction status of CCO is a good indicator of cellular oxidative metabolism and tissue oxygen consumption.

The constituents of the ETC are organised into four complexes. Each of these large complexes includes several subunits and are briefly described below:

Complex I (NADH dehydrogenase): Complex I accepts electrons with high transfer potential from reduced NADH and acts as the link between the three stages of Glycolysis, the Krebs cycle, and the ETC. The overall reaction of this complex is:

$$NADH + H^+ + CoQ \rightarrow NAD^+ + CoQH_2 \qquad (2.5)$$

CoQ is a mobile electron carrier diffusing freely in the bilipid layer of the inner mitochondrial membrane. The transfer of electrons from NADH to CoQ is an active transport meaning that it is coupled to the transfer of protons across the membrane creating a proton gradient [4].

Complex II (Succinate dehydrogenase): Complex II includes succinate dehydrogenase enzyme, which participates in both the Krebs cycle and the ETC. The outcome of this complex is a transfer of two electrons, one at a time to coenzyme Q to produce Fumarate and $CoQH_2$:

$$Succinate + CoQ \rightarrow Fumarate + CoQH_2 \qquad (2.6)$$

Both complex I and complex II donate electrons to Coenzyme Q ($CoQH_2$) which is the electron donor for complex III.

Complex III (Coenzyme Q reductase): This complex reduces cytochrome c by passing the electrons from $CoQH_2$ to it. This process is done through a unique electron transport pathway called Q-cycle. Complex III includes 11 subunits and 3 respiratory units including 2 b-type cytochromes, 1 c-type cytochrome and Rieske protein [4]. Q-cycle is a relatively complex procedure and does not fit within the scope of this thesis. Briefly, the net result is a transfer of 2 electrons from $CoQH_2$ one at a time to cytochrome c1 and from there to cytochrome c. Cytochrome c is the only

water-soluble cytochrome and is a mobile electron carrier which protects the iron content in haem groups from oxygen and other oxidising agents. It is also a substrate for complex IV.

Complex IV (Cytochrome c oxidase):

Cytochrome c oxidase (CCO) is the terminal electron acceptor in the ETC that transfers the electrons from cytochrome c to molecular oxygen and reduces it to water.

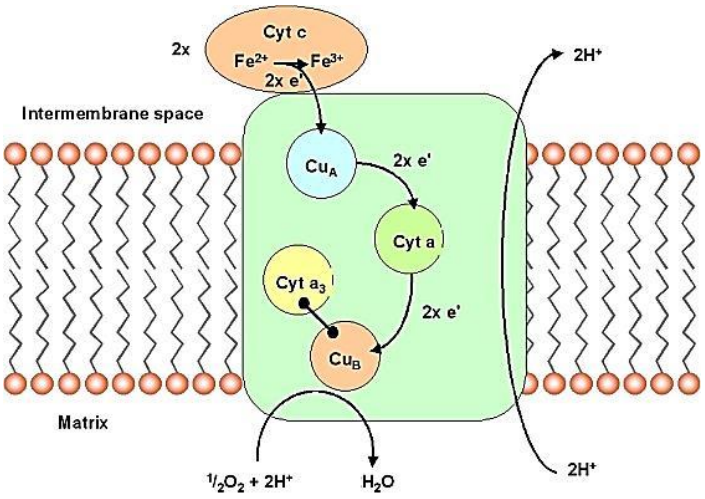

Figure 2.4: Complex IV diagram. Image taken from http://www.mikeblaber.org/oldwine/BCH4053/Lecture38/complex4_01.jpg

CCO contains four subunits including two haem and two copper centres. The haem centres include cytochrome a and cytochrome a_3 and each of the two copper centres (Cu_A and Cu_B) are associated with one cytochrome. As can be seen in Figure 2.4, the protein bound CuA is 15 Å apart from the iron bound in cytochrome a. The Cu_B and cytochrome a_3 on the other hand are very close to each other forming a binuclear metal centre [1].

Each electron from complex III is delivered to complex IV by one cytochrome c. The first cytochrome c transfers the first electron to Cu_A centre and then passes it to cytochrome a, which in turn takes the electron to Cu_B. Another cytochrome c then binds and transfers its electron to Cu_A, cytochrome a and Cu_B respectively. Containing two electrons, the binuclear metal centre is now ready for O_2 molecule to bind to it. The overall reaction in complex IV is as follows [1].

$$4cyt\ c(Fe^{2+}) + 4H^+ + O_2 \rightarrow 4cyt\ c\ (Fe^{3+}) + 2H_2O \qquad (2.7)$$

In total 34 ATPs are produced in the ETC. Adding this amount of ATP to others produced through Glycolysis and Krebs cycle (2 ATP each), the total ATP production equation can be summarised as below:

$$C_6H_{12}O_6 + 6O_2 + 38ADP + 38Pi \rightarrow 6H_2O + 6CO_2 + \mathbf{38}\boldsymbol{ATP} \quad (2.8)$$

However, it should be mentioned that the ETC is not a perfect process and ATP synthesis is inhibited by other mechanisms such as ROS (reactive oxygen species) production or uncoupling. ROS molecules are harmful by-products of oxygen and are damaging to cells that are primarily triggered by ubiquinone complex and contribute to mitochondrial dysfunction and aging [5]. Uncouplers are some proteins that impede the ATP synthesis through inhibiting the coupling between electron transport and phosphorylation reactions [6]. Nevertheless, around 90% of ATP synthesised per one molecule of glucose is generated in the ETC of the mitochondria, which confirms its crucial role in cells' respiration and survival.

2.3 Energy Metabolism in the Central Nervous System

This section provides a brief explanation of the nervous system in general with a focus on CNS and its different parts as well as their crucial role in maintaining normal body function.

The nervous system is the body's 'electrical wiring'. It is a complex network of nerves and cells carrying information to/from the brain and spinal cord to the other parts of the body through providing rapid and discrete signalling over long distances, from millimetres to one meter or more [7].

The nervous system is divided into central nervous system (CNS) including brain and spinal cord and peripheral nervous system (PNS) consisting of all other nerves in the body that lie outside of the brain and spinal cord. A simplified anatomical representation of the human nervous system is shown in Figure 2.5. The CNS is the central processing centre for all stimuli and includes the brain and spinal cord, whereas the PNS consists of the peripheral nerve, the enteric and autonomic nervous system. The main difference between the two systems is that despite the nerves of the PNS that are intrinsically capable of regeneration and repair, the CNS nerves fail to

regenerate and repair. This feature makes the CNS tissues extremely prone to permanent damage following an injury or disease. Therefore, it is crucial to study the energetics and metabolism in the CNS as it provides valuable diagnostic information in most CNS conditions and disorders. The following sections provide a more in-depth explanation of the CNS cellular constituents and tissues as the focus of this thesis.

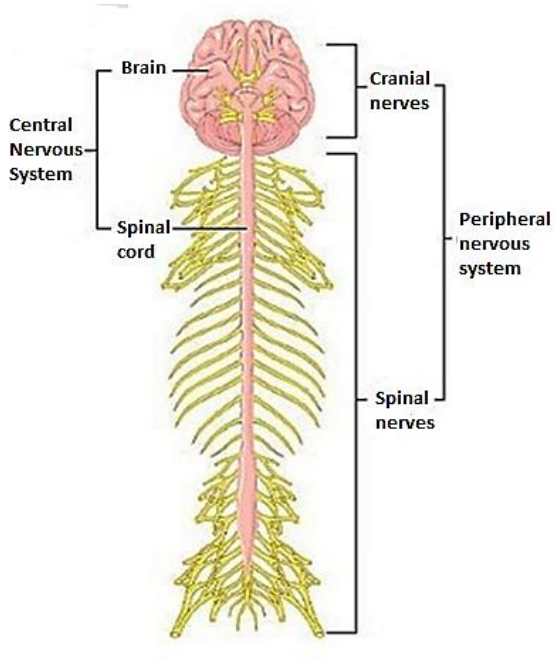

Figure 2.5: Simplified diagram of human nervous system. Image taken from https://nanotechnologyandneuroscience.files.wordpress.com/2010/11/1.jpg

2.4 Cellular Constituents of the Central Nervous System

The CNS is a complex network of two types of cells: the nerve cells or neurones that are responsible for sending, receiving, and interpreting information from all parts of the body, and the glial cells or neuroglia. Unlike neurones, the glial cells, also called non-neuronal cells of the CNS are not involved in signal transmission, but the different types of glial cells are responsible for nourishment, removal of the waste products, support, and protection of the neurones.

2.4.1 Neurones

Neurones are excitable cells that can carry electrical impulses. They communicate with each other through specialised junctions called the synapse and vary in size and shape according to their location and function [8]. There are approximately 10^{12} neurones in the CNS which mediate the transmission of nerve

impulses, also called action potentials [9]. Figure 2.6 is a diagrammatic view of a representative neurone in the CNS. A typical CNS neuron consists of three different parts: a cell body which holds the nucleus, mitochondria and ribosomes and varies in shape and size, a threadlike extension of the cell body called axon which transmits the information to its targets cells or other neurones, dendrites that are highly branched and receive information from different other nerve cells [10].

Each neurone has a single axon, which subsequently branches to make contact with other cells. Most CNS axons are covered with a fatty white material called the myelin sheath, an insulating layer that increases the speed of impulse propagation. Although the myelin sheath extends through the length of an axon, it is interrupted at regular intervals by gaps called nodes of Ranvier. At these nodes the axon is not myelinated and is in direct contact with extracellular fluid [10]. Nervous tissues contain some areas that look white (white matter), because they only include myelinated axons with no cell body. The areas of the nervous tissue that contain cell bodies and dendrites look grey (grey matter) [11].

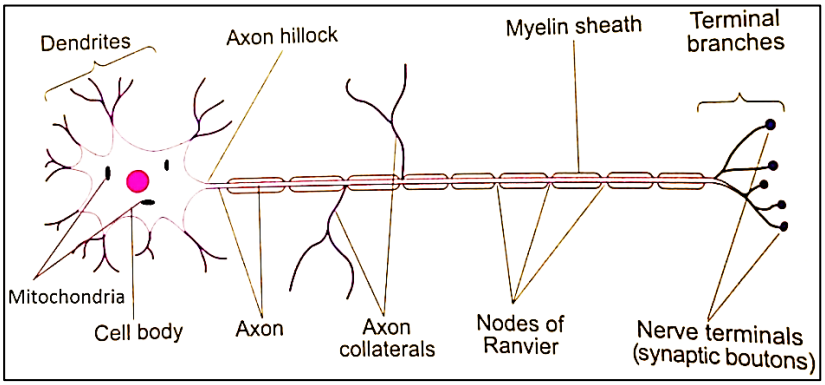

Figure 2.6: A diagrammatic representation of a CNS neurone. Image taken from [10]

Neurones are very metabolically active cells, as they constantly communicate with other parts of the body through electrical signals that are produced by a series of depolarisation (cell excitation) and repolarisation (resting state of the cell). Due to their high metabolic rate, neurones require a considerably large constant supply of energy, which is most efficiently produced via aerobic metabolism of glucose in the ETC of the mitochondria (section 2.2.3). Since this process requires large amounts of oxygen, the central nervous system requires a high blood flow, typically around 50 cc/100 grams of tissue/minute. If this value drops below around 15 cc/100 grams of

tissue/minute, neurones will begin to malfunction and lower levels result in rapid cell death [12]. This makes neurones extremely susceptible to reduction in normal oxygen supply and as mentioned earlier prone to permanent damage when oxygen is scarce (hypoxia). Strong dependence on oxygen is another major difference between the neurones with the non-neuronal cells of the CNS that are explained below.

2.4.2 Non-neuronal Cells of the CNS

There are four types of non-neuronal cells (glial cells or neuroglia) in the CNS which form about 90% of all the CNS cells [13]. Despite the essential function of neurones, there are 5-10 times more glial cells than neurones in the nervous system [8]. Even though larger in quantity, glial cells use much less energy than neurones and some of them primarily rely on anaerobic metabolism for ATP production [14]. Glial cells protect and support the neurones and play an active role in many central homeostatic and developmental processes. Figure 2.7 shows a simplified diagram of the four types CNS glial cells.

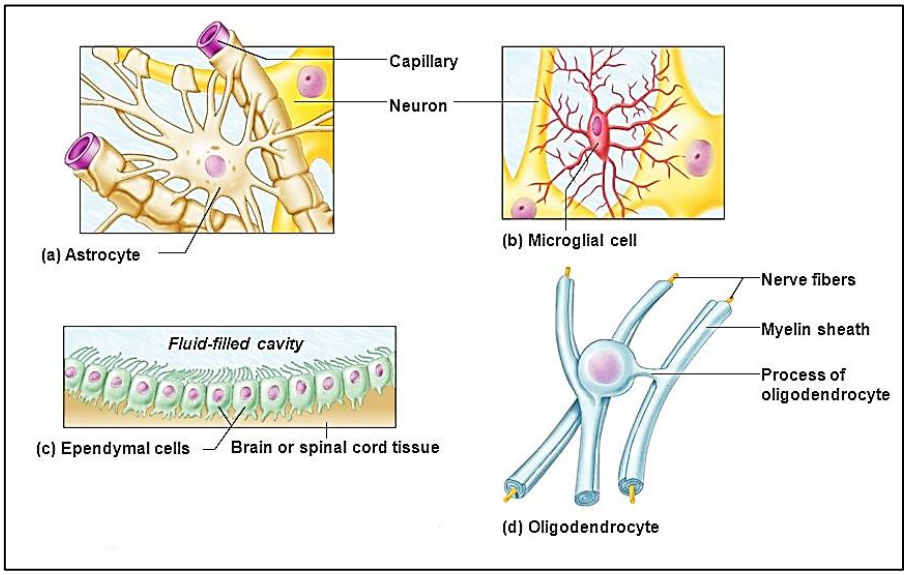

Figure 2.7: Different types of non-neuronal cells in the CNS © The Benjamin/Cummings Publishing Company, Inc., From Marieb Human Anatomy and Physiology. Image is taken from http://images.slideplayer.com/26/8543351/slides/slide_3.jpg

(a) Astroglia or astrocytes: Astrocytes are star-shaped cells with numerous long branches that connect firmly to blood vessels in order to nourish the neurones. Unlike neurones, astrocytes primarily produce ATP via anaerobic glycolysis and have low sensitivity to hypoxia [14]. They have an additional role of protecting

the nerve cells within the CNS from any changes in the composition of blood: the astrocyte branches seal closely together and form an additional barrier between the blood and the extracellular fluid in the CNS, called the blood brain barrier [7].

(b) Microglia: Microglia are the immune cells of the CNS. These mobile cells form around 10-20% of all the glial cells in the adult CNS and are responsible for protecting the CNS from injury or infection. Microglia is dispersed throughout the white and grey matter and rapidly converge on the infected or injured site of the CNS [7].

(c) Ependymal Cells: These are columnar hair-like structures, called ciliated cells, that line the central fluid-field spaces of the brain and the central canal of the spinal cord. They are believed to form and circulate the cerebra-spinal fluid (CSF), which is thought to facilitate the transport of nutrients into the brain and removal of toxic metabolites [13].

(d) Oligodendroglia or Oligodendrocytes: These cells are located in the white matter and are responsible for the generation and maintenance of myelin sheaths around axons. They account for 75% of all the glial cells in the white matter and facilitate neurotransmission [7].

2.5 Components of the Central Nervous System

Brain and spinal cord are the two main parts of the CNS that are located within a bony case formed by the skull and vertebral canal of the spinal column [7]. There is also another tissue located at the back of the eye, often neglected as part of the CNS. Despite its peripheral location, retina or the neural tissue of the eye is anatomically and developmentally part of the CNS [15],[16]. This section includes brief descriptions of the different parts of the CNS as well as their metabolic requirement.

2.5.1 Brain

The brain is the most complex organ in the human body and anatomically is comprised of four major parts; cerebrum, diencephalon, cerebellum, and brainstem, as can be seen in Figure 2.8.

Cerebrum is the largest part of the brain and constitutes 4/5 of its weight. It controls memory, personality and conscious thoughts. Longitudinally, the cerebrum splits into two hemispheres called cerebral hemispheres each divided into four

different lobes. The outer layer of cerebrum is called cerebral cortex which includes grey matter (nerve cell bodies) and the inner region is the white matter consisting of large number of myelinated nerve fibres [7]. Densely packed with over 10 billion neurones (around 10% of the total neurones in the brain), most of the neural activity of the cerebrum occurs in the cerebral cortex. The outer surface of cerebral cortex is extensively convoluted which allows a much larger surface area of the brain to be accommodated in the limited space within the skull [17].

Diencephalon Located deep within the cerebral hemispheres, the diencephalon is made up of several groups of nuclei (grey matter) situated amongst the white matter. It consists of four major subdivisions including thalamus, hypothalamus, subthalamus and epithalamus, which communicate sensory information between brain regions and controls many autonomic functions of the PNS [17].

Cerebellum Functionally divided into three parts, the cerebellum receives information from the sensory systems, the spinal cord and other parts of the brain and regulates motor movements. The deep nuclei of the cerebellum include clusters of grey matter lying within the white matter at the core, which consists of deep nuclei through which the cerebellum connects with the brain stem and the rest of the CNS. The cerebellum is densely packed with neurones (more than the cerebral cortex) and even though it weighs only about 20% of the cerebrum, its surface area comprises nearly 75% of that of the cerebral cortex. The cerebellum coordinates all the motor centres of the brain stem [17].

Brainstem is the part of the brain which connects the cerebral hemispheres with the spinal cord. It includes midbrain, pons and medulla, as well as several life-supporting centres for maintaining vital functions such as breathing and blood pressure. The nuclei of almost all cranial nerves lie within the brainstem and it also has crucial role in developing consciousness, sleep regulation, maintenance of muscle tone, posture and reflex actions. Brainstem lesions disconnect sensory inputs to the brain, blocking the brain's control over the body which results in catastrophic outcomes such as deep coma or brain death [17].

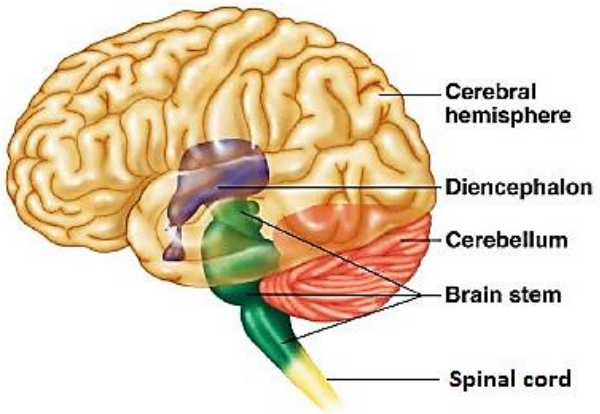

Figure 2.8: Regions of the brain © 2003 Pearson Education, Inc. publishing as Benjamin Cummings

2.5.1.1 Brain Metabolism: The brain has a high metabolic rate and its high-energy demand can only be met through aerobic metabolism mainly happening in the ETC of the mitochondria. It consists of hundreds of billions of neurones largely interconnected in different ways, as well as glial cells that are more neumerous than neurones by a ratio of around 3 to 1 [18]. That is why, even though only comprising 2% of the body weight, the brain receives 15% of the cardiac output and consumes 20% of the total oxygen and 25% of the total glucose used for whole body energy supply [19]. Also, more than 90% of the oxygen consumed by the brain is used by the ETC of the mitochondria to produce ATP [20].

The substrates required for cellular metabolism (primarily glucose and oxygen) in the brain are prepared through mechanisms in the blood brain barrier and provided via the cerebrospinal fluid. At different stages, the human brain uses different fuels for energy metabolism; for instance, under starvation for many days, the CNS can use ketone (fat derivatives) as its main source of energy. These compounds make up about 30% of the fuel for the adult brain, whereas in infants the blood-brain barrier transport of ketone is approximately 7 times as high and glucose transport is only 30% of the adult level. Also, in children amino acids (protein derivatives) transport is higher than in an adult, suggesting a higher rate of protein synthesis in developing the brain. The brain is very vulnerable to interruptions in the oxygen and glucose supply (as it cannot store glucose), hence the cranial blood vessels are controlled through autoregulation mechanism to maintain a constant blood supply to the brain [8]. If the blood flow is

stopped, unconsciousness occurs within 6-7 seconds and irreversible brain damage happens in minutes [21], [22].

2.5.2 Spinal Cord

While the human brain is a large structure, the spinal cord is a delicate, segmentally organised tube which runs through the vertebral canal of the spinal column and connects to the brain via the brain stem, as illustrated in Figure 2.9. The spinal cord is around 42-45 cm long (for women and men) [7] and like the brain, it consists of a central region of grey matter (glial cells and neuronal cell body) surrounded by white matter (myelinated axons) acting as a mediator between the brain and the body. The spinal cord first receives the nerve impulses from sensory neurones and transmits them to the brain. Then, it transmits the motor information from the brain to the motor neurones and effectors. It also acts as a minor reflex centre.

Consisting of both sensory and motor fibres, the spinal nerves arise from the spinal cord and supply the rest of the body. The CNS controls the actions of the trunk and limb through the sensory information it receives from the spinal nerves [17].

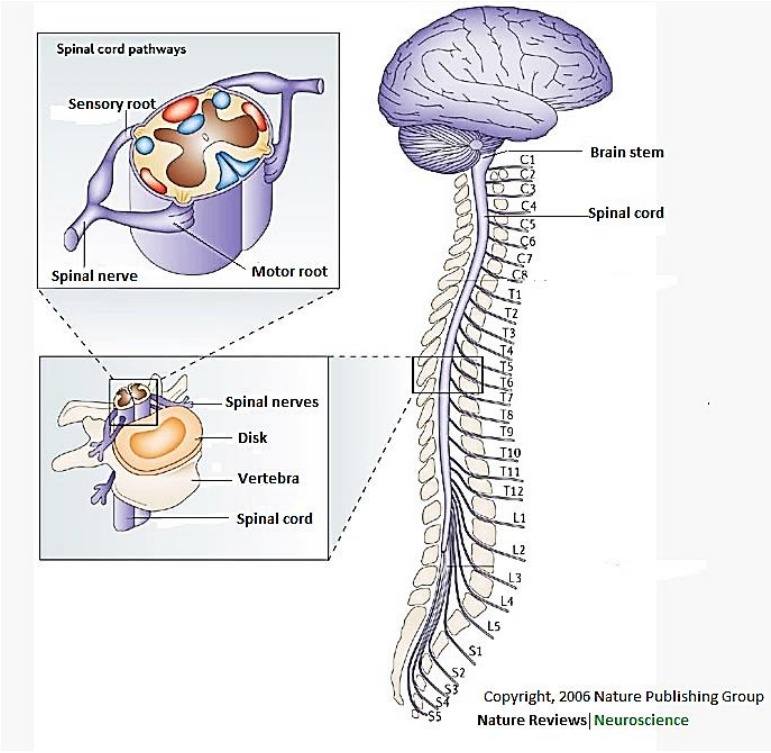

Figure 2.9: Anatomy of the spinal cord. Image taken from http://www.nature.com/nrn/journal/v7/n8/fig_tab/nrn1964_F1.html

2.5.2.1 Metabolism of the spinal cord: Being part of the CNS and having been extended from the brain, the spinal cord tissue has a high metabolic rate, even though the metabolic rate differs slightly between different anatomical areas as shown in Figure 2.9 depending on the amount of grey matter, where the nerves' cell bodies including mitochondria locate and the metabolic rate is greater [23].

Spinal cord injuries occur when the delicate spinal cord tissue is bruised, torn or pounded. This could be a result of an accident or underlying disease or disorders, which lead to a neurological deficit in certain areas of the body. When a certain part of the spinal cord has been injured, messages can no longer be communicated between the damaged part and the brain, as well as certain parts of the body. Generally the areas located below the point of injury will be impaired which could manifest in motor deficit, sensory deficit, breathing difficulty, or bowel/bladder dysfunction [24]. The areas of interest in this project are to study conditions such as multiple sclerosis (MS) where a significant change in tissue metabolism occurs as a result of spinal cord injury.

2.5.3 Retina

The retina is an outgrowth of the embryonic developing brain and have kept its connections with the brain via a bundle of fibres called the optic nerve that are in fact CNS axons [15], [25], [16]. It is is the photosensitive tissue of the eye, like a high sensitivity CCD in a camera, which translates light into nerve signals. As part of the CNS, the retina displays similarities to the brain and spinal cord in terms of anatomy, functionality, response to insult and immunology [16]. It is also the only part of the CNS that can be imaged directly, due to the high optical transparency of the eye (with transmission above 95% in the 400 - 900 nm spectral region) and therefore is very interesting as a non-invasive approach to the study of CNS tissue metabolism and diagnosis of certain CNS diseases [16].

The incoming light reaches the retina through the pupil as shown in Figure 2.10 and passes through two different layers before reaching the photoreceptors. The layer of cells in front of the retina includes retinal ganglion cells, whose axons pass through the surface of the retina and form the optic nerve. The layer between the ganglion cells and the photoreceptors contains bipolar cells that receive input from the receptors and feed the ganglion cells. There are two types of photoreceptor cells at the back of the retina; rods and cones (Figure 2.10) that very much

dependent on aerobic metabolism for ATP generation. Rods are far more numerous than cones and are responsible for our vision in dim light, whereas cones do not respond to dim light but are responsible for the colour vision and the ability to see fine details [25].

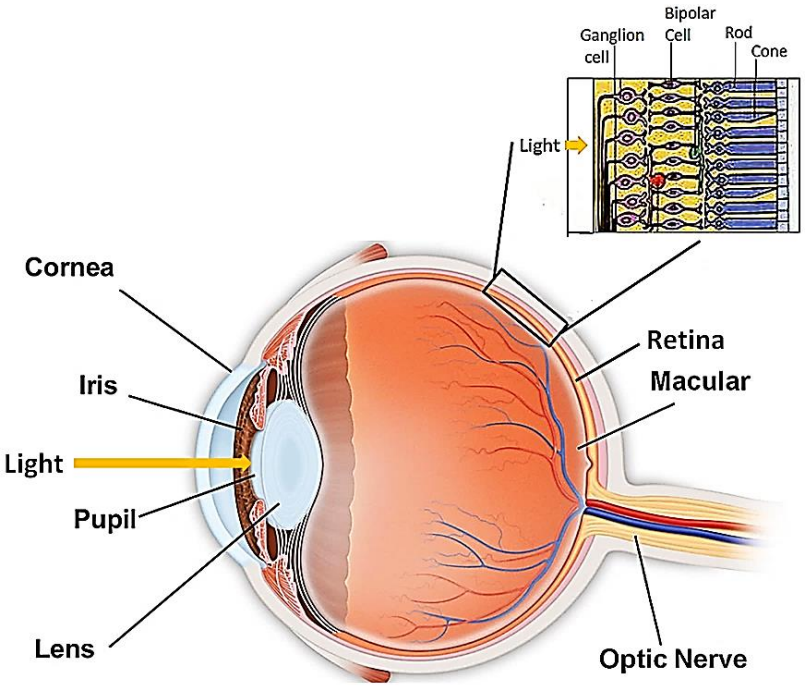

Figure 2.10: Image modified from [25] and http://www.weyeclinic.sg/images/yootheme/eyeconditions/knowingyoureyes.jpg

2.5.3.1 Metabolism of the Retina: The retina is one of the highest metabolic demanding organs and densely packed with mitochondria. It is the highest oxygen consuming tissues of the body and its energy demand and dependent on oxidative metabolism are even greater than the brain [19]. The reason behind the large metabolic demand of the retina is primarily a large number of neuronal cells compared to non-neuronal cells. Each human eye has around 125 million rods and cones compared with only 1 million ganglion cells [25] and as mentioned earlier, neurones are entirely dependent on oxidative metabolism. This is of specific importance because defects in energy metabolism often lead to a visual deficit, neuronal degeneration and eventual blindness. Changes in oxygen metabolism are believed to be involved in many of the eye diseases that often happens as a result of insufficient vascular perfusion or vascular occlusion. Therefore, being able to

quantify oxygen metabolism non-invasively is crucial for diagnosis and studies of a range of eye diseases such as age-related macular degeneration, diabetic retinopathy and glaucoma which eventually lead to blindness [26]. Therefore, in-vivo measurement of oxygen metabolism in the retina is of specific interest not just as a non-invasive way of investigating neurological conditions in the brain and spinal cord, but it also furthers the understanding of the molecular pathways of blinding diseases.

2.6 Neurovascular Regulation, Hypoxia and Inflammation in the CNS

To maintain a consistent blood supply to the all parts of the CNS, there is a strong interrelationship between the oxygenation and metabolism in the CNS with the neural activity. Figure 2.11 illustrates the tight coupling between neuronal activity and energy metabolism. The continuous blood flow is crucial to the CNS since it has very little storage of energy substrates in the form of glycogen stores to sustain energy metabolism at times of high demand, compared with other tissues such as liver and muscle [20].

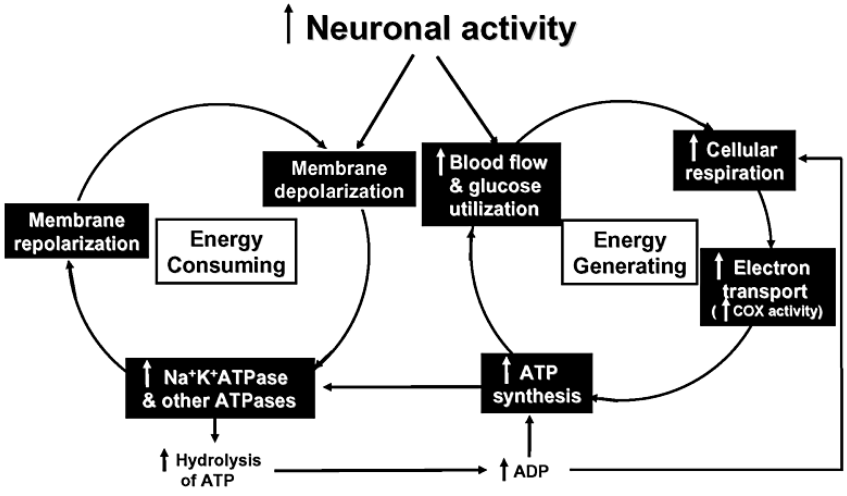

Figure 2.11: The interrelationship between blood flow, oxygenation and metabolism and neuronal activity. Image taken from [19].

There is normally a good balance between energy production and consumption in the CNS tissues and neural activity controls energy metabolism under normal conditions. However, when neuronal activity is disrupted by disease or pathology, energy supply and consumption will also be disrupted. Likewise, when neuronal

energy metabolism is disturbed, it directly affects the neuronal activity [27]. One of the crucial factors that disrupts metabolism is a reduction in substrate or oxygen delivery called hypoxia, which is described below [23].

Hypoxia: is a deficiency in the amount of oxygen reaching the tissue and in general four different conditions lead to tissue hypoxia:

Hypoxic Hypoxia- is a condition that occurs when the concentration of oxygen in the arterial blood is significantly low, mainly due to low oxygen pressure or the inability of the oxygen to diffuse into the lungs.

Anaemic Hypoxia- Anaemic hypoxia relates to a low functional haemoglobin or preferential binding of carbon monoxide. This condition is primarily caused by Iron deficiency, which leads to a reduction in oxygen carrying capacity of the blood.

Ischaemic Hypoxia- is a condition in which the blood has normal oxygen saturation, but tissues do not receive adequate oxygen to utilise due to a reduction or uneven distribution of blood flow. Ischaemic hypoxia occurs usually due to a drop in cardiac output or blockage in the arteries/arterioles.

Histotoxic Dysoxia- is the cell's inability to utilise oxygen for ATP production, mainly due to mitochondria dysfunction/impairment. In this condition, cells are not able to metabolise oxygen even though blood flow and haemoglobin oxygen saturation are adequate [28].

CNS tissues are very vulnerable to hypoxia, and any type of hypoxia can be highly damaging to the nerves as their high energy demand is primarily met by aerobic metabolism. In order to maintain a constant blood supply providing oxygen and nutrients, the CNS tissues are facilitated with different vasculature to provide sufficient blood supply to different types of cells and tissues in the CNS. This homeostatic mechanism of tight control of blood flow in the organs is called autoregulation. While all organs perform some degree of autoregulation, the CNS organs including, the brain, spinal cord and the retina are particularly sensitive to over and under perfusion. However, in the case of severe damage to the CNS, this autoregulation mechanism will be impaired that in turn causes more destructions such as permanent impairment of the mitochondrial metabolism which ultimately leads to cell death. Examples of the CNS diseases in which oxygen metabolism may be changed or impaired [29] include traumatic brain injury (TBI) [30], stroke [31],

Alzheimer ’s disease [32], and retinal pathologies such as diabetic retinopathy [33] and glaucoma [34].

Inflammation: Inflammation in general is an immune response from the body when the immune cells gather to fight off an infection, injury or damage. Inflammation which interferes with normal function of the affected body part is an important feature associated with hypoxia ischaemia (HI) and plays a critical role in mediating irreversible injury to the neurones following HI [35]. Prolonged inflammation in the CNS leads to irreversible destruction as the immune cells destroy the healthy nerves leading to neurodegeneration and cell death.

Considering the vulnerability of CNS tissues to hypoxia and inflammation with the fact that disruption of normal glucose or oxygen metabolism forms the pathophysiological basis for many neurological disorders [36], it is essential to have techniques for non-invasive assessment of tissue energetics and oxygen metabolism in health and disease.

2.7 Markers and Techniques for in-vivo Measurement of Metabolism in the CNS

To measure tissue metabolism effectively, one needs to establish some reliable quantifiable metabolic markers that are involved in oxidative phosphorylation of glucose as the primary source of ATP production in the CNS. Blood flow, glucose uptake and tissue oxygen consumption are all crucial contributing factors when considering oxygen delivery and metabolism. There are also other intermediates and metabolites that can be used for investigating tissue metabolism [19]**.**

In this section, we discuss the markers and techniques, which have been used in clinic or research to understand tissue metabolism in health and diseases. In general, clinical indicators for metabolism status can fall into six categories:

Metabolic markers:

pH: pH measurement is one of the most commonly used clinical indicators of tissue metabolic status. pH levels lower than 7.35 can be indicative of respiratory acidosis that occurs following an increased carbon dioxide levels in the blood. Respiratory acidosis occurs when lungs cannot eliminate enough carbon dioxide from the tissues as a result of conditions like hypoventilation or a low respiratory rate. For instance, metabolic acidosis or

low pH levels is a common abnormality in patients experiencing anaerobic metabolism because of tissue hypoxia [37]. In contrast, a typical reason for an alkaline pH >7.35-7.45), or respiratory alkalosis, is a result of minimal carbon dioxide in the blood typically caused by hyperventilation. An example of how alkaline pH can be used as an indicator of injury severity has been investigated in perinatal HI, where an alkaline intracellular pH and the extent of alkalosis following perinatal HI was shown to be associated with neurodevelopmental outcome and injury severity in neonates [38].

Lactate: Lactate is a product of anaerobic metabolism and an elevated lactate level can cause further injury. Therefore, raised lactate level is an indicator of a poor prognosis in critically ill patients, especially in brain injuries [37],[39], [40].

CO_2: Carbon dioxide (CO_2) has a profound but temporary effect on cerebral blood flow (CBF)as increase CO_2 levels, hypercapnia, temporarily increases cerebral blood flow through dilating cerebral arteries and arterioles and a decreased CO_2, hypocapnia, drops the CBF through vasoconstriction. It has been shown that inhaling 5% CO_2 in humans causes a CBF increase of 50% and 7% CO_2 inhalation causes a 100% increase in CBF [41].

Measurement of partial pressure of CO_2 (PCO_2) in tissues with high metabolic activity such as brain, kidney and heart, has demonstrated to reflect metabolic alterations due to perfusion failure [42], [43]. Furthermore, based on some experimental and clinical data, the venous-to-arterial PCO_2 difference, known as PCO_2 gap (a product of CO_2 production and inversely proportional to cardiac output), has been introduced as a global index of tissue perfusion which could also be used as a complementary tool to evaluate the adequacy of blood flow to global metabolic conditions [44].

Global Oxygen Delivery: is an absolute quantification of oxygen delivery and is a product of cardiac output and the oxygen content of arterial blood. The cardiac output being the flow of the blood leaving the heart to circulate in the body and the arterial blood oxygen content is the sum of oxygenated haemoglobin and the small amount of oxygen dissolved in the plasma [37].

Global Oxygen Consumption: The oxygen saturation of haemoglobin in the arterial blood is around 97% and in the mixed venous blood returning to the heart is

around 72%. This shows that not all the oxygen delivered to the tissues is taken up and consumed by cells. In fact, in healthy adults, only 250 ml of the ~1000 ml of oxygen delivered to tissues is used. The relationship between oxygen delivery and consumption is complicated and non-linear and it is very important to be monitored especially in critically ill patients [37].

Regional Blood Flow: Measuring regional blood flow is a good indicator of tissue oxygen delivery and metabolism to some extent. Specifically in brain measurements, it might be helpful in detection of tissue hypoxia [45]. Regional blood flow can be measured via MRI, PET or optical techniques such as laser Doppler flowmetry.

Regional Oxygen Delivery: Oxygen delivery (DO_2) is the volume of oxygen transported to the systemic vascular bed per minute and is the product of cardiac output and the arterial oxygen concentration. Measurement of regional DO_2 enables early detection of oxygen deprivation in individual tissues and organs making early intervention possible. Metabolic PET and NIRS are non-invasive techniques that can provide regional oxygen delivery measurement [46], [47]. .

Tissue Oxygen Utilisation: Measures of regional blood flow and tissue oxygen delivery can easily detect hypoxia, however, are unable to diagnose inadequate oxygen utilisation due to mitochondria dysfunction, which ultimately leads to impairment in ATP production and organ failure. Therefore, it is crucial to measure tissue oxygen utilisation.

Measurement of tissue oxygen utilisation is valuable in providing insight into the mitochondria of the cells and is of specific importance in CNS tissue conditions due to the irreversible damage that impaired metabolism can cause to the neurones. Luminescent oxygen probes provide measurement of NADH levels as a mitochondrial enzyme that could provide distinction between normal and abnormal cellular function but due to being invasive it is mainly used for research purposes [48]. Tissue pH and lactate levels are also good indicators of mitochondrial oxygen utilisation and can be measured by microdialysis catheters that are invasive [37], also through non-invasive techniques such as NMR and PET. Combinations of optical techniques such as laser Doppler flowmetry, diffuse correlation spectroscopy (DCS) and optical coherent tomography (OCT) have also been used for tissue oxygen delivery and metabolism mainly in research. High-energy phosphorous metabolites (Phosphocreatine,

Inorganic Phosphate, and Nucleotide Triphosphate) in the mitochondria that are involved in the phosphorylation of ADP to ATP are also useful markers for tissue oxygen metabolism. Measurement of phosphorous metabolite ratio by magnetic resonance spectroscopy has been demonstrated to provide useful information about brain intracellular metabolism. It has been used to study the brain under a variety of experimental conditions as well as clinical settings, including the cerebral metabolism in the human new-born [49]. Measurement of high-energy phosphorous metabolites in infants was first carried out in 1983 in infants as has shown to be predictive of the outcome following HI brain injury [50]–[52].

Today Blood gas analysis, is the most common tool to assess tissue oxygen delivery and metabolism at bedside. Techniques such as PET (positron emission tomography) and MRI/MRS (magnetic resonance imaging/spectroscopy) are also considered as gold standard techniques in terms of providing useful diagnostic information on tissue oxygen delivery and uptake. However, these techniques are rarely used in clinical practice due to their limitations in terms of cost, logistics, and complications involved in moving critically ill patients to the PET or MR units.

The following section briefly describes the principles and area of application of PET and MRI/MRS for evaluation of CNS tissue energetics.

2.7.1 PET

Positron Emission Tomography is a nuclear medicine imaging technique that enables measurement of organ and tissue metabolism by introducing a low-activity, short-lasting radioactive material called a tracer which binds to glucose or oxygen in the body. The tracer, which is a positron-emitting isotope, is either inhaled in gaseous form or injected into the blood stream to get distributed around the body [25] and it decays in a characteristics way giving off pairs of gamma rays. Traveling in different directions, the gamma photons are detected by pulse coincidence circuits following the photomultiplier tubes or Avalanche Photodiodes (APDs) [26]. The distribution of the isotope then produces the image, which then helps in diagnosing disease or injury in organs and tissues. In some clinics, PET accompanies MRI and/or computed tomography (CT) imaging in order to provide information that is more precise for accurate diagnosis.

A common use for PET is measuring glucose consumption rate in different parts of the body. It is also used for measuring blood flow and oxygen consumption in different parts of the brain in order to understand stroke, memory disorders such as dementia, seizures, and other central nervous system disorders [27].

Advantages: PET imaging offers high image quality and therefore improved diagnostic accuracy [29]. It provides a comprehensive physiological measurement through a wide range of measures, such as: blood flow, blood volume, oxygen consumption, glucose metabolism and tissue pH [30]. It is able to identify early onset of disease before other imaging tests such as CT or MRI [28], as it enables monitoring changes at a cellular level.

2.7.2 MRI/MRS

NMR is one of the most widely used tools to monitor the brain and quantitatively analyse its chemical compositions and structure. Magnetic resonance imaging (MRI) produces high quality anatomic images of tissues through mapping the spatial distribution of water and fat molecules in the body. It uses the spin-related magnetic properties of the protons (which are found abundantly in the body) to identify different tissues. When a strong magnetic field (usually greater than 3 Tesla) created by a superconducting magnet is applied, the protons in the probed tissues align with that field. Next when an additional time-dependent magnetic field known as a radiofrequency (RF) pulse is introduced, the protons are stimulated and spin out of equilibrium. The magnetisation vector (spin) will then precess around the equilibrium direction with a characteristic frequency, known as the resonance frequency, which is a function of the main magnetic field strength [33]. Once the RF pulse is turned off, the protons realign with the magnetic field, releasing some electromagnetic energy detectable by MR sensors. The time taken for protons realignment after the RF pulse is off and the amount of electromagnetic energy released is different depending on the environment and the chemical nature of the biomolecules.

MRI is able to differentiate between different tissue types or an abnormal tissue based on the amount of released energy and the time difference in releasing the energy [34]. Modified MRI scanners are also equipped with magnetic resonance spectroscopy (MRS) which enables measuring tissue metabolism through direct measurement of the chemical content of a broad range of metabolites in the body [35]. MRS identifies

tissue compounds based on their composition: hydrogen (^{1}H), carbon (^{13}C), phosphorous (^{31}P) and fluorine (^{19}F) that are all detectable by MR using the relevant sensors known as surface coils. However, for in-vivo tissue metabolism measurements, proton (^{1}H) and phosphorous MRS are most convenient due to the naturally higher abundance of these nuclei in tissues and therefore higher sensitivity of measurement [36].

^{1}H-MRS: Proton MRS (^{1}H-MRS) is the most widely available technique due to the wide range of observable proton metabolites in tissues. The measurement of lactate (a product of anaerobic glycolysis) and N-acetylaspartate (NAA, a marker of neuronal integrity) are the most useful markers in brain injuries [33]. Other useful metabolites that can be measured by proton MRS include lipids (products of brain destruction), Glutamine (neurotransmitter), Creatine (Cr, energy metabolism) and Choline (Cho, cell membrane marker) [38]. Due to its non-invasive nature, proton MRS has also been used in neonatal brain since the early 1990s [39], [40], [41], [42]. Other applications of ^{1}H-MRS include in the diagnosis of tumours, cerebral ischaemia and stroke, epilepsy, metabolic disorders, infections, and neurodegenerative diseases [38]. Although absolute quantification of metabolites using ^{1}H-MRS is very time consuming and difficult to measure, metabolite ratios such as NAA/Cho, NAA/Cr or Lac/NAA has shown to be reliable markers of brain tissue metabolic status following an injury [37].

^{31}P-MRS: Phosphorous MRS application predates proton MRS and it has been used to evaluate cerebral metabolism in babies since around three decades ago [37], [43]. ^{31}P-MRS is known as the best technique to estimate aerobic and anaerobic metabolism since it enables measurement of phosphate groups that are involved in oxidative phosphorylation for ATP production. Metabolites such as phosphocreatine (PCr), nucleotide triphosphates (NTP) and inorganic phosphate (Pi), phosphomonoesters and phosphodiesters can be detected using ^{31}P-MRS. Use of ^{31}P-MRS for the study of neonatal encephalopathy (NE) and the evaluation of neurodevelopmental outcome following an injury has been used to validate the broadband NIRS cytochrome measurement, which will be discussed in chapter 4.

Advantages: One of the main advantages of MRS is that unlike PET it is a non-invasive metabolism measurement technique and can be used to monitor infants, children and adults alike. Due to its non-invasive nature, repeated measurement of

metabolite concentration, metabolite flux and their response to intervention can be assessed, which makes MRS ideally suitable for in-vivo studies of human metabolism. MRS is particularly advantageous for evaluating metabolism, because it is a multimodal technique capable of measuring a broad range of biological compounds across a variety of tissues. That is because the peaks in the MR spectrum correspond not only to specific metabolites but also to the constituents of each metabolite [44]. Moreover, simultaneous with MRS, MRI scans can be obtained to provide structural/ anatomical information that can guide data acquisition and assist in data analysis and interpretation [44].

2.7.3 Optical Techniques

Optical imaging includes a broad range of techniques that use light to receive information from inside the body. They generally involve using visible or near-infrared (NIR) light to image biological organs, tissues, and cells. Photons in visible-NIR light interact with biological molecules and excite electrons without causing the damage that occurs through ionising radiation as in other imaging techniques. Popular examples are laser Doppler flowmetry, fluorescent imaging, OCT, DOT, Photoacoustic Imaging, and near infrared spectroscopy and imaging (NIRS/NIRI)) , which is the main focus of this project and will be discussed in the next chapter.

Advantages: Optical techniques for measuring metabolism significantly reduce patients' exposure to harmful radiations such as X-ray as they are non-invasive and non-ionising. Furthermore, due to the relative transparency of biological tissues to light in the deep red and NIR, systems using these wavelengths have an advantage of providing deep tissue imaging without the need of radio isotopes or contrast agents. Because optical techniques are significantly safer and faster than radiological methods, they can be used for long and repeated measurements over time to monitor disease progression or the result of treatment [53]. Optical techniques can be combined with other monitoring techniques such as MRI simultaneously to provide extra pieces of information for clinicians or in complicated experiments. They also take advantage of using different colours of light in order to see and measure different properties of an organ or tissue at the same time while other imaging techniques are limited to only one or two measurements [53].

2.7.4 Limitations of Current Clinical Techniques and Markers for in-vivo Metabolism Measurement

Despite the useful information that PET, MRS and optical techniques provide for evaluating tissue oxygen delivery and metabolism, there are still some limitations with the instruments and their measurements, discussed below, which hinders them from being bedside monitors of tissue metabolism.

PET Disadvantages: PET is dedicated expensive equipment and its main disadvantage is the use of radioisotopes and ionising radiations. The radiation from a typical PET scanner is 3 to 5 times as much as a person would receive in a year from naturally occurring background radiation and in case of CT/PET the radiation dose increases to 5 to 10 times [31]. Therefore, there is a limited amount of times a patient can undergo this procedure. Furthermore, even though short-lived, the radioactive tracer may not be suitable for people who are pregnant and breastfeeding [32].

NMR Disadvantages: One of the disadvantages of MRS is that absolute concentration measurement is very time-consuming, hence metabolite ratios are commonly used to demonstrate changes in the brain [37]. Another limitation of MRS in clinical practice is the insufficient signal-to-noise ratio, which is a characteristic of in-vivo MRS measurements and can usually be improved at the cost of increasing the acquisition time. This is also a disadvantage in monitoring physiological changes, which usually occur within a smaller time window.

Despite providing useful information about mitochondrial energetics such as high energy phosphates ratios and lactate (that are indicators of tissue metabolic status), MR scanners are dedicated expensive equipment to purchase and operate; and need specialist physicists to collect and interpret the data. They are also not available at the bedside which is a major limitation for clinical monitoring of critically ill patients in the intensive care unit (ICU) who cannot be transferred to MRI suites, which are often far away from patient care areas.

Optical techniques Disadvantages: Even though advantageous to MRS and PET for being non-invasive and being able for bedside measurement, optical techniques are usually combined with another technique to provide useful information about tissue metabolic status, such as blood flow or oxygenation measurements. Furthermore, optical techniques in the clinic are mainly used for blood oxygenation

measurement and fail to provide insight into cellular oxygen metabolism. This is crucial since disruption in oxygen supply and metabolism has been associated with many CNS diseases such as HIE, stroke, AMD, MS and other metabolic disorders that could lead to long-term neurological deficits. Therefore, further instrumentation and methodology advances are being carried out to identify a reliable bedside measure for tissue oxygen metabolism.

2.8 Metabolic Rate of Oxygen (MRO2): Towards Assigning a General Marker for Cellular Oxygen Consumption in the CNS

As discussed in the previous sections, a bedside non-invasive measurement of oxygen consumption at cellular level, crucial for CNS tissues, is missing in the clinical environment. Even though having a general bedside marker for mitochondrial oxygen metabolism, like what currently exists for tissue oxygen saturation (pulse oximeters), might seem too ambitious, the urgent need for having such bedside marker that could help in diagnosis, prevention and treatment of many neurological conditions has led the researchers towards the establishment of a reliable clinical marker for cellular oxygen utilisation.

Measuring metabolic rate of oxygen using blood flow and oxygenation measurement has been a step forward in defining a suitable marker for cellular oxygen metabolism. One of the most useful measures that have been widely studied for evaluating oxidative metabolism is measuring tissue oxygen uptake or metabolic rate of oxygen (MRO_2). MRO_2 represents a key marker for CNS tissue viability and function, as around 30 moles of ATP are generated in the presence of oxygen in the ETC of the mitochondria per one molecule of glucose. Several techniques exist for measuring MRO2, because it is challenging to be measured directly, especially in real-time [54]. Most of these techniques, however, are based on Fick's principle, which says; the amount of oxygen consumed by the tissue (MRO_2) equals the difference between the amount delivered on the arterial side of the tissue (C_a) and the amount drained on the venous side (C_v) (Evidence now suggests that oxygen can also be released from arteriole and in some conditions venule as well as capillaries [55].).

As can be seen in Figure 2.12, a simplified diagram illustrating the principle behind MRO_2 measurement, oxygenated blood enters the capillary from the arterial end and flows through the capillary with a given flow rate, BF(t). In the capillaries,

oxygen passively diffuses through the tissue and is consumed in the mitochondria (oxygen is reduced to water and ATP is produced), based on the concentration gradient between the capillary and tissue compartments. Finally, blood with lower oxygen content flows out through the venous end.

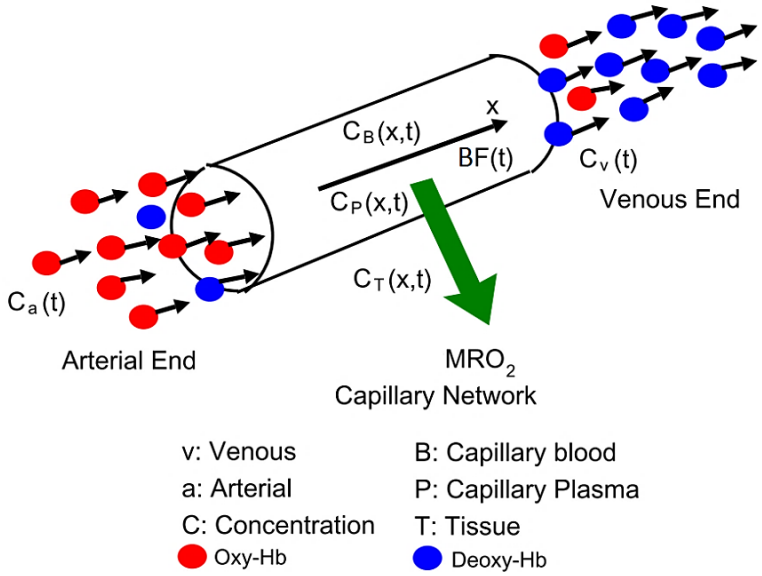

Figure 2.12: Compartmentalised model of the vasculature illustrating MRO_2 measurement. Arterial blood mainly consisting of oxygenated haemoglobin flows in the tissue from the arterial end, oxygen diffuses passively through the capillaries, and finally blood with lower oxygen content flows out from the venous end. Image taken from [56].

2.8.1 Examples of CNS-MRO2 Measurement Applications

Quantitative assessment of tissue oxygen metabolism (MRO_2) provides an important marker for different parts of the CNS in better understanding normal tissue development and function, as well as for diagnosis and directing treatment strategies in times of injuries.

$CMRO_2$ measurement is an important marker for brain function and health and abnormal levels of $CMRO_2$ have been reported in a number of neurological conditions such as Alzheimer's and Parkinson's diseases [57], [58], brain aging [59] and traumatic brain injury [60] as well as multiple sclerosis (MS) [61]. The rate of cerebral oxygen metabolism can be mostly quantified from the Fick's law:

$$CMRO_2 = CBF([O_2]_a - [O_2]_v) \qquad (2.9)$$

Where $[O_2]_a$ and $[O_2]_v$ are the oxygen contents within the arteries and veins, entering and leaving the brain respectively [3]. Even though the measurement of $CMRO_2$ is a challenging task in humans, especially in neonates [40], there has been

an extensive research on developing techniques and methodologies for measuring $CMRO_2$ in neonates' [62]–[65] and adults' [66]–[69] brain.

Even though the measurement of spinal cord blood flow (using MRI or laser Doppler) and in-vivo oxygen content (using oxygen probes) have been broadly used in the studies of spinal cord injury or a range of neurological disorders, like MS [20], [70]., there is no or very limited literature that have used "MRO_2" as an index for spinal cord oxygen metabolism in neurological disorders.

Despite the challenges with simultaneous measurement of blood flow and oxygenation in the retina [26], like brain, MRO_2 measurement is an active area of research for the retina metabolism measurement. That is because most retinal diseases are believed to be associated with alterations in oxygen metabolism, since the retina is the highest oxygen-demanding organ in human body. Therefore, precise and non-invasive quantification of metabolic rate of oxygen ($rMRO_2$) is considered to be crucial for diagnosis of many retinal disease such as age-related macular degeneration (AMD), diabetic retinopathy, and glaucoma, which ultimately lead to partial or full blindness [26].

Measuring retinal MRO_2 is not straight forward and has not been achieved until recently [71] because most of the retinal imaging methods can only measure one functional parameter, either blood flow or oxygen saturation (sO_2) [72]–[74]. Therefore, even though non-invasive quantification of $rMRO_2$ has been proposed for decades, it has had a very little success mainly due to the limitations in measuring retinal sO_2 [26]. However, recent advances in Doppler spectral domain-optical coherence tomography (SD-OCT) which enables accurate detection of blood flow, along with the development of photoacoustic ophthalmoscopy (PAOM, which has been developed on the basis of photoacoustic imaging) has made in-vivo quantification of $rMRO_2$ achievable [26], [71].

2.8.2 Challenges of MRO_2 as a Clinical Marker for Oxygen Metabolism

Currently, tissue metabolic rate of oxygen faces some challenges for being established as a real-time bedside marker for metabolism for the following reasons:

1- PET as the Gold standard tool for MRO_2 measurement is not a bedside or non-invasive monitoring technique for oxygen metabolism measurement; $CMRO_2$

measurement using PET involves exposure to radiotracers and ionising radiations, which is the primary impeding factor for its application in paediatric population. Another limitation for using PET to measure MRO_2 is the complexity of the procedure and the need of special equipment ^{15} O-PET [40].

2- Use of NMR/MRI for MRO_2 measurement also has its own limitation. First, as mentioned earlier MR scans fail as a bedside technique because for the safety purposes, they are usually located far from the intensive care and paediatric units where they are most needed. Secondly, NMR methods such as ^{13} C and ^{17}O for $CMRO_2$ measurement involve using exogenous tracers and are not suitable for use in neonatal brain [75], [76]. Other techniques that do not involve exogenous tracers for blood flow measurements, such as phase-contrast MRI [66]or arterial spin labelling (ASL) [77], are complicated and vary according to their venous oxygenation measurement techniques [40].
3- Optical techniques for measuring MRO_2 usually require more than one technique/instrument for blood flow and oxygenation measurement that limits their feasibility for bedside monitoring. Many biomedical optics groups are measuring cerebral metabolic rate of oxygen combing near-infrared spectroscopy (NIRS) and diffuse correlation spectroscopy (DCS) [63], [78] and others combine MRI and NIRS to measure $CMRO_2$ [79].

Apart from the complications in measurement techniques, MRO_2 is merely based on blood oxygen measurements and fails to provide information about mitochondrial function, which could be more specific. All these challenges, confirms the need for a non-invasive bedside measurement of tissue oxygen metabolism that could be used as an alternative to existing markers and techniques.

2.9 Cytochrome-c-oxidase, a Mitochondria-Specific Marker for Oxygen Metabolism

As mentioned earlier, MRO_2 is based on blood oxygenation measurement which is prone to being non-specific for being a marker for cellular oxidative metabolism, the main pathway of ATP production in the CNS. Also, unlike glial cells that can survive in anaerobic conditions, neurones almost entirely depend on oxidative metabolism of glucose, hence glucose and oxygen are two essential energy substrates to support the function of CNS tissues [80].

Cytochrome c oxidase is one of the key players in aerobic mitochondrial energy metabolism without which oxidative phosphorylation cannot be completed. As mentioned earlier in section 2.2.2, the majority of ATP required for tissue function is produced in the ETC of the mitochondria. However, this is not a perfect process, since oxygen in the mitochondria will also be used to form cell-damaging ROS molecules [5] and the ATP synthesis can also be inhibited through the uncoupling between the electron transfer and phosphorylation reactions [6]. Monitoring CCO in vivo provides a reliable marker for mitochondrial oxygen metabolism as it is the terminal enzyme in the ETC that accounts for around 90% of oxygen consumption in the mitochondria, actively pumping protons for the generation of ATP, and is the only enzyme that can reduce molecular oxygen to water [27]. Furthermore, CCO is responsible for the regulation of neuronal cell function and survival under physiological, pathological and protective conditions in the CNS. As such, a hallmark of many neurodegenerative diseases such as Parkinson's and Alzheimer's diseases as well as stroke is the malfunction of mitochondria including CCO and irreversible inhibition of this enzyme also leads to irreversible outcomes and death [80]. For these reasons, CCO has always been the focus of in-vitro biochemistry and medical research and the potential of CCO as an oxidative metabolic marker for neurones in the central nervous system was first introduced by Wong-Reily et al [81]. After a series of histochemical examinations in which decreased auditory and visual inputs induced a significant reduction in CCO in several brain stem auditory and visual relay nuclei, they demonstrated that the CCO reaction can be used as an oxidative metabolic marker for neurones [82]. However, the potential for the in-vivo measurement of CCO was first demonstrated by Franz Jobsis in 1977 when he used near-infrared light to monitor the redox changes of CCO enzyme based on the relatively good transparency of biological tissues to light in the NIR region. Even though Jobsis's first attempt for in-vivo measurement of CCO was challenging due to the technical limitations and also small concentration of CCO compared to haemoglobin which is also a near infrared absorber, his work established a secure foundation for the development of near infrared spectroscopy (NIRS) as a non-invasive technique for simultaneous measurement of CNS tissue oxygenation and metabolism [83]. A full description of NIRS is covered in chapter 3, including a brief literature review of the use of CCO as a marker for oxidative metabolism in different parts of the CNS.

2.10 Animal Studies and CCO Measurement

Due to their controlled nature, preclinical studies have contributed greatly to understanding optical issues surrounding the NIRS measurement of CCO. The focus of many research groups in 1980s and 1990s was to understand the CCO signal, investigate the role of CCO as a marker for cellular metabolism and its potential as a clinically relevant measure [84]–[89]. However, the diagnostic potential of CCO measurement in different clinical and preclinical settings hasn't been widely studied due to the controversies around the accuracy and validation of CCO measurement and the limitations of the instrumentation caused by the size and applicability of the broadband-NIRS systems.

The main issue with the validation of CCO signal arises from the lack of external comparators, which could assess what measurement techniques (combination of different contributing factors in CCO measurement, i.e. selection of wavelengths, absorption spectra or algorithms that will be discussed further in chapter 3) produce the most physiologically accurate CCO measurement. Unlike the NIRS-measured Hb signals can be somehow compared and validated with other parameters measured invasively such as tissue oxygen, blood volume, and arterial/venous oxygen saturation, there is no gold standard to with which to compare and validate the oxCCO signal experimentally. Despite the various studies which use integrated mathematical models of the biochemistry and physiology that assists in the interpretation of results [90]–[92], there is a need for a gold standard diagnostic technique for metabolism measurement such as PET or MRS/MRI to be used as an external comparator for the oxCCO signal measured by broadband-NIRS. Addressing this issue is the primary aim of this thesis, which will be discussed further in chapter 4.

Like any other clinical instrument, the diagnostic potentials of CCO measurement in different parts of the central nervous system need to be studied and established. While, since its first introduction by Jobsis, the interesting fact about translucency of skin and bone hence the possibility of non-invasive assessment of brain has led most of the preclinical NIRS research towards investigating in-vivo brain oxygenation and metabolism measurement [89], [93], very little or no research has been carried out for the study of spinal cord and the retina using the NIRS-CCO measurement. Another aim of this thesis is to fill this gap through some controlled

animal studies not only to validate the broadband-NIRS measurement of CCO, but also to further investigate the physiological information that the broadband-NIRS CCO measurement can provide in different parts of the CNS (brain, spinal cord and the retina) which are discussed in chapters 7 and 8.

2.11 Summary

Cells require ATP, a large energy carrying biomolecule, to function and survive. Oxidative metabolism or aerobic respiration in the mitochondria is the most efficient pathway for ATP production and nerve cells (neurones) almost entirely depend on aerobic metabolism to function and survive due to their high metabolic demand. Therefore, continuous supply of oxygen and glucose as the main energy substrates is essential specifically for the neurones in the central nervous system that unlike the peripheral nerves seldom repair or regenerate. As a result, CNS neurones are extremely vulnerable to disturbance in oxygen delivery, which can easily lead to malfunction of mitochondria and oxidative metabolism, and eventually to irreversible neurological disorders.

Mitochondrial dysfunction leads to a diverse range of devastating outcomes including cerebral palsy, epilepsy, limb paralysis, blindness, and in more severe cases death. There is a clinical need for a non-invasive portable and easily deployable monitor for CNS tissue oxygenation and metabolism. The main challenge with non-invasive measurement of tissue metabolism in the clinic is associated with the absence of a bedside marker for intracellular oxygen metabolism, as the gold standard techniques (PET and MRS) are invasive and dedicated equipment. Furthermore, the current marker that is under extensive research for tissue oxygen metabolism, metabolic rate of oxygen (MRO_2), is derived from blood oxygenation measurements (not specific to mitochondria) and requires complicated techniques and instrumentations. In this chapter, we proposed the measurement of Cytochrome c oxidase, a mitochondrial enzyme for 95% of intracellular oxygen metabolism, as a valuable potential clinical marker for oxidative metabolism in the CNS, which can be measured non-invasively through near infrared spectroscopy. Finally, the use of animal studies in understanding the optical and physiological issues around CCO measurement, validation of CCO measurement and its establishment as a valid mitochondrial marker for metabolism was discussed which is further explored as part of this thesis in chapters 4, 6, 7 and 8.

Bibliography

[1] D. A. Pocock, Gillian; Richards, Christopher.D.; Richards, "Introduction to cells and tissues," in *Human Physiology*, Fourth., Oxford University Press, 2013, pp. 47–64.

[2] L. Cole and P. R. Kramer, "The Cell," *Hum. Physiol. Biochem. Basic Med.*, pp. 3–10, 2016.

[3] G. Bale, "Development of Optical Instrumentation and Methods to Monitor Brain Oxygen Metabolism : Application to Neonatal Birth Asphyxia," 2016.

[4] B. Miles, "The Electron Transport Chain," 2003. [Online]. Available: https://www.tamu.edu/faculty/bmiles/lectures/electrontrans.pdf.

[5] S. Dröse, "Differential effects of complex II on mitochondrial ROS production and their relation to cardioprotective pre- and postconditioning," *Biochim. Biophys. Acta - Bioenerg.*, vol. 1827, no. 5, pp. 578–587, 2013.

[6] S. A. Mookerejee, A. S. Divakaruni, M. Jastroch, and M. D. Brand, "Mitochondrial uncoupling and lifespan Shona," *Mech. Aging Dev. (Mech Ageing Dev.)*, vol. 131, no. 7–8, pp. 463–472, 2010.

[7] D. A. Pocock, David.A. ; Richards, Christopher.D.; Richards, "Introduction to the Nervous System," in *Human Physiology*, Fourth., Oxford University Press, 2013, pp. 141–150.

[8] M. Hughes and T. Miller, *Nervous system*. Mosby, 2007.

[9] D. Hubel, "Introduction," *Eye Brain Vis.*, no. 1, pp. 1–10, 1995.

[10] D. A. . Pocock, Gillian; Richards, Christopher. D.; Richards, "Nerve cells and their connections," in *Human Physiology*, Fourth., Oxford University Press, 2013, pp. 99–116.

[11] P. Brodal, "Structure of the Neuron and Organization of Nervous Tissue," in *The Central Nervous System*, Oxford University Press, 2016, pp. 3–19.

[12] R. s. Swenson, "REVIEW OF CLINICAL AND FUNCTIONAL NEUROSCIENCE," *Swenson 2006*, 2006. [Online]. Available:

https://www.dartmouth.edu/~rswenson/NeuroSci/index.html.

[13] C. Hooper and J. M. Pocock, "The functions of glia in the CNS." [Online]. Available: http://www.abcam.com/neuroscience/the-functions-of-glia-in-the-cns. [Accessed: 01-Feb-2017].

[14] D. A. Turner and D. C. Adamson, "Neuronal-astrocyte metabolic interactions: understanding the transition into abnormal astrocytoma metabolism.," *J. Neuropathol. Exp. Neurol.*, vol. 70, no. 3, pp. 167–76, 2011.

[15] D. Purves, G. J. Augustine, D. Fitzpatrick, L. C. Katz, A.-S. LaMantia, J. O. McNamara, and S. M. Williams, "The Retina," *Neurosci. Ed.*, 2001.

[16] A. London, I. Benhar, and M. Schwartz, "The retina as a window to the brain-from eye research to CNS disorders.," *Nat. Rev. Neurol.*, vol. 9, no. 1, pp. 44–53, 2013.

[17] K. Dharani and K. Dharani, "Chapter 1 – Functional Anatomy of the Brain," *Biol. Thought*, pp. 3–29, 2015.

[18] D. Purves, G. J. Augustine, D. Fitzpatrick, W. C. Hall, A.-S. LaMantia, and L. E. White, *Neuroscience*, Fifth. Sinauer Associates, 2012.

[19] M. T. T. Wong-Riley, "Energy metabolism of the visual system.," *Eye Brain*, vol. 2, pp. 99–116, 2010.

[20] R. A. Desai, "the Role of Hypoxia in Neuroinflammatory Disease," University College London (UCL), 2013.

[21] H. KABAT and A. JP, "Acute arrest of cerebral circulation in man: Lieutenant ralph rossen (mc), u.s.n.r.," *Arch. Neurol. Psychiatry*, vol. 50, no. 5, pp. 510–528, 1943.

[22] A. J. Hansen, "Effect of anoxia on ion distribution in the brain.," *Physiol. Rev.*, vol. 65, no. 1, pp. 101–48, 1985.

[23] D. K. Anderson, E. D. Means, and T. R. Waters, "Spinal cord energy metabolism in normal and postlaminectomy cats.," *J. Neurosurg.*, vol. 52, no. 3, pp. 387–391, 1980.

[24] "Spinal Cord Injuries - BrainAndSpinalCord.org | Traumatic Spine Injury," *2017 BrainAndSpinalCord.org*. [Online]. Available: http://www.brainandspinalcord.org/spinal-cord-injury/. [Accessed: 07-Feb-2017].

[25] D. Hubel, "The eye," *Eye Brain Vis.*, pp. 1–22, 1995.

[26] W. Song, Q. Wei, W. Liu, T. Liu, J. Yi, N. Sheibani, A. a Fawzi, R. a Linsenmeier, S. Jiao, and H. F. Zhang, "A combined method to quantify the retinal metabolic rate of oxygen using photoacoustic ophthalmoscopy and optical coherence tomography.," *Sci. Rep.*, vol. 4, p. 6525, 2014.

[27] M. T. T. Wong-Riley, "Cytochrome oxidase: an endogenous metabolic marker for neuronal activity," *Trends Neurosci.*, vol. 12, no. 3, pp. 94–101, 1989.

[28] M. J. Donohue, "Hypoxemia & Cellular Hypoxia," 2011.

[29] S. P. Chong, C. W. Merkle, C. Leahy, and V. J. Srinivasan, "Cerebral metabolic rate of oxygen (CMRO_2) assessed by combined Doppler and spectroscopic OCT," *Biomed. Opt. Express*, vol. 6, no. 10, p. 3941, 2015.

[30] L. Østergaard, T. S. Engedal, R. Aamand, R. Mikkelsen, N. K. Iversen, M. Anzabi, E. T. Næss-Schmidt, K. R. Drasbek, V. Bay, J. U. Blicher, A. Tietze, I. K. Mikkelsen, B. Hansen, S. N. Jespersen, N. Juul, J. C. H. Sørensen, and M. Rasmussen, "Capillary transit time heterogeneity and flow-metabolism coupling after traumatic brain injury.," *J. Cereb. Blood Flow Metab.*, vol. 34, no. 10, pp. 1585–98, 2014.

[31] L. Østergaard, S. N. Jespersen, T. Engedahl, E. G. Jiménez, M. Ashkanian, M. B. Hansen, S. Eskildsen, and K. Mouridsen, "Capillary Dysfunction: Its Detection and Causative Role in Dementias and Stroke," *Curr. Neurol. Neurosci. Rep.*, vol. 15, no. 6, 2015.

[32] C. Iadecola, "Neurovascular regulation in the normal brain and in Alzheimer's disease.," *Nat. Rev. Neurosci.*, vol. 5, no. 5, pp. 347–360, 2004.

[33] E. Stefansson, "Oxygen and diabetic eye disease.," *Graefes Arch. Clin. Exp. Ophthalmol.*, vol. 228, no. 2, pp. 120–3, 1990.

[34] A. David A., K. Ronald, and T. W.Gardner, "Diabetic Retinopathy," *New Engl. Jounral Med.*, vol. 366, pp. 1227–39, 2012.

[35] F. Liu and L. D. McCullough, "Inflammatory responses in hypoxic ischemic encephalopathy.," *Acta Pharmacol. Sin.*, vol. 34, no. 9, pp. 1121–30, Sep. 2013.

[36] P. Mergenthaler, U. Lindauer, G. Dienel, and A. Meisel, "Sugar for the brain: the role of glucose in physiological and pathological brain function," *Trends Neurosci.*, vol. 36, no. 10, pp. 587–597, 2013.

[37] M. Mythen and T. Clutton-Brock, "The oxygen trail: measurement," *Br. Med. Bull.*, vol. 55, no. 1, pp. 109–124, 1999.

[38] N. J. Robertson, F. M. Cowan, I. J. Cox, and A. D. Edwards, "Brain alkaline intracellular pH after neonatal encephalopathy," *Ann. Neurol.*, vol. 52, no. 6, pp. 732–742, 2002.

[39] A. Zauner and J. P. Muizelaar, "Measuring cerebral blood flow and metabolism," *Head Inj.*, pp. 217–27, 1997.

[40] P. Liu, L. F. Chalak, and H. Lu, "Non-invasive assessment of neonatal brain oxygen metabolism: A review of newly available techniques," *Early Hum. Dev.*, vol. 90, no. 10, pp. 695–701, 2014.

[41] S. S. Kety and C. F. Schmidt, "the Effects of Altered Arterial Tensions of Carbon Dioxide and Oxygen on Cerebral Blood Flow and Cerebral Oxygen Consumption of Normal Young Men," *J. Clin. Invest.*, vol. 27, no. 4, pp. 484–492, 1948.

[42] M. Fries, M. H. Weil, S. Sun, L. Huang, X. Fang, G. Cammarata, C. Castillo, and W. Tang, "Increases in tissue Pco2 during circulatory shock reflect selective decreases in capillary blood flow.," *Crit. Care Med.*, vol. 34, no. 2, pp. 446–52, Feb. 2006.

[43] E. Almac, M. Siegemund, C. Demirci, and C. Ince, "Microcirculatory recruitment maneuvers correct tissue CO2 abnormalities in sepsis.," *Minerva Anestesiol.*, vol. 72, no. 6, pp. 507–19, Jun. 2006.

[44] E. Futier, J. L. Teboul, and B. Vallet, "Tissue carbon dioxide measurement as an index of perfusion: What have we missed?," *Trends Anaesth. Crit. Care*, vol. 1, no. 2, pp. 95–99, 2011.

[45] E. Ruokonen, J. Takala, and A. Kari, "Regional blood flow and oxygen transport in patients with the low cardiac output syndrome after cardiac surgery.," *Critical care medicine*, vol. 21, no. 9. pp. 1304–11, 1993.

[46] T. H. Yuh-Chin, "Monitoring Oxygen Delivery in the Critically Ill," *CHEST J.*, vol. 128, no. 5, p. 554S–560S, 2005.

[47] S. A. McLellan and T. S. Walsh, "Oxygen delivery and haemoglobin," *Contin. Educ. Anaesthesia, Crit. Care Pain*, vol. 4, no. 4, pp. 123–126, 2004.

[48] R. S. Hotchkiss, R. S. Rust, C. S. Dence, T. H. Wasserman, S. K. Song, D. R. Hwang, I. E. Karl, and M. J. Welch, "Evaluation of the role of cellular hypoxia in sepsis by the hypoxic marker [18F]fluoromisonidazole.," *Am. J. Physiol.*, vol. 261, no. 4 Pt 2, pp. R965-72, 1991.

[49] R. Vink, T. K. McIntosh, M. W. Weiner, and a I. Faden, "Effects of traumatic brain injury on cerebral high-energy phosphates and pH: a 31P magnetic resonance spectroscopy study.," *J. Cereb. Blood Flow Metab.*, vol. 7, no. 5, pp. 563–571, 1987.

[50] E. B. Cady, M. J. Dawson, P. L. Hope, P. S. Tofts, A. M. D. L. Costello, D. T. Delpy, E. O. R. Reynolds, and D. R. Wilkie, "Non-invasive investigation of cerebral metabolism in newborn infats by phosphorus nuclear magnetic resonance spectroscopy," *Lancet*, vol. 321, no. 8333, pp. 1059–1062, 1983.

[51] P. L. Hope, E. B. Cady, P. S. Tofts, P. A. Hamilton, A. M. D. Costello, D. T. Delpy, A. Chu, E. O. R. Reynolds, and D. R. Wilkie, "Cerebral Energy-Metabolism Studied with Phosphorus Nmr-Spectroscopy in Normal and Birth-Asphyxiated Infants," *Lancet*, vol. 2, no. 8399, pp. 366–370, 1984.

[52] D. Azzopardi, J. Wyatt, E. Cady, J. Delphy, DT, Baudin, and A. Stewart,

"Prognosis of newborn infants with hypoxic-ischemic brain injury assessed by phosphorous magnetic resonance spectroscopy," *Pediatr. Res.*, vol. 25, no. 5, pp. 445–51, 1989.

[53] C. a Fee and R. I. Pettigrew, "National Institute of Biomedical Imaging and Bioengineering: poised for the future.," *Radiology*, vol. 229, no. 3, pp. 636–637, 2003.

[54] M. J. P. Barrett and V. Suresh, "Improving estimates of the cerebral metabolic rate of oxygen from optical imaging data," *Neuroimage*, vol. 106, pp. 101–110, 2015.

[55] K. G. Lyabakh and I. N. Mankovskaya, "Role of Differences in Microcirculatory Blood Flow Velocity in Optimizing Parameters of the Skeletal Muscle Oxygen Model," in *Oxygen Transport to Tissue XXVII*, Springer US, 2006, pp. 81–86.

[56] T. Durduran, "Noninvasive measurements of tissue hemodynamics with hybrid diffuse optical methods," *Med. Phys.*, vol. 31, no. 7, p. 2178, 2004.

[57] R. L. Buckner, A. Z. Snyder, B. J. Shannon, G. LaRossa, R. Sachs, A. F. Fotenos, Y. I. Sheline, W. E. Klunk, C. A. Mathis, J. C. Morris, and M. A. Mintun, "Molecular, Structural, and Functional Characterization of Alzheimer's Disease: Evidence for a Relationship between Default Activity, Amyloid, and Memory," *J. Neurosci.*, vol. 25, no. 34, pp. 7709–7717, Aug. 2005.

[58] P. Borghammer, M. Vafaee, K. Ostergaard, A. Rodell, C. Bailey, and P. Cumming, "Effect of memantine on CBF and CMRO2 in patients with early Parkinson's disease," *Acta Neurol. Scand.*, vol. 117, no. 5, pp. 317–323, 2008.

[59] H. Lu, F. Xu, K. M. Rodrigue, K. M. Kennedy, Y. Cheng, B. Flicker, A. C. Hebrank, J. Uh, and D. C. Park, "Alterations in cerebral metabolic rate and blood supply across the adult lifespan," *Cereb. Cortex*, vol. 21, no. 6, pp. 1426–1434, 2011.

[60] T. C. Glenn, D. F. Kelly, W. J. Boscardin, D. L. McArthur, P. Vespa, M. Oertel,

D. a Hovda, M. Bergsneider, L. Hillered, and N. a Martin, "Energy dysfunction as a predictor of outcome after moderate or severe head injury: indices of oxygen, glucose, and lactate metabolism.," *J. Cereb. Blood Flow Metab.*, vol. 23, no. 10, pp. 1239–1250, 2003.

[61] Y. Ge, Z. Zhang, H. Lu, L. Tang, H. Jaggi, J. Herbert, J. S. Babb, H. Rusinek, and R. I. Grossman, "Characterizing brain oxygen metabolism in patients with multiple sclerosis with T2-relaxation-under-spin-tagging MRI," *J. Cereb. Blood Flow Metab.*, vol. 32, no. 3, pp. 403–412, 2012.

[62] C. E. Elwell, J. R. Henty, T. S. Leung, T. Austin, J. H. Meek, D. T. Delpy, and J. S. Wyatt, "Measurement of CMRO2 in Neonates Undergoing Intensive Care Using Near Infrared Spectroscopy," in *Oxygen Transport to Tissue XXVI*, New York: Springer-Verlag, 2005, pp. 263–268.

[63] N. Roche-Labarbe, S. A. Carp, A. Surova, M. Patel, D. A. Boas, P. E. Grant, and M. A. Franceschini, "Erratum: Noninvasive optical measures of CBV, StO2, CBF index, and rCMRO2 in human premature neonates' brains in the first six weeks of life," *Hum. Brain Mapp.*, vol. 32, no. 7, p. 1179, 2011.

[64] J. B. De Vis, E. T. Petersen, T. Alderliesten, F. Groenendaal, L. S. de Vries, F. van Bel, M. J. N. L. Benders, and J. Hendrikse, "Non-invasive MRI measurements of venous oxygenation, oxygen extraction fraction and oxygen consumption in neonates," *Neuroimage*, vol. 95, pp. 185–192, 2014.

[65] P. Liu, H. Huang, N. Rollins, L. F. Chalak, T. Jeon, C. Halovanic, and H. Lu, "Quantitative assessment of global cerebral metabolic rate of oxygen (CMRO2) in neonates using MRI," *NMR Biomed.*, vol. 27, no. 3, pp. 332–340, 2014.

[66] F. Xu, Y. Ge, and H. Lu, "Noninvasive quantification of whole-brain cerebral metabolic rate of oxygen (CMRO2) by MRI," *Magn. Reson. Med.*, vol. 62, no. 1, pp. 141–148, 2009.

[67] R. G. Wise, A. D. Harris, A. J. Stone, and K. Murphy, "Measurement of OEF and absolute CMRO2: MRI-based methods using interleaved and combined hypercapnia and hyperoxia," *Neuroimage*, vol. 83, pp. 135–147, 2013.

[68] P. Liu, F. Xu, and H. Lu, "Test-retest reproducibility of a rapid method to measure brain oxygen metabolism," *Magn. Reson. Med.*, vol. 69, no. 3, pp. 675–681, 2013.

[69] V. Jain, M. C. Langham, and F. W. Wehrli, "MRI estimation of global brain oxygen consumption rate.," *J. Cereb. Blood Flow Metab.*, vol. 30, no. 9, pp. 1598–1607, 2010.

[70] A. L. Davies, R. A. Desai, P. S. Bloomfield, P. R. McIntosh, K. J. Chapple, C. Linington, R. Fairless, R. Diem, M. Kasti, M. P. Murphy, and K. J. Smith, "Neurological deficits caused by tissue hypoxia in neuroinflammatory disease," *Ann. Neurol.*, vol. 74, no. 6, pp. 815–825, 2013.

[71] W. Liu and H. F. Zhang, "Noninvasive in vivo imaging of oxygen metabolic rate in the retina," *Conf. Proc. ... Annu. Int. Conf. IEEE Eng. Med. Biol. Soc. IEEE Eng. Med. Biol. Soc. Annu. Conf.*, vol. 2014, pp. 3865–3868, 2014.

[72] B. A. Berkowitz and C. A. Wilson, "Quantitative Mapping of Ocular Oxygenation Using Magnetic Resonance Imaging," *Magn. Reson. Med.*, vol. 33, no. 4, pp. 579–581, Apr. 1995.

[73] A. Harris, R. B. Dinn, L. Kagemann, and E. Rechtman, "A review of methods for human retinal oximetry.," *Ophthalmic Surg. Lasers Imaging*, vol. 34, no. 2, pp. 152–64.

[74] H. Li, B. Dong, Z. Zhang, H. F. Zhang, and C. Sun, "A transparent broadband ultrasonic detector based on an optical micro-ring resonator for photoacoustic microscopy," *Sci. Rep.*, vol. 4, p. 4496, Mar. 2014.

[75] F. Hyder, J. R. Chase, K. L. Behar, G. F. Mason, M. Siddeek, D. L. Rothman, and R. G. Shulman, "Increased tricarboxylic acid cycle flux in rat brain during forepaw stimulation detected with 1H[13C]NMR.," *Proc. Natl. Acad. Sci. U. S. A.*, vol. 93, no. 15, pp. 7612–7, 1996.

[76] X.-H. Zhu, N. Zhang, Y. Zhang, K. Uğurbil, and W. Chen, "New insights into central roles of cerebral oxygen metabolism in the resting and stimulus-evoked brain.," *J. Cereb. blood flow Metab.*, vol. 29, no. 1, pp. 10–8, 2009.

[77] Detre JA, Alsop DC., "Perfusion magnetic resonance imaging with continuous

arterial spin labeling: methods and clinical applications in the central nervous system," *Eur. J. Rad.*, vol. 30, pp. 115–124, 1999.

[78] N. Roche-labarbe, S. a Carp, A. Surova, M. Patel, A. David, P. E. Grant, and M. A. Franceschini, "Noninvasive Optical Measures of CBV, StO2 , CBF Index, and rCMRO2 in Human Premature Neonates' Brains in the First Six Weeks of Life," *Hum Brain Mapp*, vol. 31, no. 3, pp. 341–352, 2010.

[79] A. N. Massaro, M. Bouyssi-Kobar, T. Chang, L. G. Vezina, A. J. du Plessis, and C. Limperopoulos, "Brain Perfusion in Encephalopathic Newborns after Therapeutic Hypothermia," *Neuroradiology*, vol. 34, no. 8, pp. 1649–1655, 2013.

[80] S. Arnold, "Cytochrome c Oxidase and Its Role in Neurodegeneration and Neuroprotection," Springer New York, 2012, pp. 305–339.

[81] M. Wong-Riley and E. W. Carroll, "Effect of impulse blockage on cytochrome oxidase activity in monkey visual system," *Nature*, vol. 307, no. 5948. pp. 262–264, 1984.

[82] M. Wong-Riley, "Changes in the visual system of monocularly sutured or enucleated cats demonstrable with cytochrome oxidase histochemistry," *Brain Res.*, vol. 171, no. 1, pp. 11–28, 1979.

[83] F. Jobsis, "Noninvasive, infrared monitoring of cerebral and myocardial oxygen sufficiency and circulatory parameters," *Science (80-.).*, vol. 198, no. 4323, 1977.

[84] H. Matsumoto, T. Oda, M. A. Hossain, and N. Yoshimura, "Does the redox state of cytochrome aa3 reflect brain energy level during hypoxia? Simultaneous measurements by near infrared spectrophotometry and 31P nuclear magnetic resonance spectroscopy.," *Anesth. Analg.*, vol. 83, no. 3, pp. 513–8, 1996.

[85] C. E. Cooper, M. Cope, R. Springett, P. N. Amess, J. Penrice, L. Tyszczuk, S. Punwani, R. Ordidge, J. Wyatt, and D. T. Delpy, "Use of mitochondrial inhibitors to demonstrate that cytochrome oxidase near-infrared spectroscopy can measure mitochondrial dysfunction noninvasively in the brain.," *J. Cereb.*

Blood Flow Metab., vol. 19, no. 1, pp. 27–38, 1999.

[86] V. Quaresima, R. Springett, M. Cope, J. T. Wyatt, D. T. Delpy, M. Ferrari, and C. E. Cooper, "Oxidation and reduction of cytochrome oxidase in the neonatal brain observed by in vivo near-infrared spectroscopy," *Biochim. Biophys. Acta - Bioenerg.*, vol. 1366, no. 3, pp. 291–300, 1998.

[87] M. Ferrari, I. Giannini, A. Carpi, and P. Fasella, "Non-invasive near infrared spectroscopy of brain in fluorocarbon exchange-transfused rats.," *Physiol. Chem. Phys. Med. NMR*, vol. 15, no. 2, pp. 107–13, 1983.

[88] Y. Hoshi, O. Hazeki, Y. Kakihana, and M. Tamura, "Redox behavior of cytochrome oxidase in the rat brain measured by near-infrared spectroscopy Redox behavior of cytochrome oxidase in the rat brain measured by near-infrared spectroscopy," *J. Appl. Physiol.*, pp. 1842–1848, 1997.

[89] C. A. Piantadosi and F. F. Jobsis-Vandervliet, "Spectrophotometry of Cerebral Cytochrome a, a3, in Bloodless Rats," vol. 305, pp. 89–94, 1984.

[90] M. Banaji, A. Mallet, C. E. Elwell, P. Nicholls, and C. E. Cooper, "A model of brain circulation and metabolism: NIRS signal changes during physiological challenges," *PLoS Comput. Biol.*, vol. 4, no. 11, 2008.

[91] T. Moroz, M. Banaji, N. J. Robertson, C. E. Cooper, and I. Tachtsidis, "Computational modelling of the piglet brain to simulate near-infrared spectroscopy and magnetic resonance spectroscopy data collected during oxygen deprivation," no. January, pp. 1499–1509, 2012.

[92] M. Caldwell, T. Hapuarachchi, D. Highton, C. Elwell, M. Smith, and I. Tachtsidis, "BrainSignals revisited: Simplifying a computational model of cerebral physiology," *PLoS One*, vol. 10, no. 5, pp. 1–28, 2015.

[93] F. F. F. Jobsis, "Noninvasive, Infrared Monitoring of Cerebral and Myocardial Oxygen Sufficiency and Circulatory Parameters," *Science (80-.).*, vol. 198, no. 4323, pp. 1264–1267, 1977.

Chapter 3. Broadband NIRS: Towards the Development of Compact Clinical Systems

As mentioned in chapter 2, cytochrome c oxidase (CCO), measured by near infrared spectroscopy (NIRS), is a unique marker for intracellular oxygen metabolism in various CNS disease and disorders. Introduced by Jobsis 40 years ago [1], broadband continuous wave near-infrared spectroscopy (Broadband-CW-NIRS) is a non-invasive optical technique that enables in-vivo measurement of vascular haemodynamics and oxygenation, as well as intracellular oxygen consumption. The technique uses the changes in the intensity of the diffusely scattered light through the tissue to estimate changes in the concentration of optical absorbers (chromophores).

The chromophores of interest in physiological monitoring are the blood oxygen carrying molecules oxygenated and deoxygenated haemoglobin (HbO_2 and HHb) and a key enzyme for cellular respiration, cytochrome-c-oxidase (CCO) that was mentioned is a unique marker for oxidative metabolism. Due to its non-invasive nature, NIRS was used to monitor new-born infants soon after its first development and until today has been used specifically to study brain function in health and disease in many clinical and preclinical studies [2]–[5] .

Current commercial NIRS systems (including miniaturised and wireless systems) only provide HHb and HbO_2 measurement using differential spectroscopy at 2-3 wavelengths and fail to provide metabolism measurement through measuring CCO. Furthermore, current broadband-NIRS systems that provide reliable CCO measurement, are not practical for being used as a clinical instrument due to their size and weight as well as complexity of operation. This chapter starts with the principles of CW and broadband-NIRS including the interaction of NIR light with the biological tissues and CW-NIRS instrumentation. It then proceeds with the optical issues around the in vivo measurement of CCO and the broadband-NIRS systems developed at UCL. The chapter closes with discussing the limitations of current broadband systems for being used as a clinical instrument and a brief review towards miniaturisation of broadband-NIRS using off-the-shelf spectrometers, which is still very new in this field.

3.1 Near-Infrared Spectroscopy (NIRS) Fundamentals

Photons in the ultraviolet and visible region have enough energy to excite or ionise tissue by elevating the energy levels of bound electrons. Furthermore, due to the strong light absorption properties of haemoglobin and water in ultraviolet and visible spectra, optical techniques that are based on these wavelengths are limited to interrogating shallow tissue [6]. However, due to the weak absorption of haemoglobin and water in NIR region (650-1000 nm), which is also called therapeutic window, photons in NIR can penetrate longer enabling deep tissue interrogation. Also, due to their lower energy, NIR photons are safe and non-ionising to biological tissues as they only interact with the molecular bonds exciting the molecular vibrations and non-invasively provide useful information about the underlying tissue. Figure 3.13 illustrates the absorption spectra of NIRS chromophores (absorbers) in human tissue.

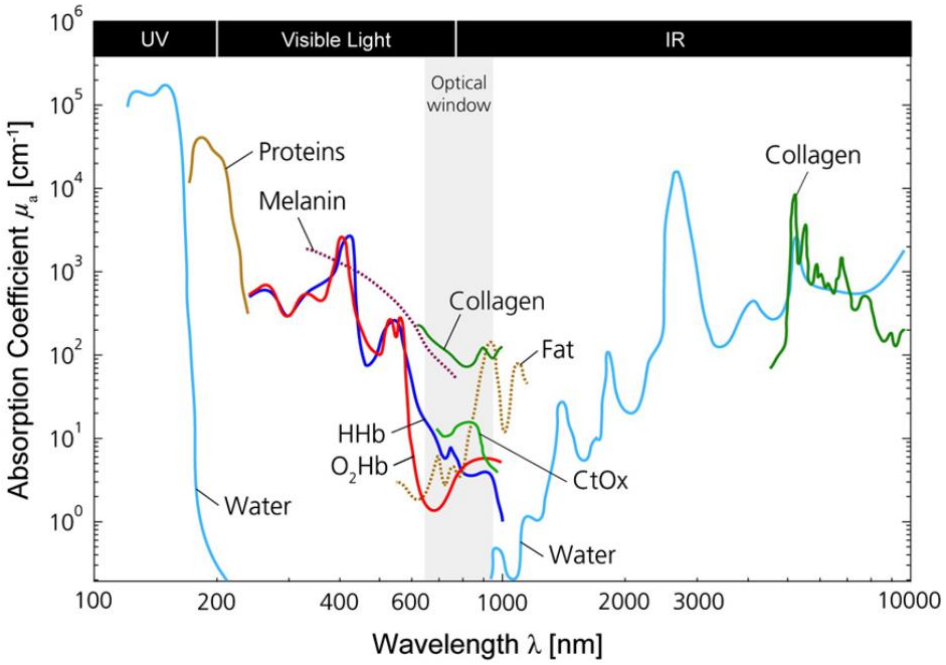

Figure 3.13: Absorption spectra for different tissue chromophores (natural logarithm base). Taken from [7]

Based on the relative transparency of biological tissues (including bones) to NIR spectrum and the oxygenation dependent light absorption characteristics of molecules such as haemoglobin and cytochrome c oxidase, NIRS enables simultaneous measurement of tissue oxygenation and metabolism. This is specifically advantageous for monitoring brain as the NIR light can easily penetrate the scalp and the skull and probe the cerebral cortex without the need for contrast agents or radioisotopes.

Originally, the use of continuous light to investigate human tissue dates back to the 19th century [8] but the feasibility of continuous and non-invasive measurement of tissue concentration of oxygenated Haemoglobin (oxyhaemoglobin, [HbO2]) and deoxygenated haemoglobin (deoxyhaemoglobin, [HHb]) and redox changes of CCO (oxidised-CCO, [oxCCO]) was first demonstrated and established by Jobsis in 1977 [1]. Due to its non-invasive nature, NIRS soon became clinically available for monitoring brain tissue oxygenation in premature infants [9] and soon after that in 1986, the first quantitative NIRS measurement was performed in sick newborn infants [10]. Since then, NIRS has been well recognised as a research tool for monitoring tissue oxygenation and haemodynamics in different clinical and preclinical studies in animals, babies and adults [11]–[14].

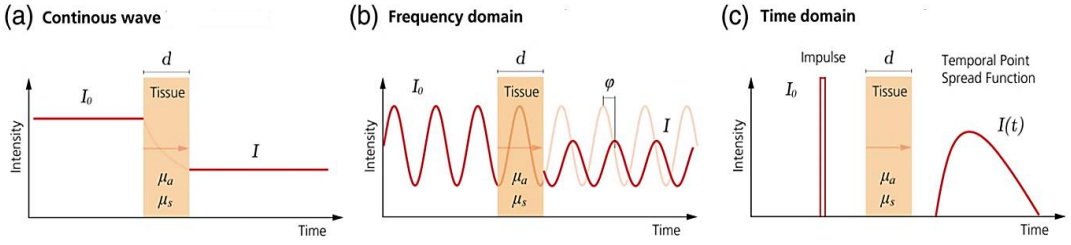

Figure 3.14: Illustration of the three different NIR measurement techniques. Image is taken from [7] In the continuous wave technology (a), the input light is emitted at a constant intensity and the changes of the intensity of light that traversed the tissue is measured. In frequency domain systems (b), the intensity of the input light is modulated and then the intensity changes of the light that passed the tissue as well as its phase shift is measured, which corresponds to the time of flight of photons. In time domain systems (c) an extremely short pule of light is sent through the tissue and the arrival times of the detected photons are measured. I_0 is the input intensity, I is the intensity of transmitted light, d is the thickness of the medium, μ_a is the absorption coefficient, μ_s is the scattering coefficient, φ is the phase shift, and I(t) is the temporal point spread function of the transmitted light.

Three major experimental techniques exist in NIRS, which are categorised by the time dependence of the source intensity incident on the tissue. These techniques are Continuous-wave (CW)-NIRS which is the oldest method, as well as time domain and frequency domain systems that are able to separate scattering and absorption effects in tissue. Time and frequency domain systems are relatively complex and expensive whereas the CW systems are cheaper and technically simpler to be used by non-experts and provide quantification of "change" in tissue concentration of oxygenated and deoxygenated haemoglobin [15],[16],[17]. CW systems are advantageous due to the capability to be miniaturised for easy application in the demanding clinical environments that is the focus of this thesis. Figure 3.14 illustrates the principles behind each NIRS methodology/technique.

3.1.1 Light-Tissue Interactions

Light propagation in biological tissues is highly dependent on the penetrating wavelength and in the NIR region the major phenomena ruling light propagation are scattering and absorption that are fully described below [6].

3.1.1.1 Scattering

Biological tissues are referred to as highly scattering or turbid media since scattering is the predominant light-tissue interaction. Scattering is caused by the variations in refractive index at a macroscopic and microscopic scale including membrane boundaries of the cells as well as at boundaries between organelles within the cells [18]. Cell nuclei and mitochondria are the most important scatters of NIR photons and because their dimensions (100 nm-6 μm) fall within the NIR window, most of these organelles interact with NIR photons through Mie regime, hence exhibit highly anisotropic forward-directed scattering. Mie regime describes light interaction with spherical objects where the size of the scatterer is compatible with the wavelength [19]. The more the photons are scattered within the tissue, the longer pathlength they travel hence the probability of absorption will significantly increase. Therefore, while the mean free path between photon scattering events is on the order of 0.1 mm, the mean absorption length due to multiple scattering can extend to 1-10 cm [20]. The contribution of single scattering event to the attenuation of light is through the following equation:

$$A = log_{10}\left[{}^{I_0}/_{I}\right] = \mu_s.d = N.s.d \tag{3.1}$$

Where A is the absolute attenuation in O.D, I_0 and I are the intensity of incident and transmitted light in photon counts, d is the optical pathlength and $\mu_s = N.s$ is the scattering coefficient (mm^{-1}) which is the probability of a photon being absorbed per unit length and is a product of the number density of scattering particles (N) and the scattering cross section of the particles (s). In biological tissues, however, NIR photons undergo multiple elastic scattering and as a result change their direction quickly.

Therefore, it is necessary to correct the above formula for the probability of a photon being scattered in a given direction at every interaction. Even though in biological tissues scattering occurs anisotropically and in forward direction, it can be considered as being isotropically distributed after travelling a few millimetres trough the tissue. That is because light loses all of its original directionality due to the typical values of tissue scattering coefficient. Therefore, according to diffusion theory the characteristic scatter of tissues can be expressed in terms of a transport scatter coefficient (μ'_s) equals the effective number of isotropic scatters per unit length:

$$\mu'_s = \mu_s(1 - g) \tag{3.2}$$

g is the scattering anisotropy factor and in it varies between 0.69>g>0.99 in biological tissues [21].

3.1.1.2 Absorption

Absorption corresponds to a loss of energy associated with molecular electronic transitions [6]. Human tissues contain a variety of substances with well-defined absorption spectra at NIR wavelengths. These substances exist in quantities that are sufficient to contribute to significant attenuation of the transmitted light. The amount of light absorption by each substance is described by its absorption coefficient μ_a:

$$\mu_a = c.\varepsilon \tag{3.3}$$

Where c is the concentration of the absorber (mol) and ε is the specific absorption coefficient (mm^{-1} mol^{-1}).

Therefore, in a non-scattering medium the attenuation of light intensity is described by the Beer-Lambert Law, which relates the light attenuation to the absorption coefficient (μ_a) multiplied by the optical pathlength which in this case equals the spacing between the source and the detector (d):

$$A = log_{10}\left[{}^{I_0}/_{I}\right] = \mu_a.d = c.\varepsilon.d \tag{3.4}$$

In biological media containing several different absorbing compounds, the overall attenuation of light is the sum of attenuations caused by each absorbing compound (also called chromophore), as can be seen in equation 3.5)

$$A = log10\left[\frac{Io}{I}\right] = [\,\varepsilon_1 c_1 + \varepsilon_2 c_2 + \varepsilon_3 c_3 + \ldots + \varepsilon_n c_n\,]d \tag{3.5}$$

3.1.2 Main NIR Absorbers

The main NIR chromophores in tissue include water, lipids, melanin (constant absorbers), as well as haemoglobin, and cytochrome c oxidase each having their own oxygenation dependent specific absorption spectrum as seen in Figure 3.15.

-Water: Due to the high concentration of water in living tissue (~80% of adult brain tissue), it is very important to consider the water absorption characteristics in NIR spectroscopy. Water has a relatively low absorption in range 200-900 nm and beyond 900 nm the absorption increases with increasing wavelength (see Figure 3.13). This high water absorption above 900 nm sets a limit for longer wavelengths used for NIRS measurements and a window of NIR transparency can be defined for tissue investigation between 650-900 nm. Water can be considered as a fixed constant NIR absorber since its concentration remains relatively constant for most clinical NIRS measurements [18]. Figure 3.15 shows the specific extinction coefficient of water across the NIR window. Between 650-900 nm the extinction coefficient increases with wavelength but stays very low (by 2 order of magnitude) relative to other chromophores (note that the water spectrum is scaled on the secondary axis).

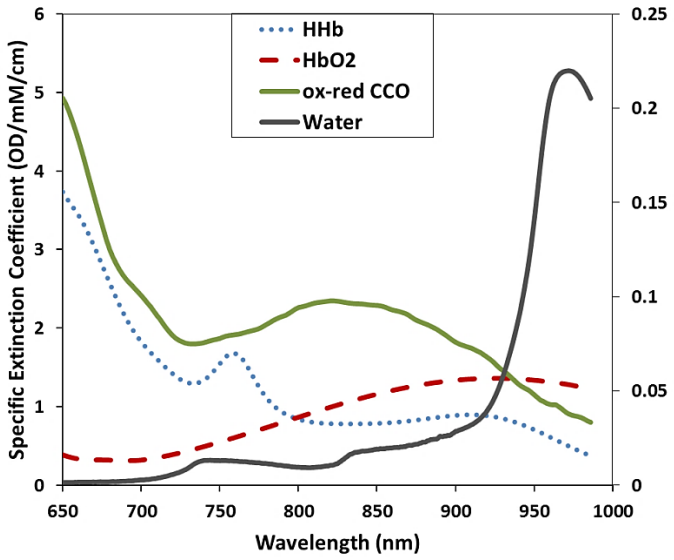

Figure 3.15: Extinction coefficient spectra for water, oxy-haemoglobin, deoxy-haemoglobin and oxidised - reduced cytochrome-c-oxidase. Note that the water spectrum is scaled on the secondary axis to be visible. Taken from [22]

-Lipids: Lipid makes around 10-40% of tissue and it can also be considered as constant absorber because its concentration in a certain tissue doesn't change during the course of a clinical measurement. The absorption spectrum of lipid is approximately the same as water having weak absorption in the NIR window <900 nm, as seen in Figure 3.13 [18].

-**Melanin:** Melanin is a complex polymer within the epidermis layer of skin and a highly effective absorber of light; hence its concentration in the skin directly affects the transmission of light through the tissue. However, its absorption of NIR is considered to be constant and oxygen independent. There are other other chromophores in the NIR in tissue, such as collagen as seen in Figure 3.13 that is considered as weak NIR absorbers since its peak absorption is >900 nm [7]. -**Haemoglobin:** Haemoglobin (Hb) is the iron-containing molecule within the red blood cells which transports oxygen from the lungs to the tissues. The light absorption characteristics of Hb are highly dependent on its binds to oxygen molecules; meaning that oxygenated (HbO2) and deoxygenated haemoglobin (HHb) have distinct absorption spectra in NIR enabling spectroscopic separation of these two compounds using only a few wavelengths (Figure 3.13 and Figure 3.15). Moreover, the haemoglobin concentration independent of oxygen saturation can also be calculated using an isosbestic point at 800 nm where the total absorbance of haemoglobin does not depend on any physical or chemical change. There are also other haemoglobin compounds with a characteristic absorption in NIR region, which are ignored in NIRS measurements because the total error from neglecting all these compounds in the in-vivo measurements is less than 1%. These compounds include carboxyhaemoglobin (HbCO) which has a low extinction coefficient in NIR and its effect in most in-vivo measurements is negligible, Haemiogobin (Hi) which exist in very low concentrations and sulfhaemoglobin (SHb) which is not present in the normal blood at all [18].

-Cytochrome c Oxidase: Cytochrome c oxidase (CCO) is the final enzyme in the electron transport chain of the mitochondria which catalyses over 95% of aerobic metabolisms within the cells hence is a reliable marker for investigating tissue oxidative metabolism. Locating in the inner mitochondrial membrane, CCO consists of four redox active metal centres, two haem iron (a and a_3) and two copper centres (Cu_A and Cu_B), as can be seen in chapter 2, Figure 2.4. Electron binding site of CCO

is the binuclear unit made of Cu_B and a_3 whereas main NIR chromophores in CCO are haem a and Cu_A centres, the latter being the primary absorbing molecule. The total concentration of tissue CCO does not vary during the course of a measurement. However, oxidised and reduced CCO have different absorption spectra in NIR region; oxidised CCO having a broad spectrum around 830 nm, which is missing in the reduced enzyme, hence they can be spectroscopically separated and the measurement of oxidised-CCO (oxCCO) can be used as an indicator for tissue oxidative metabolic state [18]. Figure 3.15 depicts the difference spectrum between the oxidised and reduced CCO enzyme.

Note: It should be mentioned that previous NIRS studies, both preclinical and clinical have referred to what we call in this thesis oxCCO signal as CytOx, Cu_A, CCO and oxCCO. However, for clarity in this thesis, the term oxCCO is used to describe the NIRS measurement of oxidation of cytochrome-c-oxidase, which arises from its redox state-dependent changes in the NIR spectrum. Although the dominant chromophore is the NIR is the Cu_A centre, other cytochrome redox centres and oxygen intermediates can also contribute to this signal.

3.1.3 Total Attenuation in Tissue

By combining the effects of multiple scattering and absorption, the Beer-Lambert law for light attenuation can be modified as:

$$A = log_{10}\left[{}^{I_0}/_{I}\right] = c.\varepsilon(\lambda).DP(\lambda) + G(\lambda) \tag{3.6}$$

The modified Beer-Lambert law (MBLL) to describe total light attenuation through the tissue was developed by Delpy et al in 1988 [23] which takes the effect of wavelength-dependent scattering (G(λ)) into account. The value of the term G is unknown as it is dependent on the measurement geometry as well as the tissue being examined. DP is the differential pathlength or the true optical distance that light travels in the tissue and equals the geometrical distance d multiply by the differential pathlength factor (DPF):

$$DP(\lambda) = d.DPF(\lambda) \tag{3.7}$$

Accounting for the effect of scattering, DPF is directly dependent on many factors including the amount of soft tissue, muscle and bone under illumination. It also

varies with the angle between source-detector probes and is wavelength dependent. In 1993, the MBLL was further modified to account for wavelength dependency of DPF [24] which allows for decreasing scattering effects at increasing wavelengths in tissue. The wavelength dependency of DPF is however almost negligible for optode spacing greater than 2.5 cm [24]. DPF also varies with wavelength through another attenuation mechanism in which high absorption of light at specific wavelength decreases the chance that light at that wavelength reaches the detector.

3.1.4 Differential Spectroscopy for Quantification of NIR Chromophores

Figure 3.16 illustrates a usual measurement situation and it is generally accepted that the measurement volume is shaped like a banana [25].

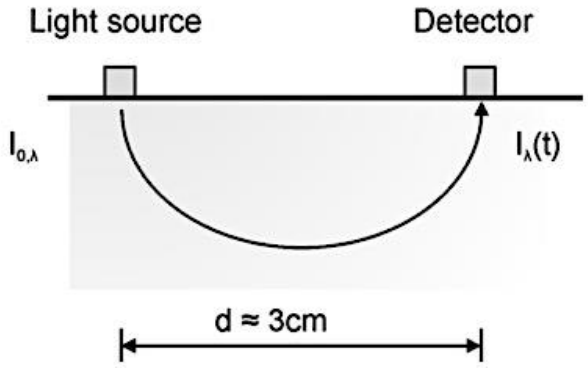

Figure 3.16: Schematic of a typical experimental setup using differential spectroscopy. Taken from [26]

Because the scattering factor G is unknown, the MBLL (eq 3.6) cannot be used to measure the absolute attenuation of light through the tissue. Therefore, absolute changes in the concentration of chromophores cannot be calculated simply using the MBLL. However, assuming no change in incident light intensity over time ($I_0(t_1) = I_0(t_2)$) and no change in losses due to scattering effect s ($G_\lambda(t_1) = G_\lambda(t_2)$), it is possible to calculate change in concentration of chromophores Δc from a measured change in attenuation ΔA. This technique is called differential spectroscopy which enables absolute quantification of changes in chromophore concentration from an arbitrary zero at the start of the measurement period based on the known differential pathlength (DP).

If $A(t_1) = A_1$ and $A(t_2) = A_2$ are the measured attenuation at two different times, the modified Beer Lambert law at each time can be written as:

$$A_1 = log_{10}\left[{}^{I_0}/_{I_1}\right] = c_1.\varepsilon(\lambda).DP(\lambda) + G_1(\lambda) \tag{3.8}$$

$$A_2 = log_{10}\left[{}^{I_0}/_{I_1}\right] = c_1.\varepsilon(\lambda).DP(\lambda) + G_1(\lambda) \tag{3.9}$$

Assuming no change in the intensity (I_0) and scattering effect G(λ), the differential attenuation can be written as:

$$\begin{gathered}\Delta A(\lambda) = A_2(\lambda) - A_1(\lambda) = log_{10}\left[{}^{I_1(\lambda)}/_{I_2(\lambda)}\right] \\ \Delta A(\lambda) = (c_2 - c_1).\varepsilon(\lambda).DP(\lambda)\end{gathered} \tag{3.10}$$

Therefore, change in concentration of a single chromophore can be determined from the measured change in attenuation relative to the first measurement:

$$\Delta c = \Delta A(\lambda).\varepsilon(\lambda)^{-1}.DP(\lambda)^{-1} \tag{3.11}$$

For *m* number of chromophores *n* number of wavelengths is required, where n must be equal or greater than m (note that the wavelength dependency of DPF is considered in equation 3.12).

$$\begin{bmatrix}\Delta c_1 \\ \Delta c_2 \\ \vdots \\ \vdots \\ \Delta c_m\end{bmatrix} = \frac{1}{d}[\varepsilon_{n,m}]^{-1}.\begin{bmatrix}\dfrac{\Delta A(\lambda_1)}{DPF(\lambda_1)} \\ \dfrac{\Delta A(\lambda_2)}{DPF(\lambda_2)} \\ \vdots \\ \vdots \\ \dfrac{\Delta A(\lambda_n)}{DPF(\lambda_n)}\end{bmatrix} \quad , \quad n \geq m \tag{3.12}$$

$[\varepsilon]_{n.m}$ is a two-dimensional matrix including the specific extinction coefficients of each chromophore with respect to wavelength.

To resolve concentration changes of oxy and deoxy haemoglobin from 3.12, it is sufficient to only use two wavelengths to solve the equation for two unknowns, especially if the wavelengths are chosen at the either side of the isosbestic point (Figure 3.15). This is possible due to the distinct absorption spectra of HHb and HbO_2 and their large concentrations in-vivo. The same way, it should be possible to resolve changes in three chromophores (HHb, HbO_2 and oxCCO) with just three wavelengths. However, due to the relatively broad absorption band of the oxidised-reduced CCO spectrum, as explained in section 3.1.2 Main NIR Absorbers and its much lower concentration in-vivo compared to that of haemoglobin, it is difficult to accurately

separate the oxCCO signal from the much larger signals due to Hb and HbO_2, using only three wavelengths [27].

To resolve this issue, various algorithms have been developed by different groups for quantification of change in the concentrations as assessed and described fully in 1995 by Matcher et al. The algorithm developed at UCL, also assessed by Matcher et al., is suitable for all geometries and optical systems as it assumes that tissue scattering and pathlength remain approximately constant throughout the course of the measurement [28], [29]. The UCL algorithm is a least square fitting procedure, finding the best fit of chromophore concentration changes based on the chromophores extinction coefficients (measured on purified solutions of the compounds [22]). The generalised form for the UCL algorithm for n number of wavelengths is termed as UCLn algorithm (3.13). It was demonstrated by Matcher et al. that using multiple wavelengths improves estimation of changes in oxCCO, so that the measurement precision increases with increasing number of wavelengths [29].

$$\begin{bmatrix} \Delta c_{HHb} \\ \Delta c_{HbO2} \\ \Delta c_{oxCCO} \end{bmatrix} = \frac{1}{d.DPF} \begin{bmatrix} \varepsilon_{HHb,\lambda 1} & \varepsilon_{HbO2,\lambda 1} & \varepsilon_{oxCCO,\lambda 1} \\ \varepsilon_{HHb,\lambda 2} & \varepsilon_{HbO2,\lambda 2} & \varepsilon_{oxCCO,\lambda 2} \\ \vdots & \vdots & \vdots \\ \varepsilon_{HHb,\lambda n} & \varepsilon_{HbO2,\lambda n} & \varepsilon_{oxCCO,\lambda n} \end{bmatrix}^{-1} \times \begin{bmatrix} \Delta A_{\lambda 1}/dpf_{\lambda 1} \\ \Delta A_{\lambda 2}/dpf_{\lambda 2} \\ \vdots \\ \Delta A_{\lambda n}/dpf_{\lambda 3} \end{bmatrix} \quad (3.13)$$

Some well-known commercial NIRS systems including NIRO 500 and NIRO 1000 by Hamamatsu Photonics KK, Japan are based on the UCL algorithms using four and six discrete wavelengths respectively (UCL_4 and UCL_6). Alternatively, when broadband spectroscopy is used (See section 3.4), all available wavelengths over some optimum range can be used that improves the measurement accuracy [29].

3.1.5 Estimation of Optical Pathlength in Conventional CW-NIRS Systems

Optical pathlength is the only term in chromophore concentration algorithms in CW-NIRS systems (such as UCLn, equation 3.13), that accounts for the effect of scattering; hence sufficient estimation of PL is essential to produce physiologically accurate representations of chromophore concentration, especially for the measurement of oxCCO (see section 3.3).

Commercial CW-NIRS systems in general assume a fixed pathlength through implementing a fixed DPF (see section 3.1.3) in the measurement algorithm which is

multiplied by the distance between source-detector probes predetermined on the probe holders (equation 3.7). The DPF can be determined experimentally through time or frequency domain systems to account for the increased PL of light to all types of scattering [23].

In time resolve technique (Figure 3.14 c), the DPF can be calculated from the measured photons' time of flight through the tissue, which is the time difference between light entering the tissue and the mean time of passing light through the tissue.

$$DPF = \frac{DP}{d} = \frac{c.t}{d.n} \tag{3.14}$$

$$\frac{c.t}{n} = DP \tag{3.15}$$

Where d is the spacing between optodes and $\frac{c}{n}$ is the speed of light in the tissue (c being the speed of light in vacuum, and n is refractive index of the tissue). Delpy et al used a time resolved system for the first time to determine the DPF of rats head through direct time of flight measurement; calculating the area under the curve of the temporal point spread function (TPSF) [23].

In frequency domain systems (Figure 3.14 b), the DPF can be calculated through the total distance that light travels through the tissue (DP). This technique can measure the total light path in real time without the need for measuring the geometrical distance which might carry inaccuracy of measurement. DP in frequency domain systems can be calculated as follows:

$$DP = \frac{\phi.c}{2\pi f n} \tag{3.16}$$

$$DPf = \frac{DP}{d} = \frac{1}{d}.\frac{\phi.c}{2\pi f n} \tag{3.17}$$

Where f is the modulation frequency, ϕ is the phase shift measured in radians, c is the speed of light in the vacuum and n is the refractive index of the medium. Duncan et al. used this technique to measure the DPF on adult head, calf and forearm as well the head of the new-born infant in 1994 [30].

An alternative method for estimating the optical pathlength was developed by Matcher et al. in 1994, known as the second derivative technique which enables real-time measurement of pathlength using the water absorption spectrum and the

broadband measured light attenuation [15]. This technique relies on broadband spectroscopy and is described fully in section 3.4.5.

3.2 Components of CW-NIRS Systems

CW-NIRS encompasses systems based on a light source that emits at a constant intensity to penetrate the tissue and very sensitive detectors to detect highly attenuated photons reaching them from the tissue surface. CW-NIRS is specifically attractive because of the wide availability of high power and spectrally narrow sources as well as sensitive detectors with high quantum efficiency over a broad range of NIR wavelengths and at a low cost. The main components of a CW-NIRS system are described below.

3.2.1 CW Light Sources

Illumination and stability are the two important features to consider when choosing a light source for CW-NIRS measurement. In general, it is desirable to have the radiated optical power as high as possible (below the tissue safety limits) to maximise the amount of light at the detector which improves the signal-to-noise ratio. Choosing a source with high optical power enables measurements at larger source-detector separations which are more sensitive to deeper tissue. However, the power should not be so high to cause tissue heating which may cause discomfort or damage to the subject or distort the measurement [7]. Stability of the light source is also crucial for the integrity of the measurement as a source with intensity fluctuations will directly affect noise at the detector [31]. Temperature changes or emitter noise that can simply be due to a noisy power supply can lead to optical drift, which is changes in the intensity of a specific wavelength over time. Stabilisation of the power supply and cooling of the light source helps to reduce the emitter noise.

Laser diodes (LDs) and light emitting diodes (LEDs) are the most common types of the light sources used in CW-NIRS instrumentation. Both LEDs and LDs are based on semiconductor technology and emit light with wavelength depending on the semiconductor material and its doping characteristics, through radiative recombination of electron-hole pairs in the active region of forwarding biased p-n junctions [32].

LDs are based on stimulated emission and have the advantages of producing narrow spectral peaks (< 1 nm) so there is higher confidence of the wavelength used in the measurement algorithm and have low divergence allowing easy coupling into optical fibres. However, they are relatively expensive, available in limited colours and often come in large packaging that makes miniaturisation challenging. When using LDs, the danger of laser radiation for the eye must be addressed [7].

LEDs are valid alternatives to LDs as they are generally low cost and smaller than LDs, which makes miniaturisation feasible. They come in a large variety of colours hence allowing more flexibility in wavelength selection. However, the spectral peaks of LEDs are wider (10-50 nm) and light coupling into the fibre is more challenging as LEDs are based on spontaneous emission producing incoherent light.

Broadband light sources based on incandescent bulbs are other types of light sources that are mainly used in broadband-NIRS and are explained in 3.4.2.1 Broadband Light Sources.

3.2.2 CW Detection Units

The most common photodetectors used in CW-NIRS include photodiodes (PDs), avalanche photodiode (APDs), photomultiplier tubes (PMTs) and charged-coupled-devices (CCDs) that are based on the photoelectric effect. The photoelectric effect is the process of a photon generating free charge carriers that are detected as an electric signal. PD and APD are the most commonly used photodetectors in CW-NIRS instruments and are based on the internal photoelectric effect in which the absorption of photons by a semiconductor p-n junction creates electron-hole pairs that produce a detectable photocurrent.

PDs have no internal signal amplification (gain) but high dynamic range, are small and easy to use since they do not require thermal or voltage stability. APDs however, are faster than PDs, have moderate signal amplification and dynamic range and come in small packages. Unlike photodiodes, APDs require a stabilised power supply and temperature control due to the dependency of the internal gain on temperature and bias voltage [7]. Both PDs and APDs are robust to ambient light exposure and not susceptible to magnetic field (are MR compatible).

Contrary to PDs and APDs, PMTs are based on external photoelectric effect during which an electron is freed from the photocathode surface by an incident photon

and is accelerated by a strong electric field knocking out several secondary electrodes from the surface of dynodes. This process is repeated in a cascade of dynodes leading to a successive multiplication of charge carriers hence a high gain in the order of 10^6-10^7 [7]. PMTs are fast with moderate dynamic range which is comparable to APDs but lower than that of PDs. The gain of the PMTs is very sensitive to the supply voltage and must be stabilised [32]. Major drawbacks of PMTs for CW-NIRS applications include their bulkiness, high vulnerability to ambient light and sensitivity to magnetic fields (NIRS measurement is usually complementary to other imaging techniques especially MRI/MRS).

Light sensors based on charged-coupled-devices (CCDs) are another type of photodetectors that are very fast and highly versatile [33] and mainly used in broadband-NIRS in combination with a spectrograph to separate the light into its spectral components. In broadband-NIRS measurement CCDs are required to record the continuous absorption spectrum of the diffuse reflectance [34]. Unlike single PDs or PMTs, the CCD sensor provides spatial information, i.e. it gives information about the distribution of light intensity across all wavelengths in an array of pixels. In spectrometers, light is passed through a system of lenses or mirrors and is dispersed normally by a diffraction grating to produce a continuous spectrum of the diffuse reflectance from the spatially separated spectral components incident on a CCD camera [7], [34]. CCDs in broadband systems need to have high sensitivity because of the reduced light power from the broadband source (leading to low SNR at the detector) as well as the light attenuation occurring in the optical bench of the spectrograph before reaching the CCD.

The main sources of noise that all the detectors have in common include shot noise, dark current and thermal noise. Shot noise is based on the quantum nature of the photons entering the detector as well as the generated carriers (due to their stochastic non-uniform temporal distribution). The shot noise power is proportional to the square root of the number of incident photons as is the SNR hence is more important at low light levels. Even though shot noise is unavoidable, it can be minimised by carefully shielding the detector from background radiation. Dark current is the current recorded in dark conditions when no photons reaching the detector, due to the thermal generation of electron-hole pairs and can be minimised by cooling of the detector.

3.2.3 Light Guides

Free space light delivery is usually inconvenient in biomedical applications. However, for small devices based on LEDs and photodiodes, the source and detector can be placed directly on the tissue in which case the light coupling losses are minimal but potential heating and electric hazards have to be prevented by the instrument [7]. An alternative way to guide the light to the tissue and the reflected light back to the detector is using optical fibres which are advantageous in terms of safety since no electronic devices are in contact with the skin. Furthermore, Use of fibres enables a more flexible geometrical design of a probe because it is important to ensure an optimal light coupling from both source and detector fibres [7]. More explanation about optical fibres is presented in 3.4.2.2 Optical Fibres.

3.3 Challenges and Considerations for In-Vivo Measurement of CCO

Even though measurement at 3 wavelengths is sufficient to calculate change in concentration of 3 chromophores ($\Delta c_{HHb}, \Delta c_{HbO2}, \Delta c_{oxCCO}$), according to the MBLL (eq. 3.12), this approach is susceptible to noise and crosstalk artefacts and may lead to inaccurate quantification of change in concentrations. Crosstalk is defined as a genuine change in one chromophore concentration inducing a spurious measured concentration change in another, which is mainly caused by the smaller concentration of CCO enzyme compared to Hb, despite its higher extinction coefficient in the NIR region (Figure 3.15). This could lead the light attenuation change due to CCO be easily masked by the larger attenuation change due to Hb and HbO_2.

Another challenge with separating the CCO signal from the Hb signals arises from the broad nature of the three chromophore peaks, especially the CCO peak, throughout the NIR region (Figure 3.15). This feature limits simple deconvolution through standard optical techniques, such as dual wavelength or derivative spectroscopy. Therefore, to successfully separate the CCO signal from the larger Hb signals, careful selection of the algorithm, the wavelengths (choice and number of wavelengths), and the extinction coefficient spectra is essential [28].

NIRS systems initially developed for measuring CCO used 3 or 4 narrow band lasers at specific wavelengths between 740-910 nm [9] and PMT for detection. Well-

known commercial systems NIRO 300 and NIRO 500 (Hamamatsu, Japan) also use 4 discrete wavelengths using laser and either PD or PMT respectively for detection [35], [36],[3]. However, measurements made at a larger number of wavelengths in spectroscopic algorithms have shown to eliminate the effects of noise and algorithm artefacts. A study by Matcher et al in 1995 showed that increasing the number of wavelengths in the measurement produces more accurate simulations and improves the in vivo measurements [29]. In this study, he assessed the separation of the oxCCO signal from the Hb signals with different number of wavelengths in a range of data: rat head, piglet head, adult forearm, and a simulated dataset. The results demonstrated that the amplitude of the spurious oxCCO signal generated by the UCL algorithms falls as the number of wavelength increases from 4 to 6 and n (>100). However, as well as the number of wavelengths, the optimum bandwidth is also a crucial factor in the accuracy of oxCCO measurement. Preclinical studies have shown that limiting the measurement bandwidth between 780 to 900 nm (gold standard) improves the resolution of oxCCO as removing shorter wavelengths reduces the contribution of HHb, which has a large peak at 760 nm as seen in Figure 3.15 [37]. Offering a full range of measurement wavelengths is a useful feature of broadband systems for oxCCO measurements that are fully described in the following section.

Estimation of the optical pathlength is another notable challenge for the in-vivo measurement of oxCCO as it is thought that the false changes resolved in oxCCO (i.e. crosstalk) could be due to pathlength changes that lead to insufficient chromophore separation [37] ,[38]. Therefore, it is useful that NIRS systems enable pathlength measurement in real-time so that one could identify whether the oxCCO measurement is simply a cross talk resulting from changes in pathlength or it is reflecting true physiology. This is feasible through second differential spectroscopy analysis (SDS) that broadband-NIRS systems can offer and provide real-time pathlength measurement.

Consequently, use of broadband-NIRS is essential to address all the challenges with oxCCO measurement in vivo through minimising crosstalk artefacts and ensuring a physiologically accurate signal is produced.

3.4 Broadband NIRS

As mentioned in the previous section, broadband-NIRS systems use the full spectrum in the NIR to resolve changes in chromophores concentration. These systems are of specific interest for quantifying changes in the redox state of CCO, because measuring attenuation at several wavelengths reduces the optical noise and significantly enhances the precision of measuring changes in oxCCO, which exists in very small concentrations relative to haemoglobin. As well as improving the measurement accuracy through removing the optical noise, use of a broadband-NIRS system enables real-time estimation of pathlength through Second Derivative Spectroscopy analysis technique, also improving the accuracy of quantifying changes in [oxCCO] by accounting for scattering changes during the measurement, which is described in the following section.

3.4.1 Estimation of Optical Pathlength in Broadband-NIRS (Second Derivative Spectroscopy)

The optical pathlength in broadband-NIRS systems can be estimated from the broadband absorbance spectrum, using the second differential of water absorption spectrum around 740 and 840 nm and an assumed tissue concentration of water with accuracies of a few percent [39] as presented by Matcher et al [15].

In this technique, knowing that the light attenuation is a function of extinction coefficient ($\varepsilon(\lambda)$) and the differential pathlength factor as well as the scattering term G are also wavelength dependent ($DPF(\lambda)\ and\ G(\lambda)$ respectively), the first derivative of the attenuation according to the Beer-Lambert law (equation. 3.6) can be written as:

$$A' = \frac{dA}{d\lambda} = \frac{d\varepsilon}{d\lambda} c.d.DPF + \frac{d(DPF)}{d\lambda} c.d.\varepsilon + \frac{dG}{d\lambda} \tag{3.18}$$

Due to the weak wavelength dependency of the scattering (being approximately linear in the NIR region), the 2nd and 3rd terms are negligible in the second derivative of the attenuation:

$$A" = \frac{d^2A}{d\lambda^2} = \frac{d^2\varepsilon}{d\lambda^2} c.d.DPF + \frac{d\varepsilon}{d\lambda}.\frac{d(DPF)}{d\lambda}.c.d \tag{3.19}$$

The equation can be further simplified to the following format, since the second term is negligible when compared to the first term:

$$A'' = \frac{d^2A}{d\lambda^2} = \frac{d^2\varepsilon}{d\lambda^2} c.d.DPF = \frac{d^2\varepsilon}{d\lambda^2} c.DP \tag{3.20}$$

Therefore, the second derivative of the attenuation equals the second derivative of the absorption coefficient ($c.\varepsilon(\lambda)$) scaled by the differential pathlength. Water absorption spectrum significantly peaks at certain wavelengths (around 820 nm and 970 nm) while other chromophores have flat spectra without any features. Therefore, knowing that the overall attenuation of light is the sum of attenuations caused by each chromophore, the second derivative of all chromophores except for water can be neglected at these spectral bands, which gives:

$$A'' = \frac{d^2A}{d\lambda^2} = \frac{d^2\varepsilon_{H2O}}{d\lambda^2} c_{H2O}.DP \tag{3.21}$$

Finally, by performing a least square fit of the second derivative of the attenuation through the tissue (A'') with the corresponding second differential spectrum of water ($\ddot{\varepsilon}_{H2O}$) and knowing the approximate tissue water concentration (c_{H2O}), the differential pathlength (DP) can be determined [15]. For instance, the optical pathlength through a baby brain ($c_{H2O} = 0.85$) for 840 nm can be calculated through equation 3.22:

$$DP\ (840\ nm) = A''\ (840\ nm) / (\ddot{\varepsilon}_{H2O}\ .0.85) \tag{3.22}$$

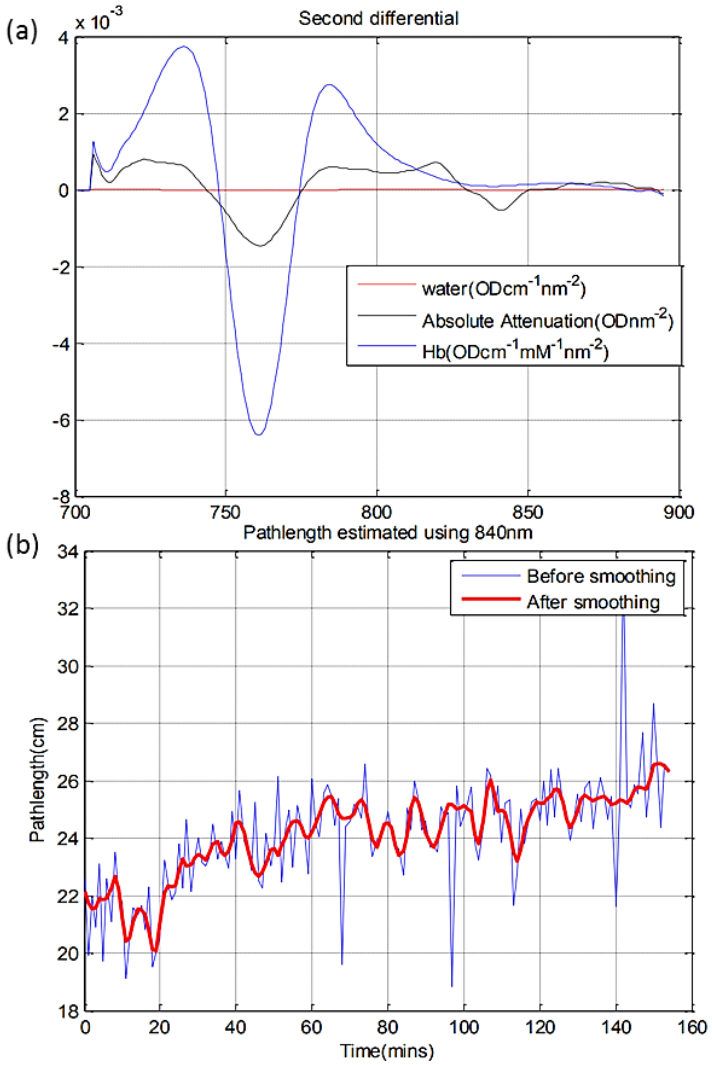

Figure 3.17: (a) second differential spectra of water, haemoglobin and light attenuation through a piglet's head (source-detector separation 4.3 cm). (b) estimated pathlength of light transmitted through the piglet's head at 840 nm.

Figure 3.17 (a) illustrates an exmple of the second differential of water absorption spectrum compared with absolute attenuation and haemoglobin spectra and (b) shows the real-time pathlength at 840 nm calculated ,based on what mentioned above, through a pigle's brain at source-detector separation of 4.3 cm. (Piglets are used as animal smodels for babies in preclinical studies, which will be discussed in chapter 4).

3.4.2 Broadband NIRS System Components

A typical broadband NIRS system includes a white (broadband) light source; suitable optical filters to eliminate short wavelengths and IR, a mirror or lens-based spectrograph to disperse the spatially resolved spectral components onto the CCD

camera and a software which calculates changes in chromophore concentrations based on the relative change in the attenuation of light through the modified Beer-Lambert law.

3.4.2.1 Broadband Light Sources

Broadband light sources are typically thermally stabilised white light bulbs filtered to the NIR region (650-900 nm). Using the complete NIR spectrum rather than just a finite number of wavelengths eliminates the need for a selection process of optimum wavelengths for calculating the concentration change of chromophores, which is usually controversial [7]. However, using broadband spectra is associated with two drawbacks which are increased computational complexity and the need for reduced light power compared to when light with a restricted wavelength range is used that leads to reduced SNR at the detector.

Common broadband light sources are based on high-pressure arc lamp or incandescent lamp. High-pressure arc lamps such as Xenon (Xe) and Mercury (Hg) lamps, consist of two tungsten electrodes in a quartz bulb filled with high-pressure gases and as seen in Figure 3.18 their emission spectra have so many spikes (peaks) in the NIR region that is not desirable for NIRS measurements [40].

Quartz tungsten halogen lamp (QTH) is the most commonly used Incandescent lamp for broadband NIRS measurement due to producing very smooth high-intensity spectrum in the visible and NIR region (Figure 3.18). The lamp output is usually collimated with an aspheric lens and focused onto the fibre input to ensure good coupling into the optical fibre.

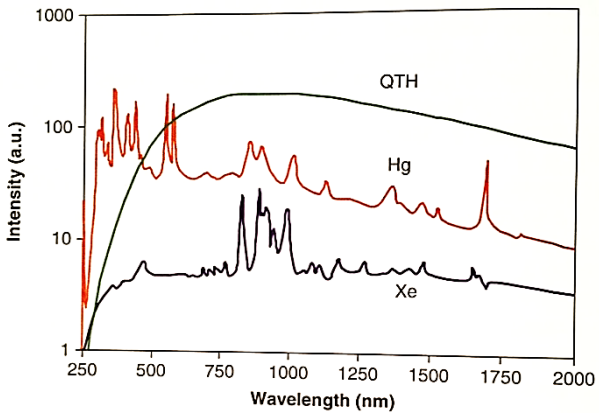

Figure 3.18: Example emission spectra of xenon arc (Xe), mercury arc lamp (Hg), and quartz tungsten halogen lamp (QTH). Image taken from [40]

3.4.2.2 Optical Fibres

Figure 3.19 illustrate the light transmission in an optical fibre which is based on the total internal reflection law. The acceptance angle of an optical fibre is determined by its numerical aperture (NA) which is in turn determined by the refractive indices of the core and cladding of the fibre:

$$NA = n_i sin\theta_{max} = \sqrt{n_{co}^2 - n_{cl}^2} \tag{3.23}$$

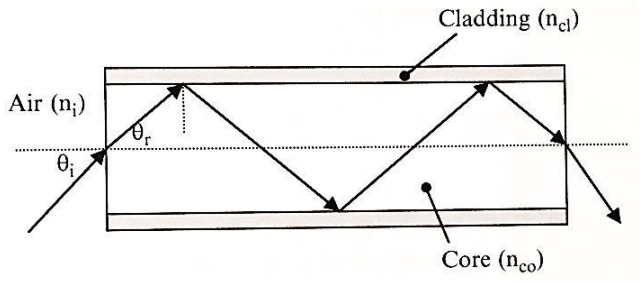

Figure 3.19: Light propagation in an optical fibre. Image taken from [40]

Where n_{co} and n_{cl} are the refractive indexes of the air, core and cladding material of the fibre and θ_{max} is the maximum acceptance angle.

Due to the low light levels in broadband-NIRS, the optical fibres need to have a high core diameter (up to 3 mm) and a high NA (acceptance angle or field of view) to effectively illuminate the tissue under interrogation and collect the diffuse light from a wide range of angles. High NA source and detector fibres can be fabricated by increasing the refractive index of the core and decreasing the refractive index of the cladding. Most commonly used optical fibres are silica/silica (core/cladding) having an NA of 0.22. There are however, customised fibres to improve light collection with NAs of 0.37 (silica/hard polymer) or 0.66 (silica/Teflon) [40].

To minimise light loss, the NA of the fibre needs to match the throughput (light collecting capability) of the spectrometer. The light loss due to NA mismatching is given by

$$Loss_{NA} = 10\log(\frac{NA_1}{NA_2})^2 \tag{3.24}$$

where NA_1 and NA_2 are the numerical apertures of the fibre and the spectrometer respectively. Theoretically, there will be no loss when $NA_1 <= NA_2$. Therefore, most broadband NIRS spectrometers are designed with large throughput and are usually very bulky. However, when $NA_1 > NA_2$, there will be a great loss at the entrance of

the spectrometer which makes miniaturisation of the broadband-NIRS instruments a challenging process. This issue will be addressed further in this thesis (Chapter 5).

3.4.2.3 Spectrograph

A spectrograph is generally referred to a prism or a diffraction grating-based instrument that is used to measure the light intensity dependence on wavelength. Fundamentally it consists of a narrow entrance slit to maintain the spectral resolution through which the light enters the spectrograph, collimating mirrors or lenses to direct the light onto a prism or grating. Lens-based spectrographs provide higher efficiency than mirror-based systems with respect to the throughput of light (over 99% transmission throughout the entire working range of the spectrograph) [41].

A prism disperses the light into its spectral components since different wavelengths of light travel with different speed through the prism (depending on the refractive index of the prism material). Therefore, the light leaving the prism is spread out into its different colours or dispersed. A diffraction grating diffracts the light into its wavelengths through transmission or reflection of light. Gratings consist of a series of closely packed grooves that have been engraved or etched into the grating's surface. The grooves diffract the light and light of the same wavelength will constructively interfere at an angle θ that is related to the grooves' spacing d, the diffraction order m, and the wavelength λ as seen in equation 3.25 below.

$$d\ sin\theta = m\lambda \tag{3.25}$$

There are two types of grating; ruled and holographic gratings each having their own advantages for specific applications. Ruled gratings usually have higher efficiency and can be blazed for specific wavelengths and they are often used in systems requiring high resolution. Holographic gratings are made using the interference fringe field of two laser beams and produce lower scatter (stray light) as they are generated optically. Therefore, they are more suitable for low-level light applications.

There are many different optical bench designs in spectrographs and the most popular one is the Czerny-Turner (CZ) configuration since it has a compact design hence is suitable for miniature spectrometers. It consists of two concave mirrors and one flat diffraction grating. The focal length of the first mirror is set so that it

collimates the light emitted from the entrance slit and directs it onto the diffraction grating. The second mirror is used to focus the dispersed light from the grating onto the detector plane as seen in Figure 3.20 [42].

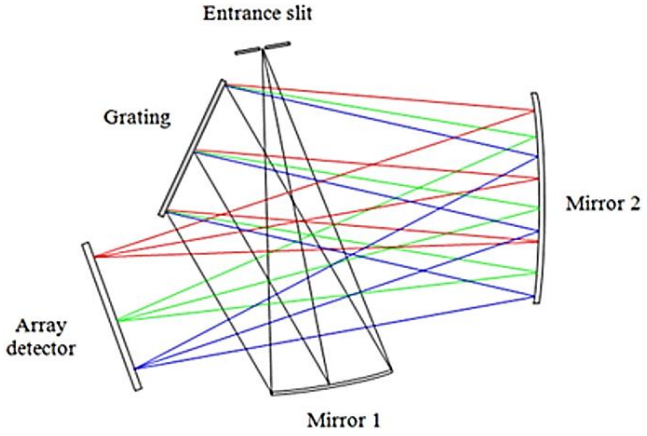

Figure 3.20: Crossed Czerny-Turner configuration offering a compact and flexible spectrograph design**.** Image taken from [43]

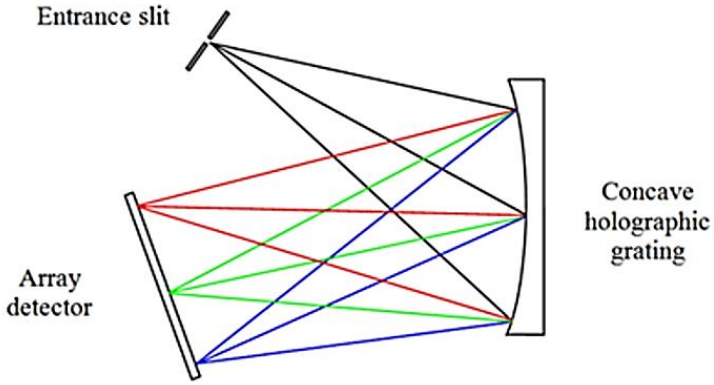

Figure 3.21 Concave-holographic spectrograph presenting up to over a 10 x reduction in stray light compared to ruled grating spectrograph design. [43]

Concave holographic grating design (Figure 3.21) is another common optical bench configuration in which the concave grating is used both as the dispersive and focusing element which in turn means the number of optical elements is reduces leading to increased throughput and efficiency of the spectrograph.

3.4.2.4 CCD

A CCD is composed of metal oxide semiconductor capacitors called pixels which are read out using the movement of electrical charge produced based on the internal photoelectric effect (see section 3.2.2 CW Detection Units). The substrate of a CCD is made of silicon but the photosensitive layer lies above the substrate and is called epitaxial layer which is silicon doped with different elements. The gate is held

at a positive charge relative to the rest of the device to attract the electrons and electrons are held in place by the positive charge above them without being able to penetrate through the gate because of the insulating layer (see Figure 3.22). This creates a potential well in which electrons are built up until the exposure is complete up to the maximum depth of the well. The electrons are then moved along the wells until they reach the end of the array through a shifting voltage. Finally, at the end of the array the electrons are pulled in the other direction and read out by the camera electronics [41].

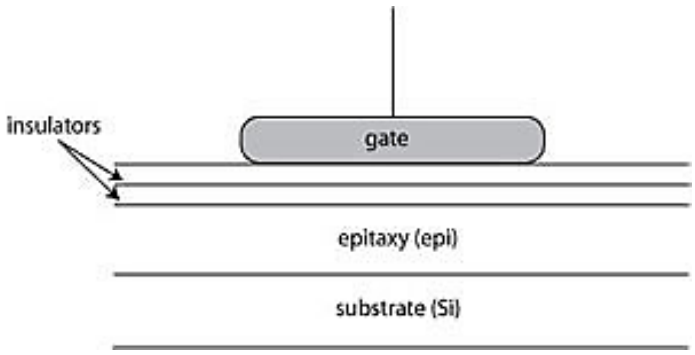

Figure 3.22: Simplified diagram of a CCD pixel. Image taken from http://www.specinst.com/Graphics/simple-ccd-04.jpg

The conventional CCDs are inexpensive to fabricate and are typically front-illuminated since the gate is located in the front. As seen in Figure 3.23, the incident light has to pass through the polysilicon gate structure before reaching the photosensitive area which significantly suppresses the quantum efficiency of the CCD.

Back-thinned or back-illuminated CCDs however, have enhanced quantum efficiency since the incoming light is incident on the ungated face of the semiconductor (see Figure 3.23) which significantly increases the probability of photons being absorbed by the photosensitive layer. As there is no light loss, the back-illuminated CCDs have higher quantum efficiency, up to 90% (Figure 3.24).

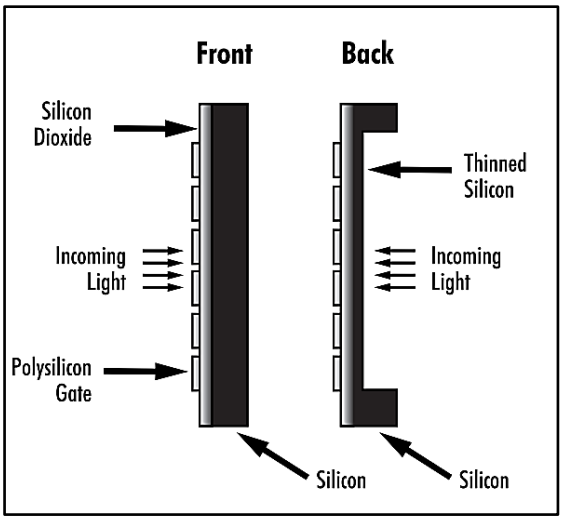

Figure 3.23: Cross-sections of a front and back illuminated CCD. Image modified from [40]

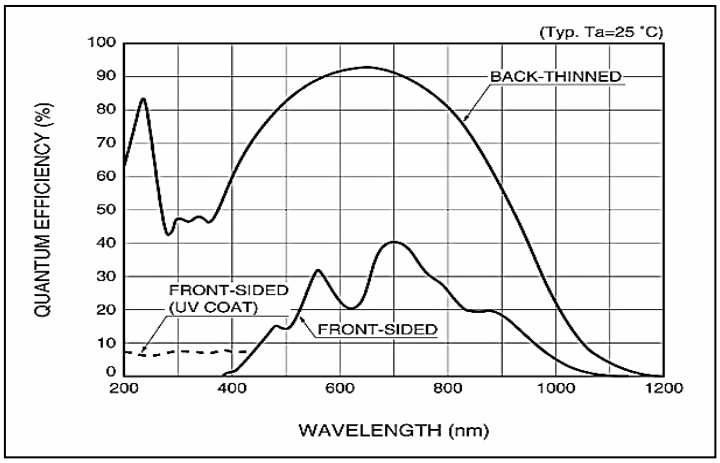

Figure 3.24: Spectral Response in the Back-thinned CCD compared to Front-illuminated. Image taken from [44]

As well as high fabrication cost and complexity, back-illuminated CCDs are affected by an unwanted etaloning effect. The etaloning effect is the light reflections between the parallel front and back surfaces of the detector because of thinning of the photosensitive layer. It also causes unwanted fringes of constructive and destructive interference, which modulate an artificial spectrum. This is specifically important in NIR spectroscopy because of the significant extent of modulation (20%) and spectral spacing of fringes that is typically 5 nm (close to the spectral resolutions in NIRS). One effective way to reduce spectrum modulation due to etaloning is spreading the light from gratings over all the rows of a CCD and then binning the whole CCD into one spectrum, this method also increases the sensitivity of the system by offering maximum light collection area.

3.4.3 Broadband NIRS Systems Developed at UCL

UCL broadband-NIRS systems have been developed in-house and focused on obtaining a more robust oxCCO signal using the complete NIR spectrum rather than just a finite number of wavelengths [29], according to what was discussed in section 3.3. Challenges and considerations for In-Vivo Measurement of CCO.

All the broadband systems developed at UCL use a halogen-tungsten based white light source, Oriel radiometric fibre optic illuminator by Newport (77501) with different detection units. The first system developed in 1995 by Springett and colleagues is a single channel system, called UCL1, which uses a mirror based spectrograph with Wrights Instrument CCD and has been used for measuring brain oxygenation and metabolism in a preclinical model of neonatal hypoxia-ischaemia [45],[14]. This system has also been used for investigating cerebral metabolism in healthy volunteers and adults with traumatic brain injury [46], [47]. A multi-distance multichannel hybrid broadband and frequency domain (FD) system called Hybrid Optical Spectrometer or PHOS have also been developed by Tachtsidis and colleagues in 2010, which includes a custom-built lens spectrograph with Princeton Instrument CCD and is used for brain oxygenation and metabolism measurement in adults with traumatic brain injury (TBI) [48] as well as in experiments on adults during hypoxia-ischaemia or during functional activations [49]–[52]. In 2014 and 2016 two variations of the pHOS system without the FD component were developed by Bale and colleagues to be used in neonates with hypoxic-ischaemic encephalopathy (called CYtochrome Research Instrument and application or CYRIL) [4], [53] and Phan and colleagues with the capacity to do imaging [54], [55]. All the UCL broadband systems have the capacity to apply the UCLn algorithm in real-time and have been shown to provide reliable measurements of the changes in the oxidation state of oxCCO.

3.5 Towards the Development of Compact Broadband-NIRS Systems in Clinic

Easy portability and application are two important characteristics of a clinical system, however, current broadband-NIRS systems utilise large light sources and highly sensitive detection units that are quite bulky, heavy and include large custom-made spectrographs and CCDs. This makes the whole system difficult to handle in

demanding clinical environments such as intensive care units. Additionally, such systems require extensive calibrations on a daily basis, which makes them impractical for use by clinicians. Therefore, there is an urgent need for the development of compact portable systems, which are easily adopted by clinicians or nurses to monitor oxygen delivery and consumption at the bedside.

"Off-the-shelf" spectrometers known as "miniature spectrometers" are small, lightweight devices that are advantageous to the typical large spectrometers in many ways. This includes low cost, high spectral resolution; use of high performance integrated CCDs, no need for routine calibrations, small footprints and wide availability. However, such spectrometers are only favourable for broadband NIRS measurements if their small size does not affect their light collection capability (see section 3.4.2.2). In this section, the main features of miniature off-the-shelf spectrometers are described including the main challenges with using them for deep tissue spectroscopy.

The main challenge for miniaturisation of broadband-NIRS is replacing the bulky custom-made detection unit, mainly designed for increased light throughput (see section 3.4.3), with a more compact easily deployable detection system. Compact reliable solid state spectrometers based on photodiode arrays or CCDs were made commercially available from the early 1990s and used in various studies [56], [57]. Since then use of handheld off-the-shelf spectrometers has increased in recent years, due to offering compactness, versatility, and low cost [58]. Following the developments in the spectrographs' optical components, array detectors, fibre optics and computing [42], [59], commercially available miniaturised spectrometers have been used for many biomedical applications including fluorescence and Raman spectroscopy. However, their utilisation in broadband-NIRS measurement of oxygenation and metabolism has not been yet well established. That is mainly due to the small slit size and the large f number (f/#) design of miniature spectrometers that significantly reduces light collection capability, which is essential for broadband NIRS. In this section, the main features of a typical miniature spectrometer are explained and their utilisation for measuring tissue oxygenation and metabolism using broadband-NIRS spectroscopy is reviewed.

3.5.1 Miniature Spectrometers

Light is directed into the optical bench of a miniature spectrometer through an entrance slit using a fibre optic cable (Figure 3.25). The slit size highly depends on the specific application but in general varies in width between 5 µm to 800 µm and height of 1 or 2 mm. The light is then collimated through a collimating mirror and is focused onto a diffraction grating which breaks the light into spectral components at slightly different angles (choose of grating also depends on the specific application and the wavelengths of interest.) A focusing mirror is used to receive the dispersed light reflected from the grating and focuses it onto the detector plane where the imaged photons are converted to electrons, digitised and read out through a USB or serial port to an external computer.

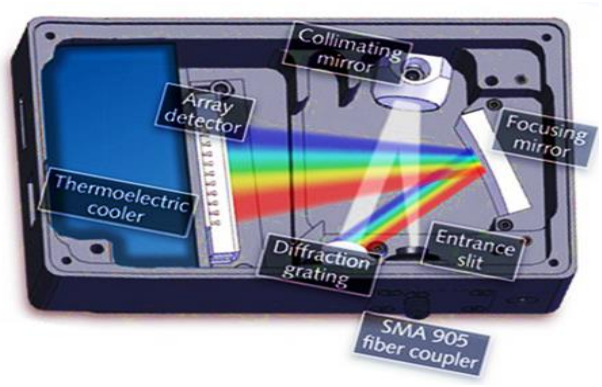

Figure 3.25: Optical bench of a miniature spectrometer [42]

Advanced miniature spectrometers usually use thermoelectric cooling for the detector to enhance its performance by producing reduced dark current hence an increased sensitivity. Finally, a software is used to interpolate the signal based on the number of pixels in the detector and the linear dispersion of the grating to create a calibration which enables the data in terms of photon counts against the wavelength over the given spectral range [43], [44].

Spectrograph design, detector technology and data processing are three important characteristics of a miniature spectrometer that need to be well investigated before choosing the spectrometer for a specific application such as broadband NIRS.

Due to its compact design, the Czerny-Turner configuration (Figure 3.20) is the most suitable optical bench for a miniature spectrometer. It typically consists of two concave mirrors and a flat diffraction grating. The spectral coverage and resolution of the system are determined by the focal lengths of the two mirrors, which can be

designed to create various degrees of dispersion. Moreover, because of its geometry with its high f-number design, it creates a flattened spectral field with very little distortion [42]. The f-number or f-value (f/#) is the ratio of focal length to the aperture diameter and states the diameter of the optical image in terms of its effective focal length [60]. It is also inversely proportional to the NA (see equation 3.23 and 3.26 below) and determines the light collecting capability of a spectrometer:

$$f/\# = \frac{1}{2NA} \tag{3.26}$$

Designing the miniaturised spectrometers with high f-values (low NA) is to minimise the image aberrations which are caused due to the off-axis geometry of the crossed Czerny-Turner optical configuration [42].

The most common detectors in miniature spectrometers are silicon multi-element detectors for which the maximum detectable wavelength is 1117 nm (due to the bandgap energy of silicon ~1.17 eV @300° K and E= hc/λ). Silicon detectors are available in three different designs including front-illuminated Charged Coupled Device (CCD), back-thinned CCD and photodiode array (PDA). However, most spectrometers have integrated CCD detectors (either front-illuminated or back-thinned) rather than PDA due to the smaller pixel size and higher sensitivity [42].

Thermoelectric Cooling (TEC) is one of the major advances in solid state detectors since it significantly reduces the dark noise. At room temperature (~22° C), a considerable amount of dark current contributes in the total signal counts. However, using the TEC (usually down to -25° C) prevents the thermal excitation of the electrons hence reduces the dark current significantly. Consequently, the total noise of the detector, which is the square root of the sum of all the noise components including readout noise, shot noise, dark noise and fixed pattern noise is significantly decreased [42]. This allows for operating the spectrometer at longer acquisition times for up to 15 minutes and greatly increases the dynamic range hence lowers the detection limit (~ increases the sensitivity) of the detector which is necessary for low-light level applications [44]. Onboard data processing is one of the major improvements in the advancement of miniature spectrometers. The use of implanted microprocessors that carry out all the data processing and manipulation with no need for sending the data to an external computer enables fast averaging, smoothing, and automatic dark current compensation to improve the SNR [42].

3.5.2 Miniature Spectrometers in Biomedical Applications

All the characteristics of miniature spectrometers make them advantageous in many applications including NIR spectroscopy, not only because of their low cost and compactness but also due to the enhanced performance owing to the recent advancements in micro-size optical components. Currently several manufacturers including Ocean Optics, offer compact spectrometers which have been used for more than a decade in a wide range of biomedical applications such as fluorescence spectroscopy [61]–[66]. However, use of off-the-shelf spectrometers for deep tissue spectroscopy and in-vivo measurement of metabolism using broadband-NIRS is not simple. Unlike conventional CW systems that can easily be miniaturised due to using 2-3 wavelengths thanks to advances in semiconductor LEDs and photodiodes, miniaturisation of broadband-NIRS is challenging, because efficient light collection is critical to broadband-NIRS monitoring. That is mainly because only a small fraction of the injected light emerges from the probed tissue and reaches the detector due to strong absorption and multiple scatterings [67]. Therefore, the light guides used for broadband-NIRS are usually large diameter fibre bundles to enhance the contact area between the detection system and the probed tissue (see section 3.4.2.2).

The main challenge for miniaturisation of broadband-NIRS is that the form factor of these fibres does not match the narrow entrance slit (< 1 mm wide) of the miniature spectrometers considered for providing a high spectral resolution. That is why broadband-NIRS spectrometers are usually large custom-built spectrographs with highly sensitive CCDs (with large active area and high quantum efficiency) to convert all the incident photons to electrical signal which can then be used to quantify chromophore change [4], [16], [38], [48], [54].

Some manufacturers have tried to solve the issue of the incompatibility of the large detector fibres with the small detection unit through implementing a removable slit on miniature spectrometers so that a single fibre guides light to the spectrometer and the sensitivity is enhanced through increased throughput at the cost of losing the spectral resolution [44]. In 2013, Wright and colleagues from Lawson Health Research Institute in Canada tried to tackle the issue of incompatibility of detector fibre diameter with spectrometer's entrance slit through designing the output of the detector fibre to mimic the typical form-factor of a spectrometer's entrance slit providing high

sensitivity while maintaining good spectral resolution [68]. The modified system based on miniature light source and spectrometer by Ocean Optics (HL 2000-HP and QE 65000, respectively) was characterised for noise and stray light performance using an approach similar to the method described by Zonios et al for characterisation of miniaturised spectrometers [58]. Using this modification they were able to utilise the miniature system for broadband-NIRS measurement across a piglet's head [68]. Two other papers have also been published by the same group in 2014 and 2016 about further modifications on the modified system to improve noise performance [67] and applying the newly modified system in a functional activation adult study [69].

Table **3.1** summarises the work done for miniaturisation of broadband-NIRS.

Table 3.1: Summary of the work done for the miniaturisation of broadband-NIRS.

First Author (Date) Title	Aims	Methods/Instrumentation	In-vivo measurement parameters	Results and Conclusion
E. Wright et al, 2013 Conversion of a low cost off-the-shelf spectrometer into a suitable instrument for deep tissue spectroscopy	Modifying an off-the-shelf spectrometer to convert it into a suitable instrument for deep tissue spectroscopy	QE65000, Ocean Optics was modified for deep tissue spectroscopy through slit removal and designing the output of the detector fibre bundle to match the form factor of the original slit (Output being made of 7 fibres with 125 microns diameter forming a strip of ~1 mm height) The modified miniature spectrometer was characterised for readout noise, shot noise, dark noise and stability test. Broadband miniature light source (Ocean Optics HL-2000-HP). Source-detector spacing 3 cm	Measurements acquired simultaneously with custom-built and modified QE65000 spectrometers in a piglet model of new-born. ICG concentration curves during normocapnia and hypercapnia was derived.	The modified spectrometer had excellent noise and spectral characteristics and produced in-vivo measurement comparable to a custom-built unit that was specifically designed for deep tissue spectroscopy. QE65000 suitable for deep tissue spectroscopy.

First Author (Date) Title	**Aims**	**Methods/Instrumentation**	**In-vivo measurement parameters**	**Results and Conclusion**
M. Diop et al, 2014 Improved light collection and wavelet de-noising enable quantification of cerebral blood flow and oxygen metabolism by a low-cost, off-the-shelf spectrometer	To investigate the ability of the modified spectrometer for quantification of cerebral haemodynamics and oxygen metabolism in a piglet.	Use of QE65000 with removed slit and fibre end modification to mimic the slit to improve throughput (Wright et al, 2013). Augmenting wavelet denoising approach to improve the precision of the chromophore estimate. Characterise the modified spectrometer by measuring read-out noise, Shot noise, dark noise, and stability test. Broadband miniature light source (Ocean Optics HL-2000-HP). NA of the detector fibre: 0.22 Source-detector separation: 3 cm	Piglet head measurement HHb, HbO_2 , H_2O and CBF measurement using intravenous injection of ICG	The modification technique enhanced the light throughput by 45% while maintaining the spatial resolution

First Author (Date) Title	Aims	Methods/Instrumentation	In-vivo measurement parameters	Results and Conclusion
R.Nosrati et al., 2016 Event-related changes of the prefrontal cortex oxygen delivery and metabolism during driving measured by hyperspectral fNIRS	To extend the application of broadband-NIRS to the measurement of event-related hemodynamic and metabolic functional cerebral responses during simulated driving.	Use of 2 QE65000 spectrometers as modified by Wright et al. and Diop et al. [67], [68]. 3 mm core diameter fibre. Thorlab OSL2BIR light source Miniature system was characterised before but used for fNIRS studies. Source-detector separation: 3 cm	HHb, HbO_2 oxCCO- Off-line data processing	First time use of miniature systems for functional activation studies in adults. First time use of miniature spectrometers for measuring oxCCO

In all the studies carried out by Wright et al [68], Diop et al [67] and Nosrati et al [69], small NA detection fibre (0.22) have been used, which matches the f-number of the miniature spectrometer modified and used in their experiment [44]. Furthermore, all these studies used a source-detector separation of 3 cm (reflection mode NIRS), which even though brain specific, does not provide deep cerebral metabolism measurement where mitochondria are densely packed and CCO concentration is higher. This limitation will also be dealt with in this thesis (Chapter 5 and 6). However, it is known that due to strong attenuation, using large NA detection fibres is critical to broadband-NIRS and using large source-detector spacing provide more accurate oxCCO measurement, since it is more specific to the deeper layers of brain tissue. Simulations and in-vivo studies have shown that oxCCO is more precisely measured at larger source-detector spacing due to the mitochondria being abundant in the deeper layers of the brain [52], [70], [71], [72]. Therefore, another hindering factor in using miniature spectrometers for broadband-NIRS oxCCO measurement which has not been addressed in the literature is the incompatibility of the large NA of the detection fibres (0.54 and 0.66), which are crucial to broadband-NIRS measurement, with the small throughput design of the miniature spectrometers to allow for the collimated light through and enhance the signal to noise ratio. A major part of this project has been dedicated to resolving this issue which is fully described in chapter 5.

Another limitation with the work done by the group in Canada for utilisation of miniature spectrometers in clinical broadband-NIRS, is the absence of on-board data processing to quantify changes in tissue concentration of HHb, HbO_2 and oxCCO, as well as no estimation of optical pathlength, which is going to be dealt with in the miniature system developed in this thesis (development of a user-friendly software, which enables real-time display of changes in the concentration of HHb, HbO_2 and oxCCO and other useful measures for clinicians to assist them in diagnosis or treatment, explained in chapter 5).

Other necessary considerations for the miniature broadband-NIRS systems to be used in clinical settings, including; cost effectiveness, easily replicability and reproducibility, are also addressed in the development of a miniature system for in-vivo measurement of tissue oxygen delivery and utilisation in this thesis.

3.6 Summary

Continuous-wave Near-infrared spectroscopy is a non-invasive technique to assess CNS tissue oxygenation and metabolism through quantification of changes in [HHb], [HbO_2] and [oxCCO] as a unique marker for oxygen metabolism at cellular level and ATP production. However, resolving the oxCCO signal in-vivo is challenging due to the smaller concentration of the mitochondrial enzyme compared to Hb and its very broad absorption peak in NIR. Use of full range of wavelengths in measurement algorithm, provided by broadband-NIRS, has enabled precise measurement of tissue changes in oxCCO. However, current broadband NIRS systems are quite bulky and heavy and require extensive calibrations on daily basis that must be carried out by a trained physicist or engineer.

Due to their favourable characteristics such as low cost, high sensitivity and wide availability, the use of miniature spectrometers with integrated CCD is a step forward towards developing compact clinical broadband-NIRS systems. However, the narrow slit and large f/# of the miniature spectrometers are in direct contrast with the large core diameter and numerical aperture of the detection optical fibres used in broadband-NIRS. Some researchers have tackled this issue by removing the narrow entrance slit of the miniature spectrometer and modifying the detector fibres (which have small NA to match the spectrometer) to mimic the form factor of the miniature spectrometer. Through this method the signal intensity could be increased to some extent and the spectral data collected at 3 cm source-detector was comparable to those produced by custom-made units. However, there are some hindering factors which have not been addressed in the literature and need to be resolved before miniature spectrometers can be used as part of a compact ‘clinical system’. These factors briefly include; mismatching the broadband-NIRS optimised detector fibres (customised with large NA) with the small NA of the miniature spectrometers, absence of on-board data processing for concentration change quantification, ,the feasibility of using larger source-detector separation which provides higher sensitivity to oxCCO changes, and finally developing a cost-effective and reproducible methodology enabling the miniature broadband-NIRS system to be used as a bedside clinical instrument for CNS tissue oxygen metabolism measurement.

Bibliography

[1] F. F. F. Jobsis, "Noninvasive, Infrared Monitoring of Cerebral and Myocardial Oxygen Sufficiency and Circulatory Parameters," *Science (80-.).*, vol. 198, no. 4323, pp. 1264–1267, 1977.

[2] J. S. Wyatt, M. Cope, D. T. Delpy, C. E. Richardson, A. D. Edwards, S. Wray, and E. O. Reynolds, "Quantitation of cerebral blood volume in human infants by near-infrared spectroscopy," *J Appl Physiol*, vol. 68, no. 3, pp. 1086–1091, 1990.

[3] P. Zaramella, F. Freato, A. Amigoni, S. Salvadori, P. Marangoni, A. Suppiej, A. Suppjei, B. Schiavo, and L. Chiandetti, "Brain auditory activation measured by near-infrared spectroscopy (NIRS) in neonates.," *Pediatr. Res.*, vol. 49, no. 2, pp. 213–9, 2001.

[4] G. Bale, S. Mitra, J. Meek, N. Robertson, and I. Tachtsidis, "A new broadband near-infrared spectroscopy system for in-vivo measurements of cerebral cytochrome-c-oxidase changes in neonatal brain injury.," *Biomed. Opt. Express*, vol. 5, no. 10, pp. 3450–66, 2014.

[5] A. Bainbridge, I. Tachtsidis, S. D. Faulkner, D. Price, T. Zhu, E. Baer, K. D. Broad, D. L. Thomas, E. B. Cady, N. J. Robertson, and X. Golay, "Brain mitochondrial oxidative metabolism during and after cerebral hypoxia-ischemia studied by simultaneous phosphorus magnetic-resonance and broadband near-infrared spectroscopy," *Neuroimage*, vol. 102, no. P1, pp. 173–183, 2014.

[6] X. Intes, V. Vivek, J. Chen, and F. S. Azar, "Multimodal Diffuse Optical Imaging," in *Biomedical Optical Imaging Technologies Design and Applications*, R. Liang, Ed. Tuscon, Arizona, Arizona: Springer Heidelberg, 2013, pp. 351–374.

[7] F. Scholkmann, S. Kleiser, A. J. Metz, R. Zimmermann, J. Mata Pavia, U. Wolf, and M. Wolf, "A review on continuous wave functional near-infrared spectroscopy and imaging instrumentation and methodology," *Neuroimage*,

vol. 85, pp. 6–27, 2014.

[8] R. Bright, "Disease of the Brain and Nervous System," *Longman*, vol. 2431, 1831.

[9] J. E. Brazy, D. V. Lewis, M. H. Mitnick, and F. F. Jobsis, "Noninvasive Monitoring of Cerebral Oxygenation in Preterm Infants: Preliminary Observations," vol. 75, no. 2, pp. 217–225, 1985.

[10] J. S. Wyatt, D. T. Delpy, M. Cope, S. Wray, and E. O. R. Reynolds, "Quantification of Cerebral Oxygenation and Haemodynamics in Sick Newborn Infants By Near Infrared Spectrophotometry," *Lancet*, vol. 328, no. 8515, pp. 1063–1066, 1986.

[11] A. D. Edwards, C. Richardson, M. Cope, D. T. Delpy, E. O. R. Reynolds, J. S. Wyatt, C. Richardson, D. T. Delpy, M. Cope, and E. O. R. Reynolds, "Cotside Measurement of Cerebral Blood Flow in Ill Newborn Infants By Near Infrared Spectroscopy," *Lancet*, vol. 2, no. 8614, pp. 1977–1978, Oct. 1988.

[12] J. S. Wyatt, A. D. Edwards, D. Azzopardi, and E. O. Reynolds, "Magnetic resonance and near infrared spectroscopy for investigation of perinatal hypoxic-ischaemic brain injury.," *Arch. Dis. Child.*, vol. 64, no. 7 Spec No, pp. 953–63, 1989.

[13] I. Tachtsidis, M. M. Tisdall, T. S. Leung, C. Pritchard, C. E. Cooper, M. Smith, and C. E. Elwell, "Relationship between brain tissue haemodynamics, oxygenation and metabolism in the healthy human adult brain during hyperoxia and hypercapnea.," *Adv. Exp. Med. Biol.*, vol. 645, pp. 315–20, 2009.

[14] I. Tachtsidis, A. Bainbridge, S. Faulkner, D. Price, E. Powell, D. Thomas, E. Cady, N. Robertson, and X. Golay, "In-Vivo Measurements of Brain Haemodynamics and Energetics using Multimodal Spectroscopy in Perinatal Hypoxia-Ischaemia," in *Biomedical Optics and 3-D Imaging*, 2012, p. JM3A.27.

[15] S. J. Matcher, M. Cope, and D. T. Delpy, "Use of the water absorption spectrum to quantify tissue chromophore concentration changes in near-infrared

spectroscopy.," *Phys. Med. Biol.*, vol. 39, no. 1, pp. 177–96, 1994.

[16] H. Z. Yeganeh, V. Toronov, J. T. Elliott, M. Diop, T.-Y. Lee, and K. St Lawrence, "Broadband continuous-wave technique to measure baseline values and changes in the tissue chromophore concentrations.," *Biomed. Opt. Express*, vol. 3, no. 11, pp. 2761–70, 2012.

[17] C. E. Cooper, "In vivo measurements of mitochondrial function and cell death following hypoxic/ischaemic damage to the new-born brain," *Biochem. Soc. Symp*, vol. 66, pp. 123–140.

[18] Elwell Clare and Hebden Jem, "Near Infrared Spectroscopy," 1999. [Online]. Available: http://www.ucl.ac.uk/medphys/research/borl/intro/nirs. [Accessed: 01-Jul-2016].

[19] T. Vo-dinh, "Optical Properties of Tissue," in *Biomedical Photonics*, 2003, p. 1787.

[20] L. V. Wang and H.-I. Wu, "Introduction," in *Biomedical Optics Principles and Imaging*, New Jersey: John Wiley & Sons, Inc., 2007, pp. 1–10.

[21] W. Cheong, S. A. Prahl, and A. J. Welch, "A Review of the Optical Properties of Tissues," *IEEE, J. Quant. Electron*, vol. 26, no. 12, pp. 2166–2185, 1990.

[22] M. Cope, "The Application Of Near Infrared Spectroscopy To Non Invasive Monitoring Of Cerebral Oxygenation In The Newborn Infant," 1991.

[23] D. T. Delpy, M. Cope, P. Van Der Zee, S. Arridge, S. Wrayt, and J. Wyatt, "Estimation of optical pathlength through tissue from direct time of flight measurement," *Phys. Med. Biol*, vol. 33, no. 12, pp. 1433–1442, 1988.

[24] M. Essenpreis, M. Cope, C. E. Elwell, S. R. Arridge, P. van der Zee, and D. T. Delpy, "Wavelength Dependence of the Differential Pathlength Factor and the Log Slope in Time-Resolved Tissue Spectroscopy," Springer US, 1993, pp. 9–20.

[25] E. M. Sevick-Muraca and B. Chance, "Photon migration in a model of the head measured using time- and frequency-domain techniques: potentials of

spectroscopy and imaging," in *Time-Resolved Spectroscopy and Imaging of Tissues*, 1991, pp. 84–96.

[26] M. Lindkvist, G. Granåsen, and C. Grönlund, "Coherent derivation of equations for differential spectroscopy and spatially resolved spectroscopy: an undergraduate tutorial," *Spectrosc. Lett.*, vol. 7010, no. January 2016, 2013.

[27] M. Cope, P. van der Zee, M. Essenpreis, S. R. Arridge, and D. T. Delpy, "Data analysis methods for near-infrared spectroscopy of tissue: problems in determining the relative cytochrome aa3 concentra- tion," in *SPIE 1431, Time-Resolved Spectroscopy and Imaging of Tissues*, 1991, vol. 1431, pp. 11–20.

[28] G. Bale, C. E. Elwell, and I. Tachtsidis, "From Jöbsis to the present day: a review of clinical near-infrared spectroscopy measurements of cerebral cytochrome-c-oxidase," *J. Biomed. Opt.*, vol. 21, no. 9, p. 91307, 2016.

[29] S. J. Matcher, C. E. Elwell, C. E. Cooper, M. Cope, and D. T. Delpy, "Performance Comparison of Several Published Tissue Near-Infrared Spectroscopy Algorithms," *Analytical Biochemistry*, vol. 227, no. 1. pp. 54–68, 1995.

[30] A. Duncan, J. H. Meek, M. Clemence, C. E. Elwell, L. Tyszczuk, M. Cope, and D. T. Delpy, "Optical pathlength measurements on adult head, calf and forearm and the head of the newborn infant using phase resolved optical spectroscopy.," *Phys. Med. Biol.*, vol. 40, no. 2, pp. 295–304, 1995.

[31] Q. Zhang, T. J. Brukilacchio, T. Gaudett, L. Wang, A. Li, and D. A. Boas, "Experimental comparison of using continuous-wave and frequency-domain diffuse optical imaging systems to detect heterogeneities," *Proc. SPIE*, vol. 4250, no. 8, pp. 219–238, 2001.

[32] J.-M. Liu, "Photonic Devices."

[33] J. J. Davenport, J. Hodgkinson, J. R. Saffell, and R. P. Tatam, "Noise analysis of a CCD based ultra-violet spectrometry system," *Proc. SPIE - Opt. Sens. Detect. II*, vol. 8439, p. 84391P, 2012.

[34] M. Cope, D. T. Delpy, S. Wray, J. S. Wyatt, and E. O. R. Reynolds, "A CCD Spectrophotometer to Quantitate the Concentration of Chromophores in Living Tissue Utilising the Absorption Peak of Water at 975 nm," Springer US, 1989, pp. 33–40.

[35] S. Suzuki, S. Takasaki, T. Ozaki, and Y. Kobayashi, "A tissue oxygenation monitor using NIR spatially resolved spectroscopy," *Proc. SPIE*, vol. 3597, no. January 1999, pp. 582–592, 1999.

[36] P. G. Al-Rawi, P. Smielewski, and P. J. Kirkpatrick, "Evaluation of a near-infrared spectrometer (NIRO 300) for the detection of intracranial oxygenation changes in the adult head.," *Stroke*, vol. 32, no. 11, pp. 2492–2500, 2001.

[37] C. E. Cooper, M. Cope, R. Springett, P. N. Amess, J. Penrice, L. Tyszczuk, S. Punwani, R. Ordidge, J. Wyatt, and D. T. Delpy, "Use of mitochondrial inhibitors to demonstrate that cytochrome oxidase near-infrared spectroscopy can measure mitochondrial dysfunction noninvasively in the brain.," *J. Cereb. Blood Flow Metab.*, vol. 19, no. 1, pp. 27–38, 1999.

[38] C. E. Cooper and R. Springett, "Measurement of cytochrome oxidase and mitochondrial energetics by near-infrared spectroscopy.," *Philos. Trans. R. Soc. Lond. B. Biol. Sci.*, vol. 352, no. 1354, pp. 669–676, 1997.

[39] H. Q. Woodard and D. R. White, "The composition of body tissues," *Br. J. Radiol.*, vol. 59, no. 708, pp. 1209–1218, Dec. 1986.

[40] J. Zhao and H. Zeng, "Advanced Spectroscopy Technique for Biomedicine," in *Biomedical Optical Imaging Technologies Design and Applications*, 1st ed., R. Liang, Ed. Tuscon, Arizona: Springer Heidelberg, 2013, pp. 1–47.

[41] G. Bale, "Development of Optical Instrumentation and Methods to Monitor Brain Oxygen Metabolism : Application to Neonatal Birth Asphyxia," 2016.

[42] R. V Chimenti, "SPECTROMETERS: Miniature spectrometer designs open new applications potential," *Laser Focus World*, 2013. [Online]. Available: http://www.laserfocusworld.com/articles/print/volume-49/issue-05/features/spectrometers--miniature-spectrometer-designs-open-new-

applicati.html. [Accessed: 11-Apr-2017].

[43] B&W TEK, "Part 4: The Optical Bench," *B&W Tek*, 2017. [Online]. Available: http://bwtek.com/spectrometer-part-4-the-optical-bench/. [Accessed: 11-Apr-2017].

[44] "QE Pro (Custom) - Ocean Optics." [Online]. Available: http://oceanoptics.com/product/qe-pro/.

[45] R. Springett, M. Wylezinska, E. B. Cady, M. Cope, and D. T. Delpy, "Oxygen dependency of cerebral oxidative phosphorylation in newborn piglets.," *J. Cereb. Blood Flow Metab.*, vol. 20, no. 2, pp. 280–9, 2000.

[46] M. M. Tisdall, I. Tachtsidis, T. S. Leung, C. E. Elwell, and M. Smith, "Near-infrared spectroscopic quantification of changes in the concentration of oxidized cytochrome c oxidase in the healthy human brain during hypoxemia," *J. Biomed. Opt.*, vol. 12, no. 2, p. 24002, 2007.

[47] M. M. Tisdall, I. Tachtsidis, T. S. Leung, C. E. Elwell, and M. Smith, "Increase in cerebral aerobic metabolism by normobaric hyperoxia after traumatic brain injury.," *J. Neurosurg.*, vol. 109, no. 3, pp. 424–432, 2008.

[48] I. Tachtsidis, L. Gao, T. S. Leung, M. Kohl-Bareis, C. E. Cooper, and C. E. Elwell, "A hybrid multi-distance phase and broadband spatially resolved spectrometer and algorithm for resolving absolute concentrations of chromophores in the near-infrared light spectrum.," *Adv. Exp. Med. Biol.*, vol. 662, pp. 169–75, 2010.

[49] A. Ghosh, I. Tachtsidis, C. Kolyva, C. E. Cooper, M. Smith, and C. E. Elwell, "Use of a hybrid optical spectrometer for the measurement of changes in oxidized cytochrome c oxidase concentration and tissue scattering during functional activation," *Adv. Exp. Med. Biol.*, vol. 737, pp. 119–124, 2012.

[50] A. Ghosh, C. Kolyva, I. Tachtsidis, D. Highton, C. E. Elwell, and M. Smith, "Reduction of Cytochrome c Oxidase During Vasovagal Hypoxia-Ischemia in Human Adult Brain: A Case Study," *Oxyg. Transp. to Tissue XXXV, Adv. Exp. Med. Biol.*, vol. 789, no. July, pp. 463–7, 2013.

[51] C. Kolyva, I. Tachtsidis, A. Ghosh, T. Moroz, C. E. Cooper, M. Smith, C. E. Elwell, N. C. Unit, L. Hospitals, and L. Wcn, "Systematic investigation of changes in oxidized cerebral cytochrome c oxidase concentration during frontal lobe activation in healthy adults," vol. 3, no. 10, pp. 27–38, 2012.

[52] C. Kolyva, A. Ghosh, I. Tachtsidis, D. Highton, C. E. Cooper, M. Smith, and C. E. Elwell, "Cytochrome c oxidase response to changes in cerebral oxygen delivery in the adult brain shows higher brain-specificity than haemoglobin," *Neuroimage*, vol. 85, pp. 234–244, Jan. 2014.

[53] G. Bale, S. Mitra, J. Meek, N. Robertson, and I. Tachtsidis, "Relationship Between Cerebral Cytochrome-C-Oxidase and Oxygenation is Associated with Brain Injury Severity in Birth Asphyxiated Infants," *Biomed. Opt. 2016*, no. July, p. TM2B.4, 2016.

[54] P. Phan, D. Highton, J. Lai, M. Smith, C. Elwell, and I. Tachtsidis, "Multi-channel multi-distance broadband near-infrared spectroscopy system to measure the spatial response of cellular oxygen metabolism and tissue oxygenation," *Biomed. Opt. Express*, vol. 7, no. 11, p. 4424, Nov. 2016.

[55] P. T. Phan, D. Highton, S. Brigadoi, I. Tachtsidis, M. Smith, and C. E. Elwell, "Spatial distribution of changes in oxidised cytochrome c oxidase during visual stimulation using broadband near infrared spectroscopy imaging," *Adv Exp Med Biol*, vol. 923, pp. 195–201, 2016.

[56] OceanOptics, "Home - Ocean Optics." [Online]. Available: https://oceanoptics.com/. [Accessed: 02-May-2017].

[57] J. F. Brennan, G. I. Zonios, T. D. Wang, R. P. Rava, G. B. Hayes, R. R. Dasari, and M. S. Fled, "Portable Laser Spectrofluorimeter System for *in Vivo* Human Tissue Fluorescence Studies," *Appl. Spectrosc. Vol. 47, Issue 12, pp. 2081-2086*, vol. 47, no. 12, pp. 2081–2086, 1993.

[58] G. Zonios, "Noise and stray light characterization of a compact CCD spectrophotometer used in biomedical applications.," *Appl. Opt.*, vol. 49, no. 2, pp. 163–9, 2010.

[59] N. a O'Brien, C. a Hulse, D. M. Friedrich, F. J. Van Milligen, M. K. von Gunten, F. Pfeifer, and H. W. Siesler, "Miniature near-infrared (NIR) spectrometer engine for handheld applications," *Next-Generation Spectrosc. Technol. V*, vol. 8374, no. 837404–1, pp. 3–9, 2012.

[60] Newport Tutorial, "Light Collection and Systems Throughput," *Newport*, 2017. [Online]. Available: https://www.newport.com/t/light-collection-and-systems-throughput. [Accessed: 11-Mar-2017].

[61] M. Johns, C. Giller, D. German, and H. Liu, "Determination of reduced scattering coefficient of biological tissue from a needle-like probe.," *Opt. Express*, vol. 13, no. 13, pp. 4828–4842, 2005.

[62] S. Bhatia, J. Ragheb, M. Johnson, S. Oh, D. I. Sandberg, and W.-C. Lin, "The role of optical spectroscopy in epilepsy surgery in children.," *Neurosurg. Focus*, vol. 25, no. 3, p. E24, 2008.

[63] K. Bensalah, D. Peswani, A. Tuncel, J. D. Raman, I. Zeltser, H. Liu, and J. Cadeddu, "Optical Reflectance Spectroscopy to Differentiate Benign From Malignant Renal Tumors at Surgery," *Urology*, vol. 73, no. 1, pp. 178–181, 2009.

[64] M. Canpolat, a G. Gökhan, M. A. Ciftçioğlu, and N. Erin, "Differentiation of melanoma from non-cancerous tissue in an animal model using elastic light single-scattering spectroscopy.," *Technol. Cancer Res. Treat.*, vol. 7, no. 3, pp. 235–240, 2008.

[65] T. Shi and C. a DiMarzio, "Multispectral method for skin imaging: development and validation.," *Appl. Opt.*, vol. 46, no. 36, pp. 8619–26, 2007.

[66] M. B. Lilledahl, O. a Haugen, M. Barkost, and L. O. Svaasand, "Reflection spectroscopy of atherosclerotic plaque.," *J. Biomed. Opt.*, vol. 11, no. 2, p. 021005–1/7, 2006.

[67] M. Diop, E. Wright, V. Toronov, T.-Y. Lee, and K. St Lawrence, "Improved light collection and wavelet de-noising enable quantification of cerebral blood flow and oxygen metabolism by a low-cost, off-the-shelf spectrometer.," *J. Biomed. Opt.*, vol. 19, no. 5, p. 57007, 2014.

[68] E. Wright, K. St. Lawrence, and M. Diop, "Conversion of a low cost off-the-shelf spectrometer into a suitable instrument for deep tissue spectroscopy," *Proc. SPIE*, vol. 8573, p. 85730V, 2013.

[69] R. Nosrati, K. Vesely, T. A. Schweizer, and V. Toronov, "Event-related changes of the prefrontal cortex oxygen delivery and metabolism during driving measured by hyperspectral fNIRS," *Biomed. Opt. Express*, vol. 7, no. 4, p. 1323, 2016.

[70] C. Kolyva, A. Ghosh, I. Tachtsidis, D. Highton, M. Smith, and C. E. Elwell, "Dependence on NIRS Source-Detector Spacing of Cytochrome c Oxidase Response to Hypoxia and Hypercapnia in the Adult Brain," *Adv. Exp. Med. Biol.*, vol. 789, pp. 353–359, 2013.

[71] I. de Roever, G. Bale, R. J. Cooper, and I. Tachtsidis, "Cytochrome-C-Oxidase Exhibits Higher Brain-Specificity than Haemoglobin in Functional Activation," in *Biomedical Optics 2016*, 2016, p. BTh4D.4.

[72] I. de Roever, G. Bale, R. J. Cooper, and I. Tachtsidis, "Functional NIRS Measurement of Cytochrome-C-Oxidase Demonstrates a More Brain-Specific Marker of Frontal Lobe Activation Compared to the Haemoglobins," Springer, Cham, 2017, pp. 141–147.

Chapter 4. The Role of oxCCO Measurement in a Preclinical Model of Neonatal Hypoxia-Ischaemia

As part of the software development in the research, this chapter discusses the study that was carried out to evaluate the broadband NIRS-Δ[oxCCO] measurement against other measurements of mitochondrial energetics provided by magnetic resonance spectroscopy (MRS) during and following hypoxic-ischaemic brain injury in the neonatal preclinical model.

Neonatal Hypoxia- Ischaemia (HI), which is typically a result to birth asphyxia or other pregnancy complications, is one of the main causes of brain damage (Hypoxic Ischaemic Encephalopathy) and death in new-born infants. Brain injury severity in infants and animals is assessed by MRS. However, using MRS is expensive and complicated which is also not available in all the clinical/preclinical settings.

In this chapter, the correlation between the Δ[oxCCO] with the MRS metabolite markers for injury severity during and after inducing hypoxia-ischaemia in piglets will be investigated to see whether the measurement of oxCCO can be used as an alternative surrogate marker instead of the ^{31}P-MRS metabolites measurement. If so, the algorithm which relates the oxCCO measurement to these markers will be implemented in the software of the miniature system to assist the clinicians with the HI insult in neonatal pigs in the absence of ^{31}P-MRS.

After a brief introduction to the broadband-NIRS measurement of Δ[oxCCO] in the preclinical study of neonatal HI, the motivations of this study are mentioned which is followed by methods (including animal preparation, MRS and broadband-NIRS measurements, HI protocol and data analysis). Next, the results produced by broadband-NIRS are presented and spectroscopically analysed and their correlation with MRS data is examined. The chapter ends with a discussion of the results followed by chapter summary.

4.1 NIRS-oxCCO Measurement in the Piglet Model of Neonatal Hypoxia-Ischaemia

Hypoxic-ischaemic encephalopathy (HIE) in newborns commonly referred to as ”birth asphyxia” is primarily caused by systemic hypoxemia and /or reduced cerebral blood flow and is the fifth largest cause of death in children younger than 5 years of

age according to WHO (World Health Organisation) [1]. It is the main cause for 23% of all neonatal deaths worldwide and one of the most common causes of mortality and morbidity in neonates as well as long-term neurological disabilities in those who survive [2]. About one third of the birth asphyxiated infants will develop HIE which ultimately leads to devastating neurological disorders such as cerebral palsy and epilepsy, as well as mental retardation, learning difficulties and other disabilities [3]. The permanent and devastating outcomes of the HI, makes it critical to identify the condition and develop effective therapeutic strategies to reduce brain injuries in the affected neonates. Preclinical animal models are used to investigate cerebral energetics and oxygen metabolism during and after hypoxic-ischaemic injury aiming to develop neuroprotective therapeutic strategies [4]. New-born pigs are usually used as animal models for human neonates, due to their comparable vascular anatomy, energy metabolism and maturity to human brain at birth [5]. Phosphorus magnetic resonance spectroscopy (^{31}P-MRS) is the gold standard technique for assessing HI simply because it measures the metabolites that are directly involved in oxidative phosphorylation and ATP production in cells. These metabolites include phosphocreatine (PCr), which is a rapidly activated reserve of high-energy phosphates in skeletal muscle and the brain; inorganic phosphate (Pi) which is the end product of ATP hydrolysis (ATP ↔ ADP + Pi) and total nucleotide triphosphate (NTP), which provides energy and phosphate group for phosphorylation and mainly includes ATP [4] (around 70% as measured in rats [6]). As seen in Figure 4.26, the spectra produced from a hypoxic ischaemic piglet's brain is very well distinct from that of the normal brain [4], [7], [8]. Furthermore, the decline in cerebral energy measured in this manner correlates strongly with the neurodevelopmental outcome following HI injury [9], [10]. ^{31}P-MRS measurements of Pi/epp, PCr/epp, and NTP/epp (see section 2.7.2) are used as indicators of metabolic recovery 1-2 hours after HI [4], [7]. All the metabolite values are normalised to epp which is a high-energy exchangeable phosphate pool (epp= Pi+ PCr + 3NTP) [4].

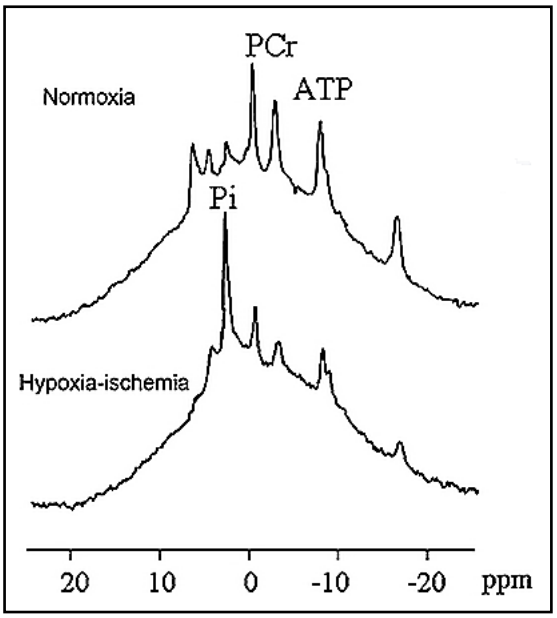

Figure 4.26: ^{31}P-MRS of a new-born piglet at baseline (top) and after 1 h of cerebral hypoxia–ischaemia (bottom). There is a good abundancy of PCr and ATP in normal brain whereas in the hypoxic-ischaemic brain these peaks are suppressed and Pi is significantly increased which is indicative of impaired oxidative metabolism. image taken from [8]

Despite the useful information that ^{31}P-MRS provides in the preclinical study of HI, MR units are expensive equipment, also not portable so the animals need to be transferred to the magnet room, which involves more complications especially following an invasive surgery. Broadband NIRS is however, a low-cost non-invasive optical technique that provides brain oxygenation and metabolism measurement complementary to ^{31}P-MRS and could be used as an alternative tool at piglets' pod side for continuous measurement of brain energetics metabolism.

Use of broadband-NIRS in preclinical study of HIE was first demonstrated by Chris Cooper and Roger Springett [11], [12]. They used a broadband-NIRS system developed by Springett et al in 1995 (here we call it UCL1) in an established piglet model of neonatal hypoxia-ischaemia [13]–[15]. The aim of this study was to focus on the usefulness that the oxCCO measurement would have in clinical environment, as well as describing conditions under which they could be confident that they are measuring real changes in the redox state of CCO molecule. The broadband NIRS system, UCL1, which was briefly described in chapter 3, section 3.4.5 and will be explained in further details in section 4.3.3 Broadband-NIRS uses a broadband light source and a broadband detection unit for more accurate measurement of oxCCO [11]. Furthermore, The UCLn algorithm was validated and tested in the piglet study by

Cooper and Springett and it was confident that the algorithm could be transferred across the species and developmental age barrier [11].

Cooper and Springett investigated the effect of hypoxia-ischaemia on the haemodynamic and energetic properties of the neonatal brain. Simultaneous NIRS and MRS measurements were made on the new-born piglet head and as seen in Figure 4.27, the large drop in the NIRS-measured oxCCO signal correlated with brain energy failure (NTP/EPP) as measured by MRS. As shown in Figure 4.27, in the initial hypoxic-ischaemic period (the insult protocol will be explained in the methods section), there is a drop in HbO_2 and a rise in HHb, accompanied by a small decrease in total Hb concentration ($\Delta[HbT]=\Delta[HbO_2]+\Delta[HHb]$). Subsequent to fall in HbO_2, there is also a reduction in oxCCO which was consistent with their previous finding [16]. The NIRS and MRS values return to close to baseline values after resuscitation (reversal of the hypoxia-ischaemia). It was also interesting to see for the first time that the reduction in oxCCO had the same time course as the fall in cerebral ATP (NTP/EPP).

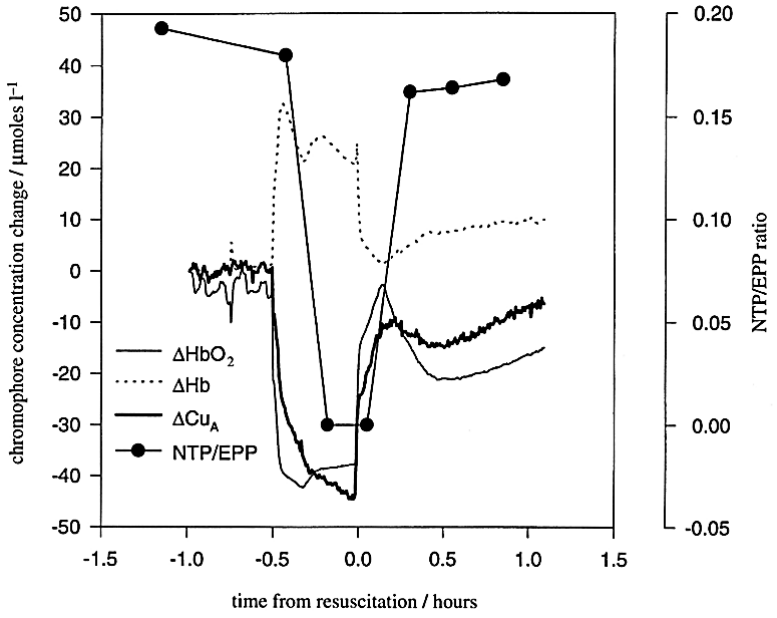

Figure 4.27: The effect of hypoxia-ischaemia on the haemodynamic and energetic properties of the neonatal brain. Simultaneous NIRS and MRS measurements were made on the neonatal piglet head. At time zero the carotid artery was occluded and FiO2 reduced to 11 %. Changes in Hb, HbO_2 and the cytochrome oxidase Cu_A redox state were calculated as described previously (UCLn algorithm). NTP (nucleotide triphosphate) was measured by MRS as a fraction of the total exchangeable phosphate pool (EPP), i.e. [NTP]/([Pi] + [PCr] + [NTP]) [15]. Cytochrome oxidase Cu_A redox state (oxCCO) changes are displayed on a x 10 expanded scale. Image taken from [11]

The data was consistent in six piglets and clearly demonstrated the usefulness of NIRS measurement of the CCO redox state (oxCCO), since a clinician viewing a

moderately raised haemoglobin oxygenation would probably conclude that the brain was not damaged, but the fall in the 'cytochrome oxidase NIRS signal' would clearly show that it was [11]. After this study, most of the attention was directed to understanding the biochemical interpretations of the oxCCO signal and its association with haemoglobin signals and oxygen delivery was investigated in different scenarios [17]–[20].

In 1998, Quaresima and colleagues presented some valid biochemical and physiological interpretation of the oxCCO signal using the same system in the piglet model. They demonstrated that small changes in oxygen delivery does not significantly affect the oxidation of CCO (Δ[oxCCO]) and large reductions in this signal reflect oxygen limitation at haem a_3/Cu_B centre which only occurs following dramatic haemoglobin desaturations [17]. However, there are other effectors that are likely to explain the small changes in the Δ[oxCCO] signals in the absence of large haemoglobin oxygenation changes; including pH, substrate supply and the presence of mitochondrial inhibitors such as nitric oxide [11].

Springett and colleagues further investigated the role of oxygen on cerebral oxidative phosphorylation in new-born piglets using simultaneous MRS and NIRS measurements in 2000 [20], [19]. In two separate studies by Springett et al., it was demonstrated that at normoxia (FiO_2=21%), oxidative phosphorylation and the oxidation state of electron transport chain are independent of cerebral oxygenation and the reduction in the oxCCO signal happens when oxygen tension (partial pressure) limits the oxidative phosphorylation capacity to maintain the phosphorylation potential. It was also shown that there is minimal interference between the haemoglobin and CCO signals in the piglet model [19].

Investigation of the broadband-NIRS oxCCO signal and its role as well as the physiological information that it could provide in the preclinical study of HI did not go any further than Springett's work in 2000. However, in 2014 Bainbridge and colleagues described the integration of broadband NIRS with ^{31}P-MRS to investigate HI in new-born pigs and discuss the physiological/biochemical dynamic relationships of these measurements [4]. The main aim of this study was to determine how Δ[oxCCO] associates with changes in energy metabolism during HI and during early recovery after reperfusion and re-oxygenation. Bainbridge and colleagues demonstrated that the measurement of Δ[oxCCO] significantly correlates with changes

in energy metabolism measured by ^{31}P-MRS (NTP/epp) during HI and early recovery after reperfusion and oxygenation [4].

4.2 Motivations and Aims

Current methods to monitor brain tissue metabolism in HI studies in preclinical models use MR methods if accessible. MR scanners are however expensive instruments and not available for all the preclinical studies. Some practicality issues also exist when it comes to running the hypoxic-ischaemic insult in the bore of a magnet which could increase the rate of mortality in piglets. MR units are not portable, and the animals need to be transferred to the magnet room, which involves more complications especially following an invasive surgery. Also, the clinicians do not have access to piglets if emergency access is required during HI (for instance in case of cardiac arrest). Furthermore, there is always a need for a trained MR physicist to run the MR systems. Can we use an optical instrument and the measurement of oxCCO to derive similar information about brain tissue energetics.

Following the work done by Bainbridge and colleagues [4], in this chapter, we aim to investigate whether broadband-NIRS and the measurement of oxCCO, can be used as a viable alternative to MRS to derive similar information about brain tissue energetics. Also, to examine whether this marker can potentially eliminate the need for using MRS during the hypoxic-ischaemic insult and can be applied independent of MR to predict the severity of early injury following hypoxic-ischaemic insult.

4.3 Methods

This section includes two parts. The first part includes a description of animal preparation, HI insult protocol, systemic and MRS data acquisition (performed by other members of the team), as well as NIRS instrumentation and data acquisition (4.3.1 Animal Preparation-4.3.4 Hypoxic-Ischaemic Insult Protocol The second part is data analysis methodology and was carried out by myself. It includes evaluation of the optical measurement of the oxCCO signal (4.3.5.1 Broadband-NIRS Residual and 4.3.5.2 Optical as well as the methodology of defining a reliable quantifiable marker based on broadband-NIRS to assess the severity of primary injury (4.3.5.3 Recovery Fraction Analysis and 4.3.5.4 Establishing a Quantifiable NIRS Measure).

4.3.1 Animal Preparation

All animal experiments were performed under UK Home Office Guidelines (Animals [Scientific procedures] act, 1986). 32 male term-born piglets aged less than 24 hours were anesthetised and surgically prepared for the experiment. Piglets were sedated using intramuscular midazolam (0.2 mg/kg), and arterial saturation (SpO_2) was continuously monitored using a pulse oximeter by Nonin Medical, USA. Using a facemask, Isoflurane anaesthesia (4% (vol/vol)) was initially given prior to tracheostomy and intubation. Piglets were mechanically ventilated, and the ventilator was adjusted to maintain partial pressure of oxygen (PaO_2) and carbon dioxide ($PaCO_2$) at 8-13 KPa and 4.5-6.5 KPa respectively, enabling arterial blood temperature correction. Heart rate and mean arterial blood pressure were also continuously monitored using an umbilical arterial catheter, which also enabled intermittent measurement of blood PaO_2, $PaCO_2$, pH, electrolytes, glucose and lactate. All subjects received continuous physiological monitoring and intensive care throughout the experiment, which lasted 48 hours and were terminated for further histological studies[4]. The piglets were positioned prone in a plastic pod and the head immobilised in a stereotactic frame including NIRS optode holders placed against the sides of the head, as seen in Figure 4.29.

4.3.2 Magnetic Resonance Imaging (MRI) and Spectroscopy (MRS)

Hydrogen-1 (proton, 1H) and phosphorus-31 (^{31}P) surface coils were used to produce radiofrequency signals in the presence of a very strong magnetic field (9.4 Tesla). Baseline imaging was carried out to look at the anatomy and structure of the brain. 1H-MR spectroscopy also provided information about baseline values of certain metabolites such as N-acetylaspartate (NAA) which is found in high concentrations in neurones and a high NAA peak represents normal neuronal activity, Choline containing compounds (Cho) and Creatine plus phosphocreatine (Cr). In addition, more complex metabolites such as lactate were measured which is a good indicator of anaerobic conditions (hypoxia) [21]. ^{31}P-MRS measurement was used to inform on seven important metabolites including phosphomonoesters (PME), inorganic phosphate (Pi), phosphocreatine (PCr), phosphodiesters (PDE), and the three phosphate groups in nucleotide triphosphate (NTP). NTP peak is a good indicator for ATP energy availability since the dominant contribution from the NTP peaks is from

ATP (around 70%)[4], [6]. All the metabolite values were normalised to epp which is a high-energy exchangeable phosphate pool (epp= Pi+PCr+3NTP) [4].

4.3.3 Broadband-NIRS

Broadband NIRS system in this study was the same system developed 20 years ago by Springett and colleagues at UCL (called UCL1) [12]. It includes a DC regulated white light source based one Quartz Halogen lamp by Newport Corporation (Oriel 77501), a mirror-based spectrometer with focusing lens (SPEX 270M), and a CCD camera by Wright Instruments.

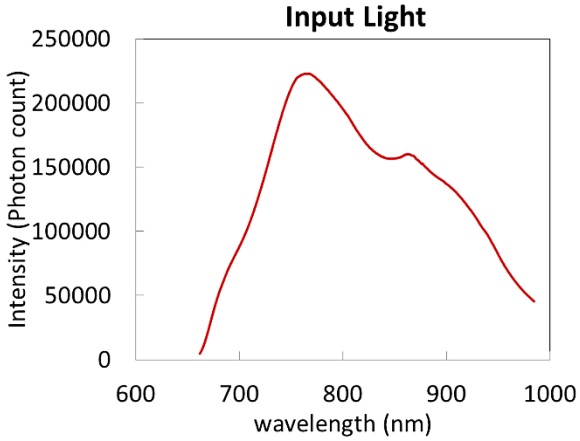

Figure 4.28: Filtered spectra spectral data from Oriel 77501, a DC-regulated Quartz Halogen lamp by Newport Co.

The source and detector probes were glass made optical fibre bundles (made by LOPTEK, Germany) with high numerical aperture (NA). The probes were securely positioned across the piglets' brain as seen in Figure 4.29.

Light from a thermally stabilized 100 W quartz halogen source was filtered before entering the fibre using 610 nm long-pass and heat absorbing filters to prevent heating the tissue (spectral data is shown in Figure 4.28). The filtered light was transmitted to the piglet's brain with an average power of about 0.2 W/nm through a 3.3 mm diameter, 7 m long optical glass fibre bundle with NA of 0.57. The light was then attenuated due to lots of scattering events within the brain and collected via a second fibre bundle with the same characteristics. Using an enclosed f-matching system, light through the detector fibre was focused onto the 400 μm entrance slit of a mirror-based 0.27 m spectrograph (270 M, Instruments SA, France) with a 300 g/mm grating blazed at 1000 nm. Optodes were placed co-linear across the head as shown in Figure 4.29 and measurement was performed in transmission mode.

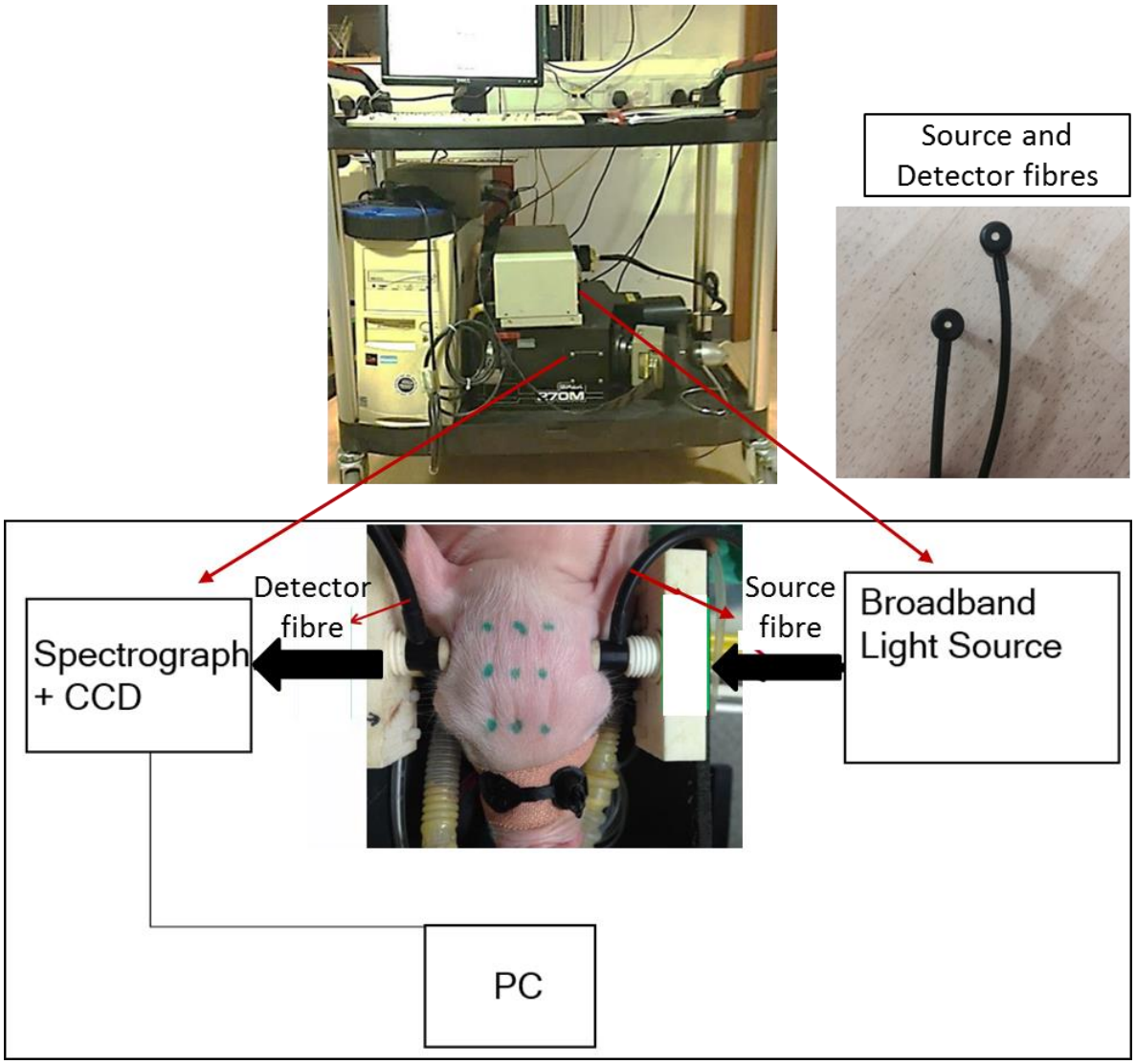

Figure 4.29: Broadband NIRS instrumentation developed by Springett et.al., in the preclinical study of Hypoxia Ischaemia [12]. The NIRS optodes are securely positioned across the head in a stereotactic frame with optode holders.

Spectral data between 650 nm and 980 nm were continuously acquired every 10 seconds on a cooled CCD with the shutter open, giving a signal of 10,000-30,000 electrons per digital conversion at 800 nm and about 1 nm dispersion per pixel and an approximate spectral resolution of less than 5 nm.

Changes in light attenuation through the brain (O.D) were used to calculate changes in the concentration of light absorbing molecules or chromophores in the brain (Δc) using the UCLn algorithm (equation. 3.13) as described in (section 3.1.4) across 780-900. The reason for choosing this spectral band is to enhance oxCCO measurement precision; firstly, to avoid the large absorption peak by HHb at 760 nm and secondly because in this band (figure 3.3), CCO is the only significant non-

haemoglobin oxygen dependent chromophore [12]. A reference spectrum was acquired prior to the measurement to characterise the input light and the differential pathlength (DP) for the 840 nm water absorption feature was obtained by fitting the second differential of the attenuation spectra to the second differential of in vitro water signal between 800 and 880 nm, assuming 85% cerebral water content in new-born brain, as performed by Matcher et.al., [22] and described fully in section 3.4.4.

After correction for the wavelength dependence of pathlength [23], changes (Δ) in the brain concentration of HHb, HbO_2 and oxCCO were calculated in real time. Changes in haemoglobin difference ($\Delta[HbDiff] = \Delta[HbO_2] - \Delta[HHb]$); indexing changes in brain oxygenation) and total haemoglobin ($\Delta[HbT] = \Delta[HbO_2] + \Delta[HHb]$); indexing cerebral blood volume) were also calculated. The measurements of Δ[oxCCO], $\Delta [HbO_2]$ and Δ[HHb] were defined to be zero at the point of first measurement. Therefore, their values over the course of the experiment represented the changes with respect to this first measurement.

4.3.4 Hypoxic-Ischaemic Insult Protocol

A surgery was performed on piglets prior to the experiment to facilitate access to the airways, blood vessels, and carotid arteries (section 4.3.1 Animal Preparation). Baseline physiological data (including heat rate, mean arterial blood pressure, arterial oxygen saturation) were collected from the piglet as well as baseline EEG and proton MRI to obtain structural and anatomical information about piglet's brain. Broadband-NIRS measurement was performed to investigate brain oxygenation and metabolism changes during the Hypoxic-Ischaemic insult and recovery. For duration of approximately 10 minutes prior to insult, whole brain phosphorus (^{31}P) MRS was recorded using a 9.4 Tesla Agilent spectrometer and a non-localised single-pulse surface-coil. The baseline MRS data were recorded with 1-minute resolution simultaneous with the NIRS data with 10 s acquisition time.

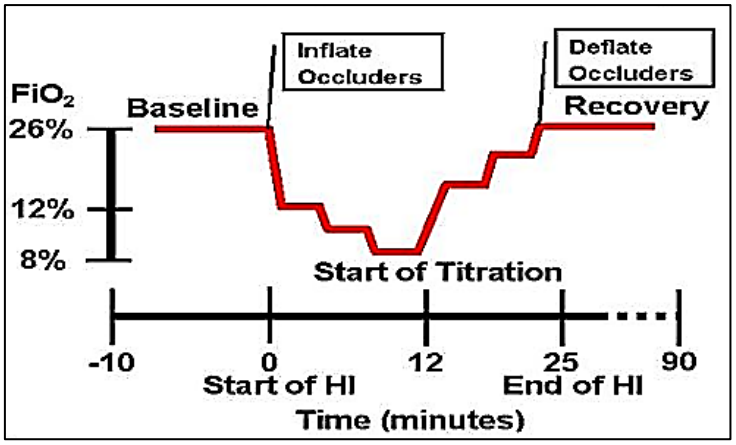

Figure 4.30: Schematic of Birth Asphyxia simulation protocol (Hypoxic-Ischaemic insult)

Figure 4.30 illustrates the protocol for simulating birth asphyxia in the piglets. The HI insult was induced inside the bore of the magnet through occlusion of both common-carotid arteries, and simultaneously reducing the fractional inspired oxygen (FiO_2) to 9% (vol/vol). After a phase called 'initial HI' (that is from the start of HI to when β-NTP peak had fallen to 40% of its baseline height), a titration phase started during which the FiO_2 was increased in steps to reach the baseline value. At the end of the insult, the occluders were deflated and the FiO_2 was restored to its normal value (21%) [4]. The piglet was monitored for 1 hour after resuscitation and MRS and NIRS scans were carried out 24 and 48 hours after HI. Physiological data including mean blood pressure (Mean BP), arterial Oxygen saturation (SpO2) and Heart Rate were acquired continuously every second.

4.3.5 Data Analysis

4.3.5.1 Broadband-NIRS Residual Analysis

Residual analysis was carried out for all the piglets, as proposed by Cooper et al, to evaluate the oxCCO measurement by broadband-NIRS [11]. To investigate the spectral changes due to the oxCCO chromophore, the UCLn algorithm (eq. 3.13) was used to derive changes in chromophore concentrations when solving only for HHb and HbO_2, as well as when solving for three chromophores (HHb, HbO_2, oxCCO). The attenuation change spectra were then back-calculated from the concentration changes and the difference between the measured attenuation spectra (ΔA, equation .3.10.) with the 2- and 3-chromophore fit were studied. If all the chromophores that determine the attenuation spectra were fitted, then the residual error from the measured

attenuation and back-calculated attenuations must be randomly fluctuating around zero (having no defined shape). However, if the residuals have defined shapes, it would suggest that there is a chromophore that was unaccounted for in the algorithm. For this purpose, attenuation change was measured between two points that the oxCCO signal had the maximum magnitude of change, i.e. baseline and nadir hypoxia-ischaemia, then it was subtracted from the back-calculated attenuations from 2- and 3-chromophores fit at those specific points. The residual analysis was carried out using a MATLAB script for all the experiments.

4.3.5.2 Optical Pathlength Analysis

Another requirement for a precise measurement of oxCCO, as demonstrated by Cooper et al.[11], is that there should be no large changes in the pathlength during the measurement.

It is important to demonstrate that the pathlength does not significantly change during the course of each experiment because any large change in oxCCO can be attributed in pathlength change (crosstalk) rather than reflecting the physiology.

4.3.5.3 Recovery Fraction Analysis

Piglets were divided into two groups of good and poor outcome based on whether they recovered 1 hour after HI or were terminated due to severe brain injury as measured by ^{31}P-MRS. To investigate how broadband NIRS measurements of $\Delta[HbO_2]$, Δ[HHb] and Δ[oxCCO] correlate with the ^{31}P-MRS markers of injury one hour after HI, data were averaged over a 5-minute window during baseline, hypoxia-ischaemia (HI) and at 1-hour recovery (Figure 4.31). Then the recovery fractions of all the NIRS, systemic and ^{31}P- MRS measurements were calculated according to the equations (4.1) and (4.2). All the measurements were normalized against the peak/nadir values during HI:

$$\frac{([5\ \text{min}\ Recovery\ after\ HI] - [Nadir])}{([5\ \text{min}\ Baseline] - [Nadir])} \times 100\% \quad (4.1)$$

$$\frac{([5\ \text{min}\ Recovery\ after\ HI] + [Peak])}{([5\ \text{min}\ Baseline] + [Peak])} \times 100\% \quad (4.2)$$

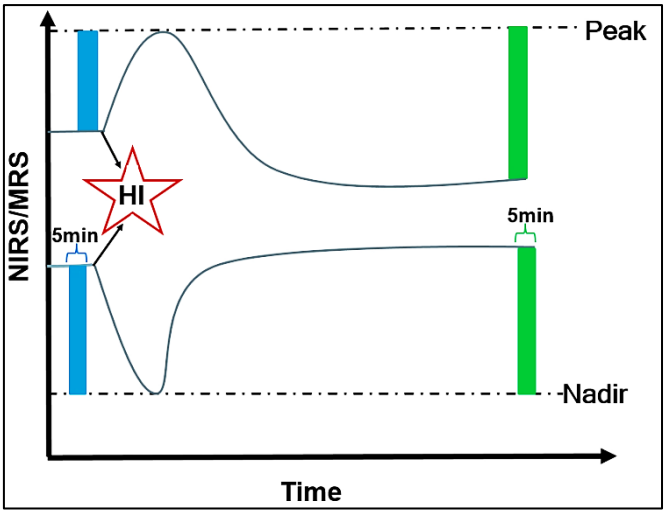

Figure 4.31: Recovery fraction calculation schematic for NIRS and systemic parameters when there was a peak (a) and nadir (b) during HI. Baseline and Recovery values were averaged over 5 minutes.

Statistical analyses were carried out in MATLAB R2015a and Microsoft Excel. Pearson's correlation and regression analysis were performed (significance threshold $p<0.05$) between the recovery fractions of NIRS data (Δ[HHb], Δ[HHb] and Δ[oxCCO]) with MRS data [NTP/epp], [Pi/epp] and [PCr/epp], as markers of brain injury severity following HI.

4.3.5.4 Establishing a Quantifiable NIRS Measure

Sensitivity and specificity analysis was carried out to determine a threshold value for the Δ[oxCCO] measurement to distinguish between poor and good outcome piglets, with maximum efficiency, using the receiver operating characteristic function (ROC) in MATLAB 2015a. A 100% sensitivity reflects the ability of the test to correctly identify all poor outcomes (true positives) whereas a 100% specificity reflects the ability to correctly identify all good outcomes (true negatives). Efficiency of the test is defined as the ratio of total correctly identified outcomes to the total number of piglets included.

4.4 Results

4.4.1 Broadband NIRS Signals During HI.

Changes in the intensity and attenuation of light traversed a piglet's brain during baseline and hypoxia-ischaemia is shown in Figure 4.32 and Figure 4.33, respectively.

The intensity spectra have two features around 760 nm and 830 nm that are attributed to deoxyhaemoglobin (HHb) and oxidised-CCO (oxCCO) (see Chapter 3, Figure 3.3).

As seen in Figure 4.32, the signal intensity during HI insult is larger than the intensity of light transmitted through piglet's brain at baseline. That is because during HI, a larger number of photons manage to exit the brain due to the reduction in blood flow and blood volume in the brain, which results in less absorption. Figure 4.33 shows the change in the attenuation of light trough the piglet's brain relative to the first measurement, according to the modified Beer-Lambert law (Eq. 3.10). As seen in the figure, at baseline, there is no major change in magnitude and shape of the attenuation spectrum relative to the first measurement. However, during HI, there is a significant change in the magnitude and shape of the attenuation spectrum due to the physiological changes in the brain, i.e. reduction in blood flow and oxygen supply hence changes in the concentration of chromophores.

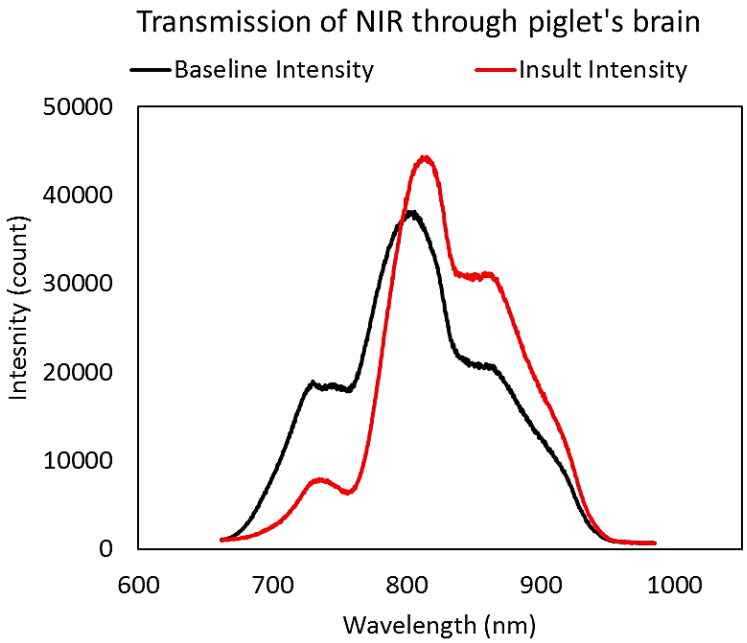

Figure 4.32: Changes in the intensity of light traversed a piglet's brain during baseline and nadir HI.

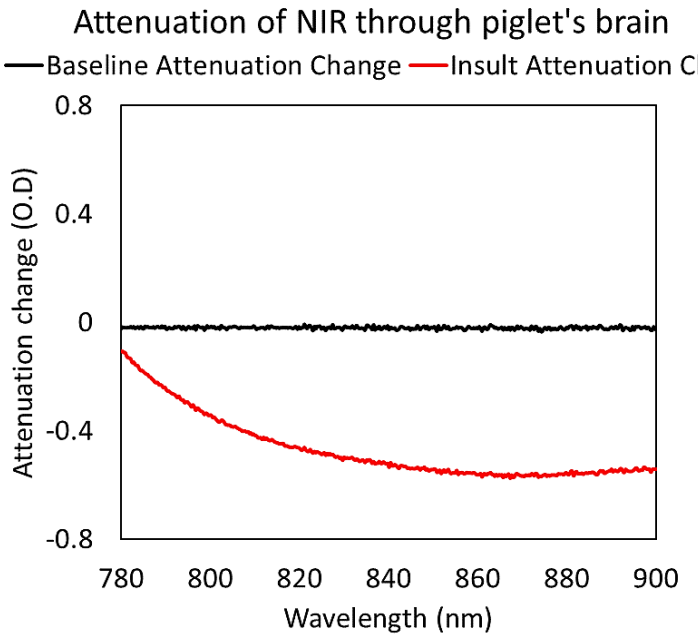

Figure 4.33 : Attenuation change at baseline and nadir HI relative to the first measurement.

Changes in concentration of HHb, HbO_2 and oxCCO during hypoxia-ischaemia (HI) in a piglet are displayed in Figure 4.34. At baseline when the piglet is in normal physiological condition and there are no variations in oxygen levels (FIO_2 kept at ~21%), all the NIRS signals are nearly stable. As soon as the insult initiates (shown in shaded red area), that is when arterial oxygen saturation (SpO_2) drops from its initial value (~98%), broadband NIRS measure of $\Delta[HbO_2]$ drops and Δ[HHb] in the field of view increases resulting in a significantly large drop in haemoglobin difference signal Δ [HbDiff] as a measure for blood oxygenation due to the limited oxygen availability (hypoxia) in the brain. Blood volume as measured by [HbT], total haemoglobin, also slightly drops during HI due to insufficient blood supply, caused by occlusion of both carotid arteries. Measurement of Δ[oxCCO], representing oxygen metabolism at cellular level also declines significantly because of insufficient blood supply and limited oxygen availability. In other words, oxygen as the final electron acceptor in the mitochondrial ETC becomes significantly reduced which consequently leads to inhibition of CCO oxidisation. As soon as the titration of oxygen starts (lightly shaded), the oxygenated haemoglobin increases, however, oxCCO signal continuous to drop. This shows that the oxCCO signal reflects the actual physiology rather than simply following the haemoglobin measurements. At the end of insult, when occluders are deflated and oxygen is revived (see the SpO_2 measurement), all the NIRS signals start recovering back to baseline values.

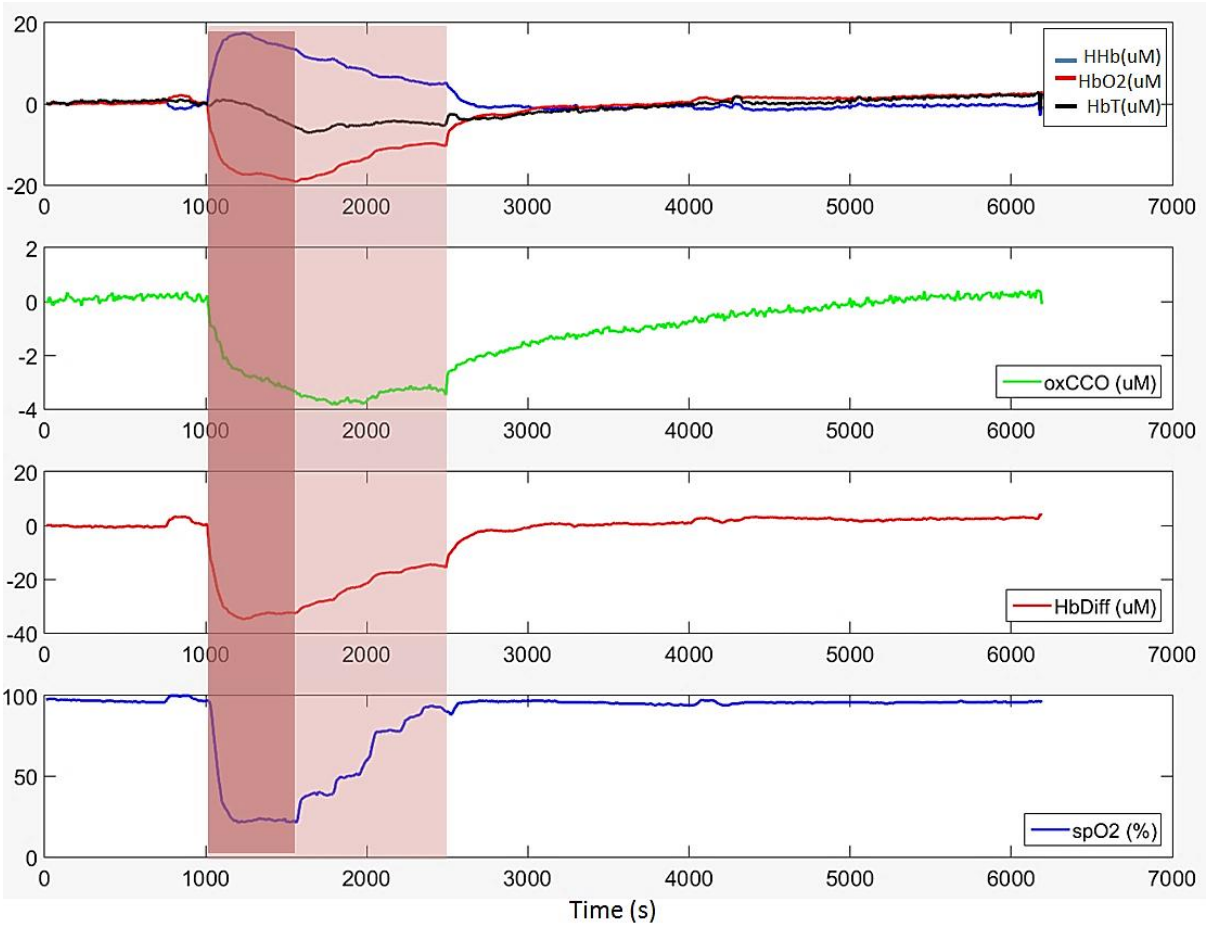

Figure 4.34: Changes in NIRS signals during HI. SpO_2 is the arterial oxygen saturation. The dark shaded area indicates the initial phase of the insult (when oxygen is gradually decreased to 8%) and the light shaded area shows the titration phase, when oxygen is increased in steps until the end of the insult (FiO_2=21%). Insult schematic is shown in Figure 4.30.

4.4.2 Residual Analysis

Figure 4.35 displays the measured attenuation spectrum at nadir HI (minimum Δ[oxCCO]), as well as the back-calculated attenuations from 2- and 3-chromophore fit. As seen in the figure, the back-calculated attenuation spectrum from the 3-chromophore fit matches the measured attenuation whilst the red attenuation spectrum

shows that when solving only for 2 chromophores, all the chromophores were not accounted for as it does not match the measured attenuation.

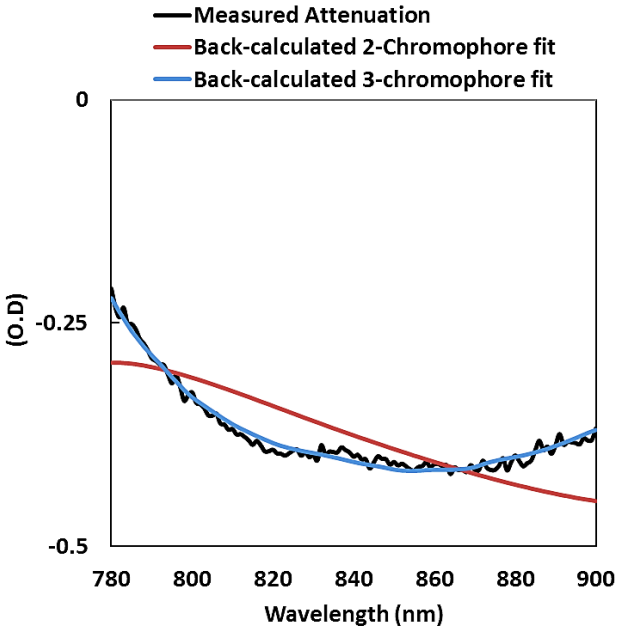

Figure 4.35: Measured attenuation spectrum at HI and back-calculated attenuations from 2- and 3-chromophore fit.

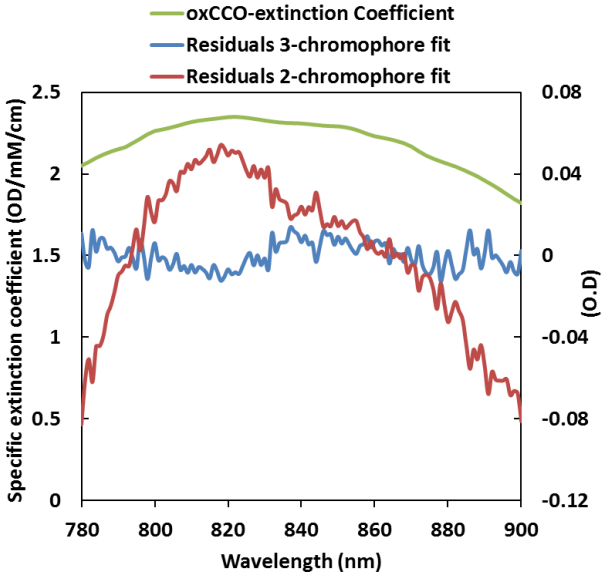

Figure 4.36: Residual error from 2- and 3- chromophore fit. The 2-chromophore fit residuals (in red) matches the extinction coefficient of oxCCO (in green), whilst the 3-chromophore fit's residual error (in blue) randomly oscillates around zero.

The residual errors from fitting back-calculated attenuation spectra when solving for 2- and 3-chromophores are shown in Figure 4.36. The residual error from 2-chromophore fit has a well-defined shape that matches the extinction coefficient spectrum of oxidised-reduced CCO between 780-900 nm. Therefore, it shows that when resolving only for [HHb] and [HbO_2], the oxCCO remains unaccounted for.

However, when solving for 3-chromophore (including oxCCO), the residual error randomly fluctuates around zero that shows all the chromophores in the field of view have been accounted for in the measurement.

Figure 4.37 shows the mean residual with standard errors from 2- and 3-chromophore fit for all the 32 piglets in the experiments which follows the same pattern as in Figure 4.36.

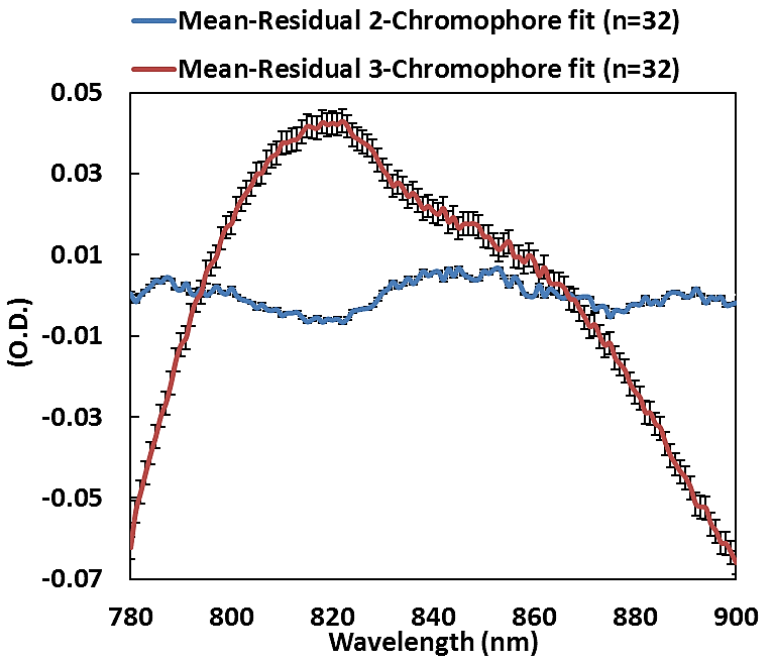

Figure 4.37 : Mean residual with standard errors from 2- and 3- chromophore fit for all the piglets in the experiment (n=32).

4.4.3 Changes in Optical Pathlength During the Experiment

Figure 4.38 illustrates changes in the optical pathlength during HI in a piglet. There is a slight increase in pathlength at HI which returns to baseline after the insult.

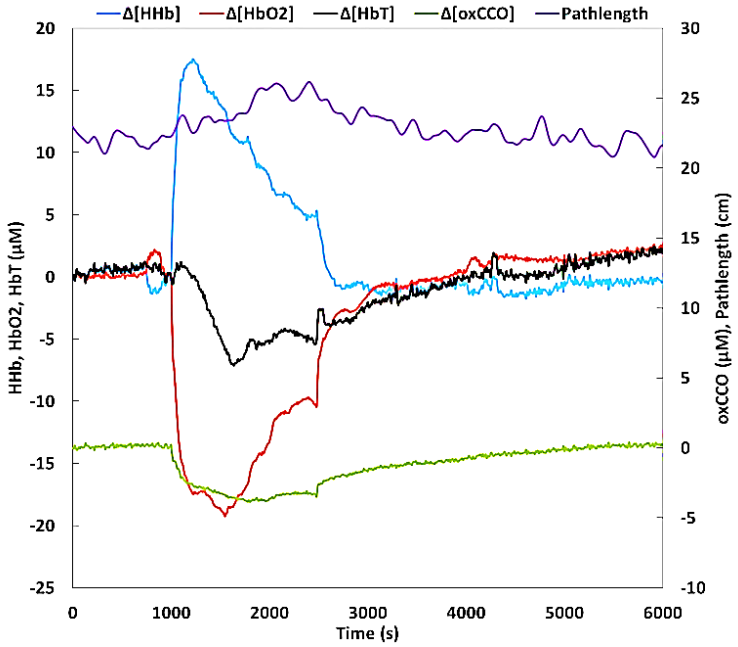

Figure 4.38: Changes in optical pathlength and chromophores' concertation during HI.

Figure 4.39 shows changes in pathlength during the measurement period for 32 piglets. Despite the distribution in pathlengths among different piglets (due to different size of the heads and some differences in scattering features in individuals), the pattern of change in optical pathlength in each piglet during insult is almost different from the others. In general, there were no major change in pathlength throughout the experiment.

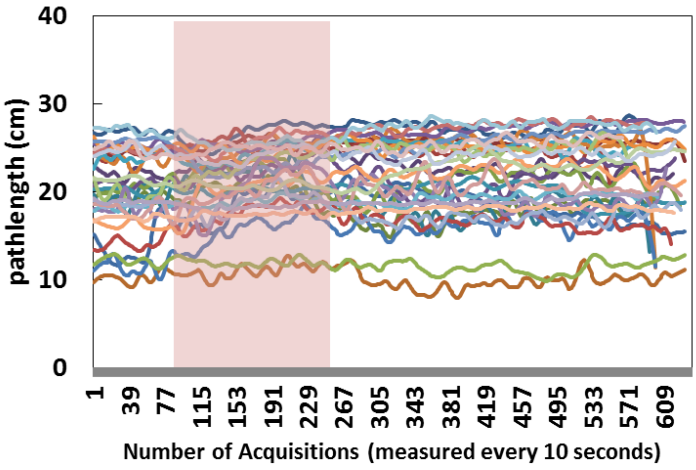

Figure 4.39: Variations in pathlength during HI showing different trends in different subjects. The shaded area represents the approximate HI period.

4.4.4 Recovery Fraction of Broadband NIRS and ^{31}P-MRS Signals Following Hypoxia-Ischaemia

20 out of 32 piglets recovered following HI, since they had the βNTP peak recovered back to at least 70% of their baseline value. The remaining 12 were terminated due to the severity of brain damage as measured by ^{31}P-MRS.

Figure 4.40 a, shows the NIRS and MRS signals changes during and 1 hour after hypoxic-ischaemic insult in a piglet with good out come and Figure 4.40 b, shows the same signals for a piglet that did not survive after the insult. Recovery fraction for all the signals were calculated according to equations (4.1) and (4.2) in MATLAB. It can be seen that piglets who recovered after HI showed a good recovery of both NIRS and MRS signals one hour after the insult (Δ[HbT]=81%, Δ[HbDiff] =102% and Δ[oxCCO] =83%) , ^{31}P-MRS (NTP/epp=105%, PCr/epp= 101% and Pi/epp=102%%). In the piglet with poor recovery, however, even though the haemoglobin signals recovered one hour after HI with recovery fractions of Δ[HbT]=163% and Δ[HbDiff]=85%, the Δ[oxCCO] signal as well as all the ^{31}P-MRS signals showed a very poor recovery at one hour post HI (Δ[oxCCO]=13%, NTP/epp=25%, PCr/epp= 28% and Pi/epp=150%).

As seen in Figure 4.40, the slow recovery of Δ[oxCCO] following HI correlates very well with slow/no recovery of ^{31}P-MRS markers with injury severity. In piglets with severe brain damage, a direct relationship can be seen between the impairment in the oxidation of CCO with the depletion of NTP/epp (as a measure for ATP) and PCr/epp (reservoir of phosphate in anaerobic conditions) as well as elevated Pi/epp (end product of ATP catabolism). This suggests an impaired mitochondrial electron transport chain and that is why cells are not able to make use of the revived oxygen supply. This trend was consistent in most piglets with no recovery after HI. Table 4.2 shows the mean recovery fraction of all the NIRS and ^{31}P-MRS metabolites at one-hour post HI. All the data are presented in mean ± standard deviation and it can be seen that in average all the piglets with poor outcome showed reduced levels of Δ[HbDiff], Δ[oxCCO], NTP/epp, PCr/epp and elevated Pi/epp which is significantly different from the corresponding values in piglets which recovered following HI. There was no difference between the recovery fraction of Δ[HbT] in two group.

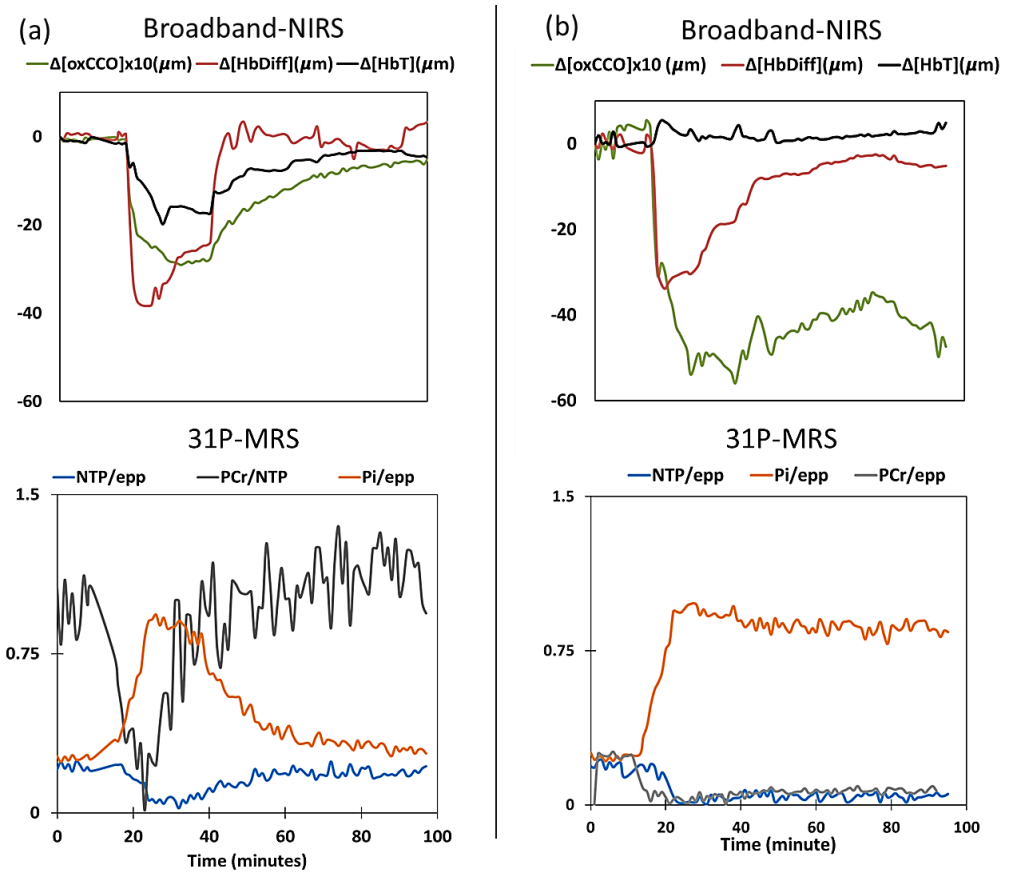

Figure 4.40: NIRS and ^{31}P-MRS signals during HI and recovery in a piglet with good outcome (a) and a piglet with poor outcome (b)

Table 4.2: Mean± SD recovery fraction of broadband NIRS and ^{31}P-MRS one hour after HI

Recovery Fraction (%)	HbT	HbDiff	oxCCO	NTP/epp	PCr/epp	Pi/epp
Poor Outcome (n=12)	111 ± 52	77 ± 16	27 ± 24	26 ± 19	37 ± 17	141 ± 11
Good Outcome (n=20)	94 ± 25	100 ± 14	87 ± 11	82 ± 13	102 ± 11	107 ± 7
p value	0.4	0.0007	0.000003	0.000003	0.000004	0.000003

4.4.5 Broadband NIRS to Identify Poor and Good outcome Following Hypoxia-Ischaemia

Table 4.3 shows the Pearson's correlation coefficient between the recovery fractions of all the NIRS signals with ^{31}P-MRS signals for all the 32 piglets. There is a very strong significant correlation between the recovery fraction of Δ[oxCCO] and

all the MRS metabolites that are indicatives of HI injury severity as (NTP/epp,Pi/epp and PCr/epp, [4], [7]). There is also a mild correlation between the recovery fraction of haemoglobin oxygenation (Δ[HbDiff]) with MRS metabolites whereas there is no association between total haemoglobin recovery fraction (Δ[HbT]) and MRS metabolites.

Figure **4.41** shows the linear regression analysis using a simple linear regression to investigate whether the recovery fraction of ^{31}P-MRS metabolites can be predicted by knowing the recovery fraction of broadband NIRS measures, in which case using the recovery fraction of the latter only, the outcome of piglets following HI can be foretold.

Table 4.3: Pearson correlation coefficient values between the Broadband NIRS and ^{31}P-MRS measurements. ** p<0.000000001, *p<0.005

Pearson correlation (r)	NTP/epp	Pi/epp	PCr/epp
oxCCO	0.9^{**}	-0.9^{**}	0.9^{**}
HbDiff	0.6^{*}	-0.5^{*}	0.6^{*}
HbT	-0.2	0.2	-0.2

There is a strong linear relationship between the recovery fraction of Δ[oxCCO] and the recovery fraction of all the ^{31}P-MRS markers for the severity of hypoxic-ischaemic injury (oxCCO vs NTP/epp, PCr/epp and Pi/epp, R^2~0.8, p<0.0000000001). This linear relationship was not seen between the recovery fraction of Δ[HbDiff] or Δ[HbT] with ^{31}P-MRS metabolites recovery fraction. . The strong linear correlation between the recovery fraction of Δ[oxCCO] and MRS metabolites, means that the recovery fraction of oxCCO could potentially be used to predict the outcome of piglets with hypoxic-ischaemic brain injury.

Sensitivity and specificity analysis was performed on the oxCCO recovery fraction of 32 piglets against their outcome one hour after HI using MATLAB (area under the curve (AUC) of 0.99 represents an excellent test). The analysis suggests a cut-off point of 71% for distinguishing between poor and good outcomes one hour after HI insult, which is 100% sensitive and specific.(Table 4.4).

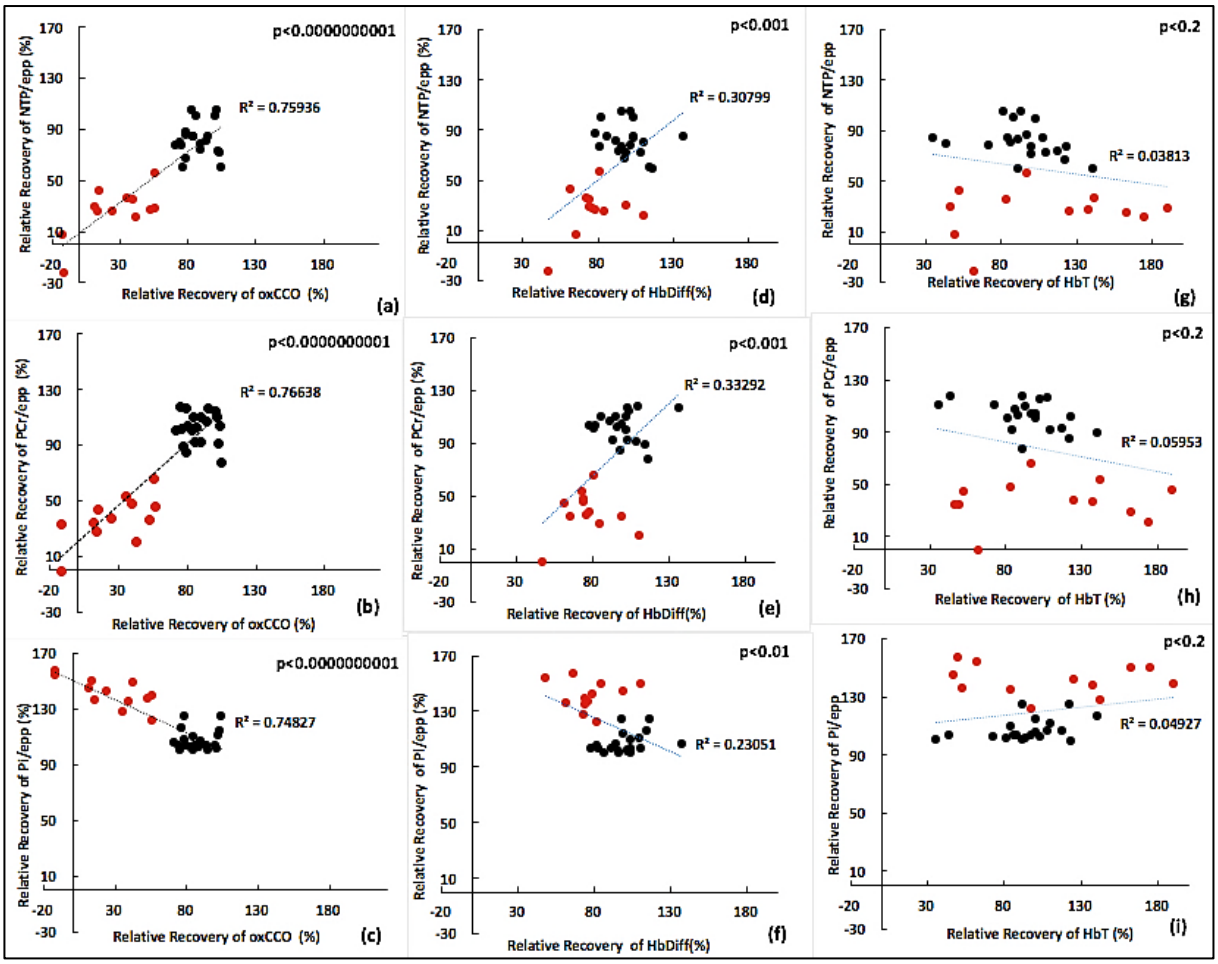

Figure 4.41: Linear regression analysis between the broadband NIRS and ^{31}P-MRS markers for injury severity following HI. Red dots represent the piglets who had a poor recovery following the HI insult and black dots represent the piglets with good recoveries after the HI as measured by ^{31}P-MRS. Plots a, b and c explain the correlation between the recovery fraction of Δ[oxCCO] with the MRS markers for injury severity and a highly significant strong linear correlation is demonstrated. Plots d, e and f indicate that there is a mild linear relationship between the blood oxygenation (Δ[HbDiff]) with ^{31}P-MRS markers for injury severity. Plots g, h and I show that there is no association between the total blood volume (Δ[HbT]) and the MRS markers for injury severity.

Table 4.4: Sensitivity specificity analysis showing the most efficient cut-off point for separating good and poor outcomes one hour after HI

AUC	S.E.	95% C.I.		Comment
0.99280	0.01773	0.95805	1.00000	Excellent test

Standardized AUC	1-tail p-value	
27.8002	0.0000e+00	The area is statistically greater than 0.5

ROC CURVE DATA

Cut-off	Sensitivity	Specificity	Efficiency
-11.00	0.0000	1.0000	0.6250
12.00	0.1667	1.0000	0.6875
13.00	0.2500	1.0000	0.7188
15.00	0.3333	1.0000	0.7500
25.00	0.4167	1.0000	0.7812
35.00	0.5000	1.0000	0.8125
40.00	0.5833	1.0000	0.8438
43.00	0.6667	1.0000	0.8750
52.00	0.7500	1.0000	0.9062
56.00	0.8333	1.0000	0.9375
71.00	1.0000	1.0000	1.0000
74.00	1.0000	0.9500	0.9688
75.00	1.0000	0.9000	0.9375
76.00	1.0000	0.8500	0.9062
79.00	1.0000	0.8000	0.8750
83.00	1.0000	0.6500	0.7812
84.00	1.0000	0.6000	0.7500
85.00	1.0000	0.5500	0.7188
86.00	1.0000	0.5000	0.6875
89.00	1.0000	0.4500	0.6562
94.00	1.0000	0.3500	0.5938
95.00	1.0000	0.3000	0.5625
100.00	1.0000	0.2500	0.5312
101.00	1.0000	0.2000	0.5000
102.00	1.0000	0.1500	0.4688
103.00	1.0000	0.1000	0.4375
104.00	1.0000	0.0500	0.4062
105.00	1.0000	0.0000	0.3750

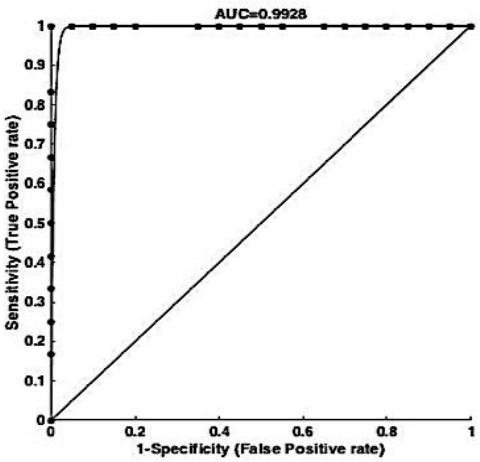

4.5 Discussion

In this study, we investigated whether broadband NIRS as a non-invasive bedside technique can be used to predict the outcome of piglets with induced Hypoxic-Ischaemic brain injury. Changes in [HHb], [HbO_2] and [oxCCO] were quantified through real-time measurement of optical pathlength at 840 nm using second differential of water absorption spectrum and assuming 85% of water concentration in piglet's brain as described in 3.4.4. [22]. Our results suggested that the pathlength during insult does not majorly change, meaning that the broadband-oxCCO measurement is not an artefact of changes in optical pathlength [11]. The residual analysis for 2- and 3-chromophore fit also showed that the oxCCO measurement is not simply an artefact of the larger haemoglobin signals, as the residuals from the 2-chromophore fit (HHb and HbO_2) had a well-defined shape similar to the specific extinction coefficient spectrum of oxCCO. The broadband NIRS measurements of Δ[HbT], Δ[HbDiff] and Δ[oxCCO] were compared with the ^{31}P-MRS metabolites measurement, NTP/epp, PCr/epp and Pi/epp, which are involved in ATP synthesis and

their measurement have shown to be a reliable marker for the severity of injury severity after HI [4], [7]. The recovery fraction (RF) algorithm was developed to quantify the severity of injury through investigating the relationship between the broadband NIRS measurements with the ^{31}P-MRS metabolites and outcome of the piglets following HI. Therefore, considering the negligible variation in pathlength during the course of each experiment, the RF of the Δ[oxCCO] signal might provide a pathlength-free quantification technique as measuring true optical pathlength in highly scattering media is very challenging.

The recovery fractions of the NIRS measurements in 32 piglets were compared against the recovery fractions of ^{31}P-MRS measurements using correlation and regression analysis. As seen in Table 4.3, there is a strong significant correlation between the recovery fraction of Δ[oxCCO] with NTP/epp, PCr/epp and Pi/epp (0.9, 0.9 and -0.9 respectively, $p<0.000001$). The negative correlation of Δ[oxCCO] with Pi/epp is due to the recovery fraction being calculated with respect to baseline, so a higher recovery fraction of Pi/epp indicates an elevated Pi level which did not go back to baseline. An elevated Pi level is a characteristic of a hypoxic-ischaemic brain injury (Figure 4.26). There was no correlation between the recovery fractions of Δ[HbT], blood volume, and ^{31}P-MRS metabolites and there was only a mild to moderate correlation between the recovery fraction of (Δ[HbDiff], blood oxygenation) with MRS metabolites [NTP/epp=0.6, PCr/epp=0.6 and Pi/epp=-0.5, $p<0.005$]. This could be due the fact that in the injured brain following HI, mitochondrial metabolism is more dependent on vascular oxygenation [24]. Linear regression analysis between the recovery fraction of Δ[oxCCO] and ^{31}P-MRS metabolites revealed that the recovery fractions of Δ[oxCCO] has the highest linear correlation with PCr/epp (R^2 =0.77). This can be explained by the fact that both Δ[oxCCO] and PCr are direct markers for oxygen metabolism and their reduction during HI is an indication of anaerobic condition. As reported previously by Bainbridge et al., PCr depletes prior to NTP (ATP) at the start of HI, because it starts donating high energy phosphates to ADP in order to produce ATP anaerobically, and that is why NTP is maintained for a short time after HI initiates [4]. Also, the reduction of Δ[oxCCO] at the beginning of HI indicates an impaired oxygen metabolism in the mitochondria. This is again in agreement with what was previously reported by Bainbridge in 2014. Investigating the dynamics of Δ[oxCCO] and MRS metabolites demonstrated that the depletion of

Δ[oxCCO] during HI in new-born pigs had no correlation with the depletion of NTP/epp [4]. However, there is still a high linear association between the recovery fractions of Δ[oxCCO] and NTP/epp (R^2=0.76) as seen in

Figure **4.41**. This shows that the oxCCO signal recovery fraction has a strong correlation with both oxygen availability and ATP synthesis in the mitochondria. Furthermore, sensitivity and specificity analysis with 99% accuracy (Area Under the Curve= 0.99) shows that the recovery fraction of Δ[oxCCO] can be used as a predictive marker for early injury severity following HI with a cut-off point of 71% between poor and good outcomes which is 100% sensitive, specific and efficient. Our results suggest that the recovery fraction of Δ[oxCCO] signal precisely reflects oxygen metabolism and ATP production at cellular level and explains the function of mitochondrial electron transport chain during and after hypoxic-ischaemic insult in piglet's brain. Moreover, this quantification technique has the capacity of evaluating metabolic response independent of optical pathlength.

4.6 Summary

In this chapter, we investigated the physiological information that the broadband NIRS-Δ[oxCCO] measurement can deliver as a marker for CNS tissue metabolism, through its correlation with measurements of mitochondrial energetics provided by ^{31}P-MRS as a gold standard technique for assessing brain injury. The Δ[oxCCO] measurement produced by UCL1 was validated through residual analysis and it was demonstrated that it was not simply a cross-talk artefact from the much larger haemoglobin signals. The recovery fraction of Δ[oxCCO] (%) showed to be a robust quantification technique to evaluate the outcome following the induced hypoxic ischaemic brain injury in piglets, since it is normalised to the nadir/peak points during HI and does not depend on small variations in pathlength (demonstrated through pathlength analysis) during the measurement period. This technique allowed defining a threshold value for Δ[oxCCO] signal with high sensitivity and specificity to distinguish between poor and good outcomes following HI.

Our results suggest that the broadband NIRS measurement of Δ[oxCCO] is a reliable indicator of mitochondrial metabolism and can be used as a cheap, non-invasive and bed/cot/pod side technique alternative to ^{31}P-MRS.

Bibliography

[1] J. Bryce, C. Boschi-Pinto, K. Shibuya, and R. E. Black, "WHO estimates of the causes of death in children.," *Lancet (London, England)*, vol. 365, no. 9465, pp. 1147–52, Jan. 2005.

[2] S. A. Zanelli, D. A. Kaufman, and D. P. Stanley, "Hypoxic-Ischemic Encephalopathy: Practice Essentials, Background, Pathophysiology," *Medscape*, 2015. [Online]. Available: http://emedicine.medscape.com/article/973501-overview. [Accessed: 14-Jun-2015].

[3] N. Nagdyman, W. Kömen, H. K. Ko, C. Müller, and M. Obladen, "Early biochemical indicators of hypoxic-ischemic encephalopathy after birth asphyxia.," *Pediatr. Res.*, vol. 49, no. 4, pp. 502–506, 2001.

[4] A. Bainbridge, I. Tachtsidis, S. D. Faulkner, D. Price, T. Zhu, E. Baer, K. D. Broad, D. L. Thomas, E. B. Cady, N. J. Robertson, and X. Golay, "Brain mitochondrial oxidative metabolism during and after cerebral hypoxia-ischemia studied by simultaneous phosphorus magnetic-resonance and broadband near-infrared spectroscopy," *Neuroimage*, vol. 102, no. P1, pp. 173–183, 2014.

[5] R. Wootton, P. A. Flecknell, and M. John, "Accurate measurement of cerebral metabolism in the conscious, unrestrained neonatal piglet: I. blood flow," *Neonatology*, vol. 41, no. 5–6, pp. 209–220, 1982.

[6] P. Mandel and P. Mandel, "Free Nucleotides In The Rat Brain During Post-Natal Development," vol. 13, pp. 591–595, 1966.

[7] E. B. Cady, O. Iwata, A. Bainbridge, J. S. Wyatt, and N. J. Robertson, "Phosphorus magnetic resonance spectroscopy 2 h after perinatal cerebral hypoxia-ischemia prognosticates outcome in the newborn piglet," *J. Neurochem.*, vol. 107, no. 4, pp. 1027–1035, Oct. 2008.

[8] L. S. De Vries and F. Groenendaal, "Patterns of neonatal hypoxic-ischaemic brain injury," *Neuroradiology*, vol. 52, no. 6, pp. 555–566, 2010.

[9] P. L. Hope, E. B. Cady, P. S. Tofts, P. A. Hamilton, A. M. D. Costello, D. T. Delpy, A. Chu, E. O. R. Reynolds, and D. R. Wilkie, "Cerebral Energy-Metabolism Studied with Phosphorus Nmr-Spectroscopy in Normal and Birth-Asphyxiated Infants," *Lancet*, vol. 2, no. 8399, pp. 366–370, 1984.

[10] D. Azzopardi, J. Wyatt, E. Cady, J. Delphy, DT, Baudin, and A. Stewart, "Prognosis of newborn infants with hypoxic-ischemic brain injury assessed by phosphorous magnetic resonance spectroscopy," *Pediatr. Res.*, vol. 25, no. 5, pp. 445–51, 1989.

[11] C. E. Cooper and R. Springett, "Measurement of cytochrome oxidase and mitochondrial energetics by near-infrared spectroscopy.," *Philos. Trans. R. Soc. Lond. B. Biol. Sci.*, vol. 352, no. 1354, pp. 669–676, 1997.

[12] C. E. Cooper, M. Cope, V. Quaresima, M. Ferrari, E. Nemoto, R. Springett, S. Matcher, P. Amess, J. Penrice, L. Tyszczuk, J. Wyatt, and D. T. Delpy, "Measurement of cytochrome oxidase redox state by near infrared spectroscopy.," *Adv. Exp. Med. Biol.*, vol. 413, pp. 63–73, 1997.

[13] E. Cady, J. Wyatt, Y. Takei, A. Lorek, C. Cooper, A. Edwards, S. Roth, D. Peebles, R. Aldridge, M. Wylezinska, D. Delpy, and E. Reynolds, "Cerebral energy failure secondary to acute hypoxia-ischaemia in the newborn pig studied by 1H magnetic resonance spectroscopy.," *Soc. Magn. Reson. Med. 12th Annu. Meet. New York, USA.. (pp. p. 1502).* , 1993.

[14] E. B. Cady, A. Lorek, J. Penrice, M. Wylezinska, C. E. Cooper, G. C. Brown, H. Owen-Reece, V. Kirkbride, J. S. Wyatt, and E. Osmund, "Brain-metabolite transverse relaxation times in magnetic resonance spectroscopy increase as adenosine triphosphate depletes during secondary energy failure following acute hypoxia-ischaemia in the newborn piglet.," *Neurosci. Lett.*, vol. 182, no. 2, pp. 201–4, Dec. 1994.

[15] A. Lorek, Y. Takei, E. B. Cady, J. S. Wyatt, J. Penrice, A. D. Edwards, D. Peebles, M. Wylezinska, H. Owen-Reece, and V. Kirkbride, "Delayed ("secondary") cerebral energy failure after acute hypoxia-ischemia in the newborn piglet: continuous 48-hour studies by phosphorus magnetic resonance spectroscopy.," *Pediatr. Res.*, vol. 36, no. 6, pp. 699–706, Dec. 1994.

[16] S. J. Matcher, C. E. Elwell, C. E. Cooper, M. Cope, and D. T. Delpy, "Performance Comparison of Several Published Tissue Near-Infrared Spectroscopy Algorithms," *Analytical Biochemistry*, vol. 227, no. 1. pp. 54–68, 1995.

[17] V. Quaresima, R. Springett, M. Cope, J. T. Wyatt, D. T. Delpy, M. Ferrari, and C. E. Cooper, "Oxidation and reduction of cytochrome oxidase in the neonatal brain observed by in vivo near-infrared spectroscopy," *Biochim. Biophys. Acta - Bioenerg.*, vol. 1366, no. 3, pp. 291–300, 1998.

[18] C. E. Cooper, D. T. Delpy, and E. M. Nemoto, "The relationship of oxygen delivery to absolute haemoglobin oxygenation and mitochondrial cytochrome oxidase redox state in the adult brain: a near-infrared spectroscopy study.," *Biochem. J.*, vol. 332 (Pt 3, pp. 627–632, 1998.

[19] R. Springett, J. Newman, M. Cope, and D. T. Delpy, "Oxygen dependency and precision of cytochrome oxidase signal from full spectral NIRS of the piglet brain.," *Am. J. Physiol. Heart Circ. Physiol.*, vol. 279, no. 5, pp. H2202–H2209, 2000.

[20] R. Springett, M. Wylezinska, E. B. Cady, M. Cope, and D. T. Delpy, "Oxygen dependency of cerebral oxidative phosphorylation in newborn piglets.," *J. Cereb. Blood Flow Metab.*, vol. 20, no. 2, pp. 280–9, 2000.

[21] N. J. Robertson and J. Cox, "Magnetic resonance spectroscopy of the neonatal brain," in *MRI of the neonatal brain*, M. A. Rutherford, Ed. W.B. Saunders, 2002.

[22] S. J. Matcher, M. Cope, and D. T. Delpy, "Use of the water absorption spectrum to quantify tissue chromophore concentration changes in near-infrared spectroscopy.," *Phys. Med. Biol.*, vol. 39, no. 1, pp. 177–96, 1994.

[23] M. Essenpreis, M. Cope, C. E. Elwell, S. R. Arridge, P. van der Zee, and D. T. Delpy, "Wavelength Dependence of the Differential Pathlength Factor and the Log Slope in Time-Resolved Tissue Spectroscopy," Springer US, 1993, pp. 9–20.

[24] G. Bale, S. Mitra, J. Meek, N. Robertson, and I. Tachtsidis, "Relationship Between Cerebral Cytochrome-C-Oxidase and Oxygenation is Associated with Brain Injury Severity in Birth Asphyxiated Infants," *Biomed. Opt. 2016*, no. July, p. TM2B.4, 2016.

Chapter 5. Development of a Portable Miniature Broadband-NIRS system: Mini-CYRIL (CYtochrome Research Instrument and appLication)

There is an urgent need for developing a compact portable system for in-vivo monitoring of oxygenation and metabolism, with better interface at bed/cot side that can be easily adopted by clinicians and without the need for daily calibration or complicated setups by physicist or engineers. This chapter describes the development of a novel portable broadband-NIRS system called mini-CYRIL 'Cytochrome Research Instrument and appLication' based on easily sourced components; "off-the-shelf" miniature light source and spectrometers by Ocean Optics. Specifically, in this chapter, challenges with miniaturisation of broadband-NIRS will be discussed and the possible solutions will be examined. The finalised mini-CYRIL system will be characterised and validated through phantom and in-vivo studies**.**

Miniature spectrometers used for broadband-NIRS have been described in chapter 3 (3.5.2) and it was mentioned that QE65000 has been modified and used by Lawson Health Research Institute in Canada for deep tissue spectroscopy [1]–[3]. However, there are some hardware and software issues concerning the utilisation of miniature spectrometers to be made into a clinical system, which have not been addressed in the literature. These include (a) Hardware issues (i) larger source-detector separations that enables probing deeper layers of the brain which is more sensitive to CCO changes [4] (ii) use of large numerical aperture (NA) detector fibres (>0.54) which are crucial to broadband-NIRS measurement (especially for large source-detector separations to ensure efficient light collection), but are incompatible with the small throughput design of the miniature spectrometers allowing the collimated light through to enhance the signal to noise ratio. (b) Software issues (i) absence of on-board data processing to quantify changes in tissue concentration of HHb, HbO_2 and oxCCO, (ii) real-time estimation of optical pathlength which improves the measurement accuracy and ensures that there are no large changes in pathlength during the measurement that could affect the oxCCO measurement (section 3.3). (iii) Absence of useful measures for clinicians to assist with the diagnosis or directing

treatment strategies. Other necessary considerations for the miniature broadband-NIRS systems to be used in clinical settings including cost effectiveness and easily replicability are also considered in the development of the miniature system for in-vivo measurement of tissue oxygen delivery and utilisation in this chapter.

The miniature system is primarily aimed to replace the UCL1 broadband-NIRS system developed and used by Springett and colleagues (explained in chapter 4) in the preclinical study of HI [5].

To compare the performance of the miniature system, experiments and measurements have been carried out using the same set up and protocol. This approach provides more robust information without having to deal with the interference between two instruments (that happens during simultaneous measurement). The input to the instruments are independent and any attempt to merge them, will significantly affect the performance of both systems, as they will not be able to operate in their normal condition. This is also true when trying to merge the detector fibres of the detection units of the miniature system and UCL1 to perform simultaneous measurement, as they have significantly different characteristics in terms of slit size and light throughput specification.

5.1 Hardware Development: Customisation of Miniature Light Source and Spectrometer

Mini-CYRIL is primarily a single channel broadband-NIRS system which uses a miniature light source, a miniature spectrometer and optical fibres which are adapted to the specific application and the tissue under examination. Different components and characteristics of mini-CYRIL's hardware are described in this section. The performance of mini-CYRIL's components are compared against the corresponding parts of the UCL1 unit which was developed by Springett et al and described in chapter 4 [5].

5.1.1 Miniature Light Source

Important considerations for choosing a light source for broadband-NIRS were described in 3.4.1. Thermally stabilised white light sources based on quartz tungsten halogen lamp (QTH) are the most commonly used sources for broadband NIRS measurement due to generating smooth high-intensity spectra covering the visible and

NIR region (Chapter 3, Figure 3.18). Mini-CYRIL uses a white light source (HL-2000-HP) based on 20 W Tungsten Halogen lamp by Ocean Optics, which is compact and small (6.2 cm ×6 cm × 15 cm), has a low output power (8 mW through 600 µm fibre integrated between 200-1100 nm) and produces a smooth spectral output in the NIR region as seen in Figure 5.43. This light source have been used by other NIRS measurements for deep tissue spectroscopy in piglets and adults [1]–[3].

5.1.1.1 Spectral Characterisation of HL-2000-HP

HL-2000-FHSA-HP produces light between 360 nm -2400 nm. It includes an integrated filter holder which enables filtering UV for tissue illumination. The miniature light source requires around 5 minutes to stabilise and has a drift of less than 0.1% per hour [6]. Figure 5.42 illustrates different parts of HL-2000-FHSA. Light from the 20 W halogen-tungsten lamp can be further filtered and focused onto the SMA connector to be coupled into the optical fibre.

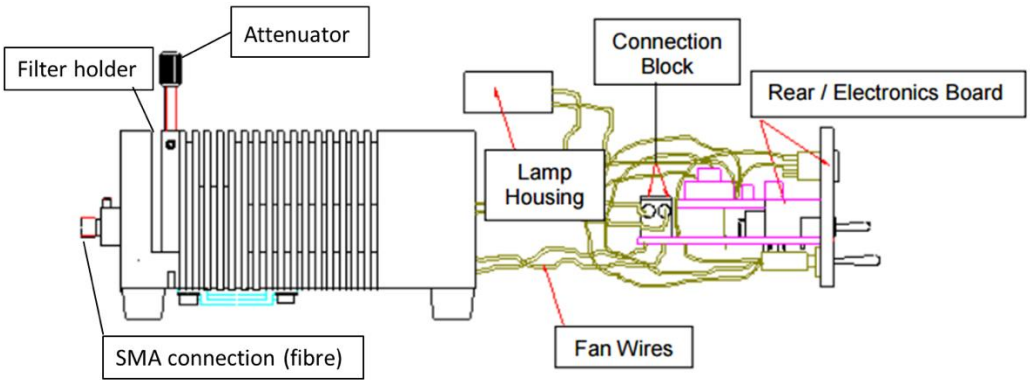

Figure 5.42: Schematic diagram of HL-2000-FHSA. Image modified from [6].

The light source is equipped with an on/off switch as well as an open/close shutter switch. As seen in Figure 5.42, the intensity of light can be adjusted for different applications or source-detector spacing using the attenuator screw.

Figure 5.43 shows the spectral output from the miniature light source, measured using a poster tube as explained in section 5.3 (Figure 5.79) and compares it with the spectral output produced using the same method by Oriel light source from UCL1(explained in chapter 4).

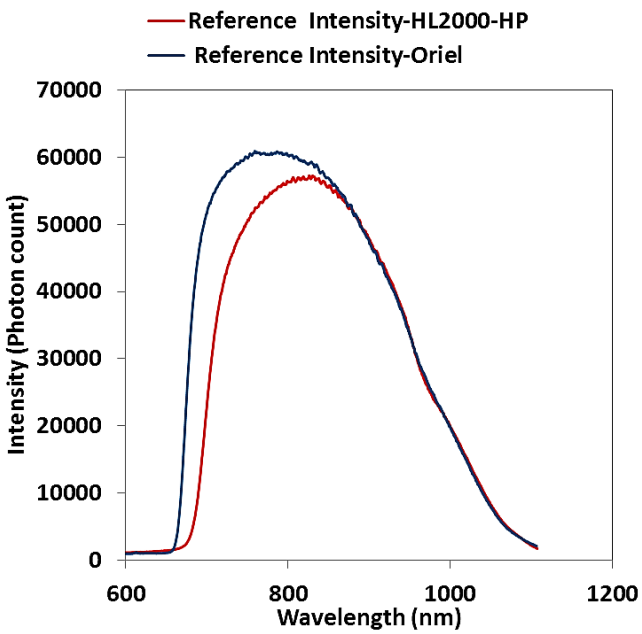

Figure 5.43: Spectra data measured through a poster tube (reference measurement) and Ventana spectrometer from the miniature source, HL-2000-FSHA-HP, and Oriel light source. The integration time is 100 ms

As displayed in Figure 5.43, the spectrum produced by the miniature spectrometer, in red, is comparable to the one produced by Oriel which is the standard white light source for broadband-NIRS applications in piglets and babies [5], [7]–[9]. Figure 5.44 shows the transmission intensity spectra through a piglet's head (source-detector: 4.5 cm) using the HL-2000-HP and the Oriel light source with the same detection unit. The spectra produced by the miniature source are almost comparable to the standard light source which shows the suitability of HL-2000-HP for broadband-NIRS applications. The peak count produced by the miniature light source through piglet's brain is around 12% less than that produced by the Oriel source. This could partly be due to the smaller core diameter of the source fibre (2.3 mm) customised for the miniature source (SMA limited), compared to the fibre adapted for the Oriel source (3.3 mm).

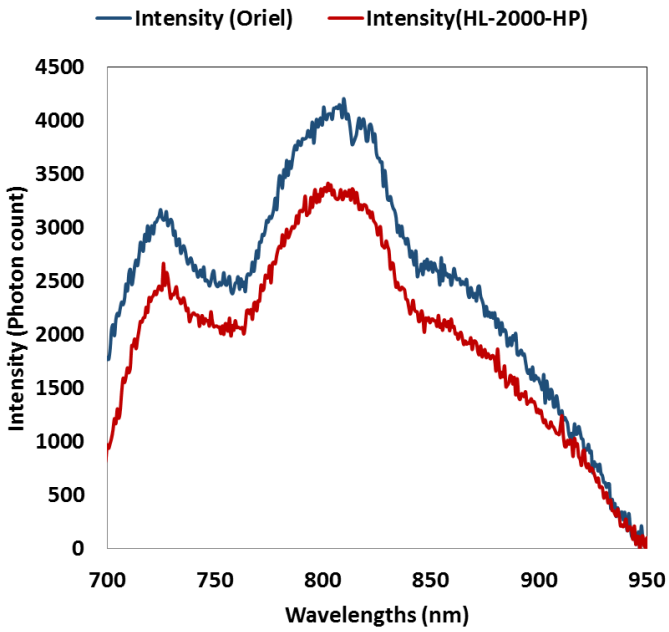

Figure 5.44: Transmission intensity spectra through piglet's head (source-detector 4.5 cm) produced by mini-CYRIL's light source (HL-2000-HP) and UCL1's light source (Oriel 77501). 10 s acquisition time.

5.1.1.2 Power Output and safety measures

The radiation used in broadband-NIRS is considered safe if the intensity is below which would cause tissue damage due to thermal heating. Being thermally stabilised, the light source uses a 20 W halogen-tungsten lamp with an integrated UV filter for protection against skin damage. The average power is 8 mW across all wavelengths. Considering that the diameter of the source fibre is 2.3 cm (spot size) hence the area being 4.15 cm^2, the power per unit area at tissue surface becomes 1.92 mW/cm^2, which is far less than the average power delivered by the entire NIR part of the sunlight on a sunny day that is more than 10 mW/cm^2 [10] , [11] . It should be noted that in broadband-NIRS, non-coherent white light is coupled into highly diverging large numerical aperture optical fibres (NA=0.57; 2θ ~70°), hence the irradiance becomes much lower as light travels through the tissue.

5.1.2 Optical Fibres

The source and detector optical fibres were identical bundles and custom-built by Loptek (Germany) with high NA (0.57) for maximum illumination and light collection. The fibres were made with a 90-degree bend at head end to ensure efficient light collection from the tissue surface. The core diameter is 2.3 mm to match the SMA

connection and both fibres were magnet compatible and 7 m long to enable simultaneous MRS measurements when needed (Figure 5.45).

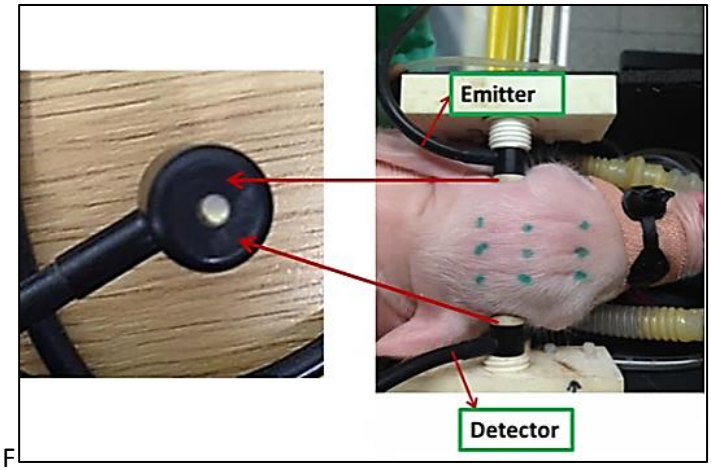

Figure 5.45: Magnet compatible NIRS-optodes fixed in optode holders placed on the sides of the piglet's head within a stereotactic frame.

5.1.3 QE65 Pro Miniature Spectrometer

As well as its small size (182×110×47 mm^3) and light weight (< 1 kg), QE65 Pro has interesting features such as high sensitivity and low noise, due to the back-thinned CCD detector which is thermoelectrically cooled (TEC) down to -15° C, high dynamic range (25000:1) and high signal to noise ratio (1000:1). These characteristics (Table 5.5) are specifically interesting for broadband-NIRS because of working with highly diffused low light levels.

The previous version of QE65 Pro, called QE65000, has been customised by Lawson Health Research Institute for deep tissue spectroscopy [1]. In this thesis, we looked at this spectrometer as a potential solution for the mini-CYRIL system. Table 5.5 compares some of the spectroscopic and detector specifications of the QE65 Pro with UCL1's detection unit (SPEX270M) that was explained in chapter 4, and used in the preclinical study of neonatal HI [5].

The optical bench of QE65 Pro is illustrated in Figure 5.46. Light from the detector fibre is coupled into the spectrometer through a rectangular slit (2) located directly behind a 905 SMA connector (1) which secures the input fibre to the spectrometer. It then passes through a bandpass filter (3) before entering the optical bench to only allow certain range of wavelengths into the optical bench (between 700-

1050 nm for this application). Like most miniaturised spectrometers, the optical bench of a QE65 Pro has symmetrical Crossed Czerny Turner design (section 3.4.3) that provides a flattened spectral field with very little distortion [12], [13]. Light entering the optical bench is focused onto the gratings (5) using a collimating mirror (4) and it is then focused onto the back-thinned CCD (7) using a focusing mirror (6).

Table 5.5: Comparison between the spectroscopic and detector specification of the custom-made and miniature spectrometer

Spectroscopic Specification	**QE65 Pro**	**SPEX270M**
Gratings	600 gr/mm	300 gr/mm
Entrance Slit Aperture	200 μm	400 μm
Optical Resolution (FWHM)	~ 3.5 nm	~ 5 nm
Detector type	Integrated CCD Hamamatsu S7031-1006 Back-Thinned /Low Etaloning /cooled	Wright Instruments CCD Cooled, Front-illuminated
Spectral Range	200-1100 nm	650-980 nm
Signal to Noise Ratio	1000:1	100:1

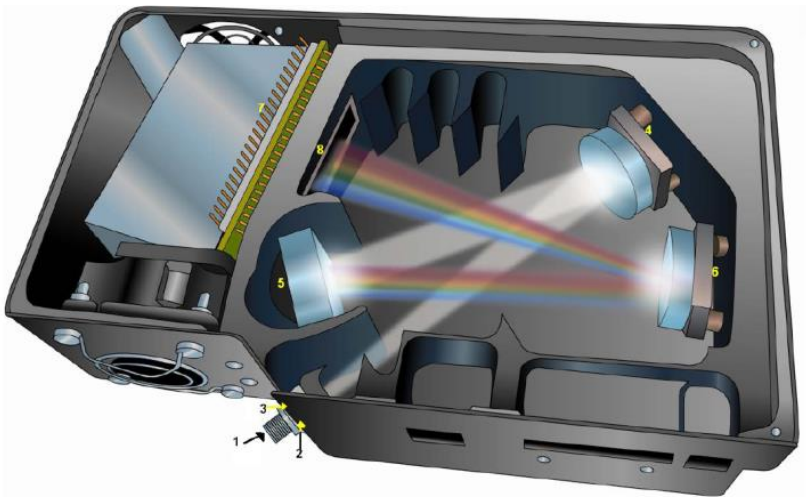

Figure 5.46: Optical Bench of the QE65 Pro. Image taken from [13].

The detector used in QE65 Pro is a 2D array back-thinned Charged Coupled Device (CCD) by Hamamatsu S7031-1006 with 90% peak quantum efficiency which is 50% higher than in typical front-illuminated CCDs (Figure 3.24). The small pixel size (24 μm^2) and the reduced etaloning back-illuminated design leads to increased sensitivity, specifically in the NIR wavelengths.

5.1.3.1 Characterisation of QE65 Pro

To investigate the thermal noise and dark count of the CCD detector, Intensity data (photon count) were acquired for 9 hours with the slit of the spectrometer closed and the thermoelectric cooling (TEC) was on. Dark count distribution between 780-900 nm (range of interest for broadband-NIRS measurement, section 3.3.) and the change in the intensity of individual wavelength over time were investigated.

The dark intensity measurement across 780-900 nm is presented in Figure 5.47 (a). The distribution has a flat shape with no prominent features and low intensity value as expected when there is no light input into the spectrograph. The mean dark intensity across all the wavelengths at time zero is 29.3 ± 5.8 and after 9 hours is 27.3 ± 5.6 counts. Figure 5.47 (b) shows the intensity change at one wavelength over time (λ = 780 nm). The intensity change has a mean value of 25 ± 2 counts over 9 hours and the small standard deviation indicates that there is no major change in the dark intensity at 780 nm. The dark noise of this spectrometer is significantly low and stable due to the on-board TEC.

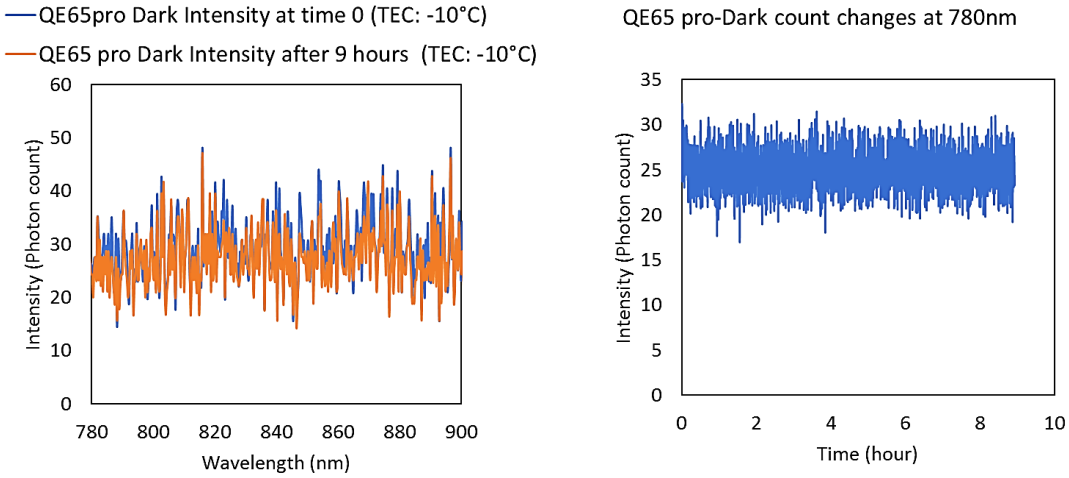

Figure 5.47: a) The dark intensity spectrum measured every second when the spectrometer's slit is closed and TEC is on at time zero and after 9 hours. (b) The dark intensity changes at wavelength 780 nm over time during the test. Acquisition time is 10 seconds.

5.1.4 Use of QE65 Pro-based Mini-CYRIL in Piglet Brain Measurement

Due to its favourable properties and most importantly its high sensitivity and low dark noise, which is ideal for low-level light detection, QE65 Pro was examined for the NIRS measurements in the piglet study (chapter 4). The following graphs compares the NIR transmission spectra acquired using Oriel light source with the QE65 Pro (Figure 5.48 (a)) and SPEX270M (Figure 5.48 (b)) through 2.3 mm and 3.3 mm diameter detector fibre bundles respectively. The total illumination power and the integration time for both systems were the same (0.2 W/nm and 10 seconds).

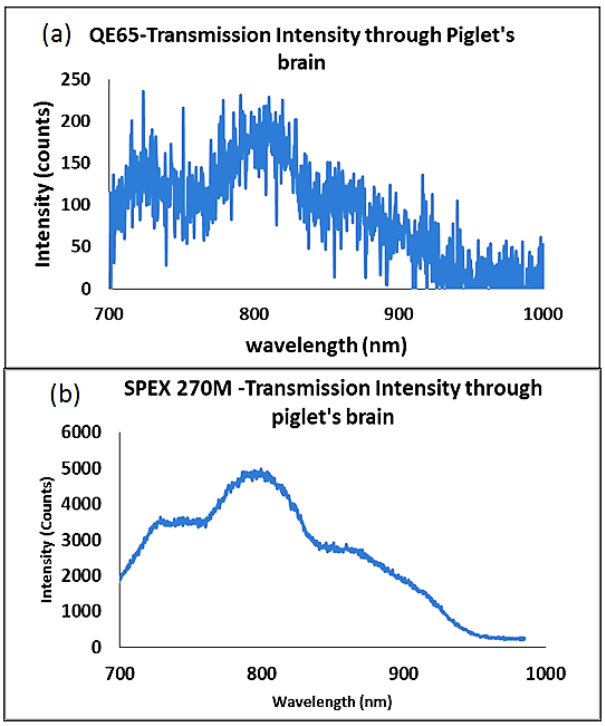

Figure 5.48: (a) Intensity data through a piglet's brain using Oriel 77501 light source and QE65 Pro spectrometer. (b) Intensity data through the same piglet's Brain using Oriel 77501 light source and SPEX 270M from UCL1. source-detector spacing 4.5 cm

Despite its high sensitivity and higher SNR (Table 5.5), the QE65 Pro demonstrated poorer performance than the SPEX270M (~ 20 times lower number of peak counts). The important factors contributing to this large amount of photon loss and noise in QE65 Pro were investigated and are summarised below:

1- **Low irradiance at the slit:** The first place where photons are lost before entering the optical bench of the spectrometer is at the entrance slit. The 2.3 mm diameter circular core of the detector fibre bundle overfills the rectangular

entrance slit of the spectrometer (0.2 × 1 mm), which significantly reduces the intensity of light entering the spectrometer (Figure 5.49).

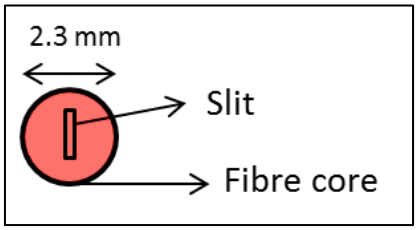

Figure 5.49: Schematic of the detector fibre end, directly at the entrance slit of the miniature spectrometer which leads to larger image size and lower irradiance at the slit.

2- **Large acceptance cone of the detector fibre against the small throughput of the spectrometer:** The large numerical aperture of the detector fibre (NA=0.57, F/0.8, see equation 3.26), which was designed to enable maximum light collection from the brain due to high attenuation, drastically overfills the small acceptance cone of the spectrometer (NA=0.125, F/4) that was designed to produce a flattened spectral field and enhance the signal to noise (SNR). This intrinsic contrast between the NA of the fibre and the spectrometer results in large amount of stray light inside the spectrometer and poor SNR since most of the light does not reach the CCD (Figure 5.50). The amount of photon loss because of NA mismatch, calculated based on equation 3.24 in chapter 3 (section 3.4.2.3), is around 1300%.

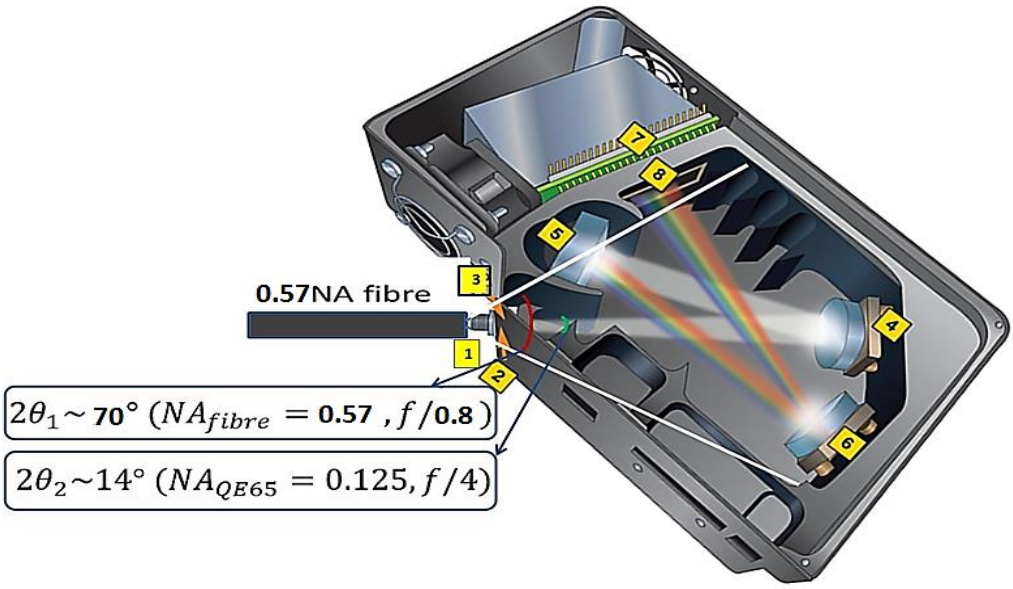

Figure 5.50: F-Number mismatch between the detector fibre bundle (NA=0.57) and QE65 Pro (f/4, NA=0.125) leading to photon loss and stray light generation inside the spectrometer (poor SNR).

5.1.5 Modification of QE65 Pro for Enhancing the Performance

This section illustrates the solutions that were investigated and examined in this thesis towards tackling the throughput issue when using miniature spectrometers for deep tissue spectroscopy using broadband-NIRS. These solutions are summarised as follows and are described in detail.

1- **F-matching** to compensate for the large f-number (NA) mismatch between the detector fibre (F/0.8) and spectrometer (F/4).
2- **Modifying detector fibre's geometry** to compensate for the small irradiance at the slit through minimising the mismatch between rectangular slit of the spectrometer and circular configuration of the fibre end.
3- **Utilising a miniature spectrometer with lower f-number** to enhance the light gathering power of the spectrometer $\left(NA = \frac{1}{2f\#}\right)$ hence total light throughput.

5.1.5.1 Improving Throughput through F-matching

The first approach to enhance light throughput was to increase the f-number of the detector fibre bundle using collimating and focusing lenses, so that the light out of the fibre is focused onto the slit of the spectrometer and most of light coming out of the fibre is coupled into the spectrometer (Figure 5.51). It was kept in mind that the compactness and easily application of the system must not be affected by the f-matching modification. The schematic design for f-matching between the 0.57 NA fibre and the 0.12 NA spectrometer is illustrated in Figure 5.52.

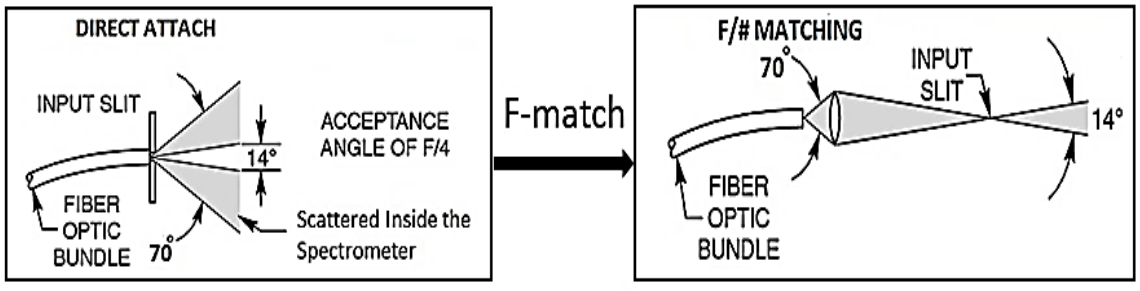

Figure 5.51: Schematic plan for F-matching between the detector fibre and the QE65 Pro. Image modified from
[14]

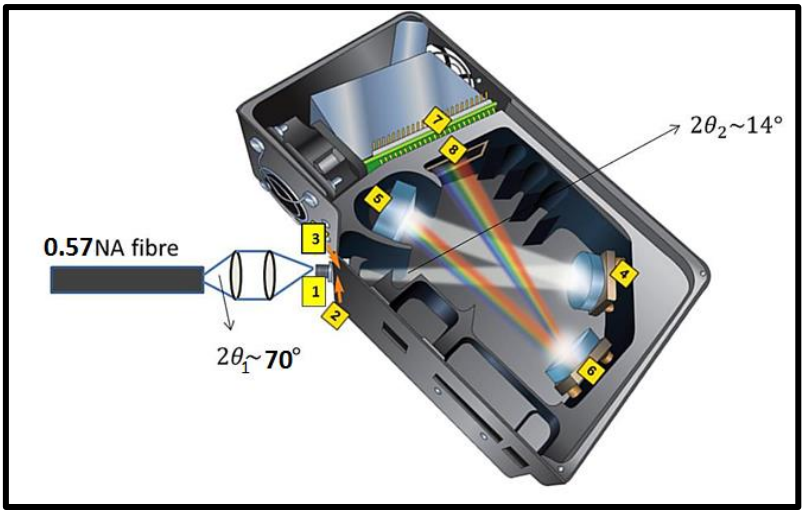

Figure 5.52: Schematic of the f-matching technique between the detector fibre and QE65 Pro. Image modified from [13].

A SMA fibre collimation package by Thorlabs with NA=0.5 and divergence angle of less than 0.09 degrees across the wavelengths of interest was used, which included collimating and focusing optics to solve for highly diverging beams out of the fibre. It was securely mounted on the fibre output through SMA connection and it was followed by a direct-attach single lens from Ocean Optics (74-DA, f/2). The direct-attach lens which was secured on the entrance of the spectrometer through SMA connection (Figure 5.53), was designed to take the collimated light in a straight path of open air and to focus it on to the slit. The fibre was securely mounted on an XYZ translation mount and after the maximum peak counts was displayed (indicative of maximum light coupled into the spectrometer), the position of the focus was fixed using locking screws in three directions as seen in Figure 5.53.

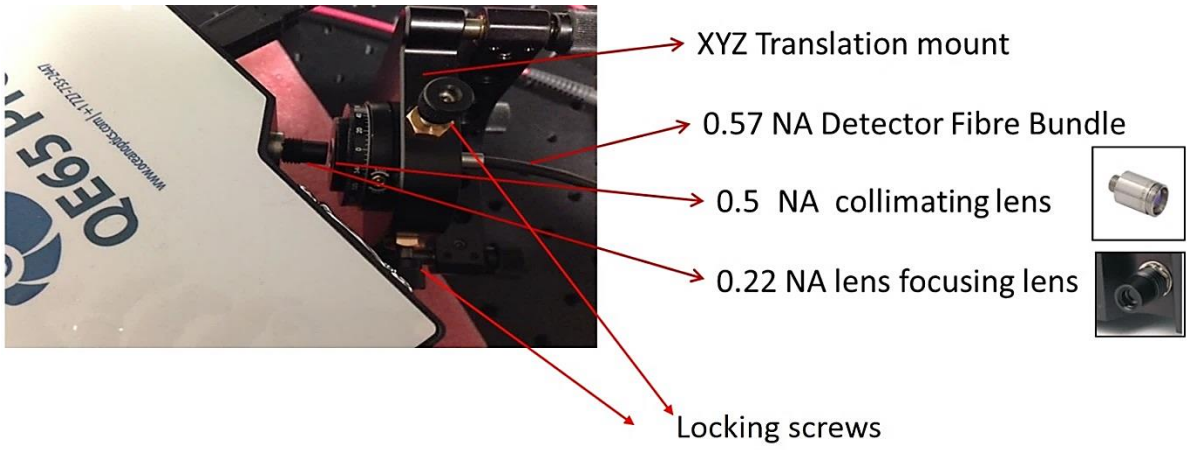

Figure 5.53: F-matching unit at the entrance of the spectrometer using collimating and focusing lenses.

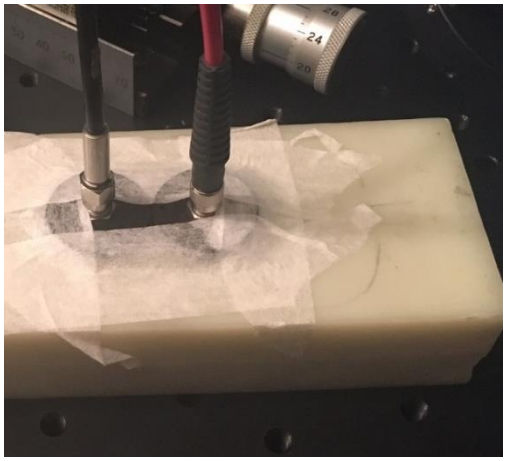

Figure 5.54: Measurement through a tissue-like phantom when the detector fibre was in direct attach position to the QE 65-pro's slit and when f-matching was used, source-detector spacing is 3 cm.

To compare the performance of the modified QE65 Pro with the original settings (fibre directly attached to the slit), a phantom was used and reflectance measurements were acquired using the two setups with the acquisition time of 10 seconds (Figure 5.54).

Figure 5.55 compares the reflectance intensity spectra through the phantom using directly attached and f-matched detector fibre (Source-detector spacing 3 cm). As seen in the figure, f-matching produced a 180% increase in the signal intensity at 780 nm. However, this amount of increase in the signal is not still comparable to the results from the UCL1 system where the transmission spectra through a piglet's head measured using the custom-made (SPEX 270M) spectrometer was more than one order of magnitude larger than that generated using QE65 Pro (Figure 5.48).

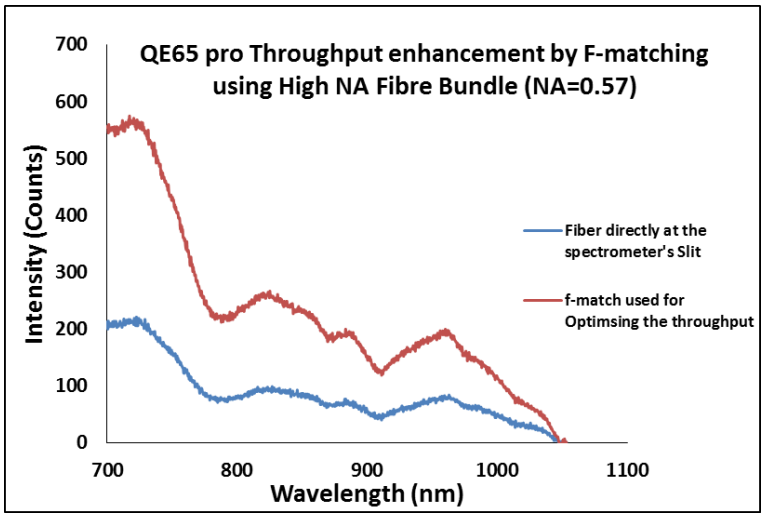

Figure 5.55: Intensity data through a phantom when fibre is directly attached against the slit of QE65 Pro (blue curve) vs. when f-matching unit (Figure 5.53) is used (Orange curve)

F-matching Limitations: Despite the relatively large increase in the signal, QE65 Pro throughput enhancement through f-matching has major limitations for medical applications. First, the total enhancement is not enough for effective use in deep tissue spectroscopy (such as head transmission mode measurement in piglets, where a minimum source-detector spacing of 4 cm is required), Secondly, the technique is practically very challenging when it comes to focusing the white light in the open air onto the slit. Furthermore, although the collimating package theoretically produces a very small divergence in our wavelength range, in practice not only are a considerable number of photons are lost in using ancillary optics, but a perfect collimation and focusing is also impractical when working with broadband light. Therefore, no matter how much the large diameter high NA fibre is successful in collecting light from the brain, most of it is lost at the slit and before entering the spectrometer.

5.1.5.2 Improve Irradiance at the Slit through Modifying Detector Fibre Geometry

The low irradiance at the spectrometer's slit, which was a result of the large size of the core (2.3 mm) against the small slit width (0.2×1 mm) as well as the geometry mismatch between the fibre's circular cross-section and the rectangular slit were another major source of loss in the head transmission mode NIRS measurement. Therefore, changing the configuration of fibres in the bundle at the spectrometer end to mimic the shape of the entrance slit, using a cross-section converter, would greatly improve light coupling efficiency and system throughput without affecting the optical resolution. As can be seen in Figure 5.56, the ideal geometry for the fibre's end at the spectrometer would be a stack of 5 fibres with 0.22 NA and 200 µm core diameter each matching the spectrometer's slit width and height (0.2 × 1 mm).

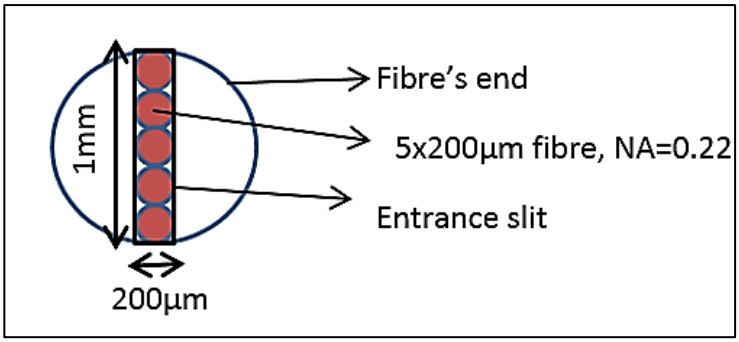

Figure 5.56: The schematic of effective fibre arrangement at the entrance slit of QE65 Pro

Diop et al in 2014 also used a relatively similar design to improve light collection and noise performance of the QE 65000 miniature spectrometer while maintaining the spectral resolution. They custom-built a fibre bundle with 0.22 NA (which matches the NA of the spectrometer) to mimic the shape of the entrance slit and the total signal enhancement that was achieved through this configuration was around 45% for source-detector spacing of 3 cm.

This design requires reducing the core diameter of the detector fibre to 1 mm instead of 3.3 mm core fibre, which was formerly used for the piglet study. Reducing the fibre diameter to less than half of its original size, significantly reduces the amount of light collected from the brain. Also, this type of modification is only beneficial in case of using fibres matching the spectrometer's f-value; otherwise, the stray light interference in the spectrometer still exists. To get all the light into the spectrometer using a large core optical fibre (2.3 mm) with a slit configuration is only useful when an additional lens is used in front of the detector, to focus the light onto the CCD (24 mm width × 1.4 mm height) and prevent the majority of the signal being imaged above and below the CCD array [12]. Placing a lens in front of the CCD is impractical in our experiment because there is no access to the optical bench. Apart from the complications in utilising the slit configuration and practicality issues, a suitable fibre for the QE65 Pro should have a NA of 0.22. These fibres are made of quartz that is much more expensive than the normal glass fibres (~£1000 vs ~£100). In addition, in this application, a 90-degree angle must be made at the end of the fibre for effective light collection from piglet's head (Figure 5.45).

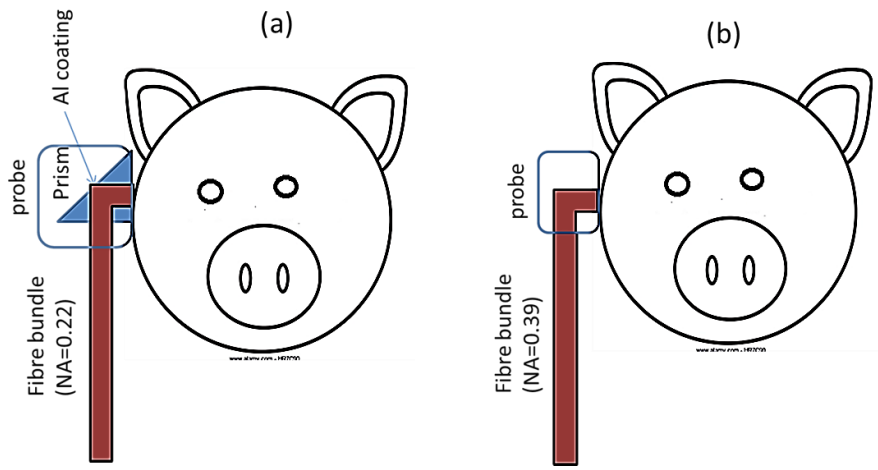

Figure 5.57: Schematic of using a 0.22 NA detector fibre to effectively collect diffused light through the piglet head. An aluminium (Al) coated prism is required to make the 90-degree bend at tissue surface which is not compatible with the strong magnetic fields of MR units.

Due to the small bend radius of quartz made fibres, this is not feasible and the solution would be integrating a magnet compatible prism at the end of the fibre to produce the required 90-degree bend (Figure 5.57 a). This adds to the cost and is not efficient as more ancillary optics results in further loss in the photon count at the detector. After discussions with the fibre manufacturer (Loptek, Germany) about how to modify fibre's geometry so that it will be easily replicable and cost effective without losing so much light (because of the prism), we decided to utilise a fibre with 0.37 NA instead of 0.22 which is very expensive and also significantly reduces the amount of light collected from the tissue surface. The 0.37 NA fibre is in less contrast (compared to 0.57 NA) with the acceptance angle of the QE65 Pro and its fabrication is more cost effective and straight forward. Furthermore, the 90-degree bend could be made without the need for a prism at head end, as can be seen in Figure 5.57 b . Therefore, a 0.37 NA fibre was made and modified to mimic the entrance slit of the QE65 Pro by LOPTEK, Germany.

As can be seen in Figure 5.58, the modified detector fibre with cross-section conversion significantly increased the signal intensity collected from piglet head at source-detector spacing of 4.5 cm (303 ± 56 % across all wavelength, 780-900 nm). There was almost a fourfold increase in the peak intensity at 810 nm, when the diffused light from a piglet's head was collected using the modified fibre (2893 peak count), with slit-configured end and 0.37 NA, compared to when a standard circular-end arrangement detector fibre with 0.57 NA was used (733 peak count). This significant

increase in the signal is associated with both the smaller mismatch between the NA of the detector fibre with the throughput of the spectrometer, and drastically larger irradiance at the spectrometer's slit, due to the fibre's end matching the slit shape.

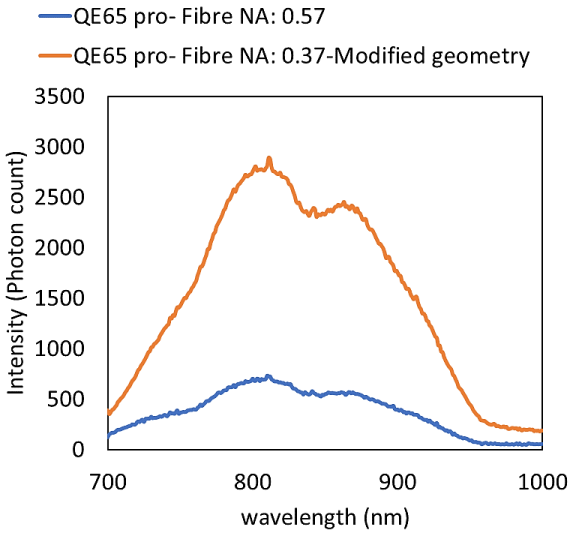

Figure 5.58: Comparison between modified fibre geometry with smaller NA (0.37) to mimic the slit of the spectrometer and using a high NA round configuration fibre end.

Limitations of Modifying detector fibre's geometry:

Modifying detector fibre's geometry could significantly enhance the throughput of QE65 Pro, compared to using a 0.57 NA detector fibre with a f-matching unit. The former caused around 295% peak enhancement in the signal and the latter induced around 180% peak signal increase (Figure 5.58 and Figure 5.55). This technique for throughput enhancement in piglet head transmission measurements (source-detector spacing > 4 cm) has some limitations as the total photon count is still half of the count produced by the UCL1 system and the cost of fibre is also very expensive compared to the standard detector fibres (£1500 vs ~£150).

From all the investigations and experiments to improve the throughput of the QE65 Pro for broadband-NIRS application (in the preclinical study of HI), none could produce a comparable performance to the UCL1 system. That is mainly because of the intrinsic small throughput of the QE65 Pro. The high f-number design in the crossed Czerny-Turner optical bench of most miniature spectrometers, which is essential for minimising the large image aberrations caused by their off-axis geometry, greatly limits the light gathering power of such compact spectrometers [12] and make them specifically inefficient for being used in the brain transmission NIRS applications

regardless of the performed modifications. It is therefore, crucially important to have a large throughput design spectrometer for deep brain tissue spectroscopy.

5.1.6 Low f/# Spectrometer (Ventana)

The next approach in this thesis was utilising a lower f-number miniature spectrometer, as the light collection capability of all spectrometers (Φ_c) is strongly determined by their f-number (f/#) according to equation (5.1).

$$\Phi_c \propto \frac{1}{(f/\#)^2} \tag{5.1}$$

Figure 5.59: Ocean Optics Ventana miniature Spectrometer with enhanced Throughput (F/2)

A low f-number miniature spectrometer from Ocean Optics, Ventana VIS-NIR (Figure 5.59) was used to investigate the role of higher throughput design despite having a lower quantum efficiency CCD, lower SNR and the absence of thermoelectric cooling (Table 5.6 and Table 5.7). The low f/# design (f/2) allows more of the coupled light into the spectrometer and the use of volume phase holographic Grating (VPH) instead of ruled grating (that is used in QE65 Pro) provides maximum diffraction efficiency with low stray light (See 3.4.3). Other spectroscopic and detector specification of the two spectrometers are compared in Table 5.6 and Table 5.7.

Table 5.6: Spectroscopic specification of Ventana vs QE65 Pro spectrometers

Spectroscopic Specification	**QE65 Pro**	**Ventana VIS-NIR**
Gratings	600 gr/mm	450 gr/mm
Entrance Aperture	200 µm × 1 mm	50 µm × 2 mm
Optical Resolution (FWHM)	3 nm	4 nm
Signal to Noise Ratio	1000:1	500:1

Table 5.7: Specification of the CCD in Ventana vs QE65 Pro spectrometers

Detector Specification	**QE65 Pro**	**Ventana VIS-NIR**
Type	CCD-Hamamatsu S7031-1006–Back-Thinned /Low Etaloning/TE Cooler	Hamamatsu S10420-1006 Back-thinned CCD /Low Etaloning/ No cooling
Spectral Range	700-1100 nm	430 – 1100 nm
Pixels	1024×58	1024 ×64
Pixel Size	24 μm^2	14 μm^2
Quantum Efficiency	90% Peak	75% Peak
Dark counts	3 counts RMS	6 counts RMS

Performance of Ventana spectrometer was compared with QE65 Pro, through a reflectance mode phantom measurement (source-detector: 3 cm) using the HL-2000-HP light source and standard 0.57 NA detection fibres.

As can be seen in Figure 5.60, the back-reflected intensity measured through Ventana spectrometer was more than one order of magnitude (peak) higher than what measured using QE65 Pro (it should be mentioned that both signals include the dark count). The higher intensity measured with the Ventana is due to its larger acceptance angel or throughput (f/2, $2\theta c \sim 29^\circ$) compared to QE65 Pro (f/4, $2\theta c \sim 14^\circ$) as well as lower mismatch between the NA of the detector fibre and the f-number of this spectrometer. These factors result in most of the reflected light be coupled light into the spectrometer according to equation 5.1. Please refer to equations 3.23 and 3.26 on chapter 3, for the relationship between NA and θc, as well as NA with f/ number .

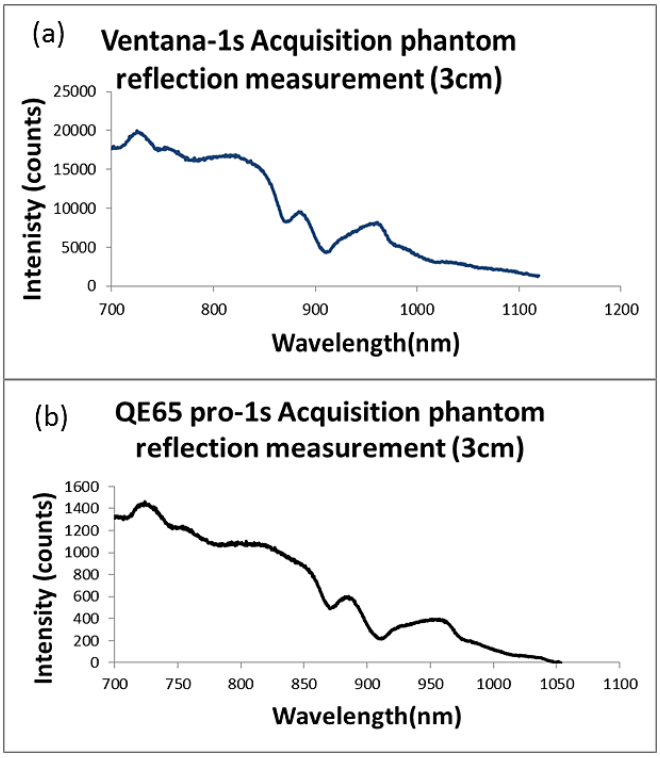

Figure 5.60: Intensity data through a tissue-like phantom (μ_a=0.02, μ_s'=0.9 [mm^{-1} mol^{-1}]) using High NA detector fibre (0.57) with (a) Ventana and (b) QE65 Pro spectrometers

The Ventana spectrometer was then used in a piglet for whole brain transmission mode measurement and its performance was compared with the results produced by the QE65 Pro and two types of fibres (NA=0.57 and modified geometry, NA=0.37). Figure 5.61 shows the intensity measurements through a piglet's brain with source-detector separation of 4.5 cm using different spectrometers and fibres mentioned above. The spectral data generated by Ventana spectrometer produced 7 times higher peak count than QE65 Pro with a circularly arranged optical fibre and around twofold increase compared to when the modified-geometry fibre was used (see Figure 5.61). the percentage increase across all wavelength using Ventana spectrometer (0.57 NA fibre) was 665 ± 146 % compared to using QE65 Pro with 0.57 NA fibre, and 68 ± 22% compared to QE65 Pro with modified 0.37 NA detector fibre. Considering that percentage increase in the signal using Ventana spectrometer (without thermoelectric cooling) was significantly greater than both modifications done to QE65 Pro (5.1.5.1 Improving Throughput through F-match and 5.1.5.2 Improve Irradiance at the Slit through Modifying Detector Fibre Geometry), it was characterised to be used in the mini-CYRIL system for broadband-NIRS brain measurements (specifically for source-detector separations > 4 cm).

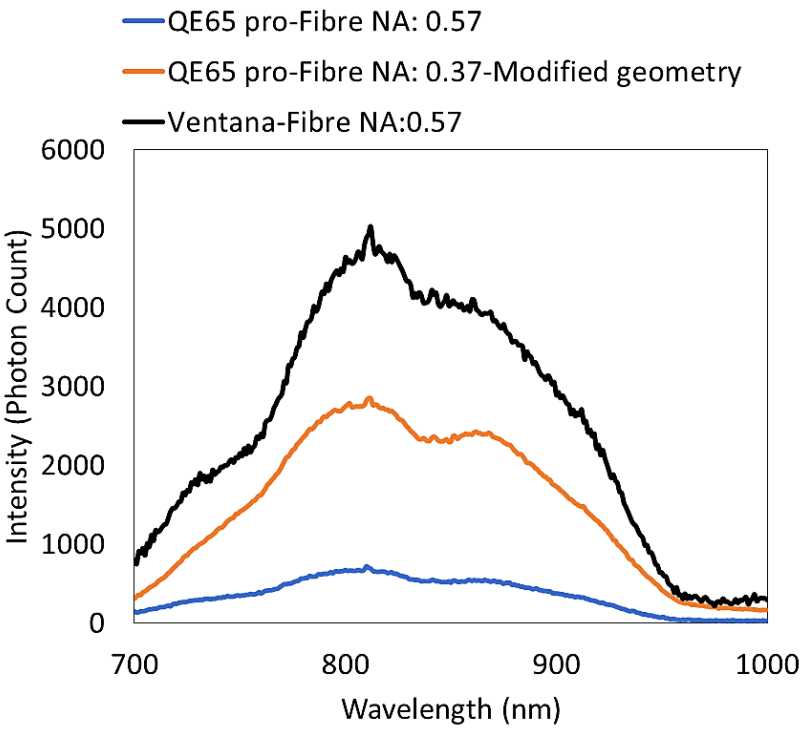

Figure 5.61: Intensity data through piglet's brain (source-detector: 4.5 cm) using High NA detector fibre (0.57) with (a) Ventana and (b) QE65 Pro spectrometers

5.1.7 Characterisation of Ventana Miniature Spectrometer

Ventana spectrometer was characterised for dark count and noise performance. Because the CCD in Ventana spectrometer is not cooled, it is important to evaluate the dark current performance of the system as it linearly increases with temperature [15]. It is also important to investigate the relationship between dark count and the integration time, as typically in broadband-NIRS the acquisition time is increased to improve signal to noise ratio.

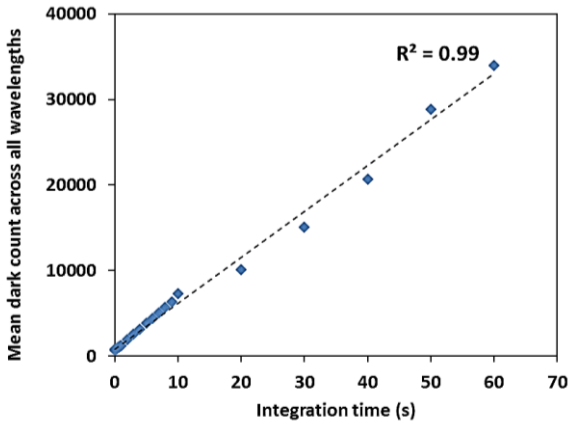

Figure 5.62: Average dark count across all wavelengths (780-900 nm) for different integration times (0.1-60 s)

The association between the dark count and the integration time is seen in Figure 5.62. The coefficient of determination 0.99 shows that the regression line almost perfectly fits the data and the dark noise in Ventana spectrometer linearly increases with increasing acquisition time.

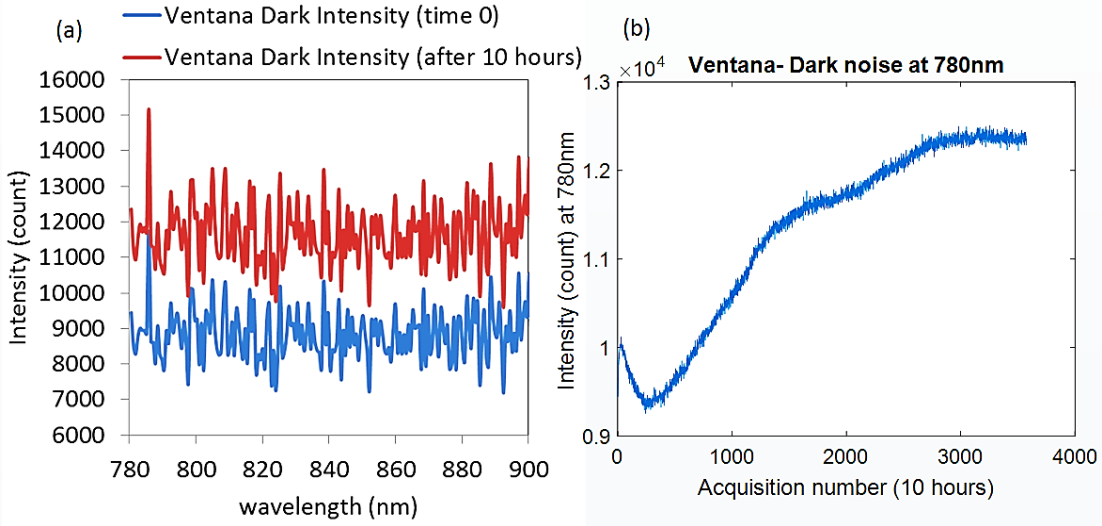

Figure 5.63: (a) Dark intensity spectrum measured every 10 seconds when the spectrometer's slit is closed at time 0 and after 10 hours. (b) The dark intensity changes at wavelength 780 nm over 10 hours.

To investigate the thermal noise and the dark count of the CCD detector in terms of magnitude and stability over time, since long hours NIRS measurement is required for the study of HI in piglets, intensity data (photon count) were acquired every 10 second for 10 hours with the slit of the spectrometer closed. Dark count distribution between 780-900 nm (range of interest for broadband-NIRS, section 3.3.) and the change in the intensity of individual wavelength over time were investigated.

The dark intensity measurement across 780 nm-900 nm at time zero and after 10 hours are presented in Figure 5.63 (a). The distribution in both cases has a flat shape with no prominent features. However, the mean dark intensity across all the wavelengths is significantly large in both cases when there is no light input into the spectrograph, being 8850 ± 725 counts at time zero. After 10 hours, there is a 32% increase in the dark count across all wavelengths (11672 ± 897) which is significant.

Figure 5.63 (b) shows the intensity change at one wavelength over time ($\lambda = 780$ nm). The change in the dark intensity at 780 nm over 10 hours has a mean value of 11297 ± 1020 counts. The considerably large standard deviation from the mean

intensity at 780 nm is a limiting factor which affects the concentration change calculations. Even though the ambient temperature was constant during the experiment, using a small fan operating over the spectrometer, the dark noise of Ventana spectrometer was significantly high and variable due to absence of an on-board TEC.

Limitation of Ventana Spectrometer: The CCD's temperature is not controlled since there is no thermoelectric cooling integrated as it was in QE65 Pro. Figure 5.47 illustrates the low dark counts of the QE65 Pro (cooled at -15° C) as well as the stability of dark count at each wavelength over time. The stability of dark count is crucial in broadband-NIRS, especially for long-hour measurements, because the differential spectroscopy technique uses the first intensity measurement to calculate the relative attenuation change. In fact, including or subtracting an inconsistent dark spectrum in the measurement algorithm results in false interpretation of change in the intensity and attenuation of the light and consequently causes significant errors in concentration measurement.

5.1.7.1 Modification of Ventana-based Mini-CYRIL

After discussion with Ventana manufacturer (Wasatch Photonics, USA), the issue of inconsistent large dark count in Ventana spectrometer was resolved by retrofitting a cooling system inside the spectrometer. The retrofit cooling is capable to consistently keep the CCD's temperature at 10 degrees below the ambient temperature (~15° C).

Figure 5.64 shows a single dark spectrum across all wavelengths (780- 900 nm) after the retrofit cooling upgrade in Ventana spectrometer (2440 ± 218), which in average is 75% less than that produced with the original spectrometer (no cooling).

To investigate the thermal noise and the dark count of the CCD detector after the retrofit cooling in terms of magnitude and stability over time, intensity data (photon count) were acquired every 10 second for 10 hours with the slit of the spectrometer closed. Dark count distribution between 780-900 nm (range of interest for broadband-NIRS, section 3.3.) and the change in the intensity of individual wavelength over time were investigated.

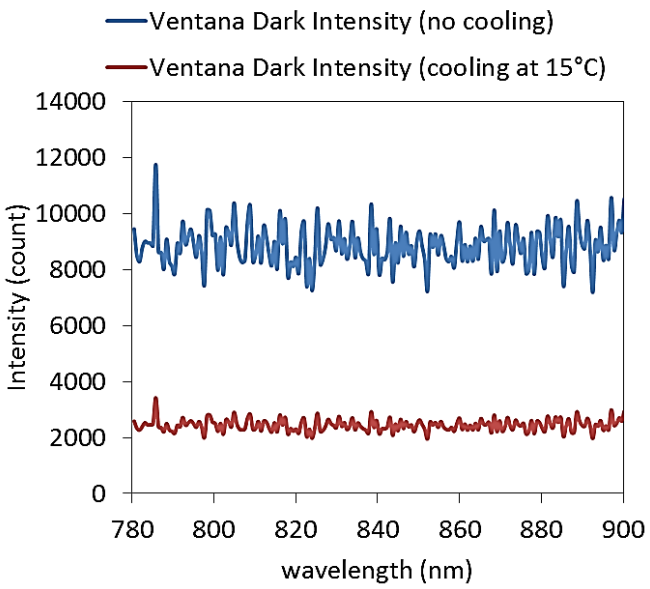

Figure 5.64: Dark intensity spectrum measured every 10 seconds when the spectrometer's slit is closed with original Ventana spectrometer (blue spectrum) and after the retrofit cooling upgrade (red spectrum) which keeps the CCD's temperature at 15° C.

The dark intensity measurement across 780 nm-900 nm at time zero and after 10 hours are presented in Figure 5.65 (a). The distribution in both times has a flat shape with no prominent features and the intensity becomes significantly lower as expected with retrofit cooling when there is no light input into the spectrograph, compared to when no cooling was implemented. The mean dark intensity across all the wavelengths at time zero is significantly smaller being 2440 ± 218 counts. After 10 hours, the average increase in dark count across all wavelengths was almost negligible (<1%) being 2472 ± 223 counts. Figure 5.65 (b) shows the intensity change at one wavelength over time ($\lambda = 780$ nm) which the intensity change has a mean value of 2625 ± 25 counts that is significantly smaller (77%) than that in the absence of cooling. The considerably small standard deviation from the mean intensity at 780 nm over 10 hours is highly significant and improves the accuracy of concentration measurement.

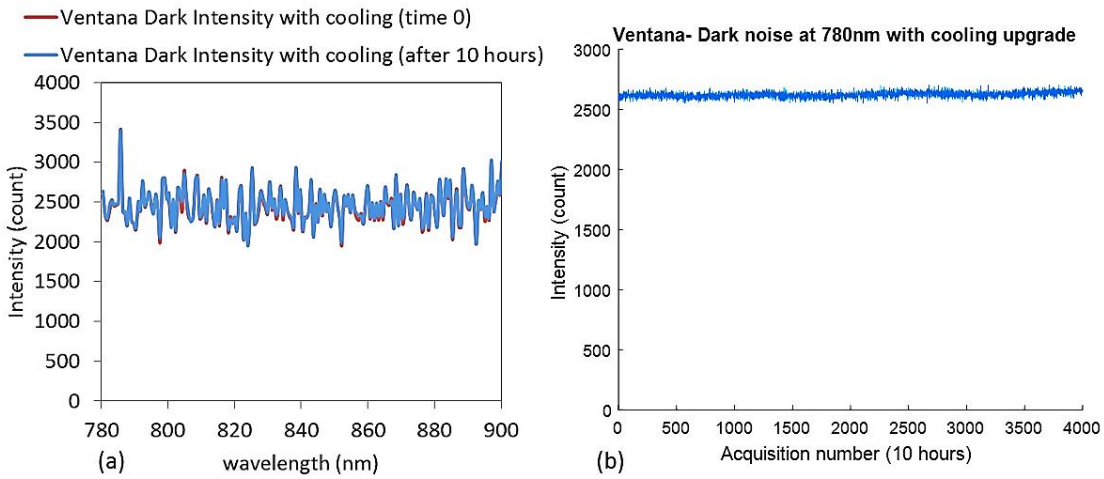

Figure 5.65: (a) Dark intensity spectrum measured across 780-900 nm every 10 seconds with upgraded unit, when the spectrometer's slit is closed at time 0 and after 10 hours. (b) The dark intensity changes at wavelength 780 nm over 10 hours.

5.2 Software Development

A program was created in MATLAB 2013a to control the miniature spectrometers using Ocean Optics MATLAB instrument driver (OmniDriver) and to collect and process the raw intensity data. The program also enabled the display and saving of the corresponding concentration data in real time.

5.2.1 The Algorithm

An algorithm for calculation of chromophore concentration was developed based on the UCLn algorithm (equation 3.13). The intensity spectra are processed to produce differential attenuation from an arbitrary baseline. Changes in the concentrations are then measured using the measured change in the attenuation of broadband-NIR spectra. In mini-CYRIL algorithm, change in attenuation is calculated using equation 3.10 and interpolated to the nearest nanometre across 780-900 nm using a spline interpolation. The UCLn algorithm is then applied to resolve changes in [HHb], [HbO_2] and [oxCCO] across 120 wavelengths using the specific extinction coefficient spectra while the wavelength dependency of DPF is accounted for (Figure 5.66).

The optical pathlength is calculated using the source-detector spacing and the measured DPF values for different tissue as measured by Duncan et al [16] or through real-time estimation of pathlength using the second differential spectroscopy technique [17] (section 3.4.5). The algorithm was tested offline through standard cuff-occlusion measurement (inducing forearm ischaemia), which is explained below before being implemented in the software.

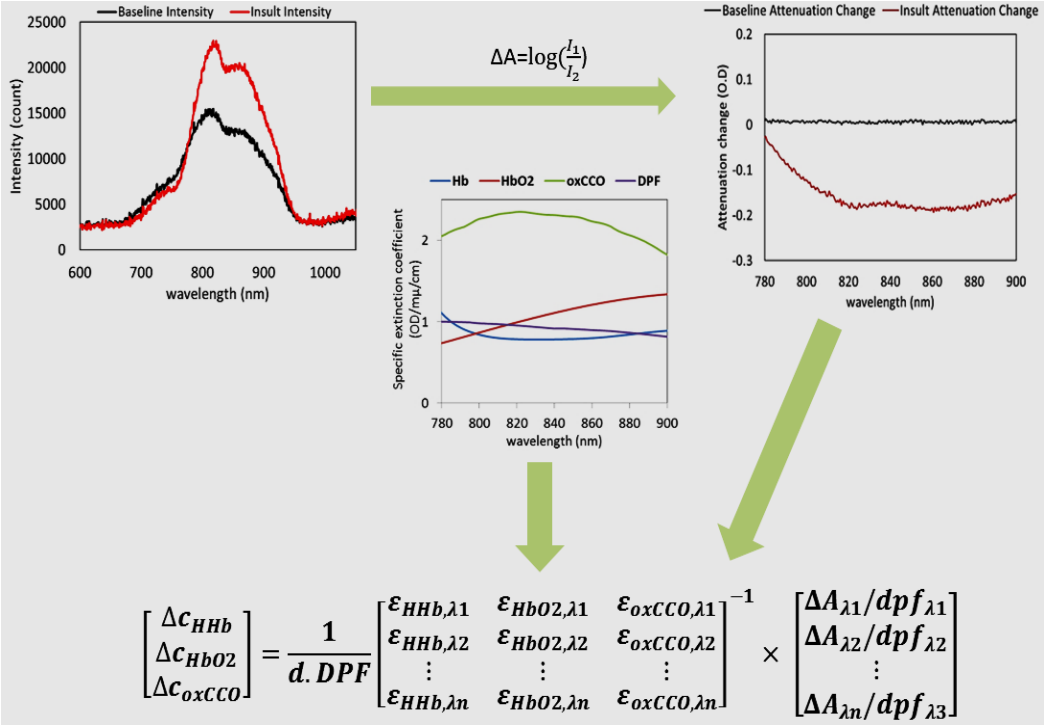

Figure 5.66: Schematic diagram of mini-CYRIL algorithm, showing modified Beer-Lambert law and the input variables. Intensity spectra, I, are recorded in real time (black and red spectra at baseline and HI). The intensity spectra are converted to change in attenuation ΔA and the changes in concentrations Δc are calculated using the UCLn algorithm with the specific extinction coefficient of the chromophores.

5.2.2 Validation of Mini-CYRIL Algorithm in-vivo (Forearm Ischaemia)

To evaluate mini-CYRIL's algorithm for calculating chromophore concentration and to investigate its capability in measuring in-vivo changes of chromophores' concentration, cuff occlusion study that was approved by the University College London (UCL) Ethics Committee was performed on a healthy adult volunteer. Cuff-occlusion is a conventional validation experiment used to evaluate the in-vivo performance of the NIRS systems [18], [19], [20], [21]. It includes occluding arteries or vein on the forearm of a healthy volunteer through a pressure

cuff and monitoring real-time changes in [HHb], [HbO_2], [HbT] and [oxCCO] if the system provides Δ[oxCCO] measurement. During forearm ischaemia, if the occlusion pressure is rapidly applied, then there should be a little change in total blood volume, although blood pooling due to gravity may produce some small change. During the occlusion desaturation should occur, which involves a sharp increase in [HHb] and an almost equal decrease in [HbO_2] [18]. Even though the magnitude of change in oxy- and deoxy-haemoglobin concentration reported in literature are slightly different depending on subjects' gender (as the DPF is gender dependent), optode separation and the duration of ischaemia, the trend of change is the same in all the studies [18]–[22]. Where Δ[oxCCO] measurement is available, only a small delayed reduction in oxCCO is expected due to the large oxygen reserve bound to muscle myoglobin, and the low oxygen consumption in the resting muscle [18], [23].

In this study, a pneumatic pressure cuff was placed loosely around the left arm of the subject while the forearm was laid on a table. The optodes were positioned over the forearm muscle (source-detector separation 4 cm) and baseline was recorded while a black cloth was wrapped around the arm and fibres to eliminate stray room light.

After after one minute of baseline measurement, the pressure cuff was rapidly inflated on the upper arm to 200-220 mmHg to prevent venous blood backflow and arterial blood inflow into the forearm for around 3-4 minutes, making sure there is no discomfort imposed on the subject. At the end of 3.5 minutes, the pressure cuff was deflated, and the arm was kept still for resting state measurement.

Figure 5.67 (a) and (b) show the intensity and attenuation spectra respectively during baseline and arterial occlusion. The difference between the shape of the intensity spectra at baseline and arterial occlusion is due to the different levels of chromophore concentrations during two states. During arterial occlusion, there is a shift of the peak in the spectrum from ~800 nm to ~820 nm, a decrease in the 760 nm shoulder due to increase in HHb concentration and an increase in ~860 nm shoulder due to the decrease in the concentration of HbO_2 as the oxygenated haemoglobin molecules are converted to deoxygenated molecules (HHb) and the oxygenated blood supply is also disrupted.

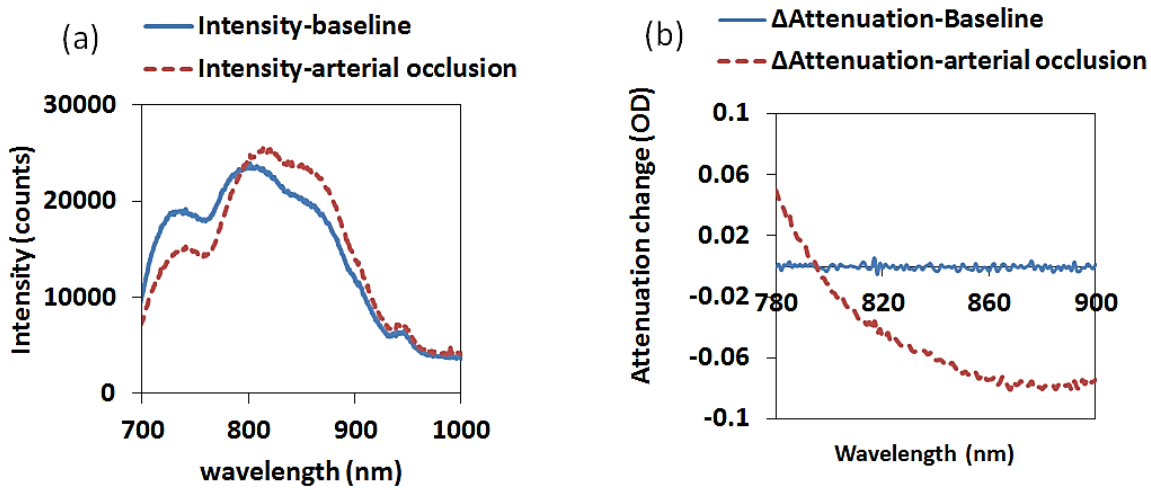

Figure 5.67: (a) Intensity spectra through arm recorded every second, during baseline and arterial occlusion (b) Attenuation change spectra relative to the first intensity measurement calculated in real time during baseline and arterial occlusion. Source-detector spacing is 2.8 cm.

Figure 5.68 shows changes in [HHb], [HbO_2],[HbT],[HbDiff] and [oxCCO] in the forearm muscle of a healthy adult volunteer. During the occlusion, the [HbO_2] decreased to a minimum of -6.4 μM and the [HHb] increased (being almost a mirror image of [HbO_2]) to a maximum of +8.4 μM, just before the pressure cuff was released. During forearm ischaemia [HbT] had a slight steady increase to 2.2 μM and [HbDiff] dropped to a minimum of -14.8 μM, which agreed with what was reported in the literature[19], [20], [21]. [oxCCO] changes were very small, however, the signal seemed to decrease gradually to -0.5 μM just before the pressure cuff was deflated, which is in agreement with the results reported recently by Lange et al through same measurements with a time domain system [22] . The small delayed reduction in oxCCO with 200 s ischaemia is comparable to what was reported by Matcher et al. and could be due to the large oxygen reserve bound to muscle myoglobin and the low oxygen consumption in resting muscle [18]. The large increase in oxCCO after the cuff is released (~3) shows evidence of cross-talk between oxCCO and haemoglobin during reactive hyperaemia phase as also reported by Matcher et al [18].

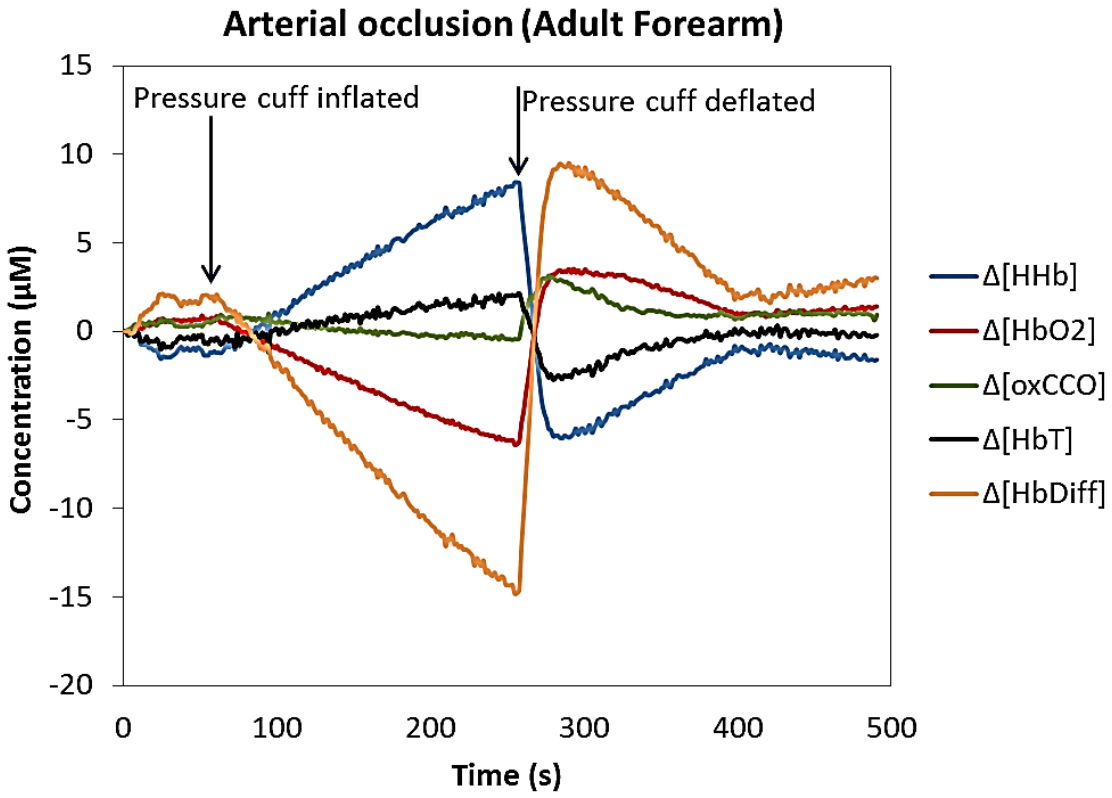

Figure 5.68: Changes in chromophores concentration during arterial occlusion in adult's forearm. The optode spacing was 4 cm and the DPF for muscle was 4.57 as measured by Duncan et al [16]. The magnitude of change in [HHb] and [HbO_2] are in agreement with the values reported in similar studies [19], [20], [21],[22].

Three versions of software were created for the mini-CYRIL system based on the validated algorithm, depending on the specific need of each application which are discussed in this section. All versions can operate both miniature spectrometers (QE65 Pro and Ventana), with minor wavelengths adjustments due to their different bandwidths.

5.2.3 Version 1

In general, the software includes three parts; the first part includes initial settings, the second part consists of acquisition and display of the raw spectral data entering the spectrometer, the third part includes the processing of the raw data, save and display. Different versions have slight variations in the third part as the first two parts are almost the same.

Figure 5.69 illustrates the main functions of the first version of the program. The program is essentially structured in three sections, presented in different colours in the

figure. The first section is the initial settings, after which the program is ready to run by pressing the Run button in MATLAB. The second and third parts are designed as 'producer-consumer' pair. The producer's job is to generate a piece of data and place it into a queue (which is basically a fixed-sided buffer). The consumer's job is to remove the data from the buffer and process it. This ensures that the producer regularly generates data without having to wait for the consumer to process it. In this program, the producer acquires the spectral data from the spectrometer at regular intervals (determined in the settings) and displays it, and the consumer collects the spectral data and calculates changes in the concentration of chromophores from changes in the attenuation of light relative to baseline using the UCL_n algorithm that was discussed in chapter 3 (eq. 3.13) and validated by Matcher et al [18]. It then displays the concentration data and saves the processed and raw data in separate files. This section describes different parts of the software in more details.

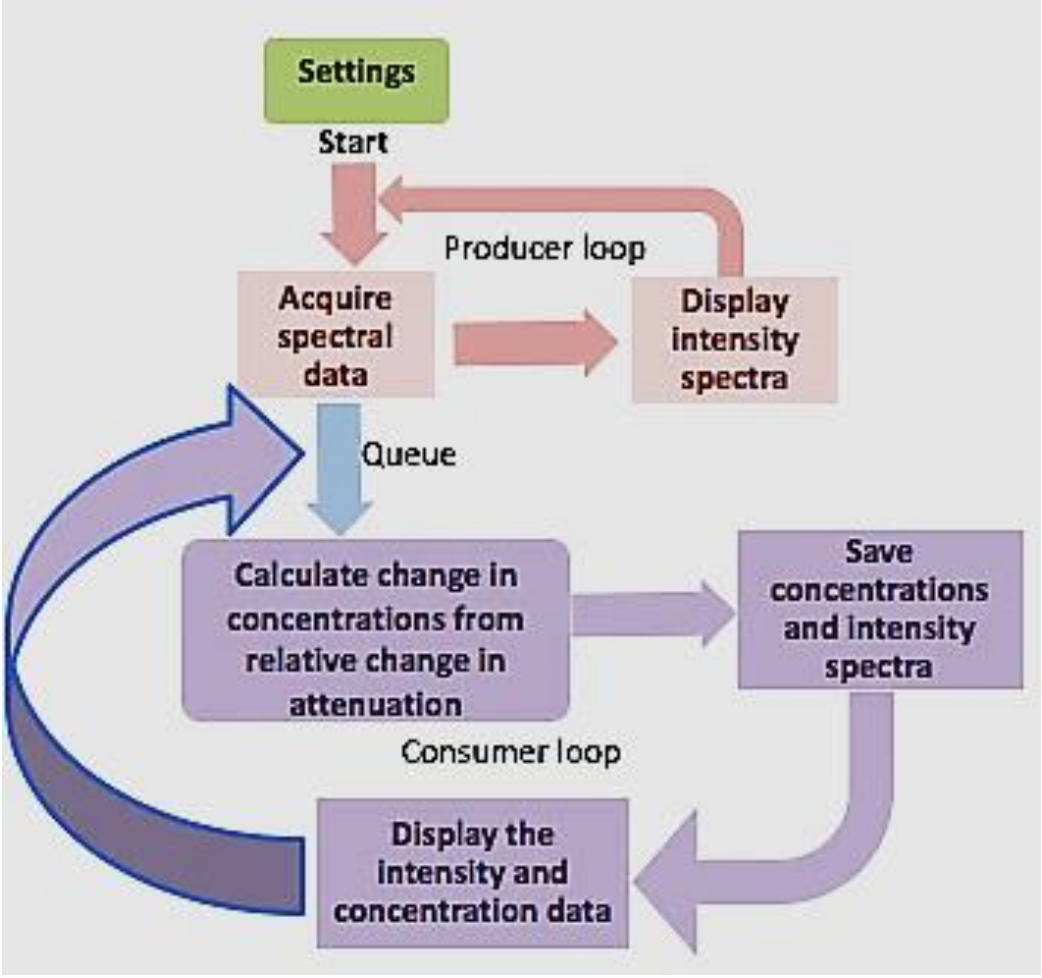

Figure 5.69: Block diagram of the main functions of the MATLAB program - version 1. The colours represent the three different sections within the program.

V1. Settings

Mini-CYRIL does not require major settings, which is an advantage for being used in clinical environment. The only parameter that needs to be adjusted prior to the measurement is the acquisition time (in microseconds) in the beginning of the program, which tends to be the same for each application. This means once the optimum integration time has been determined for a specific experiment, there will be no need to adjust it for consecutive measurements in similar experiments. The name of the file also needs to be specified at the end of the script. Prior to the data acquisition, the software asks the user to select from the different measurement modes using a pop-up menu (Figure 5.70). This allows the user to choose between performing a 'Dark measurement' , a 'reference measurement' for characterising the input light using a poster tube (section 5.3 Mini-CYRIL Calibration), 'No estimation of pathlength is required' and 'Input a fixed DPF', for calculating the change in concentrations.

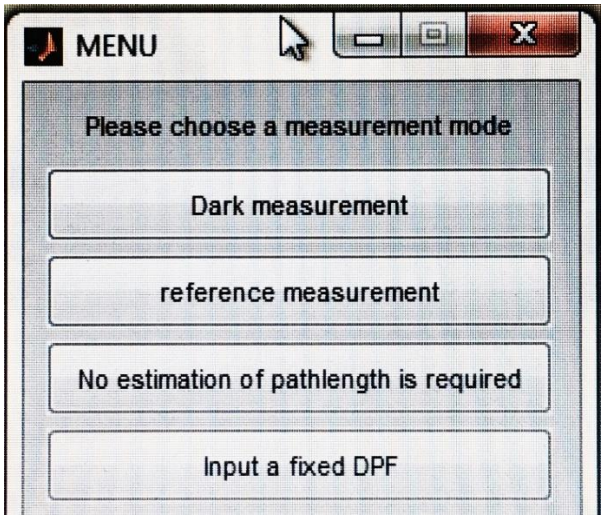

Figure 5.70: Screenshot of the pop-up menu in version 1 of the software offering the user a range of different measurement modes to select.

V1. Spectral Data (Intensity) Acquisition

When the Run button is pressed and after the user selects the relevant measurement mode, the spectrometer is programmed to acquire the intensity data versus wavelengths per the integration time using Ocean Optics MATLAB driver

(OmniDriver). The intensity data is collected across whole wavelength range (430 nm -1100 nm in Ventana and 700 nm-1100 nm in QE65 Pro) but displayed only within the NIR (650-900 nm in Ventana and 700-900 nm in QE65 Pro).

V1. Data Processing

At this stage, the spectral data is processed based on the selected measurement mode. When 'Dark measurement' and 'reference measurement' are selected, the spectral data are displayed, and concentration change are calculated (section 5.2.1 The Algorithm) without considering the pathlength (to make sure there are no major changes in the dark count). When 'No estimation of pathlength; is selected, the software generates the concentration data in μM × cm according to equation 3.13. finally, selection the last option 'Input a fixed DPF' allows the program to calculate absolute changes in chromophore concentrations using previously measured DPF values by Duncan et al. [15] (4.16 for adult forearm, 6.26 for adult head, 4.99 for new-born infant and piglet's head for source-detector spacing greater than 4 cm) as well as the known source-detector spacing.

V1. Data Saving and Display

All the raw data (intensity and measured attenuations) as well as the calculated concentrations, elapsed time and event marks are saved in a file 'Results' with a timestamp, so there is no possibility to overwrite files when starting a new measurement. Furthermore, all the intensity and concentration data as well as timestamps are saved in a separate file in real time outside MATLAB, as comma separated values (CSV). Each new measurement is appended to the CSV file to prevent loss of data in the event of system failure.

An example of data display using version 1 of mini-CYRIL's software is shown in Figure 5.71. In this version, concentrations of chromophores are displayed in real time along with the raw intensity data.

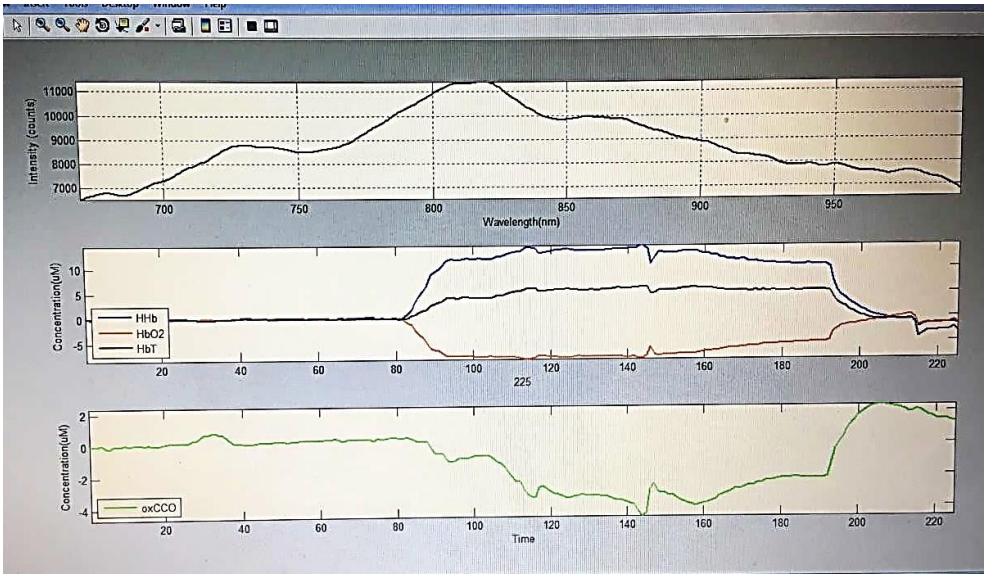

Figure 5.71: Version 1- Display of the chromophore concentrations and intensity data during inducing a hypoxic-ischaemic brain injury in piglets (Please see chapter 6 for more details). The subplots from top to bottom: Intensity data against wavelength through piglet's head, HHb (blue), HbO_2 (red) and HbT (black) concentration changes, oxCCO (green) concentration change

5.2.4 Version 2

Mini-CYRIL was upgraded to version 2, illustrated in Figure 5.72 to produce more precise measurement of absolute changes in chromophore concentrations through estimating the differential pathlength in real time. Extra features of this version include improving the processing time by modifying the data display format as well as implementing additional measurement mode to select from 'real time estimation of true optical pathlength at 840 nm' through the tissue using the second differential of water absorption spectrum and the known tissue water concentration (equation 3.22), as described in section 3.4.5 [17]. For this purpose, a reference measurement is needed prior to the experiment, to measure the absolute attenuation of light through the tissue, which is required for real-time estimation of the differential pathlength.

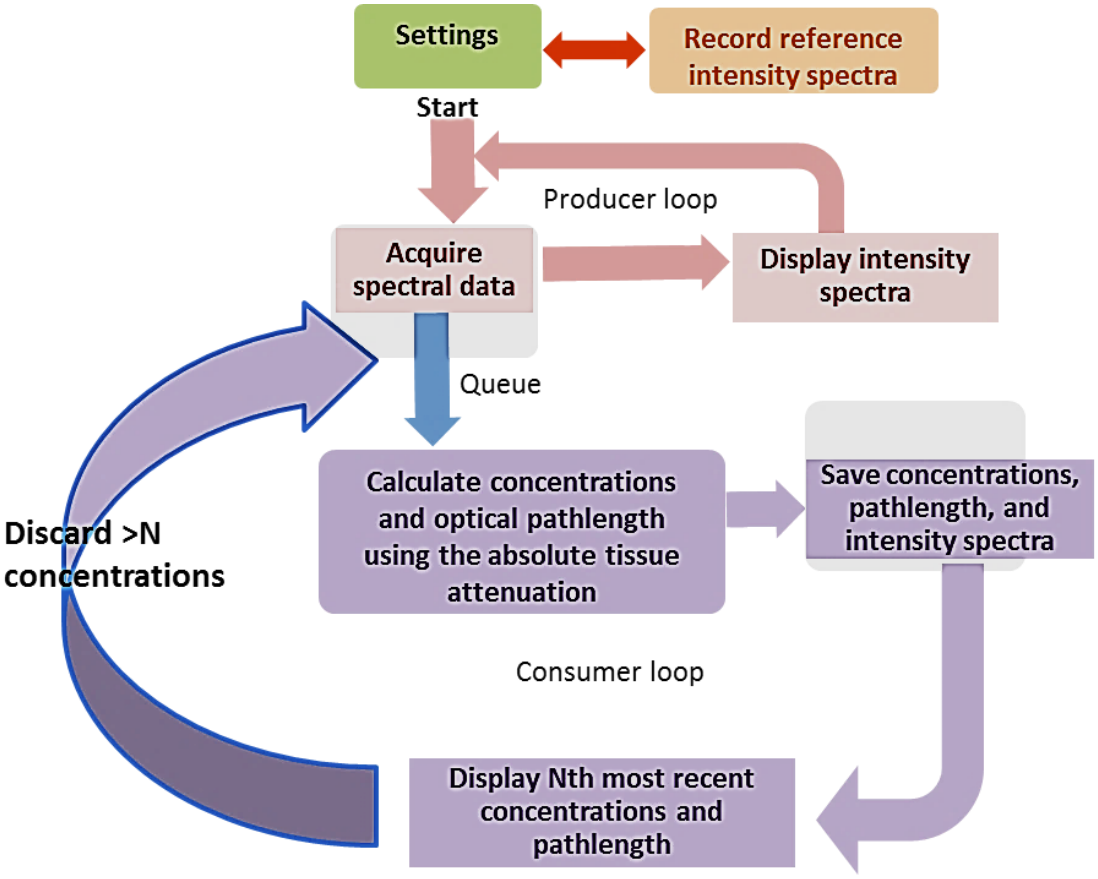

Figure 5.72: Block diagram of the main functions of the MATLAB program - version 2. The colours represent the three different sections within the program.

V2. Settings

The settings in version 2 is carried out as in version 1. In version 2, before running the program, a reference measurement needs to be acquired, since it is a prerequisite for optical pathlength calculation using second differential spectroscopy technique (section 3.4.5). Figure 5.73 shows the pop-up menu in version 2 with the extra measurement mode, 'pathlength estimation at 840 nm'.

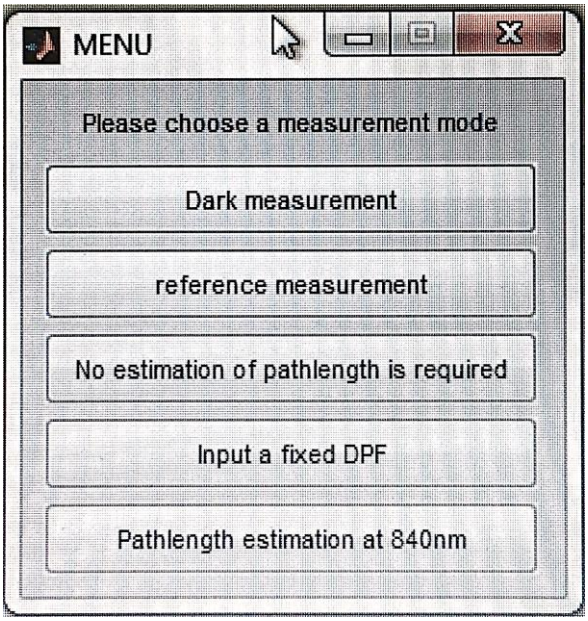

Figure 5.73: Screenshot of the pop-up menu in version 2 of the software offering the user a range of different measurement modes to select.

The reference measurement is saved as a single reference file which can be loaded when the 'pathlength estimation at 840 nm' mode is selected.

V2. Data Processing

An additional feature to data processing in version 1, which was calculating chromophore concentration change using the known optode spacing and the measured fixed DPF from the literature, is calculation and real-time display of changes in pathlength (d × DPF) which also allows more precise measurement of chromophores concentration change. Figure 5.74 illustrates the flowchart of pathlength calculation.

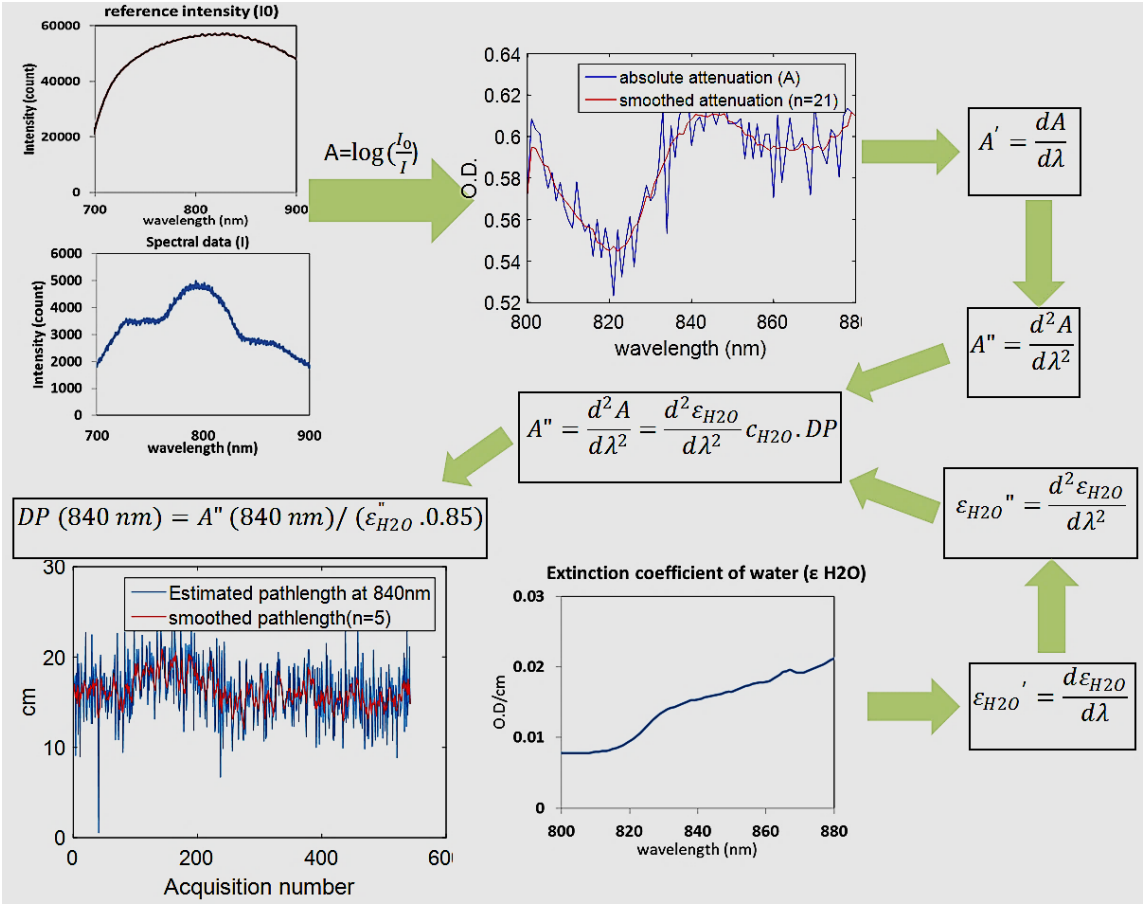

Figure 5.74: schematic diagram of pathlength calculation using the second differential spectroscopy of water, absolute attenuation spectra and the known concentration of water in piglet brain (85%) [17]. See 3.4.5 for further details.

V2. Data saving and display

Data saving and procedure is the same as version 1 with the pathlength data added to the concentration files and being included in the real-time data display (Figure 5.75).

To improve the performance of the system through reducing the data processing time, the x and y axes for concentration data were changed from being auto scaled to pre-set limits. The number of concentration data that are displayed were set to 1000 (which can also be adjusted in the script depending on the duration of the measurement). The upper limits for y axis are between -50, 50 μM for HHb, HbO_2 and HbT concentrations, and between -10, 10 μM for oxCCO and the lower limits are -10,

10 μM for haemoglobin signals and -5,5 μM for oxCCO. These limits can be adjusted depending on the application.

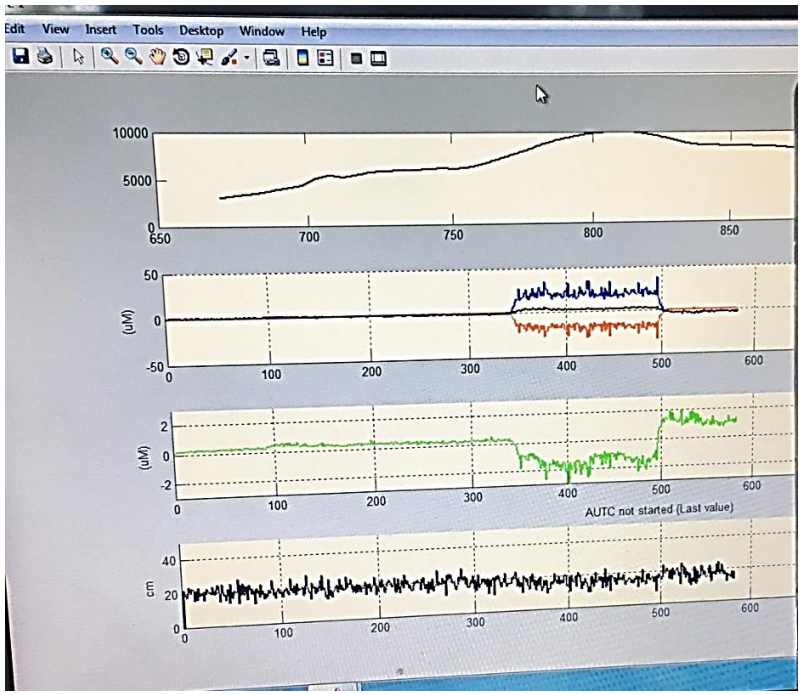

Figure 5.75: version 2- Display of the chromophore concentrations using the real-time measurement of optical pathlength during hypoxic-ischaemic brain injury in a piglet (further details in chapter 6). The subplots from top to bottom: Intensity data through piglet's head (source-detector: 4.2 cm), HHb (blue), HbO_2 (red) and HbT (black) concentration changes, oxCCO (green) concentration change, pathlength changes (black).

5.2.5 Version 2.1

Version 2.1 is a customisation of version 2 to assist with the hypoxic-ischaemic insult in the preclinical study of neonatal birth asphyxia (Chapter 4). This version allows calculation of the recovery fraction (RF) of the oxCCO signal (equations 4.1 and 4.2) as shown in Figure 5.76. The recovery fraction of oxCCO signal one hour after the resuscitation showed to be a good indicator of brain injury severity and enabled distinguishing between the poor and good outcome piglets with high sensitivity and specificity.

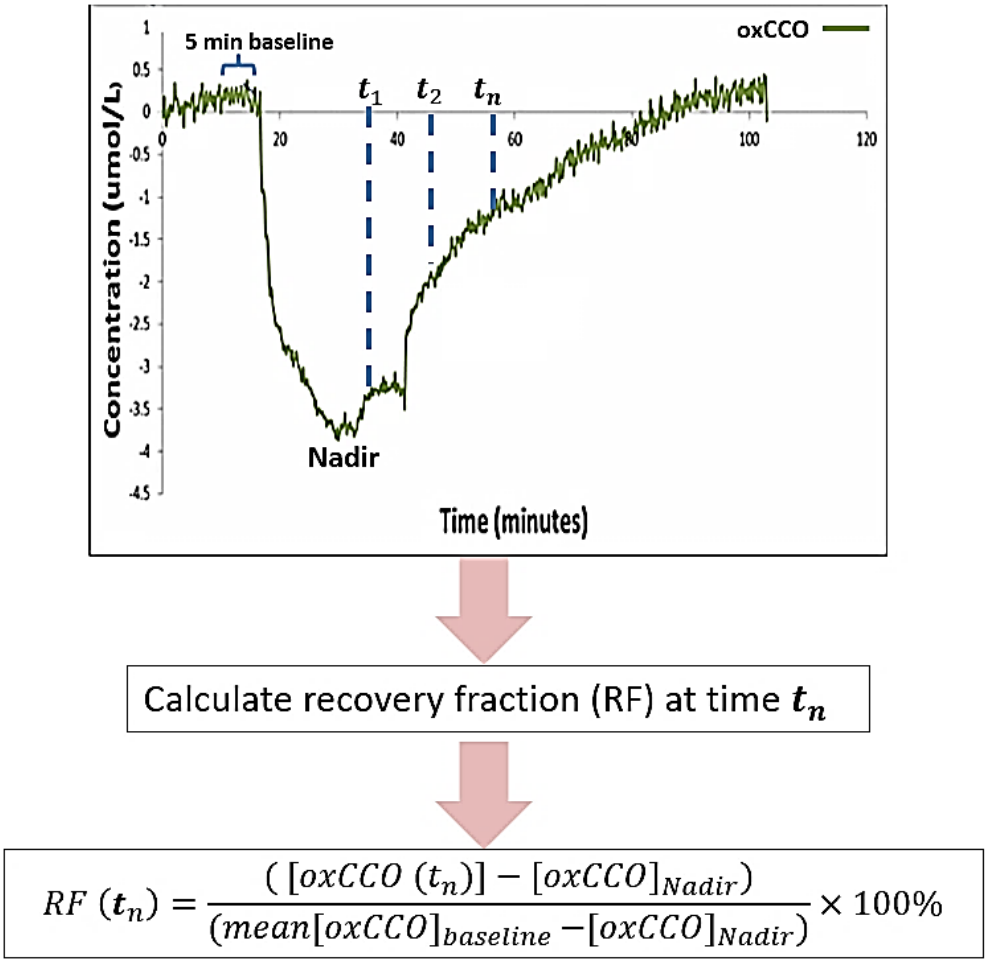

Figure 5.76: The algorithm of calculating the recovery fraction of oxCCO signal in piglets at any time (t_n) after the HI insult. The baseline [oxCCO] value is averaged over a 5-minute window just before insult. The recovery fraction of oxCCO signal has shown to be a good indicator of brain injury severity following HI insult in piglets.

An extra feature has also been added to this version, which includes calculating the area under the curve (AUTC) of the Δ[oxCCO] signal, which could allow quantification and directing a relatively consistent HI insult across piglets. Calculation of area under the curve is illustrated in Figure 5.77. The RF and AUTC calculations are activated by pressing the 'r' and 'I' keys on the concentration data display.

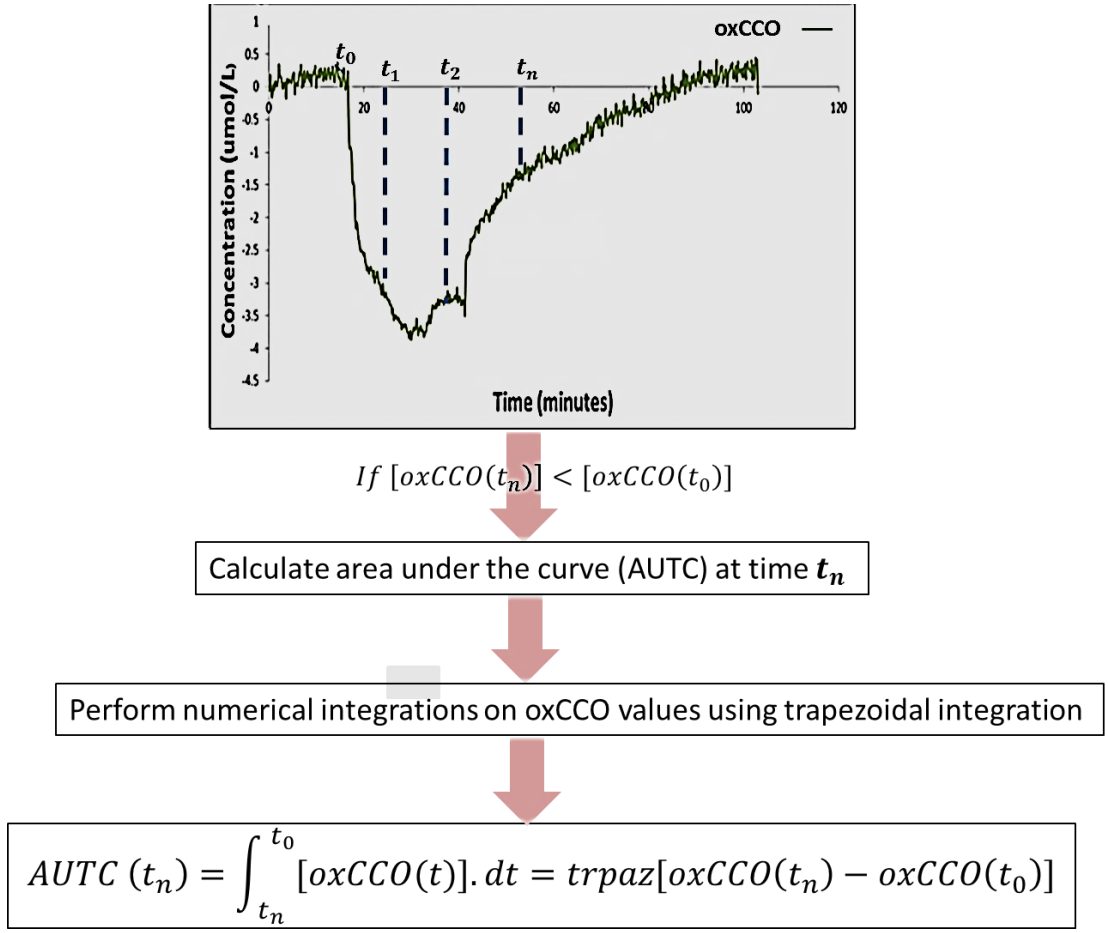

Figure 5.77: The algorithm for calculating the area under the curve of the Δ[oxCCO] signal during the HI insult. It is hypothesised that the total amount of oxCCO drop during insult is a good indicator for inducing a uniform HI. Therefore, the area under the curve is calculated only when oxCCO signal at any time during HI is smaller than the baseline value (oxCCO (t_0)), which is the mean oxCCO over 5 minutes baseline. Numerical integration on oxCCO values is performed using trapezoidal method (trapz function in MATLAB), dt being the integration time.

Figure 5.78 is a screenshot of data display using version 2.1 of mini-CYRIL's software, showing fixed scale x and y axes with the AUTC of Δ[oxCCO] display during the hypoxic-ischaemic insult (see chapter 6, section 6.3.2 for the insult protocol) as well as the real-time recovery fraction of the Δ[oxCCO] signal indicating the extent of recovery of mitochondrial oxidative metabolism following hypoxic ischaemic brain injury in piglets.

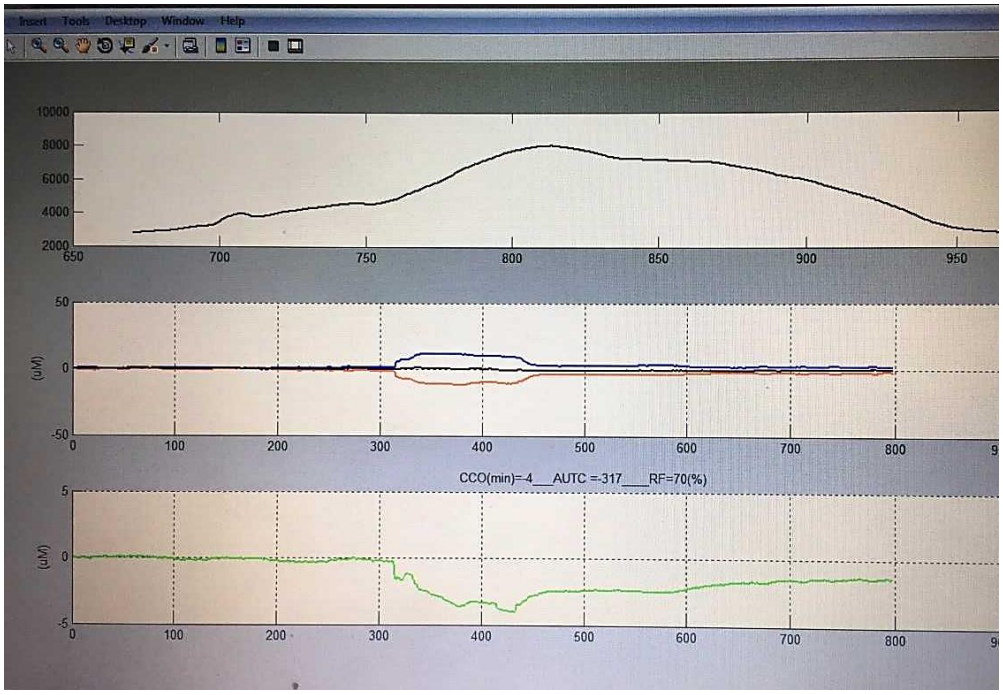

Figure 5.78: Version 2.1- Display of the chromophore concentrations with fixed scale x and y axes. Minimum oxCCO value is also displayed to assist with inducing HI, as well as the area under the curve (AUTC) and the recovery fraction (RF) of oxCCO signal during and after the HI injury to help determine the severity of insult based on the results from chapter 4. The subplots from top to bottom: Intensity data through piglet's head (source-detector: 4.2 cm), HHb (blue), HbO_2 (red) and HbT (black) concentration changes, oxCCO (green) concentration change.

5.3 Mini-CYRIL Calibration

Mini-CYRIL does not require wavelength calibration. It only needs intensity calibration (characterising the input light through the source fibre) to ensure stability and large photon count of the input light. The reference measurement will also be used for calculating concentration changes based on real-time pathlength estimation.

A poster tube, which is covered in black fabric inside and out, is used to record the intensity of light source (HL-2000-HP) through free space with no absorbing medium (Figure 5.79) while avoiding ambient light interference. The reference spectra must be collected in short integration times (~ 100 ms) and is usually collected for 20 seconds. The intensity spectra are saved as a MATLAB file which can be loaded and processed for real time calculation of optical pathlength.

Figure 5.80 presents the reference spectra in NIR region, collected using the poster tube set up for 20 seconds. The shutter on the light source was fully open and

the poster tube was held stable on a table to prevent movement artefacts affecting the measurement.

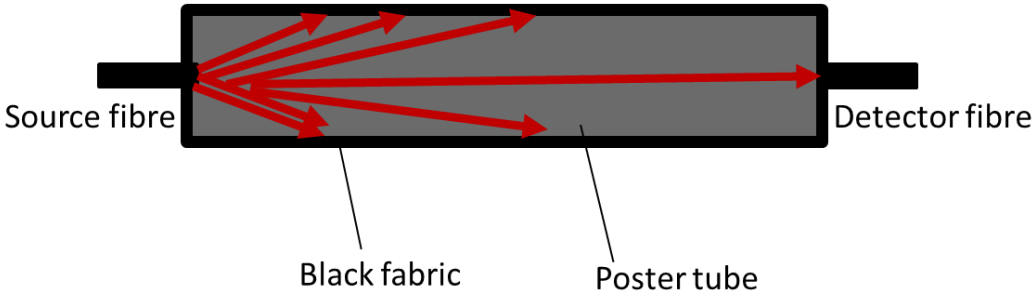

Figure 5.79: Schematic of the set up for intensity calibration and reference measurement that is required for real-time calculation of pathlength.

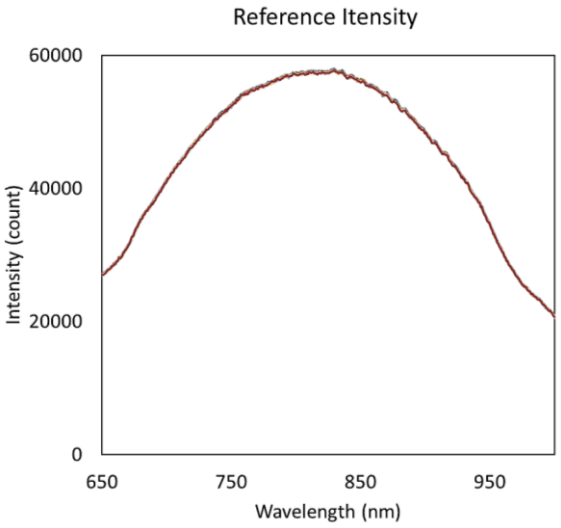

Figure 5.80: Mini-CYRIL Intensity calibration; reference measurement using a poster tube (Figure 5.79), 100 ms acquisition time.

5.4 Mini-CYRIL Stability Test

To test the stability of the system over time, studies on solid phantoms with tissue like optical properties were performed using mini-CYRIL 2 (Figure 5.81). Figure 5.82 show the changes in the spectral data and chromophore concentrations resolved on a tissue like phantom during dark (no light through the phantom), and when light was incident on the phantom at a source-detector separation of 4 cm.

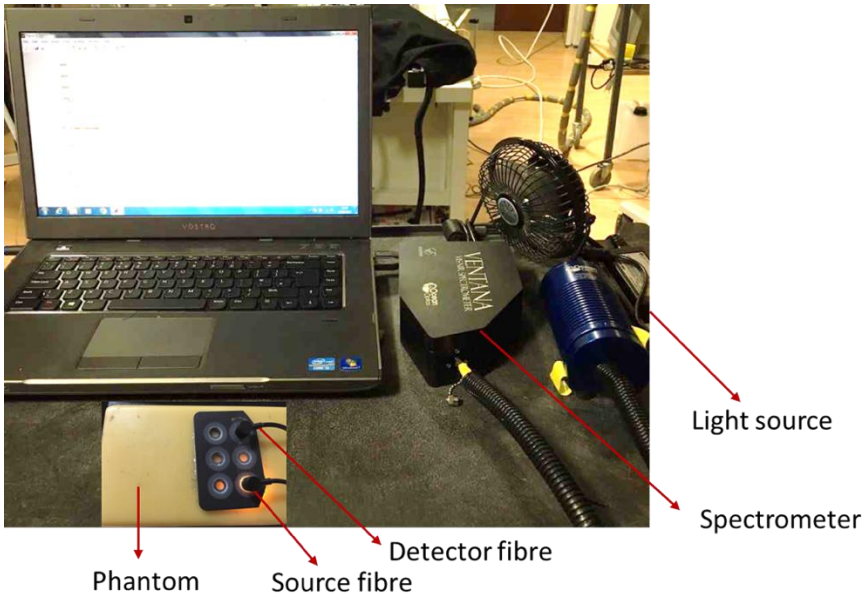

Figure 5.81: Experimental set up for testing the stability of the mini-CYRIL system using a tissue like phantom (μ_a= 0.02 and μ'_s = 0.9 [mm^{-1} mol^{-1}]).

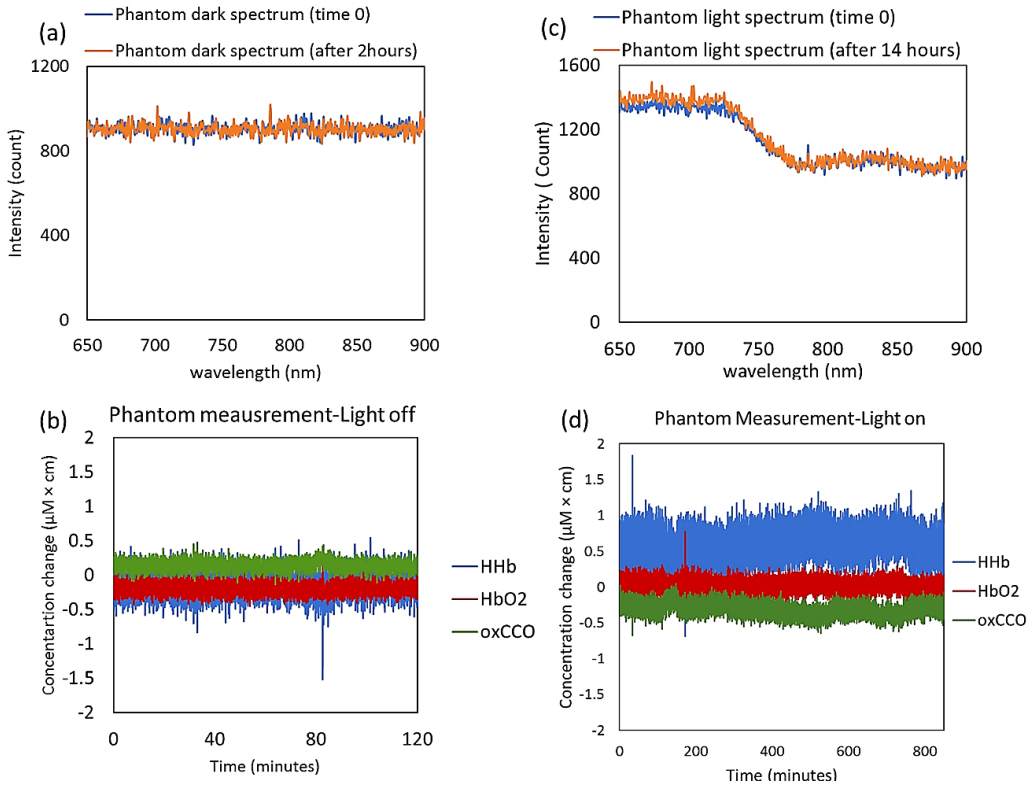

Figure 5.82: Phantom measurements in dark and light showing the stability of the mini-CYRIL system. (a) and (b) are the spectral data and concentration changes in a tissue like phantom (μ_a= 0.02 and μ'_s = 0.9, [mm^{-1} mol^{-1}]) for 2 hours when the light source's shutter was closed. (c) and (d) are the spectral data and concentration measurements for 14 hours, when the same phantom was illuminated as seen in Figure 5.81. Integration time for both measurements was 1 second and source-detector spacing 4 cm.

There is a negligible change in average dark intensity through the phantom across 780-900 nm and there are minor changes in concentration data which are stable with no drift for 2 hours (Δ[HHb]= -0.15 ± 0.16 (μM × cm), Δ[HbO_2]= -0.19±0.07 (μM × cm), Δ[HHb]= -0.14±0.07 (μM × cm)). Figure 5.82 (c) and (d), show the spectral data and concentration changes on the phantom when light was on continuously for 14 hours. The average change in the intensity of light traversing the phantom is only around 8% and there is no drift in the concentration data showing the high stability of the mini-CYRIL system over 14 hours (Δ[HHb] = 0.59 ± 0.19 (μM × cm), Δ[HbO_2] = 0.02 ± 0.08 (μM × cm) , Δ[oxCCO] = - 0.30 ± 0.09 (μM × cm)).

5.5 Mini-CYRIL Versions and Specifications

Two versions of mini-CYRIL hardware were developed based on a miniature light source HL-2000-HP and miniature spectrometers QE65 Pro and modified Ventana, for in-vivo measurement of tissue oxygenation and metabolism at the bedside. Table 5.8 summarises the specification of each system.

Table 5.8: General Specifications of mini-CYRIL1 and mini-CYRIL2

Specifications	Mini-CYRIL1 (QE65 Pro)	Mini-CYRIL2 (Ventana)
Throughput	f/4	f/2
Bandwidth	353 nm (700-1053 nm)	677 nm (430-1100 nm)
Spectral resolution	3.5 nm	4 nm
CCD Peak quantum efficiency	95%	75%
CCD pixel size	24.6 μm^2	14 μm^2
CCD pixels	1024 x 58	1024 x 64
CCD active area (mm)	24.576 × 1.392	14.336 × 0.896
CCD temperature	-15°C (40 degrees below ambient)	15°C (10 degrees below ambient)
Dark noise (single spectrum)	3 counts RMS	6 counts RMS
Signal to noise ratio	1000:1	500:1

Despite its poor performance in long source-detector measurements, QE65 Pro is capable of long hour precise measurements in applications where multiple layers of

tissue are not involved (such as in exposed tissue applications) or in small source-detector spacing (<=3 cm), for which small NA detector fibres (0.22 or 0.37) can be used.

The second version of the mini-CYRIL system is based on the modified Ventana spectrometer with retrofit cooling that can be used for deep tissue spectroscopy such as whole brain transmission mode measurement in piglets when long source detector spacing (> 3 cm) is necessary. The Ventana spectrometer is used with larger NA detector fibre (0.37 or 0.57) that enables measurement through deeper tissue layers.

Mini-CYRIL has three software versions and the latest version allows real time concentration change measurement based on real-time changes in optical path lengths and allows for the real-time calculation of recovery fraction and area under the curve of oxCCO signal, a marker for brain injury severity following HI insult. Mini-CYRIL performance was validated primarily using phantom studies and cuff-occlusion measurements and the results of concentration change during arterial occlusion (forearm ischaemia) was comparable to the values reported in the literature.

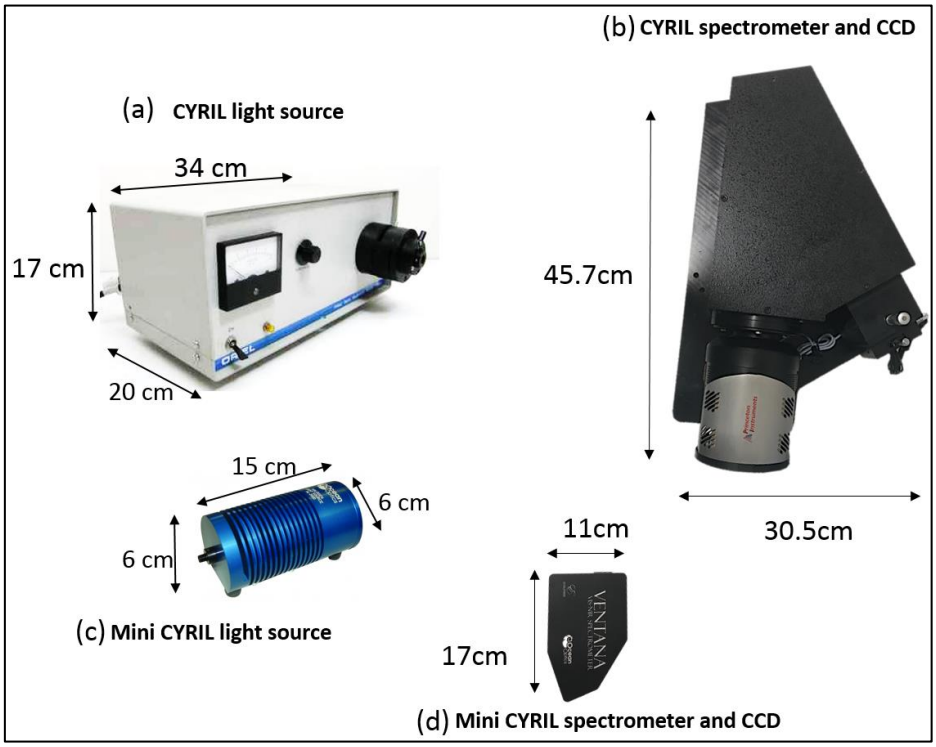

Figure 5.83: Comparison between the sizes of the Oriel (77501) light source (a) and Action series LS-785 (b) from CYRIL with HL-2000-HP (c) and Ventana VIS-NIR miniature spectrometer (d) from mini-CYRIL2.

Mini-CYRIL is primarily a single channel system (limited to one source and one detector fibre), which is due to restrictions in binning of the CCDs. However, multichannel measurement could be feasible through utilising multiple spectrometers and modifying the software to read and process the spectra from all the spectrometers, which is discussed in future work chapter 9, section 9.2.

Figure 5.83 compare the size of mini-CYRIL against the size of the original CYRIL system, which is currently being used at UCL Hospital for the study of HIE in new-born infants.

5.6 Summary

In this chapter, the development of two versions of a portable miniature broadband-NIRS system (mini-CYRIL) based on easily-sourced components for in-vivo measurement of tissue oxygenation and metabolism at bedside was described and the main issues around the utilisation of miniature spectrometers to be made into a clinical system were addressed.

The challenges with miniaturising broadband-NIRS systems arise from the intrinsic contrast between the high numerical aperture (NA) of the optical fibres (that are attached to the head to deliver light and collect the attenuated reflected light) and the small throughput design of the spectrometers (large F-number, to maintain a flattened spectral field). Despite their advantages, most importantly low cost and compactness, a major limitation of off-the-shelf spectrometers is that the design of the miniature spectrometers cannot be customised. F-matching using external collimating and focusing lenses could enhance the throughput to some extent. However, customising a lower NA detector fibre (NA=0.37) with slit configuration at the spectrometer end was more effective, though very expensive compared to standard fibres. A low f-number miniature spectrometer, Ventana, with lower cost demonstrated to significantly enhance the throughput by an order of magnitude. However, the absence of thermoelectric cooling led to large inconsistent dark current and thermal noise which could induce false changes in chromophore concentrations over time. This challenge was tackled through implementing a retrofit cooling system that kept the CCD at 10 degrees below the ambient temperature. The algorithm from Mini-CYRIL software was validated through a standard cuff-occlusion measurement

and the results from a healthy volunteer agreed with what other groups had reported. The stability of the system was also tested using long-hour phantom measurements. Mini-CYRIL is capable of absolute quantification of change in tissue oxygenation (Δ[HHb],Δ[HbO_2]) and metabolism (Δ[oxCCO]) using previously measured DPF or pathlength estimation at 840 nm. The software also provides useful quantifiable measures such as area under the curve (AUTC) or recovery fraction (RF) of the Δ[oxCCO] signal which can be used by clinicians to assess the brain injury severity and extent of recovery (will be discussed in the next chapter).

The performances of both versions of mini-CYRIL are further validated through investigating hypoxia ischaemia in piglets (chapter 6), investigating the role of hypoxia in MS studies (chapter 7) and investigating low-level light therapy (using 650 nm) in the aged retina (chapter 8).

Bibliography

[1] E. Wright, K. St. Lawrence, and M. Diop, "Conversion of a low cost off-the-shelf spectrometer into a suitable instrument for deep tissue spectroscopy," *Proc. SPIE*, vol. 8573, p. 85730V, 2013.

[2] M. Diop, E. Wright, V. Toronov, T.-Y. Lee, and K. St Lawrence, "Improved light collection and wavelet de-noising enable quantification of cerebral blood flow and oxygen metabolism by a low-cost, off-the-shelf spectrometer.," *J. Biomed. Opt.*, vol. 19, no. 5, p. 57007, 2014.

[3] R. Nosrati, K. Vesely, T. A. Schweizer, and V. Toronov, "Event-related changes of the prefrontal cortex oxygen delivery and metabolism during driving measured by hyperspectral fNIRS," *Biomed. Opt. Express*, vol. 7, no. 4, p. 1323, 2016.

[4] C. Kolyva, A. Ghosh, I. Tachtsidis, D. Highton, M. Smith, and C. E. Elwell, "Dependence on NIRS Source-Detector Spacing of Cytochrome c Oxidase Response to Hypoxia and Hypercapnia in the Adult Brain," *Adv. Exp. Med. Biol.*, vol. 789, pp. 353–359, 2013.

[5] R. Springett, M. Wylezinska, E. B. Cady, M. Cope, and D. T. Delpy, "Oxygen dependency of cerebral oxidative phosphorylation in newborn piglets.," *J. Cereb. Blood Flow Metab.*, vol. 20, no. 2, pp. 280–9, 2000.

[6] D. Ave, "Halogen Light Source with Attenuator and TTL-Shutter," no. 0, 2000.

[7] A. Bainbridge, I. Tachtsidis, S. D. Faulkner, D. Price, T. Zhu, E. Baer, K. D. Broad, D. L. Thomas, E. B. Cady, N. J. Robertson, and X. Golay, "Brain mitochondrial oxidative metabolism during and after cerebral hypoxia-ischemia studied by simultaneous phosphorus magnetic-resonance and broadband near-infrared spectroscopy," *Neuroimage*, vol. 102, no. P1, pp. 173–183, 2014.

[8] G. Bale, S. Mitra, J. Meek, N. Robertson, and I. Tachtsidis, "A new broadband near-infrared spectroscopy system for in-vivo measurements of cerebral cytochrome-c-oxidase changes in neonatal brain injury.," *Biomed. Opt. Express*, vol. 5, no. 10, pp. 3450–66, 2014.

[9] G. Bale, "Development of Optical Instrumentation and Methods to Monitor Brain Oxygen Metabolism : Application to Neonatal Birth Asphyxia," 2016.

[10] A. Bozkurt and B. Onaral, "Safety assessment of near infrared light emitting diodes for diffuse optical measurements.," *Biomed. Eng. Online*, vol. 3, no. 1, p. 9, 2004.

[11] F. F. F. Jobsis, "Noninvasive, Infrared Monitoring of Cerebral and Myocardial Oxygen Sufficiency and Circulatory Parameters," *Science (80-.).*, vol. 198, no. 4323, pp. 1264–1267, 1977.

[12] R. V Chimenti, "SPECTROMETERS: Miniature spectrometer designs open new applications potential," *Laser Focus World*, 2013. [Online]. Available: http://www.laserfocusworld.com/articles/print/volume-49/issue-05/features/spectrometers--miniature-spectrometer-designs-open-new-applicati.html. [Accessed: 11-Apr-2017].

[13] "QE Pro (Custom) - Ocean Optics." [Online]. Available: http://oceanoptics.com/product/qe-pro/.

[14] Newport Tutorial, "Light Collection and Systems Throughput," *Newport*, 2017. [Online]. Available: https://www.newport.com/t/light-collection-and-systems-throughput. [Accessed: 11-Mar-2017].

[15] Hamamatsu, "CCD image sensors," pp. 1–9.

[16] A. Duncan, J. H. Meek, M. Clemence, C. E. Elwell, L. Tyszczuk, M. Cope, and D. T. Delpy, "Optical pathlength measurements on adult head, calf and forearm and the head of the newborn infant using phase resolved optical spectroscopy.," *Phys. Med. Biol.*, vol. 40, no. 2, pp. 295–304, 1995.

[17] S. J. Matcher, M. Cope, and D. T. Delpy, "Use of the water absorption spectrum to quantify tissue chromophore concentration changes in near-infrared spectroscopy.," *Phys. Med. Biol.*, vol. 39, no. 1, pp. 177–96, 1994.

[18] S. J. Matcher, C. E. Elwell, C. E. Cooper, M. Cope, and D. T. Delpy, "Performance Comparison of Several Published Tissue Near-Infrared Spectroscopy Algorithms," *Analytical Biochemistry*, vol. 227, no. 1. pp. 54–68, 1995.

[19] D. Haensse, P. Szabo, D. Brown, J.-C. Fauchère, P. Niederer, H.-U. Bucher, and M. Wolf, "A new multichannel near infrared spectrophotometry system for functional studies of the brain in adults and neonates.," *Opt. Express*, vol. 13, no. 12, pp. 4525–38, 2005.

[20] T. Muehlemann, D. Haensse, and M. Wolf, "Wireless miniaturized in-vivo near infrared imaging.," *Opt. Express*, vol. 16, no. 14, pp. 10323–30, Jul. 2008.

[21] B. Shadgan, W. D. Reid, R. Gharakhanlou, L. Stpublisher-ids, and A. J. Macnab, "Wireless near-infrared spectroscopy of skeletal muscle oxygenation and hemodynamics during exercise and ischemia," *J. Spectrosc.*, vol. 23, no. 5–6, pp. 233–241.

[22] F. Lange, L. Dunne, and I. Tachtsidis, "Evaluation of Haemoglobin and Cytochrome Responses during Forearm Ischaemia using Multi-Wavelength Time Domain NIRS," *Adv. Exp. Med. Biol.*, vol. 977, no. in press, pp. 67–72.

[23] C. R. Honig, R. J. Connett, and T. E. J. Gayeski, "O2 transport and its interaction with metabolism; a systems view of aerobic capacity," *Med. Sci. Sport Excercise*, vol. 24, no. 1, pp. 47–53, 1992.

Chapter 6. Mini-CYRIL2 in the Preclinical Study of Neonatal Hypoxia Ischaemia

This chapter describes the application of mini-CYRIL2 in the preclinical study of neonatal hypoxic ischaemic encephalopathy (HIE) in new-born pigs. In chapter 4, the HIE studies in the neonatal preclinical model were introduced and the use of broadband NIRS (UCL1 instrument) to monitor hypoxic-ischaemia (HI) was thoroughly discussed. The UCL1 instrument was replaced with the mini-CYRIL2 system and in this chapter, I demonstrate its use and compare the two instruments through spectroscopic data analysis as well as the measurements of HHb, HbO_2 and oxCCO that both systems provide during HI and recovery.

6.1 Introduction

As mentioned in chapter 4 (section 4.3.4), hypoxia ischaemia was induced in piglets' brain in the bore of the magnet and controlled based on reductions in ATP levels (β-NTP, as measured by ^{31}P-MRS). Following successful results in chapter 4, where the recovery fraction of oxCCO one hour after HI correlated strongly with ^{31}P-MRS markers for injury severity and was predictive of the outcome in piglets with brain injury, it was suggested that broadband-NIRS measurement of oxCCO could be used independent of MRS to quantify HI depth and severity in piglets. Therefore, due to the high cost of using MRS and the complications regarding the transfer of the piglets after an invasive surgery to the magnet room as well as severely limited accessibility to piglets in case of an emergency during and after the HI; it was decided that mini-CYRIL2 and the oxCCO measurement be used for directing the HI insult in new-born pigs.

6.2 Aims

The aim of this study was primarily to evaluate the performance of mini-CYRIL2 in the field, through pursuing the following objectives:

- Investigating the ability of mini-CYRIL2 to collect high light intensity data transmitted through piglets' brain.

- Analysing the spectroscopic concentration data for evaluation of crosstalk between the haemoglobins and cytochrome-c-oxidase concentrations.
- Evaluating the stability of the system in producing consistent concentration data that can be used by clinicians during HI and recovery.
- Investigating the influence of optical pathlength estimation method (using fixed DPF or differential pathlength estimated based on absolute attenuation spectra) on the concentration data and validating the generated concentration changes based on the data produced by UCL1 during HI (which was discussed in chapter 4).

6.3 Methods

All animal experiments were performed under UK Home Office Guidelines (Animals [Scientific procedures] act, 1986). Animals were prepared and monitored for the experiment as described in chapter 4, section 4.3.1 and were terminated after the course of the experiment (48 hrs) for further histological studies.

6.3.1 Broadband-NIRS

Mini-CYRIL2 was used for broadband-NIRS transmission mode measurement through the piglets' brain. The experimental set up is presented in Figure 6.84. The source and detector fibres were identical, and securely mounted on the either side of the head. The fibres were designed with high numerical aperture (0.57 NA) and 2.3 mm core diameter (SMA limited) to collect highly scattered diffused light from the brain. At the head-end, the fibres had a 90° bend to effectively direct the light to/from the piglet's head as seen in Figure 6.84.

Light from the thermally stabilised 20 W halogen tungsten source was transmitted to piglet's brain (power per unit area ~1.9 mW/cm^2) using the source fibre. The input light spectrum is presented in Figure 6.85.

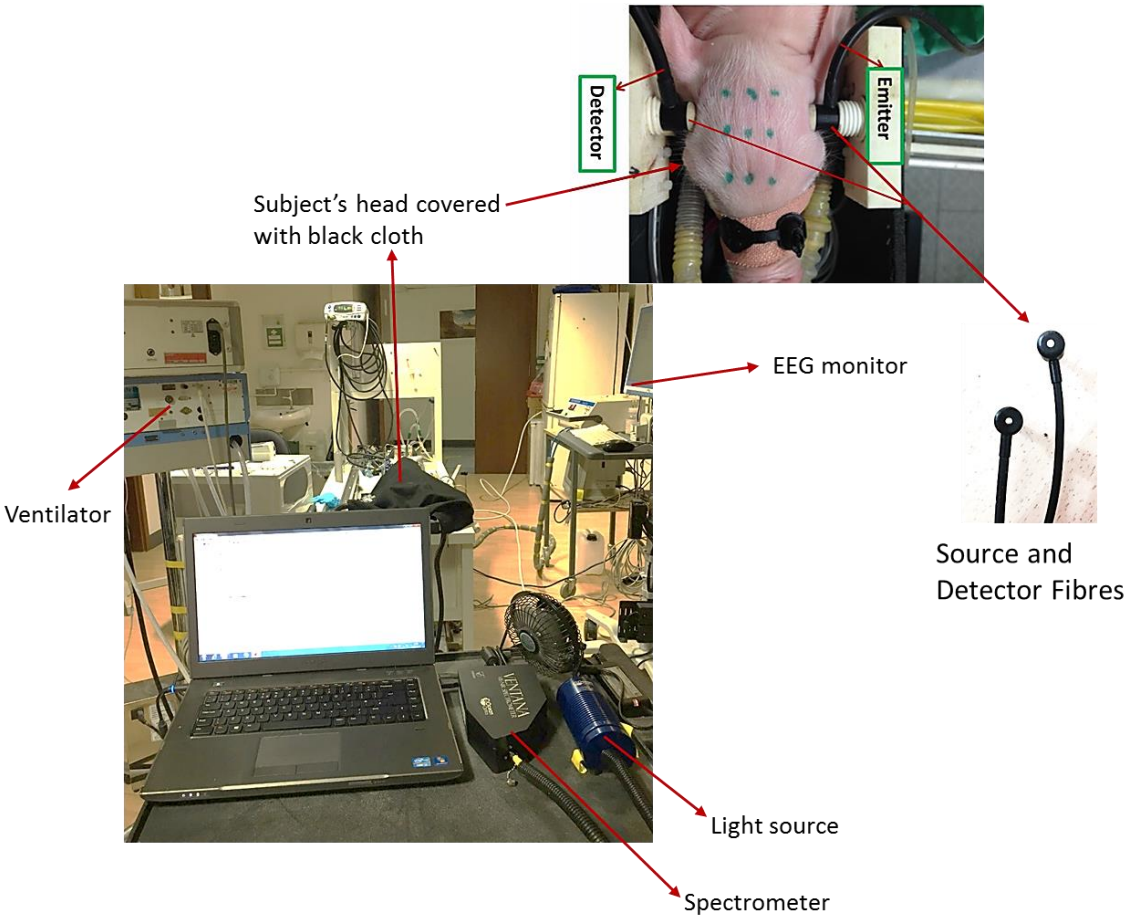

Figure 6.84: Experimental setup for piglet brain transmission mode measurement using mini-CYRIL 2 at the UCL institute of Neurology (IoN) in the preclinical study of hypoxia ischaemia

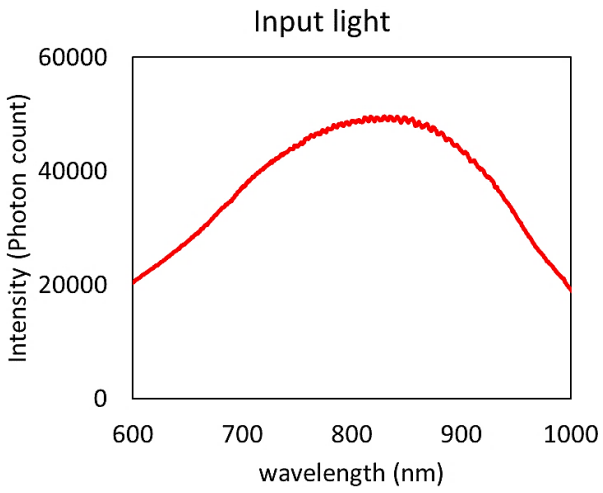

Figure 6.85: Mini-CYRIL2 Reference spectrum measurement (light input to piglet's brain).

The diffused light was collected from the surface of the head using the detector fibre as seen in Figure 6.84. Spectral data between 600 nm and 1100 nm were

continuously acquired every 10 seconds using the Ventana miniature spectrometer with retrofit cooling on (CCD temperature at 15° C), giving a signal of 10,000-30,000 electrons per digital conversion at ~810 nm and an approximate spectral resolution of 4 nm.

Mini-CYRIL software version 2.1 (See section 5.2.3) was used to produce real-time quantification of change in the concentration of HHb, HbO_2 and oxCCO through calculating optical pathlength (either through multiplying a fixed DPF with the optode distance, or through second differential spectroscopy using the second derivative of the water absorption, as proposed by Matcher et al.[1] and described in section 3.4.5). The measurements of Δ[oxCCO], Δ [HbO_2] and Δ[HHb] were defined to be zero at the point of first measurement. Therefore, their values over the course of the experiment represented the changes with respect to this first measurement. Changes in total haemoglobin concentration (Δ[HbT]),which can be used as an indicator of changes in blood volume were calculated from the sum of Δ[HbO_2] and Δ[HHb]. Also, the difference between Δ[HbO_2] and Δ[HHb] known as change in haemoglobin difference concentration Δ[HbDiff] was calculated subsequently which provides indication of tissue oxygenation and oxygen delivery [2].

This version of the software also enabled real-time calculation of the recovery fraction (RF) and area under the curve (AUTC) of the oxCCO signal (See section 5.2.4) to assist the clinicians with quantifying the HI and making sure a uniform insult is induced across all the subjects.

6.3.2 HI Protocol

For duration of approximately 10 minutes prior to insult, baseline physiological data (including heat rate, mean arterial blood pressure, arterial oxygen saturation) as well as baseline EEG and broadband-NIRS were recorded to ensure the piglets are in normal physiological condition before the induction of HI.

Figure 6.86 illustrates the protocol for the HI insult. At the beginning of HI, the occluders around carotid arteries were inflated and fractional inspired oxygen (FiO_2) was reduced stepwise from room air (~21 %) to 6 % (first being decreased to 16 %, after 1 minute to 11 %, and after 2 minutes dropped to 6%). The ‘i’ key on the data collection laptop was pressed at the start of HI, to initiate calculating the AUTC of the oxCCO signal to closely monitor the total amount of drop in oxCCO and prevent it

from dropping to critically low values. Reduction of FiO_2 to 6% usually took about 3 minutes after which the FiO_2 was held at this value for around 20 minutes while monitoring for drop in oxCCO signal (at this stage usually the electrical activity of the brain was suppressed, and the EEG was flat). During the HI, the aim was to achieve between of 3-4 μM drop in the oxidised-CCO signal and/or an AUTC between 300-400 at the end of the HI, while maintaining the mean arterial blood pressure (MABP) at or above 24 mmHg. If the oxCCO signal dropped below -3.5 μM or blood pressure reduced below 24 mmHg or was unstable, before the HI period ended, the FiO_2 was titrated (usually 1% every minute) to stabilise the animal. At the end of the insult period (lasting 20-25 minutes), the occluders were deflated and the oxygen was revived to room air while the animal was continuously monitored with mini-CYRIL2, EEG and physiological data (the 'Recovery' period in Figure 6.86).

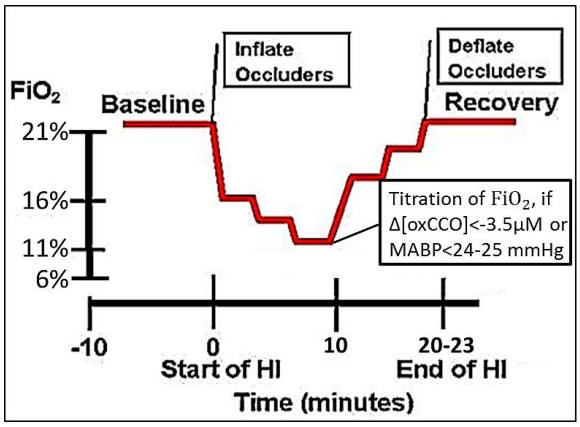

Figure 6.86: Schematic of HI insult protocol

6.3.3 Data Analysis

Data analysis in this study include broadband-NIRS cross-talk (residuals) and optical pathlength analysis, as well as resolving haemoglobin and oxCCO signals during HI and recovery that are described below. In general, the performance of mini-CYRIL2 in the preclinical study of HI was compared with the performance of the UCL1 broadband-NIRS instrument (as discussed in chapter 4 (section 4.3.3)).

6.3.3.1 Broadband-NIRS Raw Data Analysis

The intensity and attenuation spectra produced by mini-CYRIL2 was compared against the raw data produced using the UCL1 system in chapter 4. Residual analysis was also carried out for all the piglets, as proposed by Cooper et al, to evaluate the accuracy oxCCO measurement by broadband-NIRS and to ensure it is not a crosstalk from larger haemoglobin signals [3]. To investigate the spectral changes due to the oxCCO chromophore, the UCLn algorithm (equation 3.13) was used to derive changes in chromophore concentrations when solving only for HHb and HbO_2, as well as when solving for three chromophores (HHb, HbO_2, oxCCO). The attenuation change spectra were then back-calculated from the concentration changes and the difference between the measured attenuation spectra (ΔA, equation 3.10.) with the 2- and 3-chromophore fit were studied. If all the chromophores that determine the attenuation spectra were fitted, then the residual error from the measured attenuation and back-calculated attenuations must be randomly fluctuating around zero (having no defined shape). However, if the residuals have defined shapes, it would suggest that there was a chromophore that has been unaccounted for in the algorithm. For this purpose, attenuation change was measured between two points that the oxCCO signal had the maximum magnitude of change, then it was subtracted from the back-calculated attenuations from 2- and 3-chromophores fit at those specific points. A script was developed in MATLAB to carry out the residual analysis for all studies.

6.3.3.2 Concentration Data Analysis during HI and Recovery

Changes in the concentration of chromophores produced by mini-CYRIL2 during insult and recovery were calculated using two different approaches for pathlength estimation; fixed DPF and differential pathlength measured through second derivative spectroscopy technique (see chapter 5, sections 5.2.2 and 5.2.3). The concentration data produced by these two methods were validated using the data that UCL1 generated for similar HI studies in piglets (discussed in chapter 4) to ensure mini-CYRIL2 measurements reflect true physiology in piglets.

When group data were used, results were mean ± standard deviation (SD).

6.4 Results

6.4.1 Mini-CYRIL2 – Broadband NIRS Raw Data Analysis

Changes in the intensity of light traversed through a piglet's brain during baseline and hypoxia-ischaemia is displayed in Figure 6.87 (a). The intensity spectra produced by mini-CYRIL2 have two features around 760 nm and 830 nm attributed to HHb and oxidised-CCO (See absorption spectra of chromophores, Figure 3.13, section 3.1.2). During HI, a larger number of photons manage to exit the brain due to the reduction in blood flow and blood volume in the brain, hence less light attenuation. Table 6.9 presents average peak and mean intensity incident and transmitted through piglets' brain across 780-900 nm (n=24).

Change in the attenuation of light trough the piglet's brain during nadir HI, relative to the first measurement, is presented in Figure 6.87 (b). As can be seen in the figure, at baseline, there is no major change in magnitude and shape of the attenuation spectrum relative to the first measurement. However, during HI, there is a significant change in the magnitude and shape of the attenuation spectrum due to the physiological changes in the brain, i.e. reduction in blood flow and oxygenation.

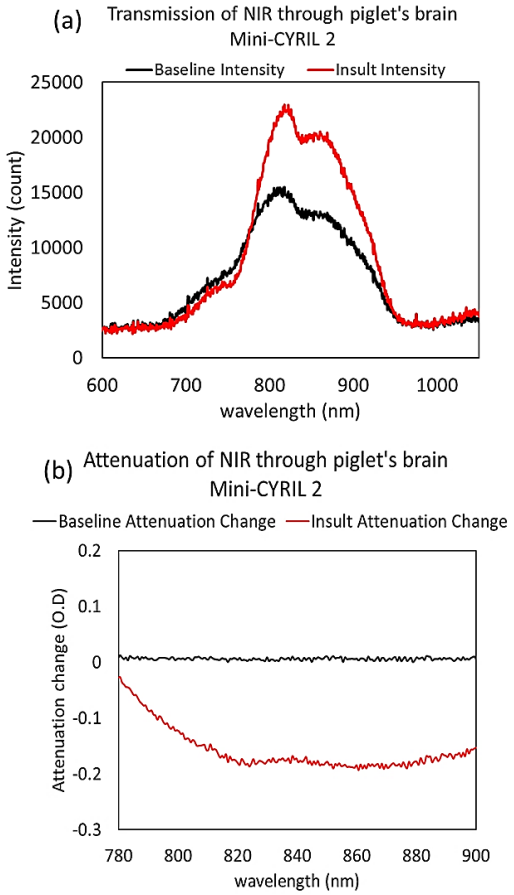

Figure 6.87: (a) Changes in the intensity of light traversed a piglet's brain during baseline and nadir HI. (b)Attenuation change at baseline and during HI relative to the first measurement.

Table 6.9: Average peak intensity of light going in and coming out of the piglet's brain measured with mini-CYRIL2 at baseline (source-detector spacing being 4.2 ± 2 cm) in 24 piglets.

Light into piglets' brain n=24	**Photon Count ± SD / Integration Time**	**Wavelength (nm)**
Group mean Peak intensity	52981 ± 54 / 100 ms	839 ± 6
Group mean intensity across all wavelengths	50817 ± 1937 / 100 ms	780 – 900
Light out of piglets' brain n=24		
Group mean peak intensity	12296 ± 4841 / 10 s	810 ± 4
Group mean intensity across all wavelengths	9685 ± 3711 / 10 s	780 – 900

6.4.1.1 Comparison of the Raw Data from Mini-CYRIL2 and UCL1

There is a slight difference in the shape of the input spectrum produced by both systems, due to different characteristics of the light source and detection units, including the quantum efficiency and size of the CCDs (large, high quantum efficiency CCD in UCL1, with maximum photon count of 25×10^4, versus the miniaturised CCD used in Ventana spectrometer with maximum photon count of 6×10^4 as seen in Figure 6.88. Furthermore, the CCD camera in the UCL1 system is cooled down to -70° C hence significantly reduces the thermal noise, which is clearly seen in Figure 6.88).

As well as the CCD specifications, the higher throughput design and the larger core diameter of the source and detector fibres in the UCL1 system (3.3 mm in UCL1 versus 2.3 mm in mini-CYRIL2 which is SMA limited) lead to a much greater intensity signal than mini-CYRIL2. Limitations with miniature spectrometers have been thoroughly discussed in chapter 5, section 5.1. However, mini-CYRIL2 produces a broader wavelength range which is a benefit for broadband-NIRS measurement.

Even though the transmission intensity spectra produced by mini-CYRIL2 has considerably lower peak count (nearly half the counts generated by UCL1 at HI), the spectral features are comparable to the spectra from UCL1, demonstrating mini-CYRIL2's high signal to noise and spectral resolution. Please note that these measurements were performed in two different animals during two different insult protocols (Sections 6.3.2 and 4.3.4).

The attenuation spectra measured during baseline and insult using mini-CYRIL and UCL1 are compared in Figure 6.89. In both systems, there is no change in the attenuation during baseline. At hypoxia-ischaemia however, there is a significant drop in the attenuation of transmitted light due to reduction in blood flow and oxygen supply.

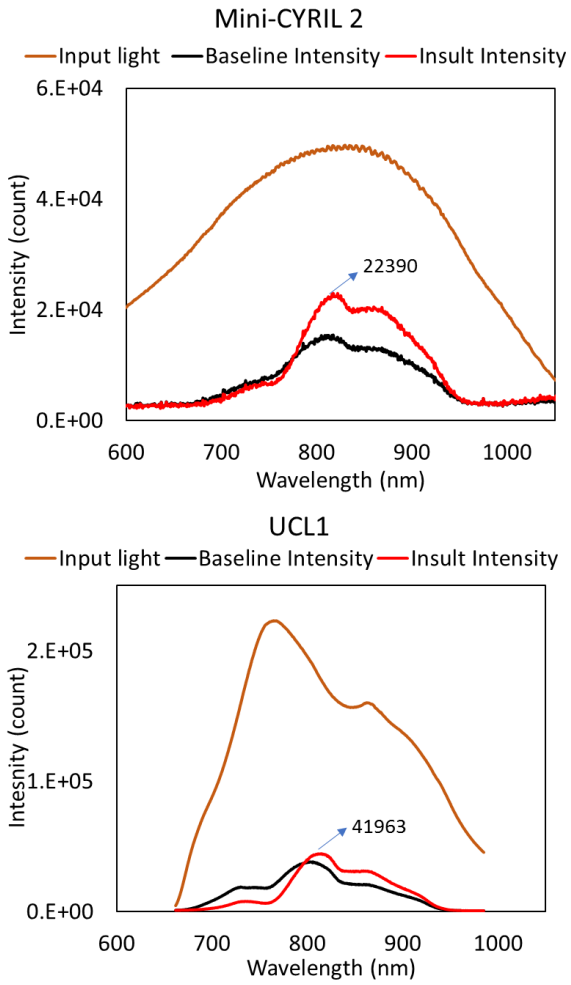

Figure 6.88: Incident and transmitted light spectra trough a piglet's brain during baseline and hypoxia-ischaemia (HI). Lower counts in the reference spectrum using mini-CYRIL2 is due to the limitation of CCD that saturates above 60000 counts.

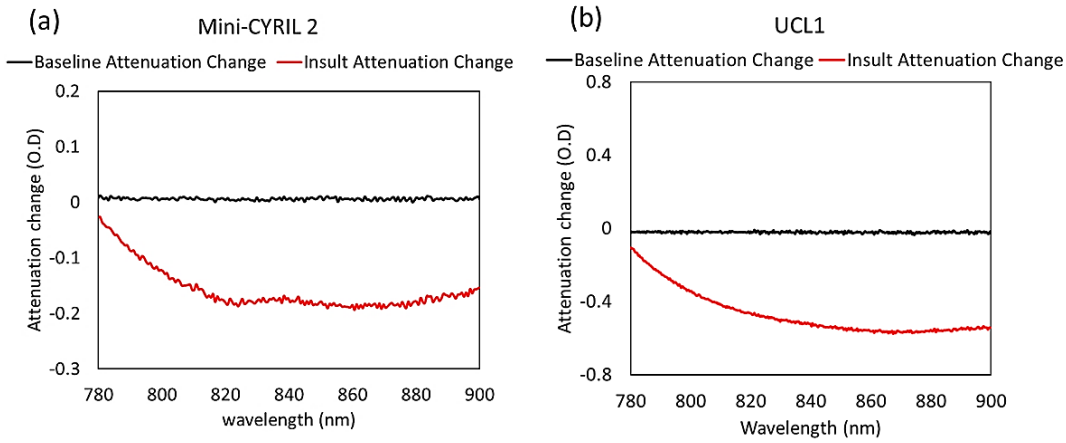

Figure 6.89: Attenuation spectra measured at baseline and insult using mini-CYRIL2 (a) and UCL1 system (b)

6.4.1.2 Residual Analysis

Figure 6.90 illustrates the residual analysis to investigate crosstalk in mini-CYRIl2's oxCCO measurement. Measured attenuation spectrum at HI as well as the back-calculated attenuations from 2- and 3-chromophore fit were studied. The back-calculated attenuation from 3-chromophore fit (in blue) matched the measured attenuation whilst the back-calculated attenuation when solving only for 2 chromophores (red), does not fit the measured attenuation (Figure 6.90 a). This shows that all the chromophores were not accounted for when resolving only for 2 chromophores. The residual errors from fitting back-calculated attenuation spectra when solving for 2- and 3-chromophores are shown in Figure 6.90 b. The residual error from 2-chromophore fit has a well-defined shape that matches the extinction coefficient spectrum of oxidised-reduced CCO between 780-900 nm. Therefore, it shows that when resolving only for HHb and HbO_2, the oxCCO remains unaccounted for. However, when solving for 3-chromophore (including oxCCO), the residual error randomly fluctuates around zero that shows all the chromophores in the field of view have been accounted for in the measurement.

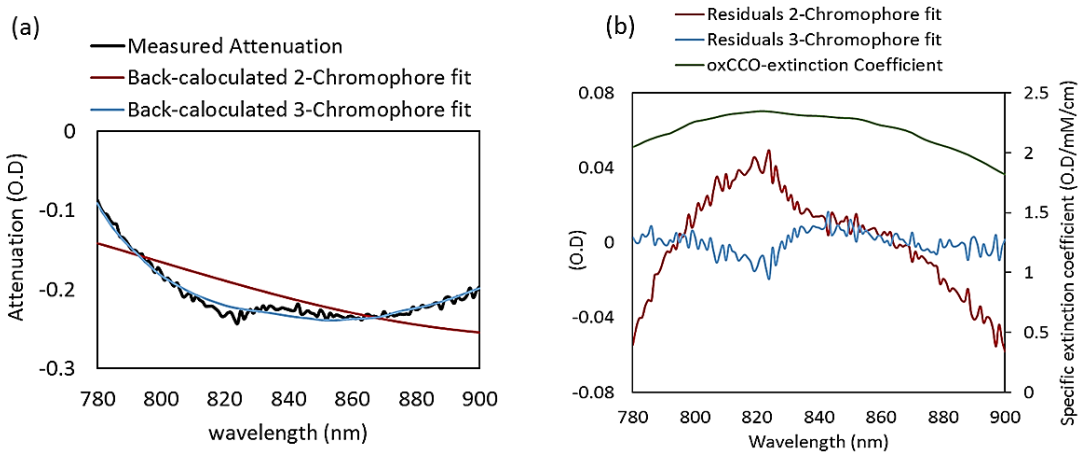

Figure 6.90: (a) Measured attenuation spectrum at HI and back-calculated attenuations from 2- and 3-chromophore fit (b) Residual error from 2- and 3- chromophore fit. The 2-chromophore fit residuals (in red) matches the extinction coefficient of oxCCO (in green), whilst the 3-chromophore fit's residual error (in blue) randomly oscillates around zero.

Figure 6.91 shows the residual errors from 2- and 3-chromophore fit for 24 piglets and Figure 6.92 presents the mean residuals with standard errors for 2- and 3-

chromophore fit for all the piglets in the experiment which follows the same pattern as discussed above.

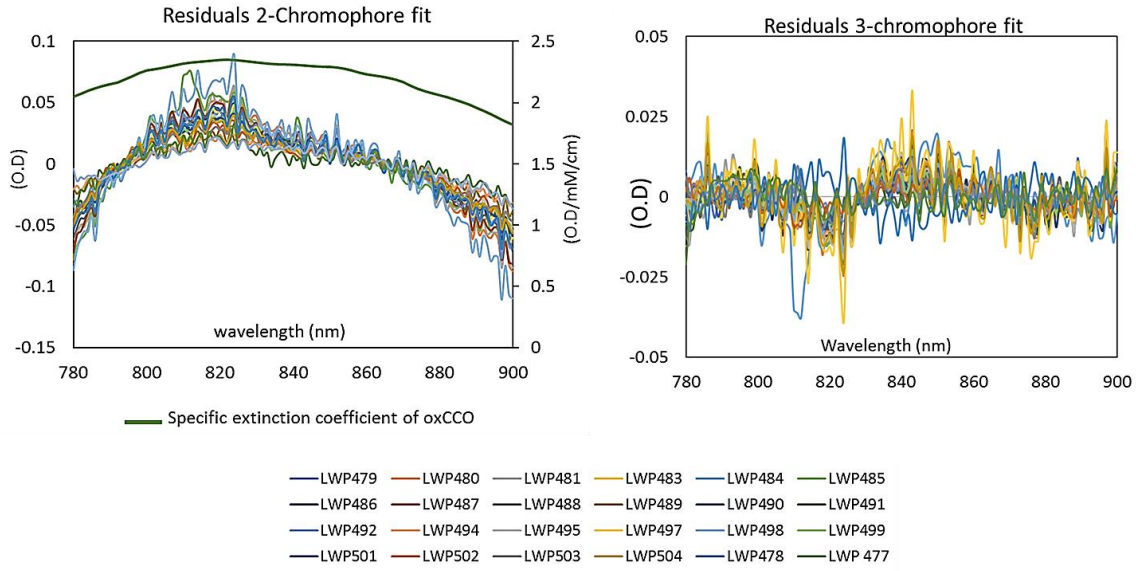

Figure 6.91: Residual errors from 2- and 3- chromophore fit for all the piglets in the experiment (n=24).

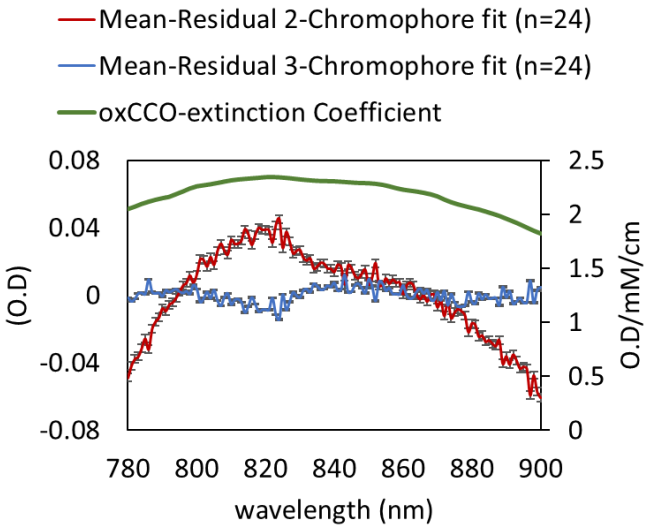

Figure 6.92: Mean residual with standard errors from 2- and 3- chromophore fit for all the piglets in the experiment (n=24).

The average mean residual from 2-chromophore fit across all wavelength is 0.002 ± 0.030 (O.D) with a peak of 0.045 O.D at 824 nm, showing that a chromophore

with peak absorption in this wavelength range (similar to oxCCO extinction coefficient spectrum) was not accounted for when resolving only for HHb and HbO_2. However, when oxCCO is considered in the calculations, the average mean residual from 3-chromophore fit across all wavelength (780-900) is 0 ± 0.005 (O.D) with 4 decimal place precisions, demonstrating a perfect fit when resolving for 3 chromophores.

6.4.3 Mini-CYRIL2 Concentration Data Analysis During HI and Recovery

As mentioned in chapter 3 (section 3.1.5), the true optical pathlength exceeds the geometric pathlength (source-detector separation) by a factor called differential pathlength factor (DPF). Most broadband-NIRS systems including the ones developed recently at UCL [4], [5] assume a fixed tissue DPF (measured using time-resolved systems) to estimate the optical pathlength. The UCL1 system however, used the raw attenuation and water absorption spectra to estimate real time changes of pathlength in the tissue based on the known concentration of water (with accuracies of a few percent) using the method proposed by Matcher et al [1], which accounts for real-time changes in tissue scattering and was fully describe in chapter 3, section 3.4.5.

As mentioned in chapter 5, both mini-CYRIL versions are capable of calculating the concentration change in [HHb], [HbO_2] and [oxCCO] using either fixed DPF or second differential spectroscopy of water (sections 5.2.2 and 5.2.3). In this study, we propose calculation of chromophores' concentration during HI and 1-2 hours recovery in new-born pigs, calculated via both pathlength estimation methods. The concentration data were then validated via comparing with the concentration values produced by UCL1 (chapter 4).

6.4.3.1 Fixed DPF for the Optical Pathlength:

By using a predefined optical pathlength, a tissue specific value (DPF) is assumed to account for the effect of tissue scattering. In this study, the DPF for piglet's brain was assumed 4.99 as measured by Duncan et al. for new-born infants [6] (since piglets have the same structural developments as new-born infants). Changes in concentration of HHb, HbO_2 and oxCCO during hypoxia-ischaemia (HI) in a piglet as measured by mini-CYRIL2 based on DPF = 4.99 and source-detector spacing of 4.2

cm, are shown in Figure 6.93. At baseline when the piglet was at normal physiological condition and there were no variations in oxygen levels (FiO_2 ~21%), all the NIRS signals were nearly stable. As soon as the insult initiated (shown in shaded red area), that is when occluders around the carotid arteries were inflated and FiO_2 dropped from 21% to 16% and arterial oxygen saturation (SpO_2) reduced from its initial value (~97%), broadband NIRS measure of $\Delta[HbO_2]$ decreased to minimum of -11.5 μM and Δ[HHb] in the field of view increased to maximum of 13.1 μM. During HI, Δ[HbT] increased briefly to 2.4 μM before slightly decreasing later to -0.7 μM. The Δ[HbDiff] signal drastically dropped at HI initiation reaching its minimum (-24.1 μM) just before titration started. Measurement of Δ[oxCCO], fell rapidly at the start of HI minimising during titration to -3.6 μM and then increased during recovery.

As soon as the titration of oxygen started (lightly shaded), oxygenated haemoglobin increased, however, oxCCO signal continued to drop demonstrating the independence of the oxCCO from haemoglobin signal. At the end of insult, when occluders were deflated and inspired oxygen was returned to normal (see the FiO_2 and SpO_2 measurement), all the NIRS signals started recovering back to baseline values.

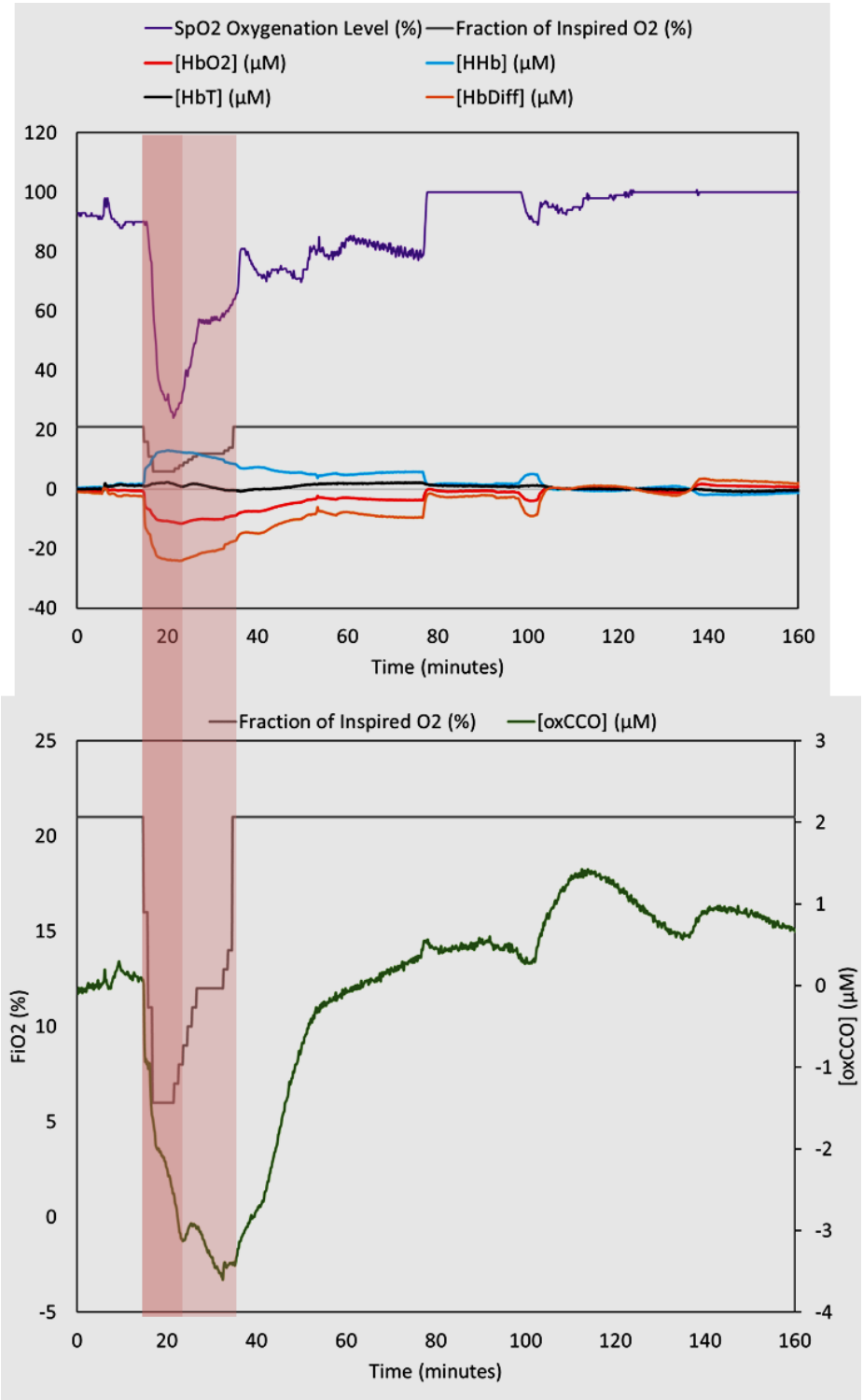

Figure 6.93: Changes in NIRS signals during HI. FiO_2 (fractional inspired oxygen) and SpO_2 (arterial oxygen saturation) are plotted to show changes in broadband-NIRS in response to changes in oxygen levels. The dark shaded area indicates the initial phase of the insult (when oxygen is gradually decreased to 6 %) and the light shaded area shows the titration phase, when oxygen is increased in steps until the end of the insult (FiO_2 = 21 %). The step change in the SpO_2 signal around 80 minutes is due to the pulse oximeter malfunction. Insult schematic is shown in Figure 6.86.

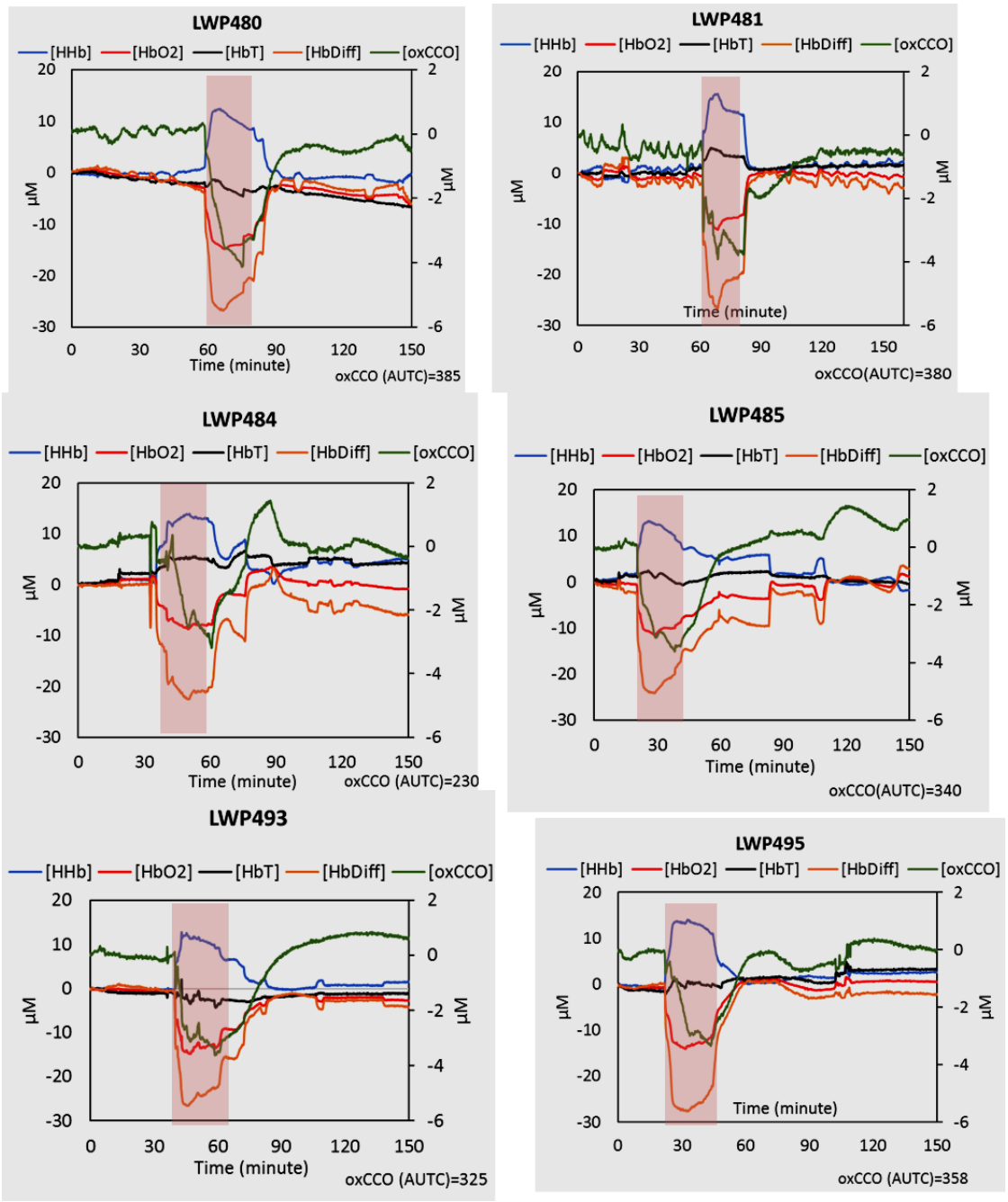

Figure 6.94 : Changes in total haemoglobin concentration (Δ[HbT]), haemoglobin difference concentration (Δ[HbDiff]), oxy-haemoglobin concentration (Δ[HbO2]), deoxy-haemoglobin concentration (Δ[HHb]) and the concentration of oxidized cytochrome-c-oxidase (Δ[oxCCO]) during HI. The shaded area indicates the HI period. Insult schematic is shown in Figure 6.86.

Figure 6.94 presents other examples of changes in the concentration of HHb, HbO_2, oxCCO, as well as HbT and HbDiff as measures of blood volume and oxygenation

respectively in 6 piglets, during HI and up to 90 minutes recovery. Even though there were some differences between the HI protocol in chapter 4 and in this study, changes in the concentrations of NIRS chromophores had the same pattern when measured with mini-CYRIL2 and with UCL1. The magnitudes of maximum change in the concentrations during HI are summarised in Table 6.10. In all the piglets (n = 24), there was a consistent trend in changes in the concentration of chromophores. At the beginning of HI, there was a dramatic increase in Δ[HHb] (mean maximum 14.4 ± 2.1 μM) and a decrease in Δ[HbO_2] (mean minimum -13.6 ± 2 μM). During HI, Δ[HbT] generally increased momentarily (mean maximum during initial HI 2.97 ± 1.85 μM) before dropping later (mean minimum -2.74 ± 2.76 μM) and Δ[HbDiff] declined at HI initiation reaching its minimum value before titration providing an indication of tissue ischaemia (mean minimum during HI period (-27.17 ± 2.75 μM). In all piglets, Δ[oxCCO] dropped rapidly at the start of HI and minimised during titration (mean minimum -3.6 ± 1.2 μM) and then increased during recovery towards baseline. These trends of change in NIRS signals during HI and recovery agree with what has was reported by Bainbridge et al. in 2014 [7]. In a comprehensive study, our colleagues at the UCL Institute of Neurology (IoN) investigated brain mitochondrial oxidative metabolism during and after cerebral HI in new-born pigs by simultaneous phosphorus MRS and broadband-NIRS (UCL1) measurement.

The drop in [HbO_2] and rise in [HHb] during HI was due to the limited oxygen availability (hypoxia) and restricted blood (ischaemia) in the brain. Bainbridge and colleagues demonstrated that the drop in Δ[oxCCO] during HI was strongly associated with the drop in ATP, by extension, the ^{31}P-MRS measurement of NTP/epp [7]. Therefore, the decreased oxCCO during HI could be interpreted as impairment of the mitochondrial ETC due to insufficient blood and oxygen supply. In other word, significant drop in oxygen as the final electron acceptor in the ETC led to reduction of oxCCO which in turn resulted in the failure in production of ATP through ATP synthase. During recovery from HI not only were the [HbO_2] and [HHb] restored, but also the [oxCCO] signal started to recover as the ETC activity recovered and oxidative phosphorylation resumed. However, in some of the piglets the primary damage was so severe that the [oxCCO] signal did not recover to baseline within an hour after the resuscitation such as LWP486 and LWP503 (Table 6.10).

Table 6.10: Changes in mini-CYRIL2 signals during HI based on fixed optical pathlength (DPF=4.99). All the concentartion changes are expressed in μM.

Subject	Δ[HHb]	Δ[HbO_2]	Δ[oxCCO]	Δ[$HbT]_{max}$	Δ[$HbT]_{min}$	Δ[HbDiff]	oxCCO AUTC (%)	oxCCO 1h-RF (%)
LWP479	14.31	-16.84	-4.07	1.44	-10.90	-27.90	430	61.4
LWP480	12.43	-14.78	-4.14	0.23	-4.66	-26.73	385	81.4
LWP481	15.60	-11.11	-3.92	5.01	-0.76	-26.71	380	91.8
LWP483	18.48	-12.06	-6.91	4.40	-0.23	-26.75	322	78.10
LWP484	13.90	-8.74	-3.19	6.64	-0.06	-22.49	230	90.28
LWP485	13.12	-11.55	-3.60	2.39	-0.74	-24.08	340	109.84
LWP486	11.03	-14.11	-4.42	0.20	-1.25	-24.71	355	8
LWP487	14.88	-16.08	-3.56	4.51	-6.45	-29.36	349	63.92
LWP488	17.22	-13.71	-2.18	5.27	0.00	-30.27	150	138.79
LWP489	10.25	-11.43	-3.57	0.51	-3.51	-21.47	332	51.96
LWP490	14.69	-13.70	-3.35	2.39	-2.09	-27.92	327	80.34
LWP491	16.68	-14.66	-3.64	4.00	-1.07	-31.27	294	106.87
LWP492	15.93	-12.89	-1.79	4.13	-0.80	-27.91	170	110.18
LWP493	12.84	-14.80	-3.61	2.07	-4.30	-26.64	325	122.84
LWP494	11.93	-11.47	-3.31	2.45	-0.46	-23.26	298	87.37
LWP495	14.18	-14.09	-3.34	1.48	-2.12	-27.62	358	89.55
LWP497	17.85	-14.26	-6.70	4.56	-4.66	-31.97	727	116.36
LWP498	15.63	-13.51	-3.29	3.65	-0.08	-28.26	298	102.77
LWP499	12.99	-14.06	-3.35	0.50	-4.88	-26.05	502	63.9
LWP500	16.31	-12.21	-1.89	5.28	-0.20	-28.48	162	171.69
LWP501	15.90	-15.22	-2.89	5.19	-3.62	-30.07	275	91.14
LWP502	13.19	-18.11	-2.35	1.63	-7.66	-30.43	241	80.93
LWP503	15.20	-14.63	-3.21	2.07	-4.27	-28.43	311	26.15
LWP504	11.89	-11.65	-4.04	1.32	-1.00	-23.32	332	67.61

6.4.3.2 Estimated Differential Pathlength at 840 nm

In this section, the NIRS concenatrtion data calculated based on differential pathlength at 840 nm (measured using the absolute attenuation data, as explained in section 5.2.3) will be discussed.

Figure 6.95 illustrates changes in the concenatrtion of HHb, HbO_2, HbT, HbDiff and oxCCO during HI and approximately 2 hours after the insult, calculated based on a changing pathlength that was calculated using the known concenatrtion of water in piglet's brain. It can be seen that there is a minor drop in the pathlength during HI (shaded area), which gradually recovers back to baseline after rescusitation. However, the overal mean pathlength is (15 ± 0.98 cm) is around 30% (6.5 cm) smaller than when pathlength was estimated using a fixed DPF (4.99) and source-detector spacing of 4.3 cm. The minor drop in optical pathlength during HI could be indicative of ischaemia leading to a reduction in light absorption and scattering through piglet's brain.

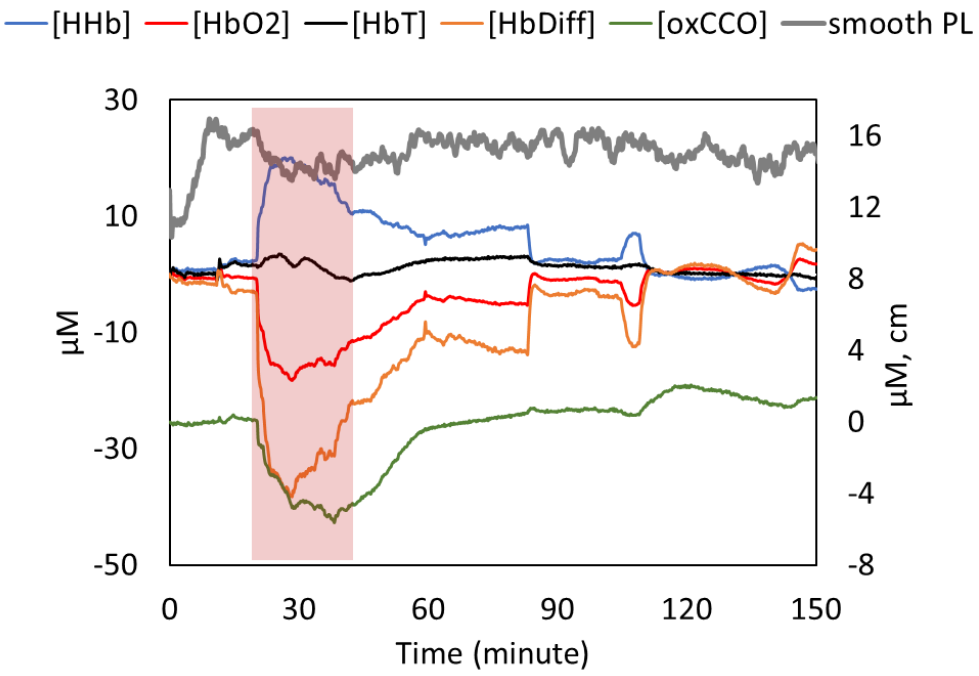

Figure 6.95: Changes in NIRS measurements during HI, as measured by mini-CYRIL2 based on second derivative spectroscopy for pathlength change measurement. The shaded area indicates the HI period.

Changes in the optical pathlength for individual piglets (n=10) can be observed in Figure 6.96 , which illustrates pathlength changes during baseline, HI and up to 2 hours recovery for n=10 piglets. It can be seen that there are only slight changes in

pathlength during HI in most of the pigs, considering the dramatic large changes in chromophores' concentrations during HI that can be seen clearly in Figure 6.95. This observation means that the criteria for accurate measurement of oxCCO is met, as there should be no large changes in pathlength during the measurement [3]. However, the mean pathlength during the experiment is different between different subjects, even though the source-detector spacing for all the subjects was kept the same (between 4 - 4.3 cm depending on the size of the head). This difference in true optical pathlength was further investigated and no association was found between the small differences in source-detector spacing with the increased/decreased optical pathlength as can be seen in Figure 6.97 (Coefficient of determination for correlation, R^2=0.07).

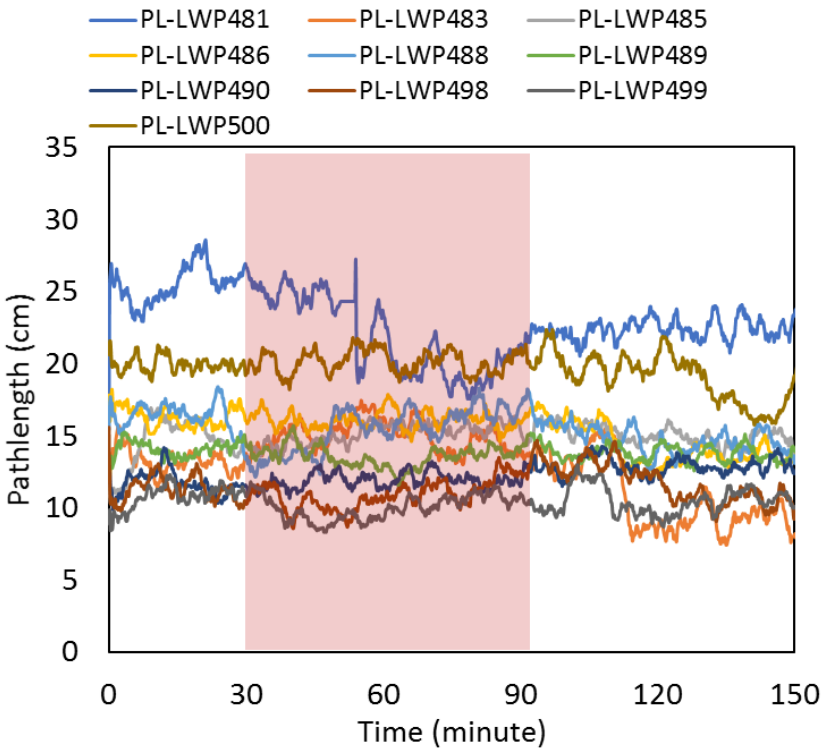

Figure 6.96: Variations in optical pathlength in different piglets during the experiment (baseline, HI and recovery period). The HI period for all the animals is shaded.

The dispersion in the differential pathlength among different subjects (mean 15 ± 4 cm, range 12.5 cm) despite almost the same optode spacing (mean 4.2 ± 0.1 cm, range 0.3 cm), could significantly affect the concentration measurement as concentration changes are inversely affected by the optical pathlength according to the modified Beer-Lambert law (Chapter 3, equation 3.13). Therefore, using fixed DPF in

this study, has led to underestimation of changes in [HHb], [HbO_2] or [oxCCO] which is specifically important when clinicians use the magnitude of change in the concentrations as a lead to direct the HI.

The influence of pathlength estimation method on the concentration change data during HI and recovery was further investigated and is discussed in the following section.

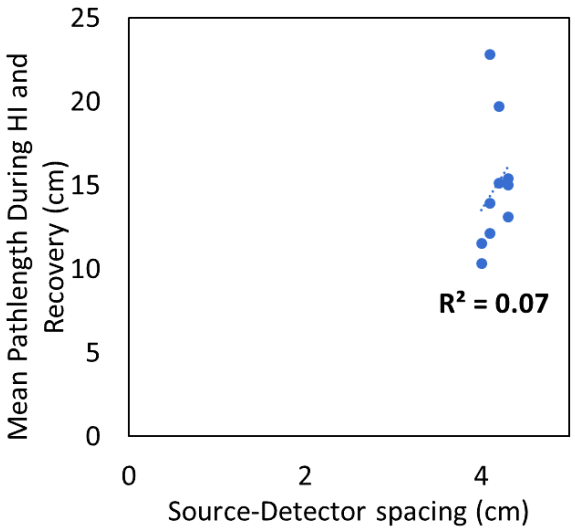

Figure 6.97: The relationship between mean optical pathlength measured through second derivative spectroscopy with source-detector spacing in n=10 piglets, showing no association between increased optical pathlength with source-detector separation.

6.4.3.3 Comparison between Calculated Concentration of Chromophores During HI using Fixed and Real-time Pathlength Estimation

Figure 6.98 illustrates changes in [HHb], [HbO_2] and [oxCCO] during HI and recovery based on fixed DPF method and source-detector separation for calculating pathlength, which is shown in dashed purple line, and using second differential of absolute attenuation and water absorption spectra to estimate differential pathlength at 840 nm (chapter 5, section 5.2.4).

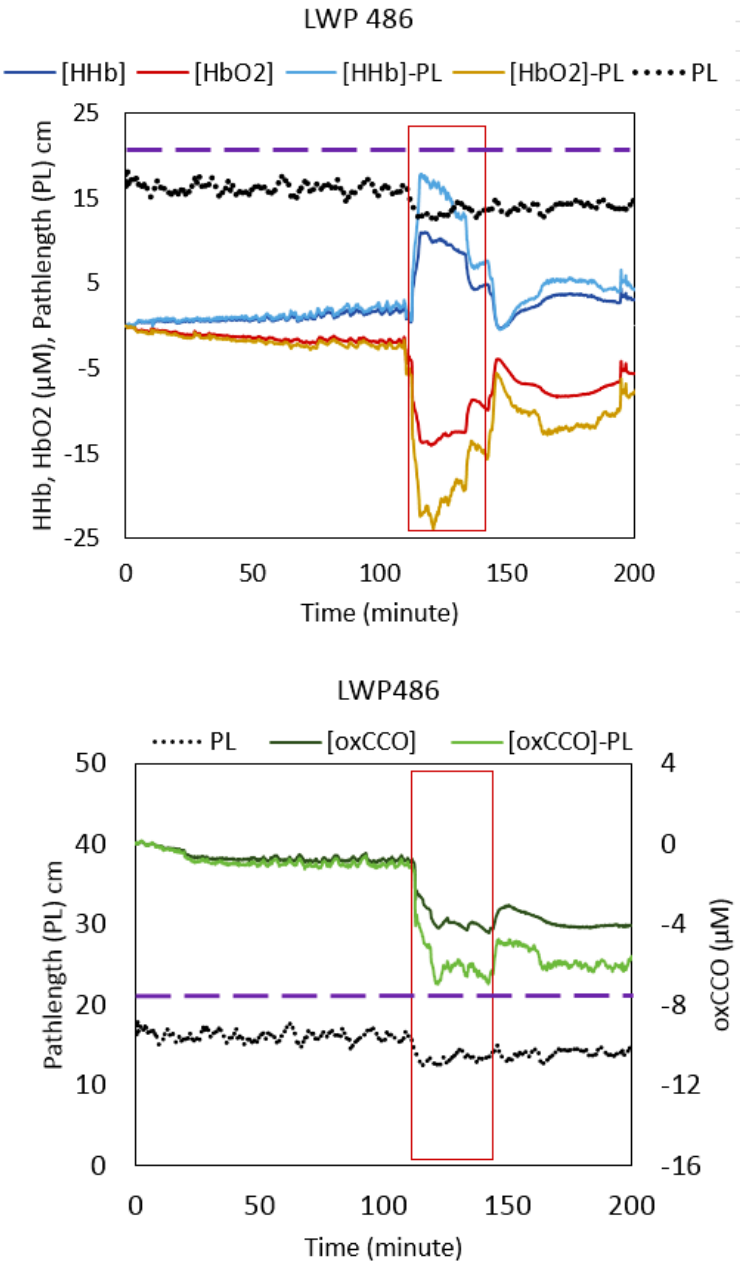

Figure 6.98: Comparison between measured change in [HHb], [HbO_2] and [oxCCO] when a fixed pathlength shown in purple dashed line, is used (DPF=4.99 and d=4.2 cm) and when changes in pathlength is estimated using second differential of absolute attenuation spectra as proposed by Matcher et al [1] (see chapter 5, section 5.2.4).

The mean optical pathlength measured through absolute attenuation measurement was 15.1 ± 1.3 cm which was approximately 5 cm (28%) smaller than the estimated pathlength using a fixed DPF (4.99) and optode spacing of 4.2 cm. As a result of this difference, when using a fixed DPF, the concentration of [HHb], [HbO_2]

and [oxCCO] were underestimated (Table 6.10) around 23% at baseline for all chromophores, more than 38, 40 and 37% for [HHb], [HbO_2] and [oxCCO] respectively at nadir HI (when the pathlength value decreased by 23%, as can be seen in Figure 6.98) and 33% during recovery for all chromophores.

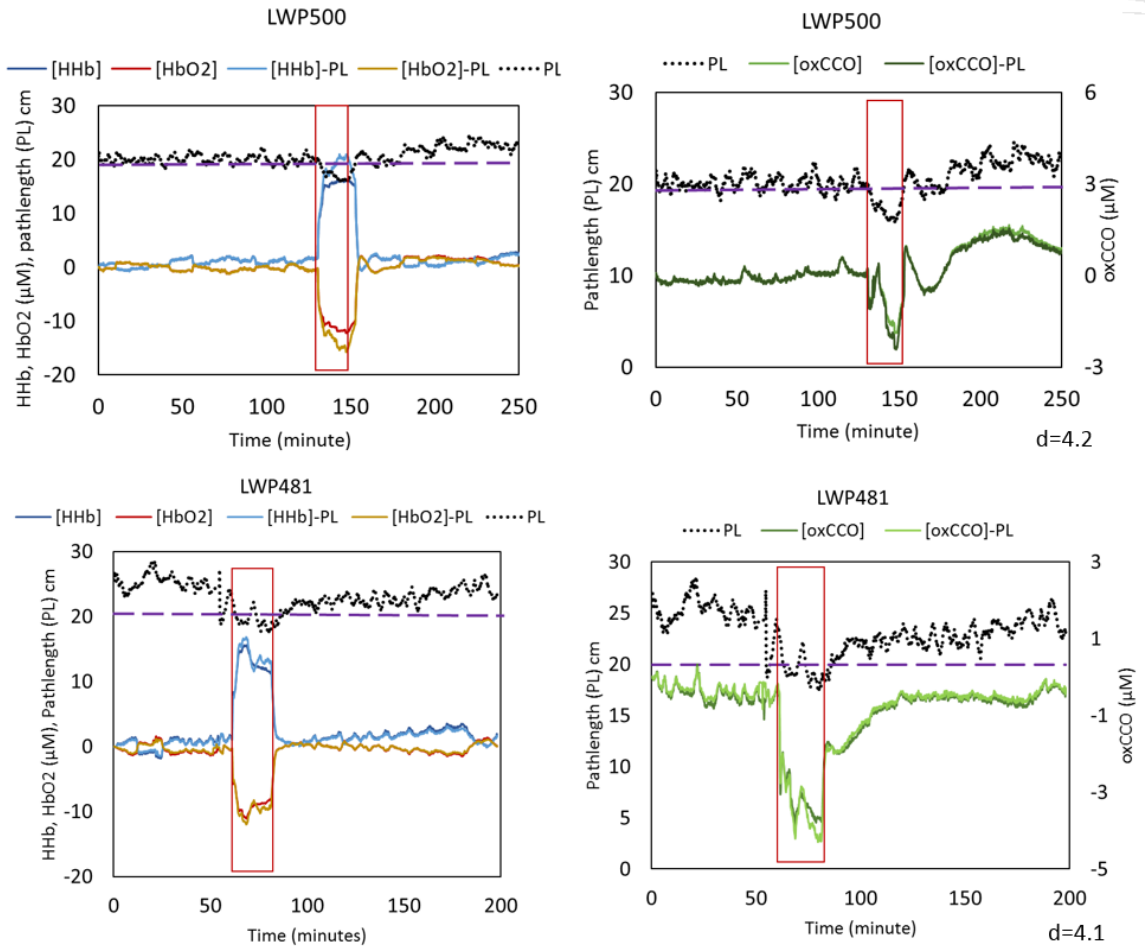

Figure 6.99: Examples of estimated fixed pathlnegth (DPF=4.99) almost fitting the measuerd pathlength based on absolute attenuation spectra. There are minor differences between concenatrtion data between measured change in [HHb], [HbO_2] and [oxCCO] when a fixed pathlength shown in purple dashed line, is used (DPF=4.99 and d=4.2 cm and 4.1 cm) and when changes in pathlength is estimated using second differential of absolute attenuation spectra. There is a 24 % and 28 % drop in pathlength in LWP500 and LWP481 respectively that leads to underestimation of NIRS measurements at nadir HI.

Figure 6.99 presents examples from 2 piglets in which the pathlength estimation at fixed DPF almost fits the differential pathlength measured through absolute light attenuation at 840 nm. The concentration data based on fixed DPF measurement also

fit the concentration data using second differential pathlength estimation. However, at nadir HI, when the pathlength dropped by ~24 % in LWP500 and ~28 % in LWP481, using a fixed DPF led to 22 % underestimation of all the NIRS signals in LWP500 and less than 8 % in LWP481.

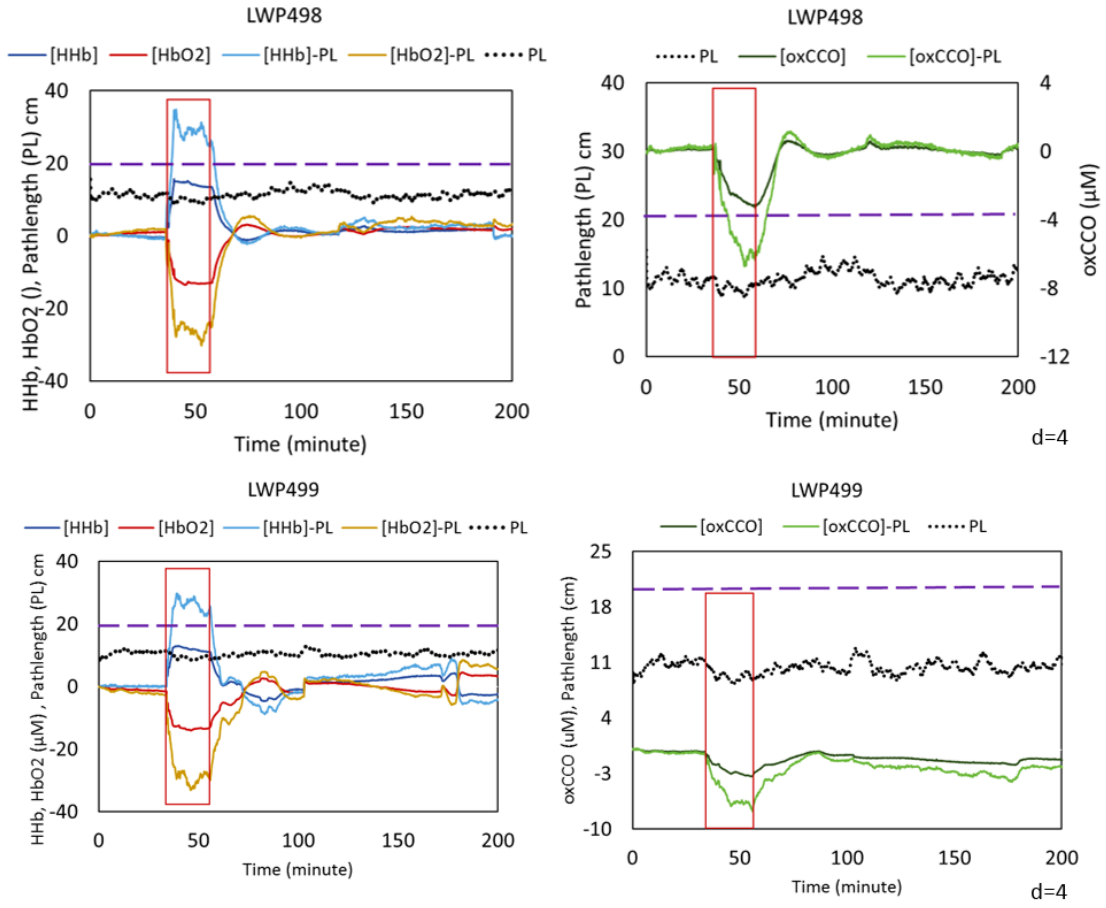

Figure 6.100: Examples of estimated fixed pathlnegth (DPF=4.99) significantly overestimating the measuerd pathlength based on absolute attenuation spectra. There are significant differences between concentration data between measured change in [HHb], [HbO_2] and [oxCCO] when a fixed pathlength shown in purple dashed line, is used (DPF=4.99 and d=4 cm) and when changes in pathlength is estimated using second differential of absolute attenuation spectra. Largest contrast between concentration measurements using two pathlength estimation technique is seen at nadir HI when there is a further 20% drop in the optical pathlength.

Figure 6.100 and Figure 6.101 illustrate six other examples of when the pathlength estimated using fixed DPF, significantly overestimates the actual pathlength changes during the measurement period and it can be clearly seen that the concentration changes were considerably underestimated in all cases, mostly at nadir HI when there is a further 20% drop in the optical pathlength.

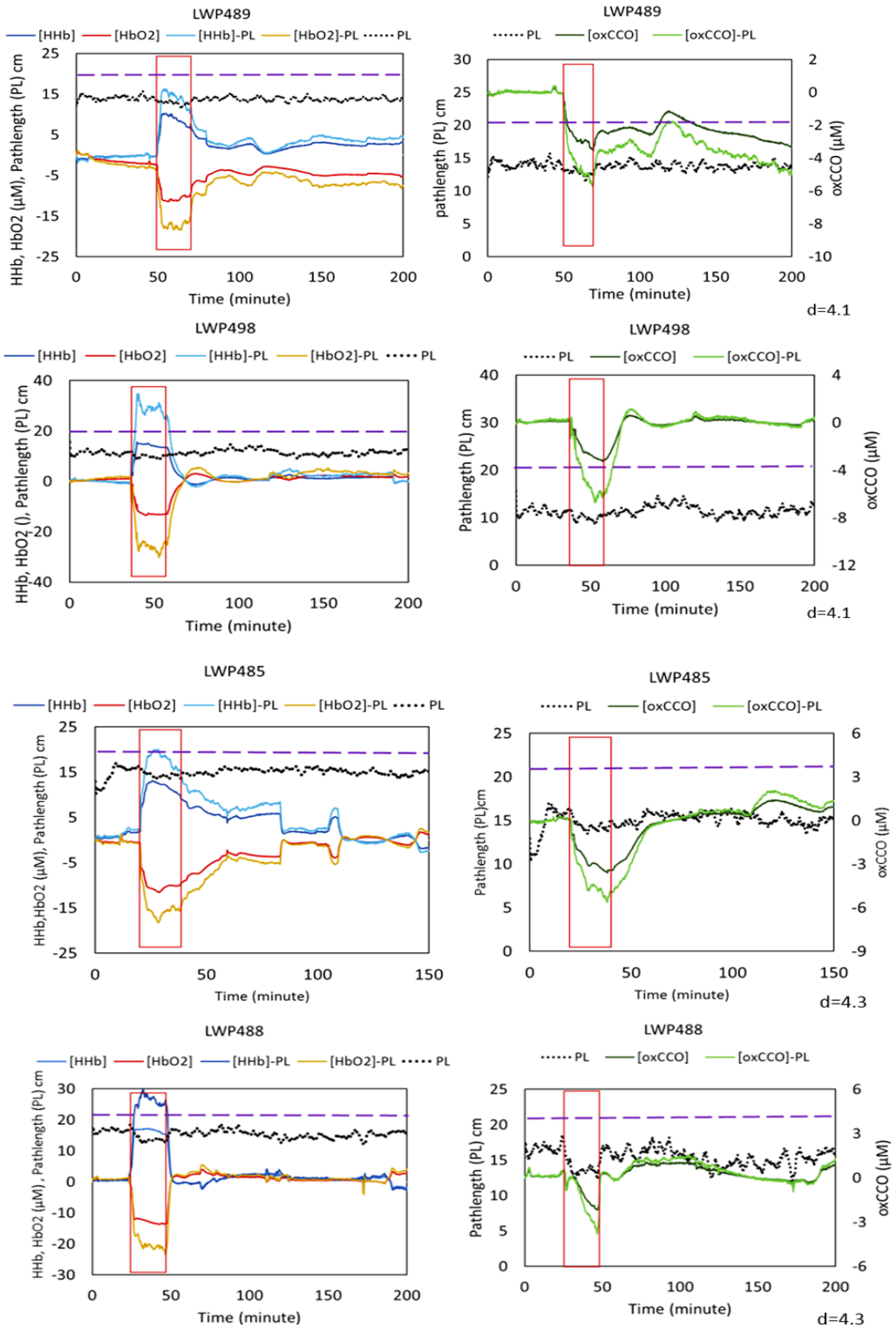

Figure 6.101: Examples of estimated fixed pathlnegth (DPF=4.99) significantly overestimating the measuerd pathlength based on absolute attenuation spectra. There are significant differences between concenatrtion data between measured change in [HHb], [HbO_2] and [oxCCO] when a fixed pathlength shown in purple dashed line, is used (DPF=4.99 and d=4.1 and 4.3 cm) and when changes in pathlength is estimated using second differential of absolute attenuation spectra. Largest contrast between concentration measurements using two pathlength estimation technique is seen at nadir HI when there is a further 20% drop in the optical pathlength.

Table 6.11: Maximum changes in NIRS measurements during HI as measured with mini-CYRIL2 based on real-time pathlength measurement

Subject	$\Delta[HHb]_{HI}$ (μM)	$\Delta[HbO_2]_{HI}$ (μM)	$\Delta[oxCCO]_{HI}$ (μM)	$max\Delta[HbT]_{HI}$ (μM)	$min\Delta[HbT]_{HI}$ (μM)	$\Delta[HbDiff]_{HI}$ (μM)	Mean Pathlength (cm)
LWP481	16.8	-12.0	-4.3	5.4	-0.6	-28.8	22.8 d=4.1
LWP483	25.5	-20.5	-5.4	21.0	-0.4	-45.9	13.1 d=4.3
LWP485	20.0	-18.2	-5.6	3.6	-1.1	-38.2	15.0 d=4.3
LWP486	17.9	-23.9	-7.0	1.4	-8.3	-41.0	15.1 d=4.2
LWP488	29.8	-23.4	-3.8	8.4	-4.3	-51.3	15.4 d=4.3
LWP489	16.3	-18.4	-6.0	3.8	-5.5	-34.3	13.9 d=4.1
LWP490	28.1	-27.1	-6.2	4.3	-4.3	-55.2	12.1 d=4.1
LWP498	34.8	-30.3	-6.7	14.3	-0.1	-62.7	11.5 d=4
LWP499	29.7	-33.1	-7.7	5.6	-10.4	-61.4	10.3 d=4
LWP500	21.0	-15.7	-2.4	5.9	-0.2	-36.6	19.7 d=4.2

Table 6.11 shows maximum changes in NIRS measurements during HI as measured with mini-CYRIL2 based on real-time measurement of pathlength. Comparing the NIRS measurements of [HHb], [HbO_2], [oxCCO], max[HbT], min[HbT] and [HbDiff] during HI in Table 6.10 and Table 6.11 demonstrate that except for one subject (LWP 481) , in all other cases the pathlength is overestimated when using fixed DPF, leading to underestimation of concentration values that could affect the interpretation of the estimation of HI severity. For instance, that could result

in pushing the nadir [oxCCO] beyond the defined limit (-3 to -4 μM) which would lead to irreversible cell damage.

6.5 Discussion

Mean maximum and minimum changes in broadband-NIRS measurements of [HHb], [HbO_2], [oxCCO], [HbT] and [HbDiff] during HI, as measured by mini-CYRIL2 based on two methods for calculating the optical pathlength (discussed in the previous section) were compared with the same measurements produced by UCL1 (described in chapter 4), to validate the concentration data generated through these two methods (Table 6.12). It can be seen that in average the mean increase in [HHb] and decrease in [HbO_2] during HI is more than 70% and in [oxCCO] around 50% greater when differential pathlength is estimated using the absolute attenuation measurement (n=10) compared to when a fixed estimated pathlength is used to calculate concentration changes (n=24). As seen in Table 6.12, when real-time pathlength is used, there is a larger dispersion among the maximum and minimum change in the haemoglobin signals compared to when a fixed DPF is used (despite a smaller n number). However, the minimum [oxCCO] change is more concentrated when optical pathlength is estimated real time based on the absolute attenuation measurement during the course of the experiment.

Table 6.12: Comparison between mean ± SD of the maximum and minimum changes in the concentration of chromophores during HI measured by mini-CYRIL2 (based on fixed DPF and real-time pathlength) and UCL1.

Mean ± SD at nadir HI (μM)	$\Delta[HHb]$	$\Delta[HbO_2]$	$\Delta[oxCCO]$	$max\Delta[HbT]$	$min\Delta[HbT]$	$\Delta[HbDiff]$
Mini-CYRIL2 (Fixed DPF) n=24	14.4 ± 2.1	-13.6 ± 2	-3.6 ± 1.2	2.9 ± 1.8	-2.7 ± 2.8	-27.1 ± 2.8
Mini-CYRIL2 (Real-time pathlength) n=10	24 ± 6.1	-22.3 ± 6.3	-5.5 ± 1.5	7.4 ± 5.6	-3.5 ± 3.5	-45.5 ± 11.1
UCL1 n=32	22.7 ± 7.7	-22.6 ± 7.8	-4.3 ± 1.6	4.0 ± 4.2	-5.6 ± 4.9	-41.9 ± 12.5

The concentration data produced by mini-CYRIL2 is closer in mean magnitude of change during HI, to the data produced using UCL1 (n=32), when changes in optical pathlength is accounted for in calculating the concentration of chromophores compared to when a fixed pathlength is used.

Furthermore, there was no association between the differential pathlength in piglets (n=10) with the source-detector spacing (Figure 6.97) which demonstrates the variations of scattering in different subjects and the necessity of real time estimation of pathlength during HI.

Mini-CYRIL2 is advantageous to current broadband-NIRS systems for having real-time pathlength estimation implemented in the software as well as enabling long hours measurement with high dark count stability due to controlled CCD temperature because of retrofit cooling upgrade, while changes in pathlength is accounted for (see chapter 5, section 5.1.7 for dark count characterisation of the Ventana spectrometer).

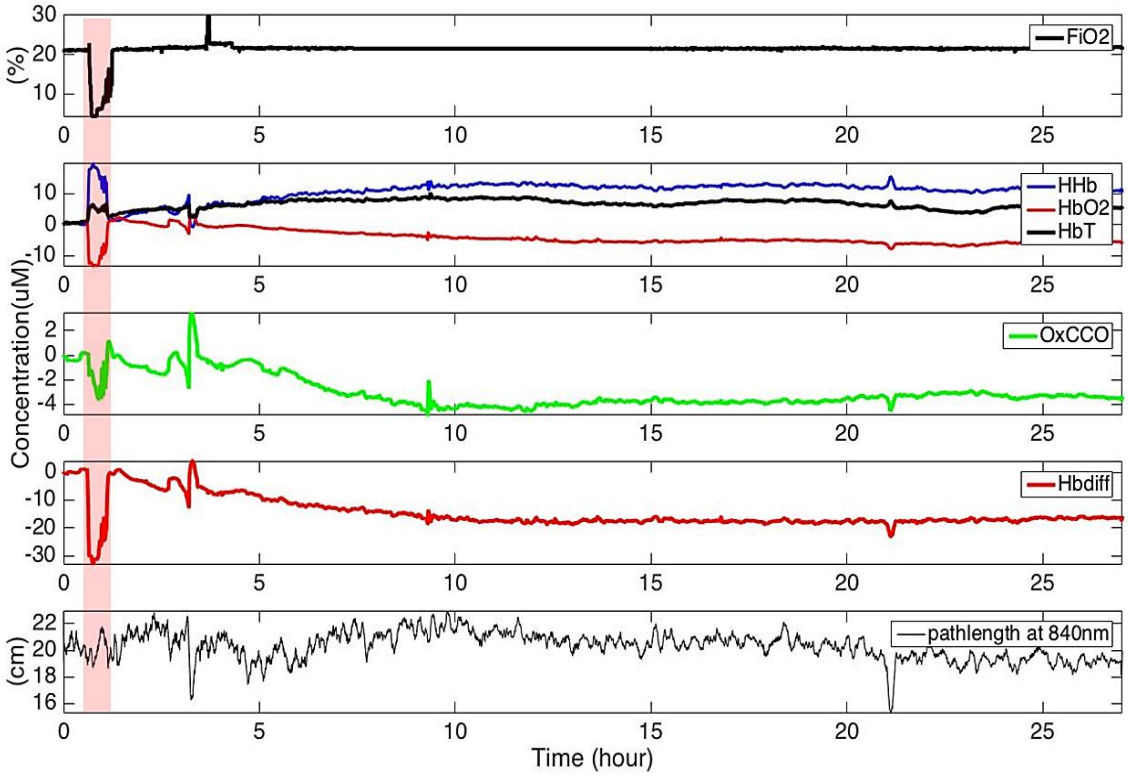

Figure 6.102: Mini-CYRIL2 measurement of [HHb], [HbO_2] and [oxCCO] on piglet's brain during hypoxia and 25 hours recovery period, based on real-time estimation of differential pathlength.

Figure 6.102 shows an example of mini-CYRIL2 real-time measurement of differential pathlength and chromophore concentrations during hypoxia and 25 hours recovery period. All the piglets that were discussed in this chapter, were studied for more than 24 hours after the HI insult which was not the scope of this thesis to discuss those data. Improving the concentration measurement accuracy based on changing pathlength, mini-CYRIL2 is especially beneficial as a cot-side tool for babies affected with HI in which changing pathophysiology may change the nature of the anatomy (e.g. through swelling or oedema) during the measurement period.

The challenge with estimating concentration of chromophores based on real-time pathlength is that the noise level on the raw intensity data needs to be very low, and the reference measurement that is used for calculating absolute attenuation must be significantly larger in intensity compared to the transmitted intensity (possibly with maximum photon count before the saturation of CCD) to ensure correct attenuation measurement even in times of changing pathophysiology, since the absolute attenuation directly affects the differential pathlength estimation during the measurement.

6.6 Summary

Mini-CYRIL2 with high throughput design was validated in-field for the first time in the preclinical study of neonatal hypoxia-ischaemia. It was demonstrated that mini-CYRIL2 is capable to collect high intensity transmission data through piglets' brain for optode separations greater than 4 cm. The intensity and attenuation spectra were comparable in shape to the spectra produced by the much larger UCL1 unit, even though slightly smaller in size, the high signal to noise ratio in mini-CYRIL2 enabled precise measurement of change in concentration of [HHb], [HbO_2] and [oxCCO] accounting for changes in differential pathlength during the course of the experiment which could be over 24 hours. The concentration measurements were analysed for crosstalk in all the subjects and it was demonstrated that a 3-chromophore fit for resolving of [HHb], [HbO_2] and [oxCCO] perfectly fit the measured attenuation through piglet's brain, while the residuals for a 2-chromophore fit had a defined shape as specific extinction coefficient of oxCCO. The stability of the system to produce consistent concentration measurements during HI and recovery was investigated in 24 piglets. The miniature system is also capable of calculating Area Under The Curve and Recovery Fraction of oxCCO signal during HI and recovery, providing useful quantitative values for clinicians to lead the HI insult. Finally, analysis was carried out to investigate the influence of using a fixed pathlength (DPF × d) compared with using a changing pathlength estimated from absolute attenuation spectra, on the precision of concentration measurement specifically during HI. The results from changing pathlength were in closer agreement with the data produced by UCL1 and data reported in the literature, compared to when a fixed DPF was used.

Mini-CYRIL2, has replaced the UCL1 system at the UCL Institute of Neurology and is currently being used to monitor the HI insult and investigate treatment efficacy using oxCCO measurement.

Bibliography

[1] S. J. Matcher, M. Cope, and D. T. Delpy, "Use of the water absorption spectrum to quantify tissue chromophore concentration changes in near-infrared spectroscopy.," *Phys. Med. Biol.*, vol. 39, no. 1, pp. 177–96, 1994.

[2] P. J. Kirkpatrick, J. Lam, P. Al-Rawi, P. Smielewski, and M. Czosnyka, "Defining thresholds for critical ischemia by using near-infrared spectroscopy in the adult brain.," *J. Neurosurg.*, vol. 89, no. 3, pp. 389–394, 1998.

[3] C. E. Cooper and R. Springett, "Measurement of cytochrome oxidase and mitochondrial energetics by near-infrared spectroscopy.," *Philos. Trans. R. Soc. Lond. B. Biol. Sci.*, vol. 352, no. 1354, pp. 669–676, 1997.

[4] G. Bale, "Development of Optical Instrumentation and Methods to Monitor Brain Oxygen Metabolism : Application to Neonatal Birth Asphyxia," 2016.

[5] P. Phan, D. Highton, J. Lai, M. Smith, C. Elwell, and I. Tachtsidis, "Multi-channel multi-distance broadband near-infrared spectroscopy system to measure the spatial response of cellular oxygen metabolism and tissue oxygenation," *Biomed. Opt. Express*, vol. 7, no. 11, p. 4424, Nov. 2016.

[6] A. Duncan, J. H. Meek, M. Clemence, C. E. Elwell, L. Tyszczuk, M. Cope, and D. T. Delpy, "Optical pathlength measurements on adult head, calf and forearm and the head of the newborn infant using phase resolved optical spectroscopy.," *Phys. Med. Biol.*, vol. 40, no. 2, pp. 295–304, 1995.

[7] A. Bainbridge, I. Tachtsidis, S. D. Faulkner, D. Price, T. Zhu, E. Baer, K. D. Broad, D. L. Thomas, E. B. Cady, N. J. Robertson, and X. Golay, "Brain mitochondrial oxidative metabolism during and after cerebral hypoxia-ischemia studied by simultaneous phosphorus magnetic-resonance and broadband near-infrared spectroscopy," *Neuroimage*, vol. 102, no. P1, pp. 173–183, 2014.

Chapter 7. Mini-CYRIL1 Investigating the role of Hypoxia in Neuro-Inflammation in an Animal Model of Multiple Sclerosis

Neurological deficits in neuro-inflammatory diseases such as Multiple Sclerosis (MS) have shown to be closely associated with spinal cord tissue hypoxia. In this chapter, the correlation between neurological deficits and tissue hypoxia in an animal model of MS is investigated using mini-CYRIL1. After a brief introduction to the motives behind this study, aims and objectives are presented. The chapter follows with methods including animal preparation, study protocol, broadband-NIRS measurement and concludes with spectroscopic and group data analysis as well as a discussion of the results.

7.1 Introduction

As mentioned in chapter 2, CNS (brain and spinal cord) tissue relies on a continuous and rich blood supply to sustain its high metabolic activity. The vulnerability of CNS tissue to hypoxia and inflammation, due to the high dependence of CNS neurones on aerobic metabolism, was explained in chapter 2 (section 2.6). Hypoxia is associated with many neurological disorders including multiple sclerosis (MS) [1]. MS is a neurodegenerative disease of the CNS with a wide range of symptoms and severity that varies from slurred speech to limb paralysis. Figure 7.103 is a simplified illustration of a neurone affected by multiple sclerosis. Myelin sheath in the MS-affected neurone is damaged which leads to interruption in the neuronal signalling, as seen in Figure 7.103.

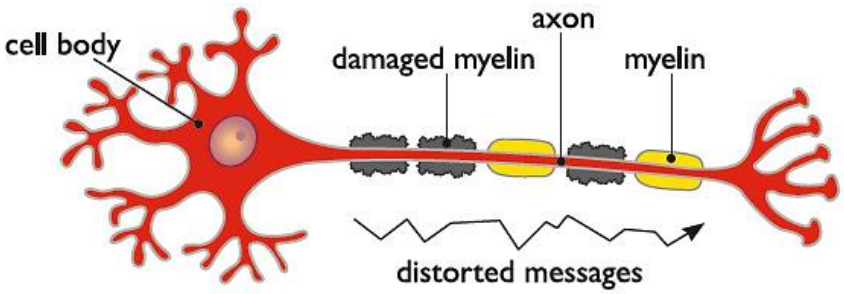

Figure 7.103: A simplified diagram of a neurone affected by multiple sclerosis. Damaged myelin sheath in CNS neurones leading to distorted electrical signals to/from the brain. Image taken from http://www.closerlookatstemcells.org/stem-cells-and-medicine/multiple-sclerosis

Demyelination and degeneration of axons have been known as the main cause of the neurological deficit in MS, which leads to the abnormal electrical activity of neurones. However, studies have shown that inflammation in the absence of demyelination might be sufficient to cause neurological dysfunction [2].

Our colleagues in the Neuro-Inflammation Centre of the UCL institute of neurology (IoN) demonstrated the presence of hypoxia in the inflamed spinal cord of animal models of MS [3]. In a comprehensive study by Davies et al, chemical, physical, immunohistochemical and therapeutic evidences suggested that there is significant tissue hypoxia in experimental autoimmune encephalomyelitis (EAE), an animal model for multiple sclerosis. Figure 7.104 shows average tissue oxygen tension via in vivo measurements within the grey matter of the lumbar spinal cord using an oxygen probe. The data presented are for control rats with no deficit (functional deficit score of zero) and rats in which EAE was induced with functional deficit scores ranging between 1-9 (score of 9 was indicative of bilateral hindlimb and tail paralysis). As seen in the figure, the oxygen concentration was significantly reduced in more severely affected animals during the first peak of the disease. This study demonstrated that spinal cord tissue hypoxia contributes to the neurological deficits in animal models of MS, however, the mechanism through which hypoxia leads to loss of function is unknown. In other words, it is not clear whether the hypoxia is sufficient to compromise mitochondrial function. If so, the hypoxia might somehow be the cause of the neurological deficits in neuroinflammatory diseases.

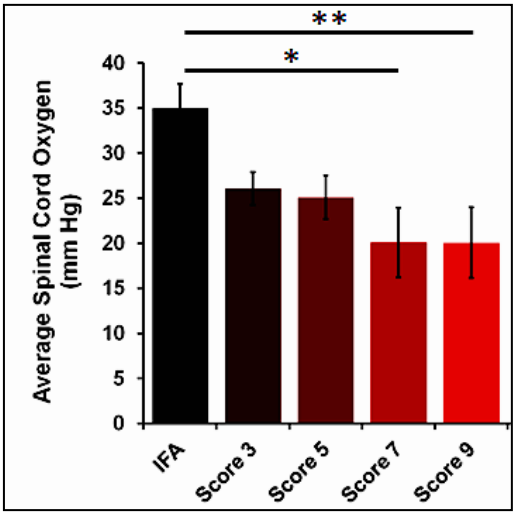

Figure 7.104: Average spinal cord oxygen tension (PO_2) in control and EAE-induced rats. Functional deficit scores Score 0: No deficit, Score 9: bilateral hind limb and tail paralysis. Image taken from [3].

Some studies have investigated tissue hypoxia in MS brain using commercially available NIRS systems that allow measurement of [HHb] and [HbO_2] [4]. Others have used commercial NIRS devices to study functional activation in different brain regions in MS patients [5], [6]. To the author's knowledge, no studies have reported the use of NIRS in the spinal cord of MS patients, however, some studies have described the use of NIRS to non-invasively detect spinal cord oxygenation and perfusion during surgical procedures [7]–[11].

7.2 Aims

The aim of this study is to use the broadband-NIRS mini-CYRIL system for the first time to investigate the role of hypoxia and mitochondrial function in neurological deficits caused by inflammation through real time measurement of spinal cord tissue oxygenation (Δ[HHb], Δ[HbO_2]) and metabolism (Δ[oxCCO]).

7.3 Methods

7.3.1 Animal preparation

The study protocol was approved by the institutional ethics committee, licensed under the UK Animals (Scientific Procedures) Act of 1986, and conducted according to the ARRIVE guidelines. Animals were provided with food and water ad libitum throughout. Animals were terminated at the end of the experiments.

Experimental autoimmune encephalomyelitis (EAE) was induced in adult Dark Agouti (DA) rats by immunization with recombinant myelin oligodendrocyte protein (rMOG) in incomplete Freund's adjuvant (IFA); control animals received an emulsion of IFA and saline, or sterile saline alone. Animals were weighed and assessed blindly on a daily basis for functional deficit on a 10-point scale. A score of 0 signified no functional deficit and a score of 9 was indicative of bilateral hindlimb and tail paralysis. Please refer to the paper by Davies et al. for further details [3]. 11 EAE-induced and 9 control rats were under general anaesthesia for the experiment (2% isoflurane) and underwent lumbar laminectomy, a procedure that enlarges the spinal canal and enables access to the spinal cord for the in-vivo experiment.

7.3.2 Study Protocol

The subjects were exposed to 5 minutes of inspiratory hyperoxia (FIO_2=100% Oxygen) following a 5-minute stable baseline (room air (FIO_2=21%)) as seen in Figure 7.105. After the hyperoxia, the inspired oxygen was switched back to 21% and the animals were monitored for 5 minutes of recovery period. The subjects were continuously monitored for their physiological responses during the experiment at a sampling rate of 15 Hz. These measurements included the arterial saturation (SpO_2), heart rate and respiratory rate.

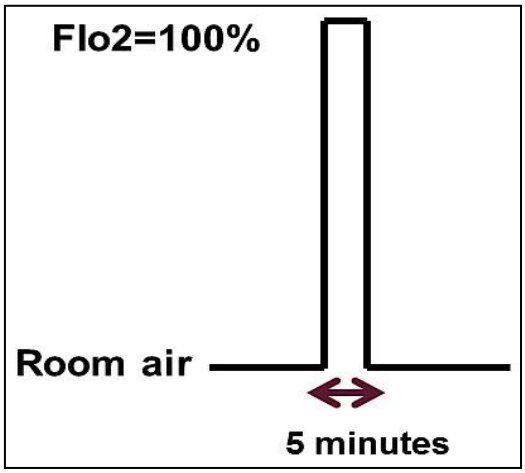

Figure 7.105: Hyperoxia protocol

7.3.3 Broadband NIRS Measurement

MINI-CYRIL1 as described in chapter 5 was used to measure changes in spinal cord tissue oxygenation and metabolism in-vivo. Software version 1 was used which calculates changes in [HHb], [HbO_2] and [oxCCO] in μ.cm without estimating the pathlength, as the spinal cord tissue DPF was not known. Figure 7.106 illustrates the experimental set up for broadband-NIRS exposed spinal cord measurement. Narrow needle probes (500 μm diameter) by Moore Instruments were used as source and detector fibres and placed on the spinal cord grey matter. Care was taken to avoid the large vein in the middle, which could interfere with the measurement due to the large absorption.

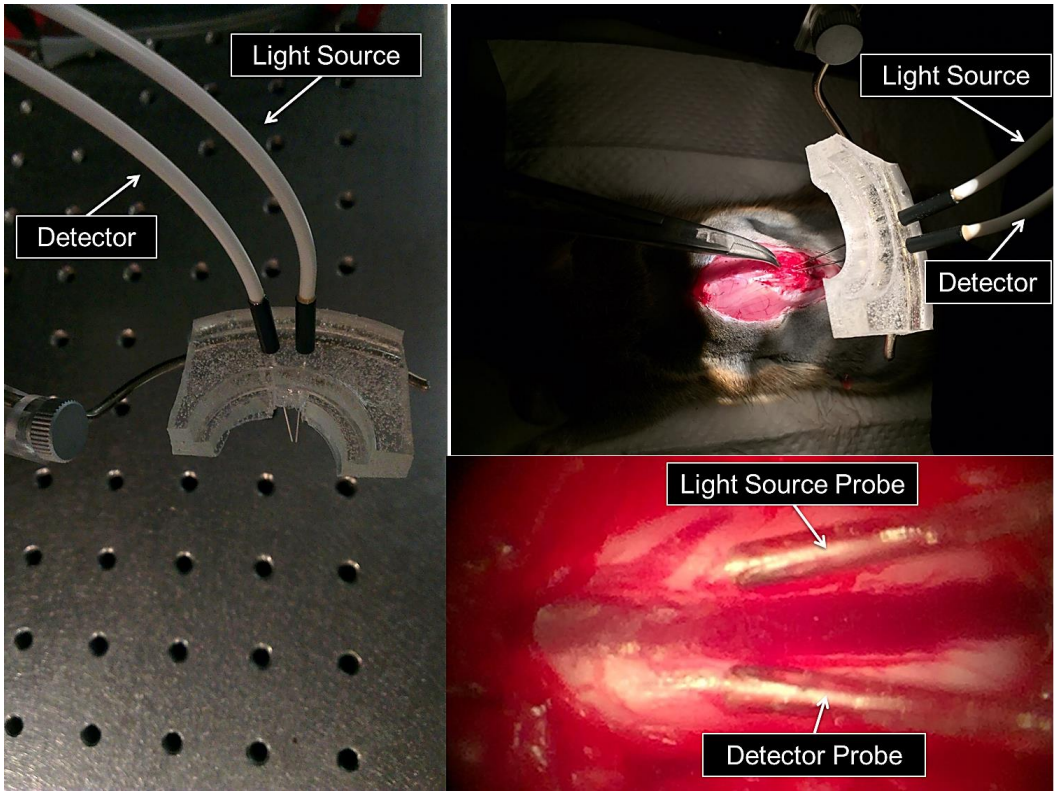

Figure 7.106: Experimental setup for Broadband NIRS measurement of spinal cord tissue oxygenation and metabolism using mini-CYRIL1

To enhance the signal to noise ratio, the acquisition time was set at 10 seconds, as the source and detector fibres had very small diameters causing them to produce a very weak intensity signal at 1 second acquisition time.

7.3.4 Broadband-NIRS Data Evaluation (Residual Analysis)

To evaluate broadband-NIRS concentration measurement (especially the Δ[oxCCO] signal, as CCO exist in very small concentrations in vivo), residual analysis was carried out as proposed by cooper et al [12] and performed in chapter 4 (see section 4.3.5.1). Briefly, the attenuation-change spectra at peak hyperoxia (780-900 nm) were back calculated from the concentration changes calculated using UCLn algorithm (see equation 3.13) when solving only for two chromophores (HHb and HbO_2) and when solving for three chromophores (oxCCO also included). Then, the difference between the real attenuation spectra (calculated from the measured changes in the intensity of back reflected light, according to equation 3.10) with the back-calculated attenuation spectra from the 2- and 3-chromophore fit were studied.

7.3.5 Concentration Data Analysis

Total haemoglobin (blood volume, $\Delta[HbT]=\Delta[HbO_2] + \Delta[HHb]$) and haemoglobin difference (blood oxygenation, $\Delta[HbDiff]=\Delta[HbO_2]-\Delta[HHb]$) concentrations were derived, and average changes in [HbT], [HbDiff] and [oxCCO] during the whole 5 minutes of hyperoxia were calculated and normalised to baseline. A non-parametric Wilcoxon Rank Sum test was performed in MATLAB to compare the mean changes in [HbT], [HbDiff] and [oxCCO] during hyperoxia between groups (control and EAE) and non-parametric correlation analysis (Spearman's Rank-Order correlation) was carried out to investigate the association between broadband-NIRS parameters and the severity of the neurological deficit, based on the total deficit score value.

7.4 Results

7.4.1 Spectroscopic Analysis of the NIRS Data

Figure 7.107 illustrates the steps for calculation of the concentrations based on measured intensity and attenuation of light through the spinal cord using mini-CYRIL1 as explained in chapter 5 (5.2.1).

Figure 7.108 and Figure 7.109 illustrate an example of the residual analysis that was performed for evaluation of the broadband-NIRS oxCCO measurement. Figure 7.108 shows the measured attenuation spectrum in an EAE-induced rat as well as the back-calculated attenuations from the 2- and 3-chromophore fit. As seen in the figure, the back-calculated attenuation from the 3-chromophore fit matches the measured attenuation, whilst the red attenuation spectrum shows that when solving only for 2 chromophores, all the chromophores were not accounted for, as it does not match the measured attenuation.

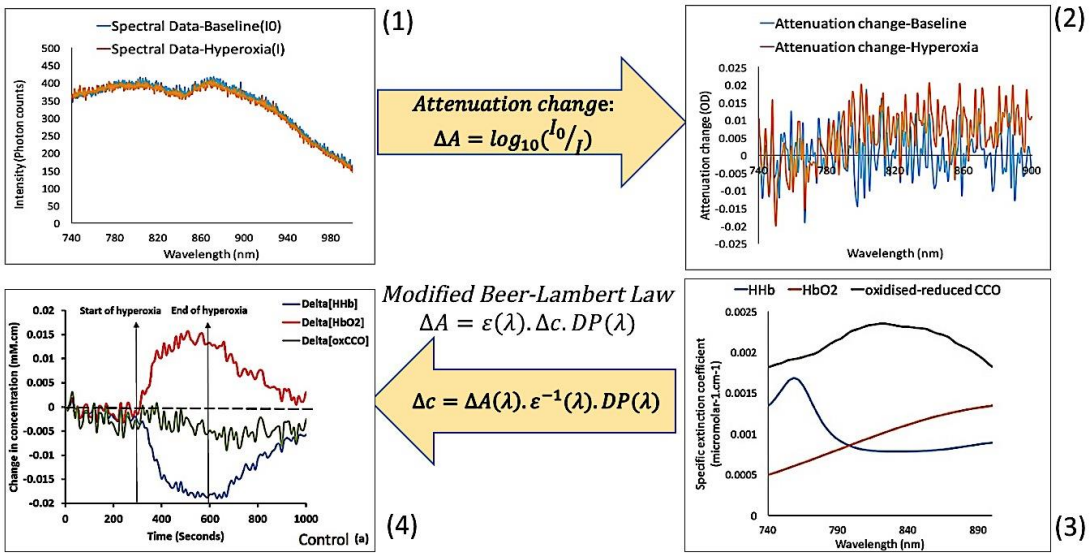

Figure 7.107: 1) Light traversed the spinal cord tissue, I, is collected every second. (2) Changes in the attenuation of light between 740-900 nm are calculated relative to baseline (ΔA). (3)&(4) Changes in the concentration (Δc) of Oxy and Deoxy-Haemoglobin ([HbO_2] &[HHb]) as well as cytochrome-c-oxidase ([oxCCO]) are calculated in real-time using the known specific extinction coefficients ($\varepsilon(\lambda)$) and the UCLn algorithm which is based on the modified Beer-Lambert law. DP (λ) is the wavelength-dependent optical pathlength which is not accounted for in this experiment, as only the trend of change was of interest for this study. So, all the concentration measurements are expressed in µM × cm.

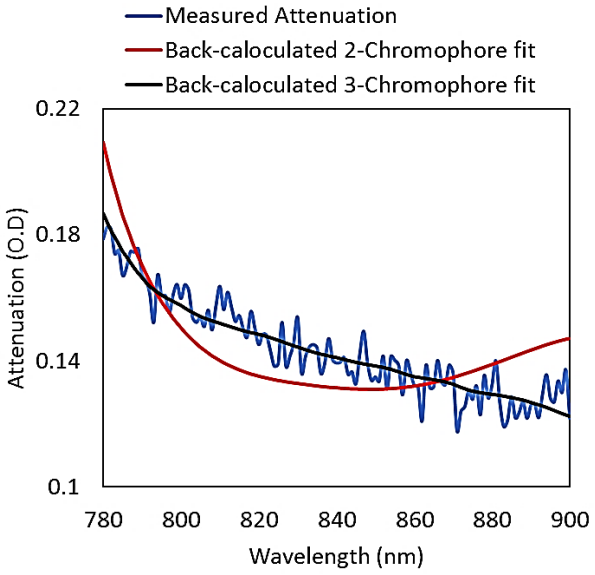

Figure 7.108: Real attenuation spectrum (calculated from the measured change in intensity) and the back-calculated attenuations from 2- and 3-chromophore fit.

The residual errors from fitting back-calculated attenuation spectra when solving for 2- and 3-chromophores are shown in Figure 7.109. The residual error from 2-chromophore fit has a well-defined shape that matches the extinction coefficient spectrum of oxidised-reduced [CCO] between 780-900 nm. Therefore, it shows that when resolving only for [HHb] and [HbO_2], the [oxCCO] remains unaccounted for. However, when solving for 3-chromophore (including [oxCCO]), the residual error randomly fluctuates around zero, showing that all the chromophores in the field of view have been accounted for in the measurement.

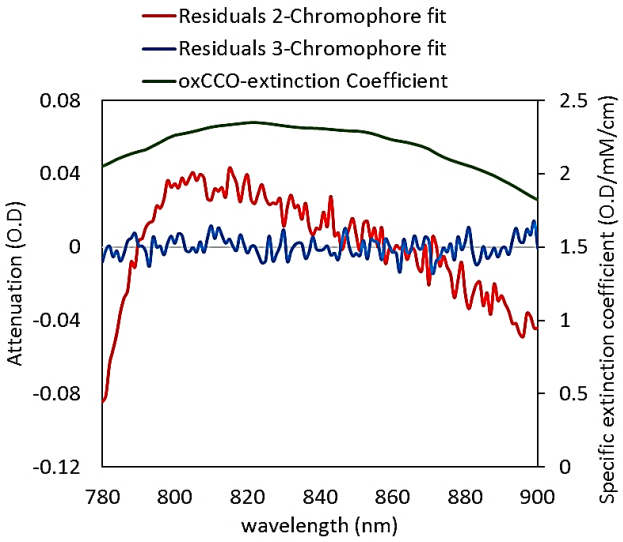

Figure 7.109: Residual error from 2- and 3- chromophore fit. The 2-chromophore fit residuals (in red) match the extinction coefficient of oxCCO (in green), whilst the 3-chromophore fit's residual error (in blue) randomly oscillates around zero**.**

7.4.2 Changes in NIRS Concentration Data During Hyperoxia

Figure 7.110 displays how the concentration of chromophores changed during hyperoxia in a control and EAE-induced rat. It is clear seen that despite an increase in [HbO_2] and a decrease in [HHb] in the control rat during hyperoxia, there is no change in the trend of [oxCCO] (Figure 7.110 a). On the other hand, in the EAE-induced rat not only is there a greater increase in [HbO_2] and larger decrease in [HHb] compared to the control rat, but there is also an increase in [oxCCO] which is not observed in the control rat (Figure 7.110 b).

Figure 7.111 presents changes in total haemoglobin [HbT] as a measure for blood volume change, and haemoglobin difference [HbDiff] as a measure for blood oxygenation change during hyperoxia. In the EAE-induced subject there is a larger increase in blood oxygenation (peak [HbDiff]~ 40 μM × cm) compared to the control rat, (peak [HbDiff]~33 μM × cm) and an increase in total blood volume is seen in the EAE-induced rat which is not observed in the control subjects.

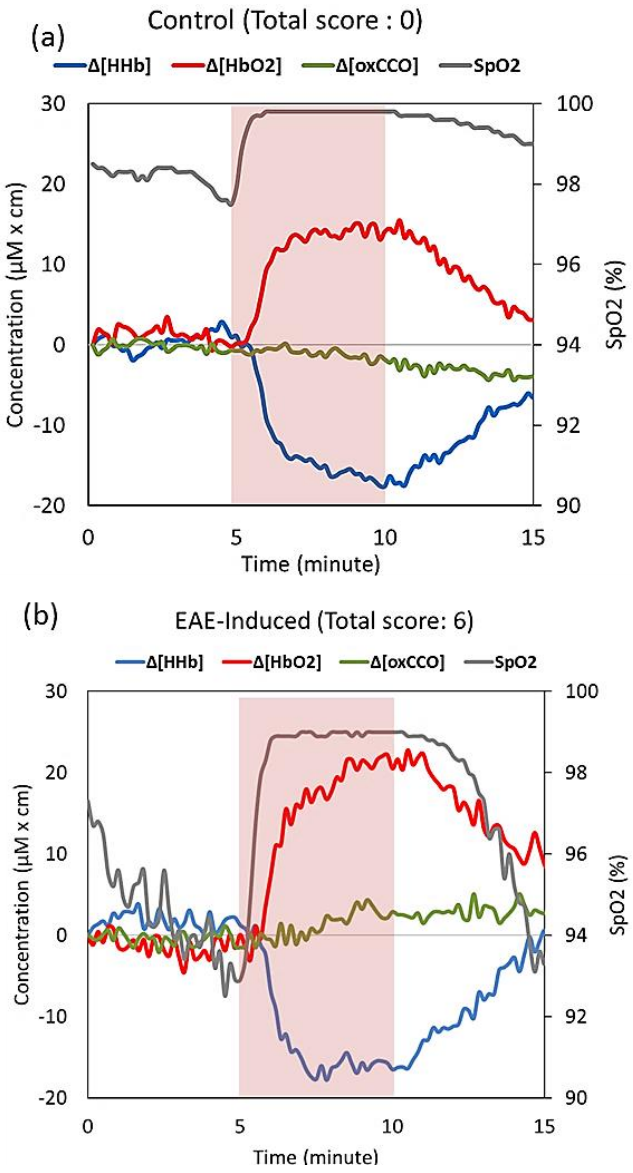

Figure 7.110*:* Changes in the concentration of HHb, HbO_2 and oxCCO during 5 minutes of hyperoxia in a control (a) and EAE-induced (b) rat. Changes in HbT (blood volume) and HbDiff (blood oxygenation) have also been derived and plotted.

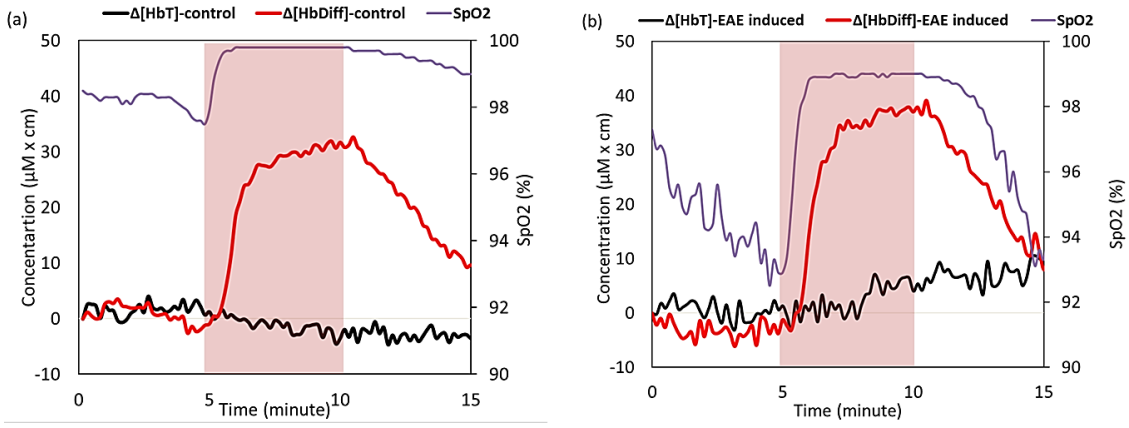

Figure 7.111: Haemodynamic response during hyperoxia in the spinal cord tissue of a control (a) and an EAE rat (b). A larger increase in total blood volume ([HbT]) and blood oxygenation ([HbDiff]) is seen in the EAE-induced rat.

The results from group analysis are shown in Figure 7.112, Figure 7.113 and Figure 7.114. Each data point in the figures represents the mean concentration change during the 5-minute hyperoxia normalised to baseline for each subject. The EAE group had a more significant increase in their spinal cord oxygenation (Δ[HbDiff, Figure 7.112) and oxidative metabolism (Δ[oxCCO], Figure 7.113) compared to the control group (see Table 7.13). However, the blood volume change (Δ[HbT]) during hyperoxia is not statistically different between groups, despite there being a tendency for blood volume to increase during hyperoxia in the EAE-induced rats as shown in Figure 7.114.

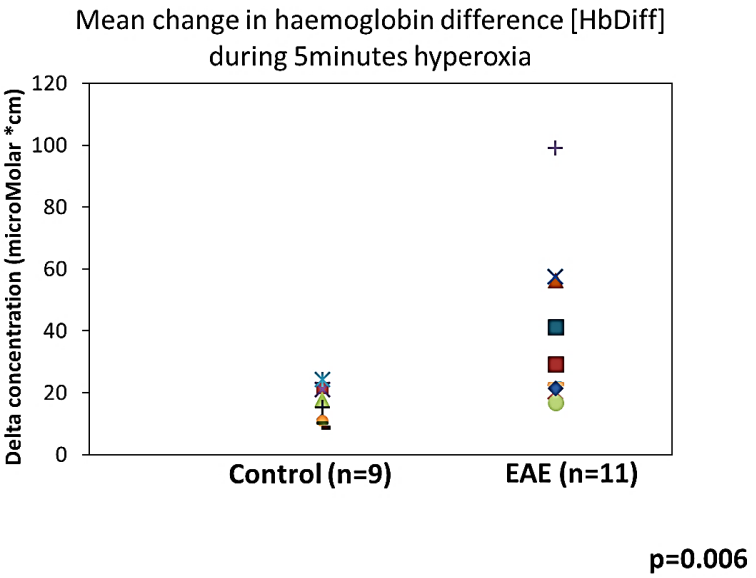

Figure 7.112: Change in haemoglobin difference (Δ[HbDiff]=Δ[HbO_2]-Δ[HHb]) during hyperoxia is significantly greater in the EAE than the controls. Δ[HbDiff]EAE-Δ[HbDiff]Control=21.53(µmolar × cm)

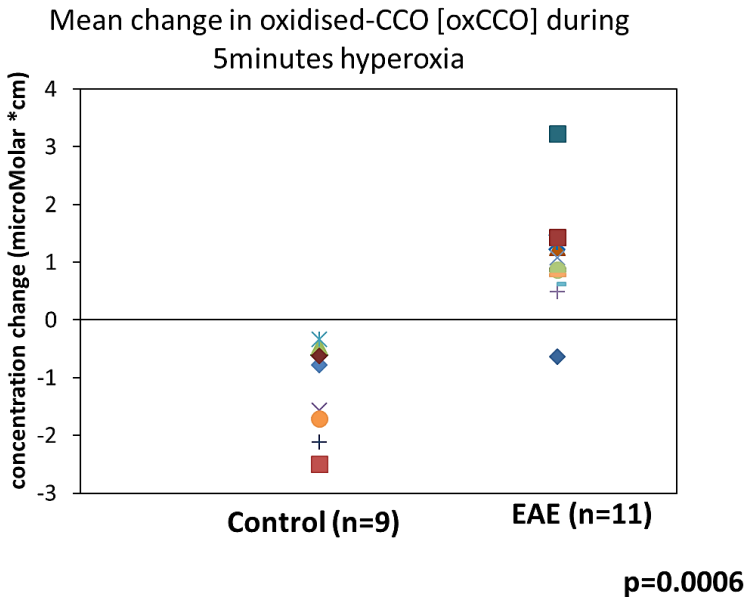

Figure 7.113: Change in Cytochrome c oxidase, Δ[oxCCO] during hyperoxia is significantly greater in EAE than control animals. $\Delta[oxCCO]_{EAE}$- $\Delta[oxCCO]_{Control}$=+2.22(µmolar × cm)

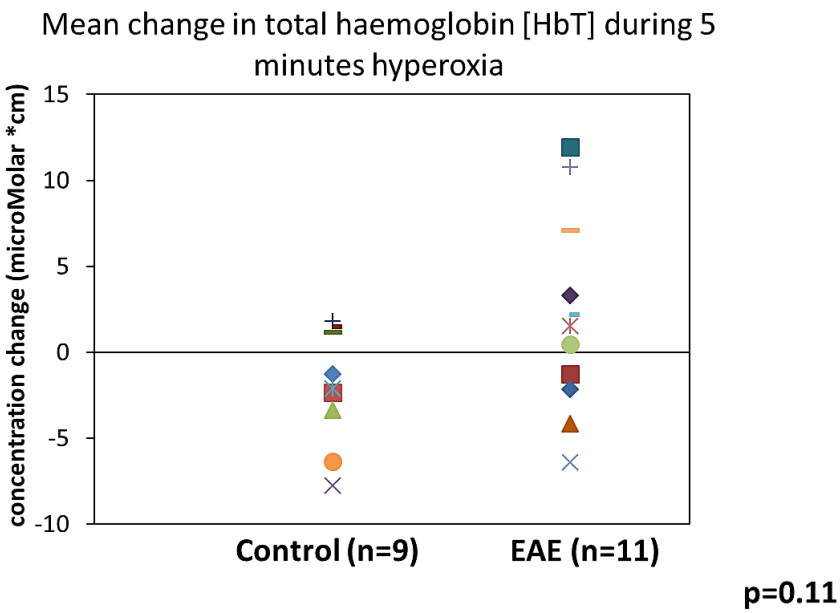

Figure 7.114: Change in total haemoglobin (Δ[HbT]=Δ[HbO_2]+Δ[HHb]) during hyperoxia is not significantly different between the EAE and the controls. Δ[HbT]EAE-Δ[HbT]Control=4.2(μmolar × cm)

Table 7.13 summarises the mean ± standard deviation (SD) changes in blood volume, oxygenation and metabolism in EAE and control animals for 5-minute hyperoxia based on their [HbT], [HbDiff] and [oxCCO] change measured by mini-CYRIL1 system. In general, the EAE animals have a greater increase in their blood oxygenation and mitochondrial metabolism with high statistical significance (p=0.006 and p=0.0006 respectively). The larger blood volume increase in the EAE rats is not statistically different from the control group.

Table 7.13: Group mean ± SD change in NIRS measurement during hyperoxia in control and EAE-induced rats

Mean ± SD (μM ×cm) / **Groups**	**[HbT]**	**[HbDiff]**	**[oxCCO]**
Control	-2.08 ± 3.18	15.71 ± 5.39	-1.19 ± 0.75
EAE	2.11 ± 5.58	37.24 ± 25.64	1.03 ± 0.77
Difference (EAE-Control)	+ 4.20, p = 0.11	+ 21.53, p = 0.006	+ 2.22, p = 0.0006

The strength and direction of association between the broadband-NIRS measurements of blood volume change (Δ[HbT]), blood oxygenation change (Δ[HbDiff]), and change in oxidative metabolism (Δ[oxCCO]), with the total functional deficit score (a measure of both disease severity and duration) was investigated using Spearman's rank order correlation test. As seen in Table 7.14, there is a significantly strong positive association between the Δ[HbDiff] signal measured by mini-CYRIL1, with the total functional deficit score. Furthermore, there is a significant moderate to strong correlation between the (Δ[oxCCO]) signal with the total deficit score, but no association was observed between the change in blood volume during hyperoxia with the total deficit score.

Table 7.14: Non-parametric correlation between broadband-NIRS measurements with total functional deficit score

Spearman's Rank-Order correlation	**[HbT]**	**[HbDiff]**	**[oxCCO]**
Total Functional Deficit Score	$r_s = 0.2$ P=0.5	$r_s = 0.7$ P=0.002	$r_s = 0.5$ P=0.03

Regression analysis was carried out to further investigate the nature of the relationship between broadband-NIRS measurements of oxygenation and metabolism provided by mini-CYRIL1 with the disease severity and duration in the EAE-induced rats. Figure 7.115 illustrates the correlation between the magnitude of change in [oxCCO] and [HbDiff] during hyperoxia against the total functional deficit score in all rats. Total function deficit score is simply the sum of daily scores, and animals with a higher total score have had a more severe and prolonged disease course.

Figure 7.115 shows that there is a strong quadratic association between the change in the oxidation of cytochrome c oxidase with the total functional deficit score in all the rats, while there is only a mild linear correlation between the change in haemoglobin difference with the total functional deficit score.

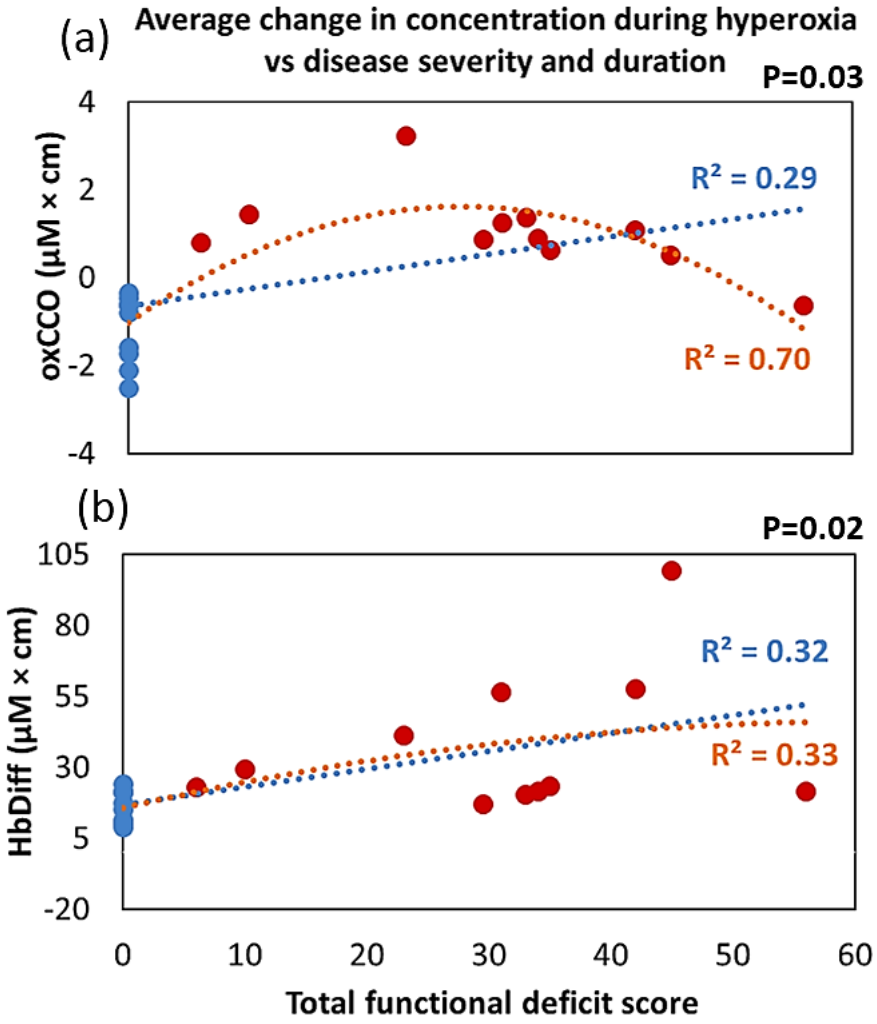

Figure 7.115: Linear (blue dotted line) and quadratic (orange dotted line) regression analysis between change in [oxCCO] (a) and [HbDiff] (b) during hyperoxia with the total functional deficit score (measure of disease severity and duration). Animals with a milder form of the disease and early on in their disease course have lower scores. Animals with higher total scores have had prolonged disease that includes some major structural changes.

7.5 Discussion

Transient inspiratory hyperoxia enhanced optically measured blood oxygenation ([HbDiff]) in all the rats and mitochondrial oxidative metabolism ([oxCCO]) in EAE-induced rats, as measured by mini-CYRIL1. The residual analysis demonstrated that Δ[oxCCO] measurement in this experiment was genuine. The magnitude of increase in haemoglobin difference was significantly greater in EAE-induced than control rats, which was strongly associated with the total deficit score in all the rats (Table 7.14). This finding agrees with the presence of tissue hypoxia in the inflamed spinal cord of

the animals, previously demonstrated by Davies et al in 2013 through tissue oxygen measurements [3] and is also in agreement with recent finding by Johnson et al in 2016 showing the presence of grey matter hypoxia in the brain of the EAE-induced mice [13]. Despite the increase in blood oxygenation during hyperoxia, no significant increase in the oxidation state of cytochrome was observed in control rats, which could possibly be due to the CCO molecules in the spinal cord being fully oxidised, hence cannot oxidise further from baseline during hyperoxia. This was also suggested by some animal studies in which an increase in FIO_2 to 100% did not induce any change in the oxidation state of CCO while stimulating a consistent increase in the HbO_2 signal, measured on anaesthetised rats' brain [14], [15]. However, a steady rise in the [oxCCO] signal was observed during hyperoxia experiments which were performed on healthy adult volunteers [16], [17]. Nevertheless, it should be mentioned that the adult studies were carried out on healthy awake humans rather than anaesthetised animals and it is highly likely that anaesthesia will have a significant impact on the CCO oxidation. Because the metabolic rate decreases under anaesthesia, a lower oxygen delivery is required to meet demands [18].

In the EAE-induced rats, changes in oxCCO during hyeproxia seemed to follow a quadratic pattern with respect to the total functional deficit score. A simple interpretation of this behaviour could be: At the early stage of the disease, the mitochondrial respiration could be inhibited by localised tissue hypoxia as shown in tissue oxygen measurements and biochemical studies. Therefore, the oxidation of CCO or mitochondrial function could be enhanced through an increase in systemic oxygenation. This finding agrees with improved mitochondrial function by oxygen therapy in animal models [3] and in adults with MS [19]. In the later stages of the disease however, as the deficit severity and duration progress, the increase in systemic oxygenation cannot further boost mitochondrial metabolism, potentially due to the impaired electron transport chain (ETC) and oxidative metabolism, as prolonged hypoxia leads to irreversible damage to the cells.

7.6 Summary

This chapter described the application of mini-CYRIL1 for the in-vivo measurement of spinal cord tissue oxygenation and metabolism in animal models of MS for the first time, in order to investigate the role of hypoxia in neuroinflammatory diseases. The accuracy of broadband-NIRS measurement produced by mini-CYRIL1 was evaluated through residual analysis. Changes in oxygenated and deoxygenated haemoglobin as well as oxidised-cytochrome c oxidase was measured in real-time during transient inspiratory hyperoxia. According to the pilot results, EAE-induced rats demonstrated a higher blood oxygenation ([HbDiff]), which agrees with previous studies confirming the presence of hypoxia in the inflamed spinal cord of rats. Additionally, there was an increase in mitochondrial oxygen metabolism ([oxCCO]) in mild and moderate EAE which could imply that mitochondrial function in the inflamed EAE spinal cord is restricted by tissue hypoxia and can be upregulated by an increase in oxygen delivery. This finding agrees with some of the therapeutic approaches in the treatment of MS. Finally, the strong quadratic association that was observed between Δ[oxCCO] and the total EAE score could further illustrate the role of hypoxia in neuroinflammatory disease.

Bibliography

[1] R. A. Desai, "the Role of Hypoxia in Neuroinflammatory Disease," University College London (UCL), 2013.

[2] A. Bitsch, C. Wegener, C. da Costa, S. Bunkowski, C. D. Reimers, H. W. Prange, and W. Brück, "Lesion development in Marburg's type of acute multiple sclerosis: from inflammation to demyelination.," *Mult. Scler.*, vol. 5, no. 3, pp. 138–146, 1999.

[3] A. L. Davies, R. A. Desai, P. S. Bloomfield, P. R. McIntosh, K. J. Chapple, C. Linington, R. Fairless, R. Diem, M. Kasti, M. P. Murphy, and K. J. Smith, "Neurological deficits caused by tissue hypoxia in neuroinflammatory disease," *Ann. Neurol.*, vol. 74, no. 6, pp. 815–825, 2013.

[4] R. Yang and J. F. Dunn, "Reduced cortical microvascular oxygenation in multiple sclerosis: a blinded, case-controlled study using a novel quantitative near-infrared spectroscopy method.," *Sci. Rep.*, vol. 5, no. October, p. 16477, 2015.

[5] J. J. Jimenez, R. Yang, N. Nathoo, V. P. Varshney, A.-M. Golestani, B. G. Goodyear, L. M. Metz, and J. F. Dunn, "Detection of reduced interhemispheric cortical communication during task execution in multiple sclerosis patients using functional near-infrared spectroscopy.," *J. Biomed. Opt.*, vol. 19, no. 7, p. 76008, 2014.

[6] J. Stojanovic-Radic, G. Wylie, G. Voelbel, N. Chiaravalloti, and J. DeLuca, "Neuroimaging and cognition using functional near infrared spectroscopy (fNIRS) in multiple sclerosis," *Brain Imaging Behav.*, vol. 9, no. 2, pp. 302–311, 2015.

[7] A. J. Macnab, R. E. Gagnon, and F. a Gagnon, "Near infrared spectroscopy for intraoperative monitoring of the spinal cord.," *Spine (Phila. Pa. 1976).*, vol. 27, no. 1, pp. 17–20, 2002.

[8] S. A. LeMaire, L. N. Ochoa, L. D. Conklin, R. A. Widman, F. J. Clubb, A. Ündar, Z. C. Schmittling, X. L. Wang, C. D. Fraser, and J. S. Coselli, "Transcutaneous near-infrared spectroscopy for detection of regional spinal ischemia during intercostal artery ligation: Preliminary experimental results," *J. Thorac. Cardiovasc. Surg.*, vol. 132, no. 5, pp. 1150–1155, 2006.

[9] N. H. Badner, G. Nicolaou, C. F. M. Clarke, and T. L. Forbes, "Use of spinal near-infrared spectroscopy for monitoring spinal cord perfusion during endovascular thoracic aortic repairs," *J. Cardiothorac. Vasc. Anesth.*, vol. 25, no. 2, pp. 316–319, 2011.

[10] A. Moerman, I. Van Herzeele, C. Vanpeteghem, F. Vermassen, K. François, and P. Wouters, "Near-infrared spectroscopy for monitoring spinal cord ischemia during hybrid thoracoabdominal aortic aneurysm repair," *J Endovasc Ther*, vol. 18, no. 1, pp. 91–95, 2011.

[11] R. P. E. Boezeman, E. P. van Dongen, W. J. Morshuis, U. Sonker, E. H. J. . Boezeman, F. G. . Waanders, and J.-P. P. M. de Vries, "Spinal Near-Infrared Spectroscopy Measurements During and After Thoracoabdominal Aortic Aneurysm Repair: A Pilot Study," *Adult Card.*, vol. 99, pp. 1267–1274, 2015.

[12] C. E. Cooper and R. Springett, "Measurement of cytochrome oxidase and mitochondrial energetics by near-infrared spectroscopy.," *Philos. Trans. R. Soc. Lond. B. Biol. Sci.*, vol. 352, no. 1354, pp. 669–676, 1997.

[13] T. W. Johnson, Y. Wu, N. Nathoo, J. A. Rogers, V. W. Yong, and J. F. Dunn, "Gray matter hypoxia in the brain of the experimental autoimmune encephalomyelitis model of multiple sclerosis," *PLoS One*, vol. 11, no. 12, pp. 1–22, 2016.

[14] C. Cooper, M. Sharpe, C. Elwell, R. Springett, J. Penrice, L. Tyszczuk, P. Amess, J. Wyatt, V. Quaresima, and D. Delpy, "The cytochrome oxidase redox state in vivo.," *Adv. Exp. Med. Biol.*, vol. 428, pp. 449–56, 1997.

[15] Y. Hoshi, O. Hazeki, Y. Kakihana, and M. Tamura, "Redox behavior of cytochrome oxidase in the rat brain measured by near-infrared spectroscopy Redox behavior of cytochrome oxidase in the rat brain measured by near-infrared spectroscopy," *J. Appl. Physiol.*, pp. 1842–1848, 1997.

[16] I. Tachtsidis, M. M. Tisdall, T. S. Leung, C. Pritchard, C. E. Cooper, M. Smith, and C. E. Elwell, "Relationship between brain tissue haemodynamics, oxygenation and metabolism in the healthy human adult brain during hyperoxia and hypercapnea.," *Adv. Exp. Med. Biol.*, vol. 645, pp. 315–20, 2009.

[17] C. Kolyva, A. Ghosh, I. Tachtsidis, D. Highton, C. E. Cooper, M. Smith, and C. E. Elwell, "Cytochrome c oxidase response to changes in cerebral oxygen delivery in the adult brain shows higher brain-specificity than haemoglobin," *Neuroimage*, vol. 85, pp. 234–244, Jan. 2014.

[18] S. A. McLellan and T. S. Walsh, "Oxygen delivery and haemoglobin," *Contin. Educ. Anaesthesia, Crit. Care Pain*, vol. 4, no. 4, pp. 123–126, 2004.

[19] M. Bennett and R. Heard, "Hyperbaric oxygen therapy for multiple sclerosis.," *Cochrane database Syst. Rev.*, no. 1, p. CD003057, 2004.

Chapter 8. Mini-CYRIL1 Investigating The Effect of 670 nm Light Exposure (Low-Level Light Therapy) on the Redox State of Mitochondria

Mitochondria play a key role in aging and disease, and their ATP production is significantly reduced with age because of progressive inflammation, cell loss and death. In this chapter, the use of mini-CYRIL1 is proposed to non-invasively measure in-vivo changes in aged retinal haemodynamics and mitochondrial respiration following exposure to 670 nm LED, which improves mitochondrial performance and reduces inflammation. After a brief introduction to the motives behind this study, aims and objectives are presented. The chapter follows with methods including animal preparation, study protocol, broadband-NIRS measurement and ends with spectroscopic, individual and group data analysis as well as a discussion of the results.

8.1 Introduction

The retina is one of the most energy consuming components of the human body because of the high metabolic rate of photoreceptors, which exist abundantly in mitochondria [1] (see chapter 2, section 2.5.3). However, as the retina ages, there is a significant reduction in mitochondrial function and ATP production [2] as well as progressive inflammation that leads to cell loss and death [3].

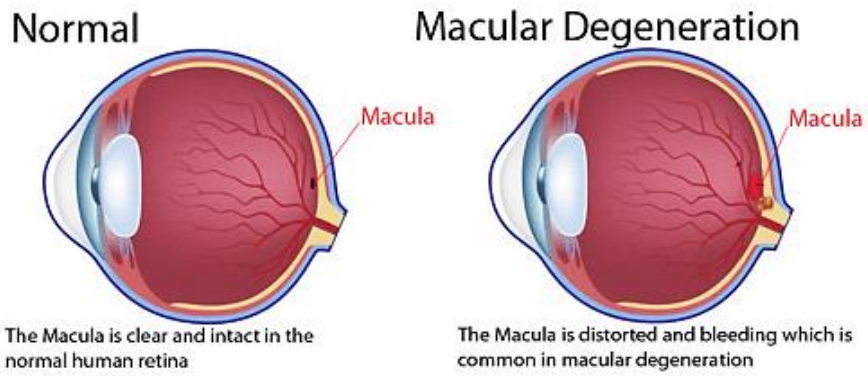

Figure 8.116: Simplified diagram of a normal macula and macular degeneration. Image taken from http://www.optometriceyesitenc.com/wp-content/uploads/2013/10/Macular-Degeneration-z.jpg

Age related macular degeneration (AMD) is one of the conditions associated with ageing and inflammation and is the leading cause of losing central vision, usually in both eyes, in people over the age of 65. The macula is the area near the centre of the retina responsible for detailed central vision, providing the vision required for precise activities such as reading and writing and the ability to appreciate colours.

Figure 8.116 illustrates a normal macula (a black oval area) compared with a distorted macula, which is common in macular degeneration. According to the NHS, approximately every 1 in 10 people over 65 in UK have some degree of AMD and it is predicted that by 2020 almost 700000 people will have AMD in the UK [4].

Low-level laser/light therapy (LLLT) (also known as photobiomodulation), refers to the use of low-level light in the red to near-infrared range (650–1100 nm) to stimulate cellular functions for physiological or clinical benefits [5]. The history of using near infrared light for reducing pain, inflammation, and healing of deeper tissues and nerves dates to more than forty years ago after the invention of lasers. It was first thought that this effect is due to the coherence of the laser light, but after the experiments with non-coherent light (LEDs) showed a similar effect, it was known that the photobiomodulation is simply a characteristic of red/near-infrared light [6]. The mechanism of LLLT is not clearly understood but proposed to be due to the strong absorption of cytochrome-c-oxidase (CCO) in red- NIR region [7]. In fact, CCO has shown to be responsible for more than 50% of the absorption greater than 800 nm [6]. The more the activity of CCO increases, the more oxygen consumption and ATP is produced via mitochondrial oxidative phosphorylation.

Recently, our colleagues at the UCL institute of ophthalmology (IoO) showed that absorbance of one of the wavelengths in the range of interest in LLLT, 670 nm light, improves mitochondrial respiration in the retina of aged animals, increasing their membrane potentials and improving ATP production. In this study, Begum et al. demonstrated that the enhanced ATP production in the aged retina was in turn associated with reduced retinal inflammation both in normal mice and the models of age related macular degeneration (AMD) where inflammation appears early and is relatively aggressive [8].

Currently there is no way of identifying people that might be of risk of AMD. As there is evidence that mitochondria are particularly vulnerable in animal models of

this disease, it is critical that a predictive biomarker is established and broadband-NIRS measurement may represent a step towards this.

8.2 Aims

The aim of this study is to use broadband-NIRS mini-CYRIL1 system for the first time to investigate LLLT in the retina of aged rats using transient 670 nm low-power LED light exposure through real-time measurement of retinal tissue haemodynamics and oxygenation (Δ[HHb], Δ[HbO2]) as well as mitochondrial metabolism (Δ[oxCCO]). In this study, we aim to investigate whether the broadband-NIRS measurement of Δ[oxCCO], as a key enzyme in photobiomdulation and mitochondrial respiration, can provide a valuable biomarker in aging and AMD.

8.3 Methods

8.3.1 Animal Preparation

All animals were used with the approval of University College London ethics committee under a UK Home Office project license (PPL 70/8379). All animal procedures conformed to the United Kingdom Animal License Act (1986) and local regulations. Animals were terminated at the end of the experiments.

Aged female rats (Dark Agouti and Lister Hooded) of approximately 12 months were used in this study. Rats have the advantage of possessing larger eyes than mice, which enables easier access to the retina using broadband-NIRS probes. Animals were anaesthetised with 0.3 ml of a mixture of ketamine (0.56 mls) and Dormitor (0.37 mls) in water (0.56 ml) and their pupils dilated with Tropicamide. They were then secured on a bite bar with the body supported.

8.3.2 Broadband NIRS Measurement

Healthy tissues of the eye chamber are highly transparent to visible-NIR region due to the absence of strongly absorbing chromophores and this optical transparency in the eye provides a unique opportunity for imaging the retina [9]. In this study, mini-CYRIL1 was used to investigate retinal haemodynamics, oxygenation and metabolism during photobiomodulation using 670 nm LED illumination. The optical fibres were specifically customised for this study (Figure 8.117) with small diameter (0.6 mm core

diameter), small numerical aperture (0.37 NA) and 2 m long in order to effectively direct/collect the light to/from the retina (LOPTEK, Germany).

Figure 8.118 illustrates the experimental set up for broadband-NIRS measurement on the retina of aged rats. Both optical fibres had needle-like probes as seen in Figure 8.117 (6 cm long, 1.6 mm diameter), which enabled them to be held in a micromanipulator and secured against the corneal surface. The Corneal surface had a layer of viscotears placed on it to prevent dehydration

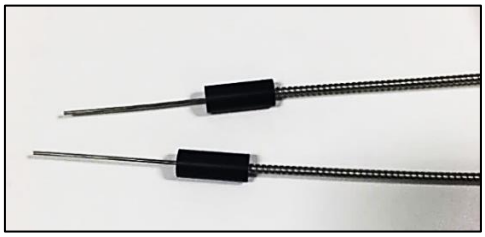

Figure 8.117: Broadband-NIRS source and detector optical fibres designed for reflectance measurement of the retina with small numerical aperture (0.37) and small core diameter (600 μm).

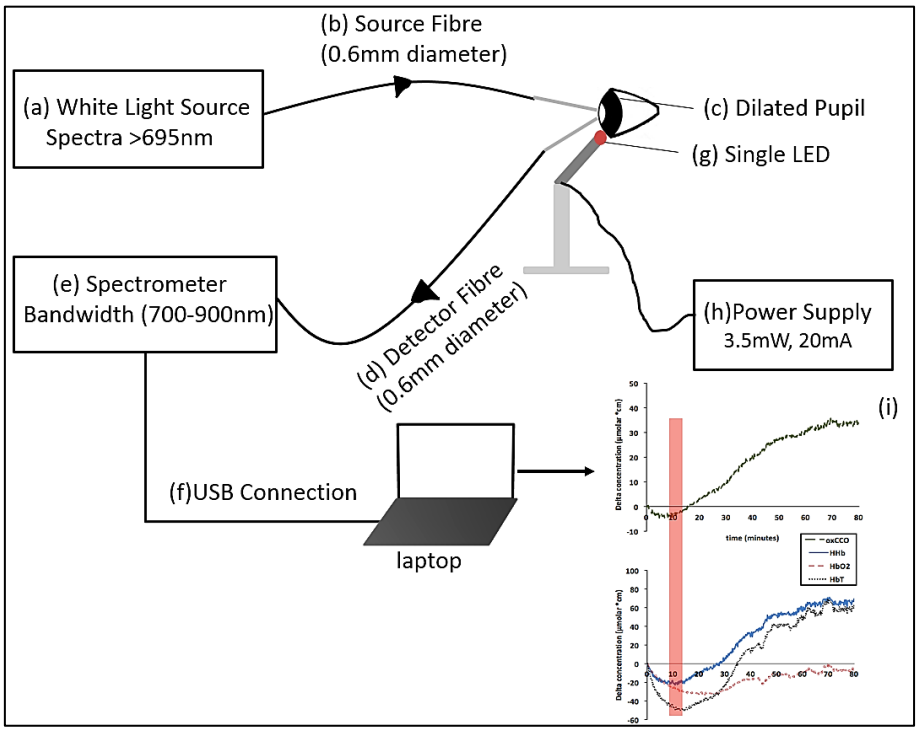

Figure 8.118: Experimental setup; Light from a thermally stabilised halogen-tungsten white light source (a) is filtered for spectra longer than 695 nm and via a 0.6 mm diameter optical fibre (Numerical aperture 0.37) it illuminates the retina through the fully dilated pupil (c). The back reflected light is collected via an identical optical fibre (d) and enters the optical bench of a miniature spectrometer (e) The spectral data are sent to the laptop via USB connection(f). Changes in the attenuation of back reflected light are converted to real-time changes in the concentration of oxy and deoxy haemoglobin ([HbO2] and [HHb]) as well oxidized cytochrome c oxidase (oxCCO). A single 670 nm LED (g) is securely mounted adjacent to the optical fibres in clear line of sight of the eye approximately 5-8 mm from the cornea and fully illuminates the eye with 3.5 mW power at 20 mA (h). Real-time changes in chromophores' concentration Δ[HHb], Δ[HbO2] and Δ[oxCCO] at baseline, during and up to two hours after 670 nm-LED illumination (i). Image produced for [10].

Light from the miniature light source was filtered for the NIR region (cut-on >695 nm) and transmitted to the retina through the dilated pupil using the source fibre, as seen in Figure 8.118. The retina was fully illuminated and the total power transferred across all wavelengths was less than 8 mW and no thermal effects or damages were observed. The back reflected light from the retina was collected using the detector fibre which was securely mounted at ~40° with respect to the source fibre. The optical fibre probes held in a micromanipulator were held at approximately 90° to the corneal surface to avoid specular reflection from the eye. The detected light was focused onto the entrance slit of the miniature spectrometer (specifications discussed in chapter 5, section 5.1.3).

Real-time Spectral data between 700 and 1100 were acquired and focused on an integrated back-thinned CCD detector with a sampling frequency of 0.1 Hz and approximate spectral resolution of 3.15 nm. Mini-CYRIl software version 1 was used to calculate real-time changes in retinal concentration of Δ[HHb], Δ[HbO2] and Δ[oxCCO] using changes in the attenuation of light between 780 and 900 nm. Optical pathlength was not accounted for in the calculations as the DPF for the eye tissue is not known and requires careful study and modelling of eye tissues. Here, we are only interested in monitoring trends of change and absolute quantification of change is not in the scope of this thesis.

Changes in haemoglobin difference (Δ[HbDiff] = Δ[HbO_2] - Δ[HHb]) as a measure for retinal blood oxygenation and changes in total haemoglobin (Δ[HbT] = Δ[HbO_2] + Δ[HHb]) indicative of retinal blood volume were also derived. All the concentration values over the course of each experiment indicated the change with respect to the first measurement.

8.3.3 Broadband-NIRS Data Evaluation (Residual Analysis)

To evaluate the accuracy of broadband-NIRS concentration measurement and to ensure that all the chromophores in the field of view were accounted for in the calculations, residual analysis was carried out as proposed by cooper et al [11], illustrated and performed in chapter 4 (section 4.3.5.1) and chapter 7 (section 7.4.1). Briefly, the attenuation-change spectra at maximum oxCCO change across 780-900 nm, were back calculated from the concentration changes calculated using UCLn algorithm (equation 3.13) when solving only for two chromophores ([HHb] and

[HbO_2]) and when solving for three chromophores (including oxCCO). Subsequently, the difference between the real attenuation spectra (calculated from the measured changed in the intensity of back reflected light, according to equation 3.10), with the back-calculated attenuation spectra from the 2- and 3-chromophore fit were studied.

8.3.4 Study Protocol

A single 670 nm LED (3.5 mW, 20 mA) secured on a metal rod was placed adjacent to the fibre optic probes in clear line of sight of the eye of 9 rats approximately 5-8 mm from the corneal surface (Figure 8.118). During this time rats were in a darkened environment of approximately 2 lux. The eye was exposed to the 670 nm light source for 5 mins and reflections as well as real-time measurement of change in [HHb], [HbO_2] and [oxCCO] were recorded over the next 1-2 hours. In 4 other rats, a long baseline measurement was taken without exposure to 670 nm, and then the eye was exposed to a single 420 nm blue LED (placebo) at the same energy and over the same time as the 670 nm source. Light of such shorter wavelengths inhibits mitochondrial enzyme activity by reducing oxygen consumption and oxidative phosphorylation [12]–[14], and as such has the opposite effects of 670 nm light.

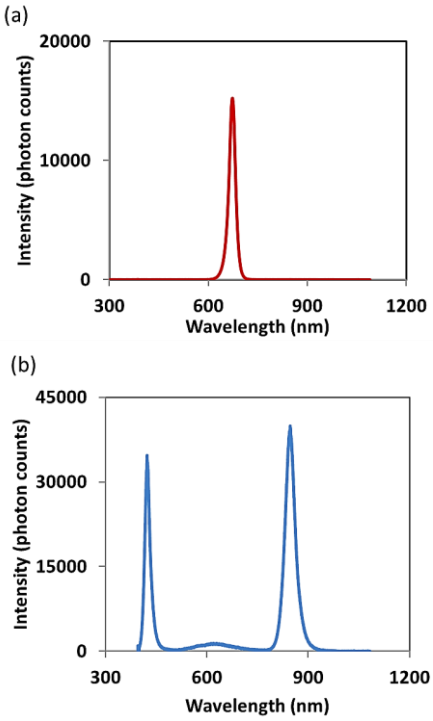

Figure 8.119: Emission spectra of the red LED (670 nm) and the blue LED (420 nm), measured by two different spectrometers from Ocean Optics (HR2000 and Ventana VIS-NIR respectively).

Data were collected in three groups: red LED exposure, no exposure and blue LED exposure. The emission spectra of the red and blue LEDs are presented in Figure 8.119.

A tissue like phantom was used prior to the experiment to investigate the effect of LED light exposure and no variations were observed in the trend of change in the concentrations through the phantom, ensuring that any changes in the retina chromophores' concentration reflects true physiology rather than an optical artefact.

8.3.5 Concentration Data Analysis

The data analysis was performed in Microsoft Excel and MATLAB 2015. Changes in [oxCCO], [HbT] and [HbDiff] were averaged over a 5 min window at baseline and progressively 5 min intervals after LED exposure and for the non-exposure group at 20 min after the start of measurement (Figure 8.120). A non-parametric Kruskal-Wallis test was used to determine overall significance over the time examined in each group. Afterwards, a Non-parametric Wilcoxon Rank Sum test was performed on the progressive measurements of Δ[oxCCO], Δ[HbDiff], and Δ[HbT] to investigate significant changes in concentrations before and at subsequent periods after the LED exposure.

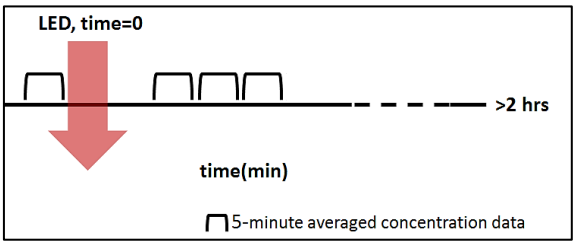

Figure 8.120: Schematic of concentration data pre-processing. Changes in [oxCCO], [HbT]=[HHb]+[HbO2] and [HbDiff]=[HbO_2]-[HHb] are averaged progressively over 5 minutes. Non-parametric test was performed to compare the magnitude of changes in the concentrations before and after red and blue LED exposure or 20 minutes after the start of the measurement when the retina wasn't exposed to any light.

8.4 Results

8.4.1 Spectroscopic Analysis of the NIRS Data

Figure 8.121 illustrates measured intensity and attenuation spectra of the back reflected light from the retina using mini-CYRIL1, as explained in methods. During and after the retina was exposed to 670 nm-LED, there was a significant drop in the recorded reflectance from the retina, as seen in Figure 8.121 (a). The reduction in measured light intensity from the retina following 670 nm illumination could signify an increase in chromophore concentration leading to more scattering and absorption and resulting in larger attenuation, as seen in Figure 8.121 (b). The attenuation change after 670 nm is around 0.04 O.D larger than the attenuation change at baseline.

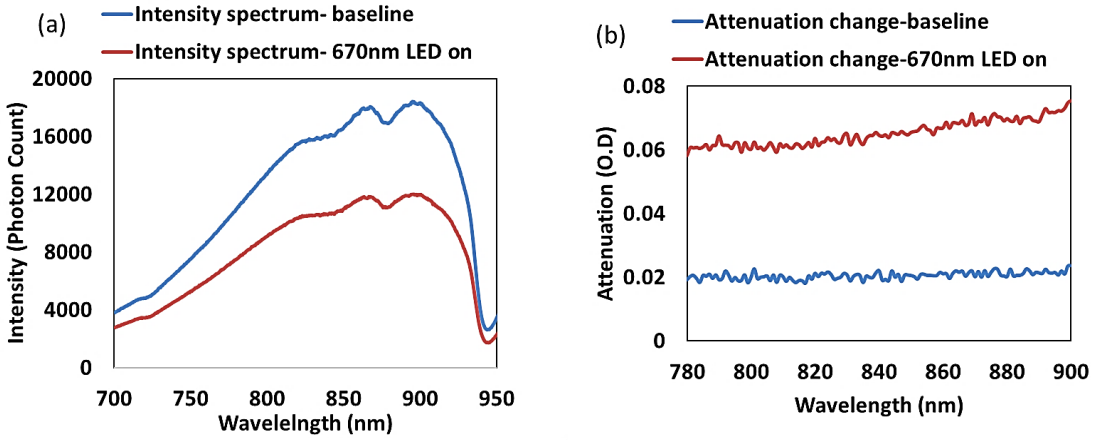

Figure 8.121: (a) Measured reflected intensity spectra from the retina at baseline and after 670 nm illumination (b) Attenuation change spectra with respect to the first measurement at baseline and after exposure to 670 nm LED.

Figure 8.122 illustrates an example of the residual analysis that was performed for evaluation of the broadband-NIRS oxCCO measurement. Figure 8.122 (a) shows the measured attenuation spectrum through the retina during 670 nm exposure as well as the back-calculated attenuations from 2- and 3-chromophore fit. As seen in the figure, the back-calculated attenuation from 3-chromophore fit matches the measured attenuation whilst the red attenuation spectrum shows that when solving only for 2 chromophores, all the chromophores were not accounted for, as it does not match the measured attenuation.

The residual errors from fitting back-calculated attenuation spectra when solving for 2- and 3-chromophores are shown in Figure 8.122 (b). The residual error from 2-chromophore fit has a well-defined shape that matches the extinction coefficient spectrum of oxidised-reduced CCO between 780-900 nm. Therefore, it shows that when resolving only for [HHb] and [HbO_2], the [oxCCO] change remains unaccounted for. However, when solving for 3-chromophore (including oxCCO), the residual error randomly fluctuates around zero, showing that all the chromophores in the field of view have been accounted for in the measurement.

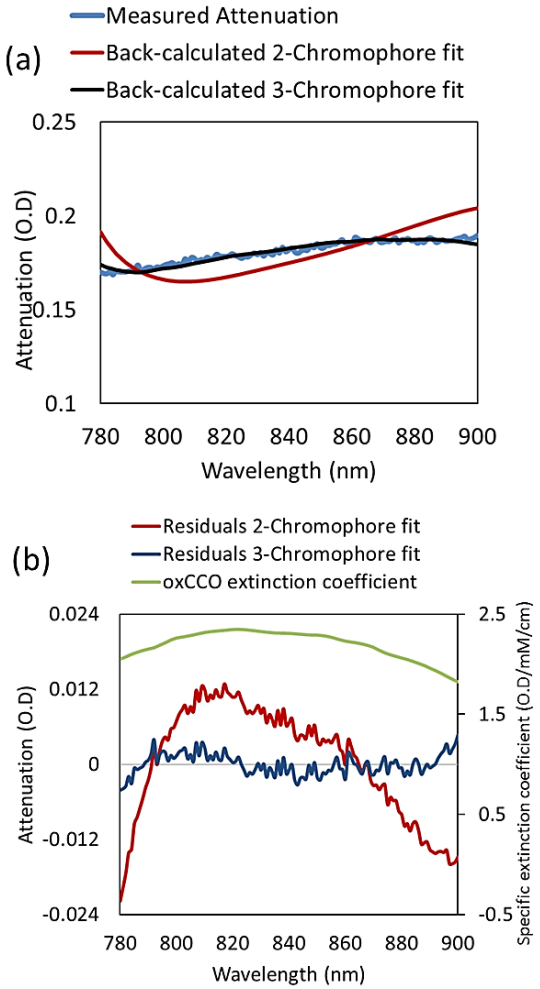

Figure 8.122: (a) Real attenuation spectrum (calculated from the measured change in intensity) and the back-calculated attenuations from 2- and 3-chromophore fit. (b) Residual error from 2- and 3- chromophore fit. The 2-chromophore fit residuals (in red) matches the extinction coefficient of oxCCO (in green), whilst the 3-chromophore fit's residual error (in blue) randomly oscillates around zero.

8.4.2 Changes in NIRS Concentration Data During Red LED Exposure

Following exposure to 670 nm LED for 5 minutes, there was a significant rise in the concentration of oxCCO as early as 5 minutes post illumination, as seen in Figure 8.123. The ascending [oxCCO] signal following LED exposure which leads the increase in [HHb],[HbO_2] and [HbT] signals could indicate increased mitochondrial respiration and oxygen consumption in retinal cells leading to increased ATP production. The enhancement in ATP levels, due to the absorption of 670 nm by cytochrome c oxidase could additionally increase the oxygen demand of the cells, which can be met by an increase in blood flow. Although the changes in blood flow cannot be directly measured with our NIRS system, the consistent rise in [HHb], [HbO_2] and [HbT] following the increase in [oxCCO] could be symptomatic of flow increase (Figure 8.123).

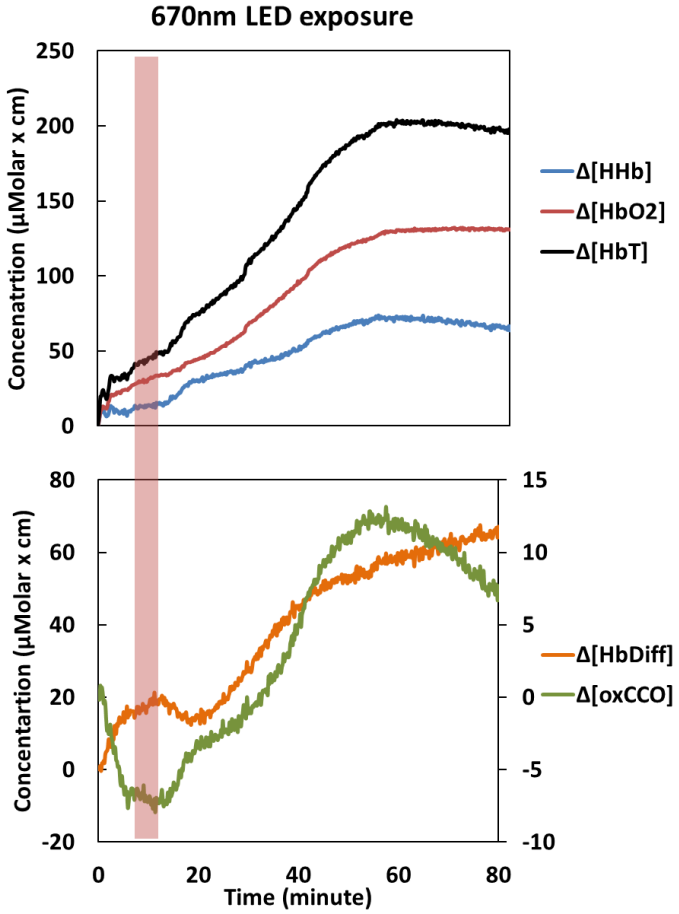

Figure 8.123: Changes in the concentration of oxygenated and deoxygenated, total and difference haemoglobin Δ([HHb], [HbO_2],[HbT] and [HbDiff]) as well as Cytochrome c oxidase (Δ[oxCCO])following 5-minute exposure to 670 nm, showing an increase in the oxidation of CCO as well as increase in retinal blood oxygenation and blood volume.

8.4.3 Changes in NIRS Concentration Data During Blue LED Exposure

Figure 8.124 illustrates changes in broadband-NIRS measurements of retinal oxygenation, haemodynamics and metabolism following exposure to 420 nm light. Apart from the dramatic change in the concentrations (optical artefact), which occurs during 420 nm illumination (due to enhancement in the light level as the blue LED had a peak around 845 nm), there was no significant change in the trend of haemoglobin or cytochrome c oxidase signals compared to what was observed when the retina was exposed to 670 nm LED with the same power.

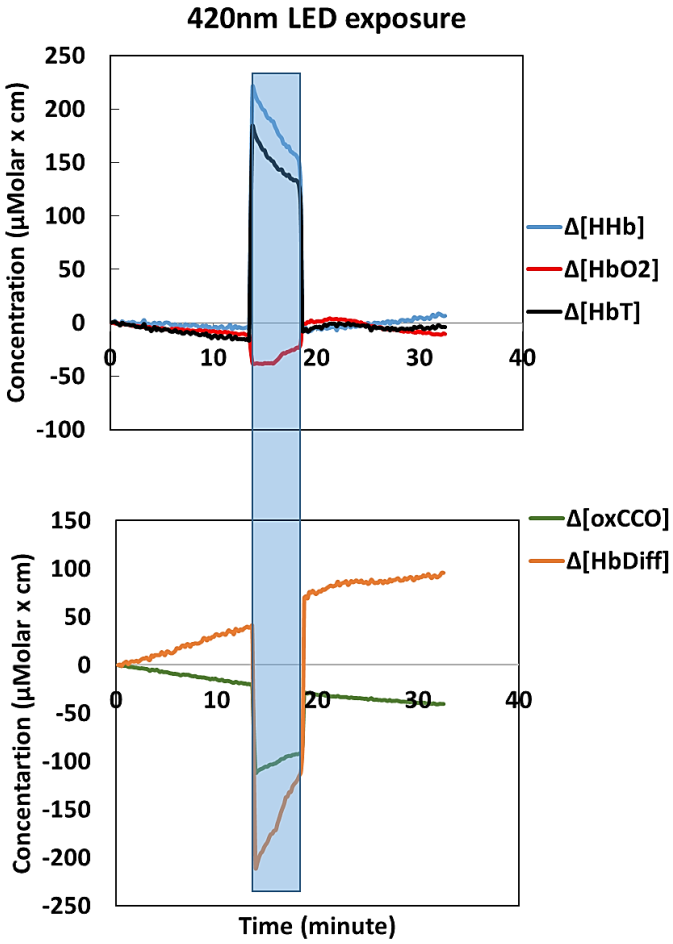

Figure 8.124: Changes in the concentration of oxygenated and deoxygenated, total and difference haemoglobin Δ([HHb], [HbO_2],[HbT] and [HbDiff]) as well as Cytochrome c oxidase (Δ[oxCCO])following 5-minute exposure to 420 nm, showing no significant change in the trend of broadband-NIRS signals.

8.4.4 Changes in NIRS Concentration Data – No LED Exposure

When the retina was continuously monitored with mini-CYRIL1 for changes in oxygenated and deoxygenated haemoglobin as well as cytochrome-c-oxidase, no significant changes were observed in the trends of concentration signals when no LED light was incident on the retina. As seen in Figure 8.125, minor changes and inconsistent variations occurred during the 50 minutes baseline measurement, which were not significant and could reflect the high metabolic activity of retinal cells.

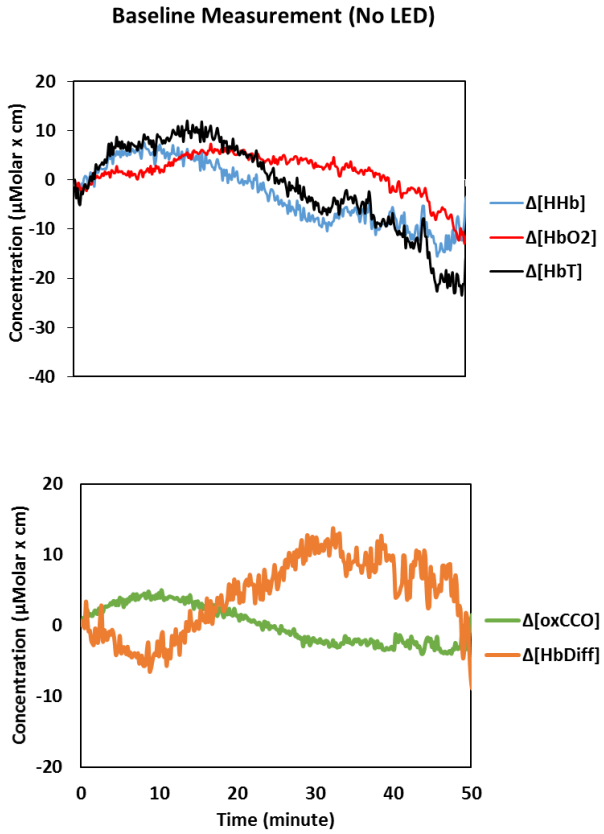

Figure 8.125: Changes in the concentration of oxygenated and deoxygenated, total and difference haemoglobin Δ([HHb], [HbO_2],[HbT] and [HbDiff]) as well as Cytochrome c oxidase (Δ[oxCCO]) for 50 minutes baseline measurement showing no significant change in the trend of broadband-NIRS signals.

8.4.5 Group Data Analysis

The results from group data including red (670 nm) and blue (420 nm) LED exposure as well as no exposure group are presented in this section.

There was a progressive increase in the [oxCCO] following 5 minutes of 670 nm exposure over baseline measurements, as shown in Figure 8.126. Progressive changes above baseline were first apparent as early as 5-10 minutes post exposure and continued over the period of exposure for up to 1-2 hours. These changes were

significant overall (p=0.008, n=9). This was not seen when the retina was exposed to a blue 420 nm LED with the same illumination power or when continuous measurement was performed without being exposed to additional LED illumination (p=0.9 and p=0.7 respectively, n=4). Changes in response to the 420 nm LED resulted in a non-significant decline in [oxCCO], and there was only a small positive drift in [oxCCO] when no light was present.

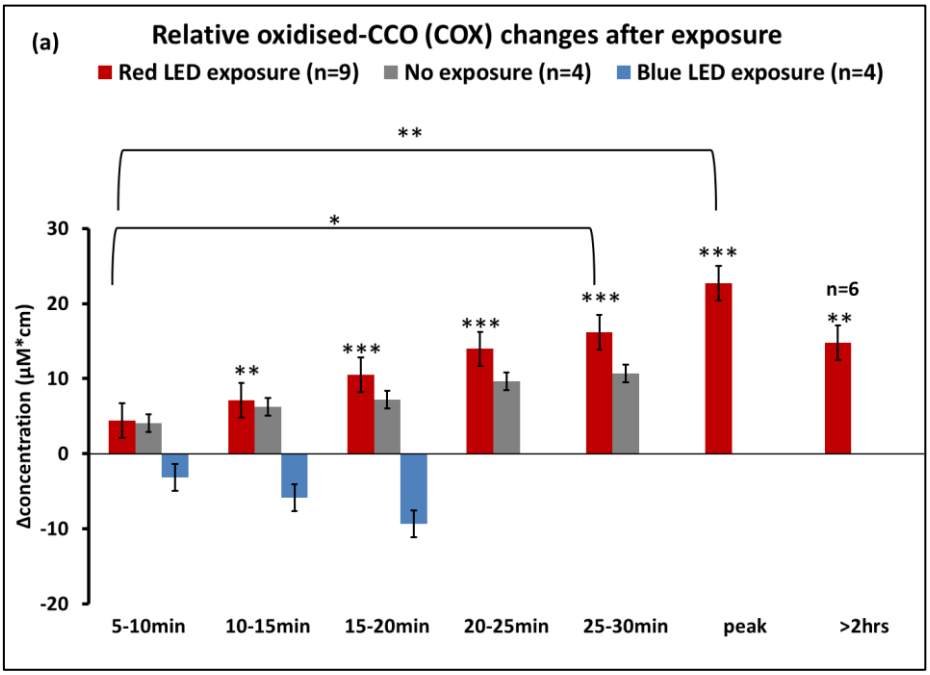

Figure 8.126: Progressive measurements following LED/hypothetical LED exposure for Δ[oxCCO], Δ[HbT]= Δ[HHb]+ Δ[HbO2] and Δ HbDiff = Δ [HbO2]- Δ [HHb], starting at 5 minutes after LED is off. Data is averaged over 5 minutes and re-baselined. Point 0 represents the time after LED exposure. Asterisks on the individual bars represent significant difference compared to baseline being zero in the graph (* p<0.05, **p<0.01, ***p<0.0005). There is a significant increase in retinal Δ[oxCCO] following the red LED exposure relative to baseline as early as 10 minutes after the LED went off (n=9). The Δ[oxCCO] remains significantly higher for about 2 hours post red LED (n=6). There is no significant difference between the mean change in Δ[oxCCO] before and after the blue or with no exposure (n=4). Image was produced for [10].

It was possible to extend the monitoring period in some animals for up to 2 hours, and in these animals the increase in [oxCCO] reached a maximum at approximately 1 hour. At this point it was >5 times greater than at 5-10 mins post exposure. The progressive increases in [oxCCO] were all statistically significant compared to baseline measurements, except those taken at 5-10 minutes (See Figure 8.126 legend. At 1-hour p=0.00004, n=9). Measurements at 25-30 minutes and peak were also significant against those at 5-10 minutes. After approximately 1 hour,

[oxCCO] declined gradually but was still significantly greater than baseline (p=0.001, n=6). It was not possible to extend the monitoring period significantly beyond 2 hours in most animals because of the combined influences of age and general anaesthetic, which resulted in physiological decline that would have likely impacted our results.

Following 670 nm exposure, there was a significant rise in total haemoglobin concentration ([HbT]) in the retina reflecting increased blood volume over the monitoring period (Figure 8.127 p=0.04, n=9). This progressive increase was statistically significant at each stage over baseline from 15-20 minutes post 670 nm exposure onwards. The progressive increase continued until approximately 1 hour when the difference over baseline was maximal (p=0.006, n=9), but even after this declined, it was still significantly greater than at baseline (p=0.04, n=6) at 1-2 hours. These changes were not seen when the retina was exposed to 420 nm or left unexposed (p=0.9 and p=0.2 respectively, n=4 in each group). As seen in Figure 8.127, the results for [HbT] reflect those found for [oxCCO] (Figure 8.126), but with around a 5-minute delay in terms of the progression of changes.

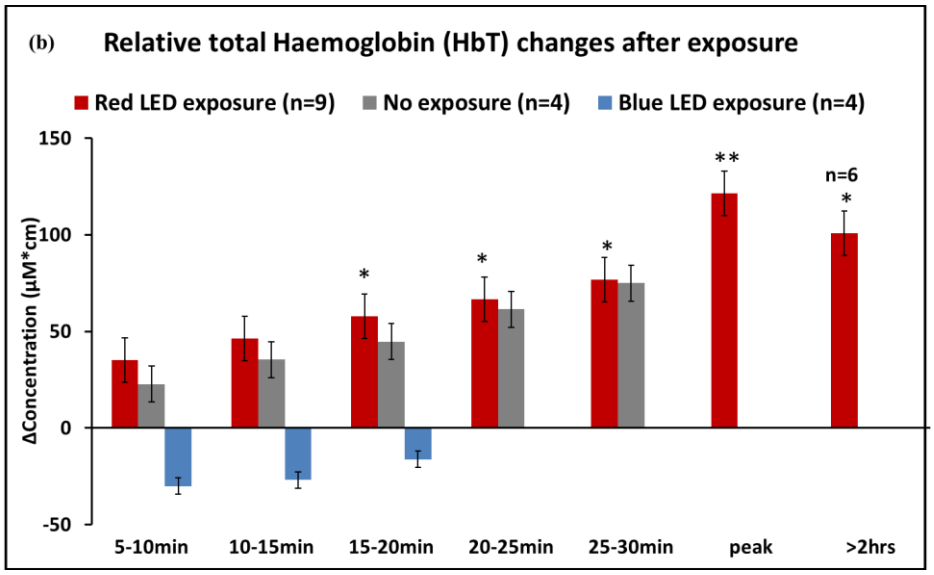

Figure 8.127: Progressive measurements following LED/hypothetical LED exposure for Δ[oxCCO], Δ[HbT]= Δ[HHb]+ Δ[HbO2] and Δ HbDiff = Δ [HbO2]- Δ [HHb], starting at 5 minutes after LED is off. Data is averaged over 5 minutes and re-baselined. Point 0 represents the time after LED exposure. Asterisks on the individual bars represent significant difference compared to baseline being zero in the graph (* p<0.05, **p<0.01, ***p<0.0005). Retinal total haemoglobin change (Δ[HbT], indicative of blood volume) increased significantly as early as 15 minutes after the red LED exposure, and remains significantly higher than baseline for up to 2 hours. There is no significant different between the change in [HbT] before and after blue LED exposure or when the retina is not exposed to any LED.

Figure 8.128 illustrates changes in haemoglobin difference in treatment (670 nm) and control groups (420 nm and no exposure). No significant changes were

observed in the Δ[HbDiff] signal, indicative of blood oxygenation, following exposure to red or blue light. There were no changes in the retinal difference haemoglobin concentration, as measured with mini-CYRIL1, when the retina was not exposed to any light.

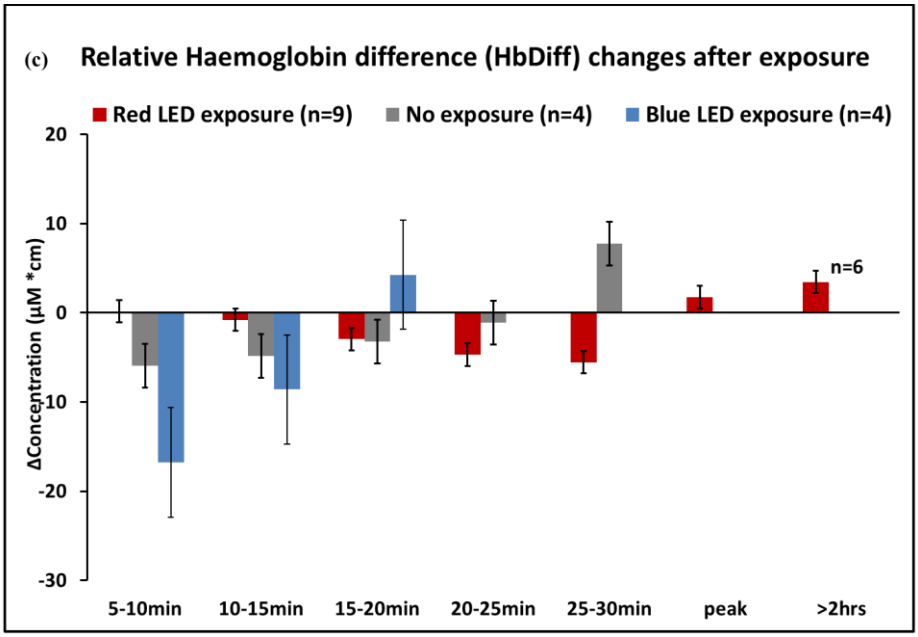

Figure 8.128: Progressive measurements following LED/hypothetical LED exposure for Δ[oxCCO], Δ[HbT]= Δ[HHb]+ Δ[HbO2] and Δ HbDiff = Δ [HbO2]- Δ [HHb], starting at 5 minutes after LED is off. Data is averaged over 5 minutes and re-baselined. Point 0 represents the time after LED exposure. Asterisks on the individual bars represent significant difference compared to baseline being zero in the graph (* $p<0.05$, ** $p<0.01$, *** $p<0.0005$). There is no significant difference in retinal haemoglobin difference (Δ[HbDiff], indicative of blood oxygenation) before and after red/blue/LED or no exposure.

8.5 Discussion

Our results suggest that exposure to 670 nm light for 5 minutes has a significant positive impact on mitochondrial oxidative metabolism in the retina. Real-time measurement of oxy and deoxy haemoglobin as well as cytochrome c oxidase using mini-CYRIL1 on the retina of old rats demonstrated a significant increase in the oxidation of cytochrome c oxidase followed by a delayed significant rise in total haemoglobin concentration, [HbT], after exposure to low power 670 nm LED. The time course of this event fits fits within other longer-term changes that occur in response to this light. Recently our colleagues at the UCL Institute of Neurology found that there were significant enhancements in retinal ATP production and also reduced retinal inflammation within 3-5 days of similar exposure to 670 nm light [15], [16].

No significant change was observed in the concentration of haemoglobin difference signal, [HbDiff], which is indicative of blood oxygenation level. The delayed increase in total haemoglobin concentration [HbT] following the 670 nm exposure and the rise in [oxCCO] are indicative of an increase in retinal blood volume due to higher consumption and accordingly higher blood demand, but possibly also vasodilation.

It is important to mention that our signal is the product of both venous and arterial flow derived with a bias towards the central retina. Furthermore, we have no control for the possibility of venous congestion and blood volume accumulation independent of flow. For these reasons, we are conservative in any possible interpretation of these results.

A non-significant reduction in [oxCCO] following exposure to 420 nm light was observed, which is consistent with data showing that shorter wavelengths of light suppress retinal metabolism [12]–[14]. When the retina was not exposed to any LED light, there was no significant changes or consistent trends in haemoglobin and cytochrome-c-oxidase signals, although there were insignificant changes in the concentrations due to the high metabolic activity of the retina.

While our results are clear, we cannot explicitly exclude the possibility that the light used in the analysis of reflection from the retina, which had a cut on >695 nm was without influence. However, there was almost no overlap in the spectrum of this and the 670 nm LED. In addition, there was a large difference in the energies of the two light sources. Hence, we consider that any influence was minimal and would not impact on the interpretation of our results.

As discussed in chapter 2, mitochondria play a key role in aging and disease as they provide the ATP required for cellular function. When the energy is decreased, inflammation occurs which can ultimately lead to cell death [17]. When inflammation is established or there is immune vulnerability ageing can overturn into disease, particularly AMD, which is the largest cause of blindness in the Western world in people over the age of 65 [18], [19]. In a mouse model of AMD, ATP production declines significantly long before the retinal phenotype develops in this model, which could suggest that mitochondrial function might have a major role in the early development of AMD [2]. The premature decline of ATP may be reflected by changes in [oxCCO] in response to 670 nm light, because current experiments at the Institute

of Ophthalmology are showing that 670 nm exposure has little impact on young animals, presumable due to their mitochondria being healthy. However, this will not be the case with age or early AMD.

In this study, we used broadband-NIRS for the first time to monitor the retina of old rats and assumed that the detected back reflected light was attenuated by the retina tissue and its cellular contents. This technique can also be used to evaluate age related changes in the human macula with exposure to 670 nm light, although further computational simulations of light diffusion through the eye may be needed to refine the technique for larger eye size and to confirm the exact origin of the signal.

8.6 Summary

In this chapter, the effect of 670 nm light on the redox state of mitochondria was investigated using mini-CYRIL 1 and the broadband-NIRS measurement of oxygenated and deoxygenated haemoglobin as well as cytochrome c oxidase. Our results demonstrated a consistent enhancement in the Δ[oxCCO] signal indicative of cellular oxidative metabolism and ATP production as early as 5-10 minutes post 670 nm LED exposure, which was not seen when the retina was exposed to a blue (420 nm) LED or when it was left unexposed. Our results suggest that mitochondrial function can be improved in aged retina through exposure to 670 nm LED light. This finding agrees with previous results in the literature produced using 670 nm at the same energy. A significant increase in total retinal blood volume was observed during the measurement period 15-20 minutes post exposure to 670 nm, which was not seen in any other cases, suggesting an enhanced need for blood supply following improved oxidative metabolism and increased oxygen consumption.

Mitochondria play a key role in ageing and diseases such as age related macular degeneration (AMD) as they provide the majority of ATP required for cellular function. When this is reduced, inflammation develops and this can progress to cell death [17]. Therefore, it is important to establish a biomarker in the retina that could help identify declining function of the mitochondria that may lead to AMD. Our pilot results suggest that the broadband-NIRS measurement of oxCCO produced by mini-CYRIL1 could be a potential predictive marker for retinal mitochondrial function and AMD.

Bibliography

[1] R. A. Linsenmeier and L. Padnick-Silver, "Metabolic dependence of photoreceptors on the choroid in the normal and detached retina," *Investig. Ophthalmol. Vis. Sci.*, vol. 41, no. 10, pp. 3117–3123, 2000.

[2] K. C. Calaza, J. H. Kam, C. Hogg, and G. Jeffery, "Mitochondrial decline precedes phenotype development in the complement factor H mouse model of retinal degeneration but can be corrected by near infrared light," *Neurobiol. Aging*, vol. 36, no. 10, pp. 1–8, 2015.

[3] C. López-otín, M. a Blasco, L. Partridge, and M. Serrano, "Europe PMC Funders Group The Hallmarks of Aging," vol. 153, no. 6, pp. 1194–1217, 2013.

[4] NHS website, "Macular degeneration - NHS Choices." [Online]. Available: http://www.nhs.uk/conditions/macular-degeneration/Pages/Introduction.aspx. [Accessed: 01-Jul-2017].

[5] X. Wang, F. Tian, S. S. Soni, F. Gonzalez-Lima, and H. Liu, "Interplay between up-regulation of cytochrome-c-oxidase and hemoglobin oxygenation induced by near-infrared laser," *Sci. Rep.*, vol. 6, no. April, p. 30540, 2016.

[6] M. R. Hamblin and T. N. Demidova, "Mechanisms of low level light therapy," *Proc SPIE*, vol. 6140, pp. 1–12, 2006.

[7] D. Pastore, M. Greco, and S. Passarella, "Specific helium-neon laser sensitivity of the purified cytochrome c oxidase.," *Int. J. Radiat. Biol.*, vol. 76, no. 6, pp. 863–70, Jun. 2000.

[8] R. Begum, M. B. Powner, N. Hudson, C. Hogg, and G. Jeffery, "Treatment with 670 nm Light Up Regulates Cytochrome C Oxidase Expression and Reduces Inflammation in an Age-Related Macular Degeneration Model," *PLoS One*, vol. 8, no. 2, pp. 1–11, 2013.

[9] V. Tuchin, "Optical Models of Eye Tissues," in *Tissue Optics: Light Scattering Methods and Instruments for Medical Diagnosis (Second Edition)*, Second Edi., Bellingham, Washington: SPIE, 2007, pp. 257–288.

[10] P. Kaynezhad, I. Tachtsidis, and G. Jeffery, "Optical monitoring of retinal respiration in real time: 670 nm light increases the redox state of mitochondria," *Exp. Eye Res.*, vol. 152, 2016.

[11] C. E. Cooper and R. Springett, "Measurement of cytochrome oxidase and mitochondrial energetics by near-infrared spectroscopy.," *Philos. Trans. R. Soc. Lond. B. Biol. Sci.*, vol. 352, no. 1354, pp. 669–676, 1997.

[12] E. Chen, P. G. Söderberg, and B. Lindström, "Cytochrome oxidase activity in rat retina after exposure to 404 nm blue light.," *Curr. Eye Res.*, vol. 11, no. 9, pp. 825–31, Sep. 1992.

[13] E. L. Pautler, M. Morita, and D. Beezley, "Hemoprotein(s) mediate blue light damage in the retinal pigment epithelium.," *Photochem. Photobiol.*, vol. 51, no. 5, pp. 599–605, May 1990.

[14] L. M. Rapp, B. L. Tolman, and H. S. Dhindsa, "Separate mechanisms for retinal damage by ultraviolet-A and mid-visible light.," *Invest. Ophthalmol. Vis. Sci.*, vol. 31, no. 6, pp. 1186–1190, 1990.

[15] I. Kokkinopoulos, A. Colman, C. Hogg, J. Heckenlively, and G. Jeffery, "Age-related retinal inflammation is reduced by 670 nm light via increased mitochondrial membrane potential," *Neurobiol. Aging*, vol. 34, no. 2, pp. 602–609, 2013.

[16] D. Gkotsi, R. Begum, T. Salt, G. Lascaratos, C. Hogg, K. Y. Chau, A. H. V Schapira, and G. Jeffery, "Recharging mitochondrial batteries in old eyes. Near infra-red increases ATP," *Exp. Eye Res.*, vol. 122, pp. 50–53, 2014.

[17] J. Nunnari and A. Suomalainen, "Mitochondria: In sickness and in health," *Cell*, vol. 148, no. 6, pp. 1145–1159, 2012.

[18] H. R. Coleman, C.-C. Chan, F. L. Ferris, and E. Y. Chew, "Age-related macular degeneration," *Lancet*, vol. 372, no. 9652, pp. 1835–1845, 2008.

[19] U. Chakravarthy, T. Y. Wong, A. Fletcher, E. Piault, C. Evans, G. Zlateva, R. Buggage, A. Pleil, and P. Mitchell, "Clinical risk factors for age-related macular degeneration: a systematic review and meta-analysis," *BMC Ophthalmol.*, vol. 10, no. Journal Article, p. 31, 2010.

Chapter 9. Discussion

This chapter summarises the work done, emphasising on the main findings which address the aims and objectives of this thesis in section 9.1. Section 9.2 describes future steps that need to be taken to develop and validate mini-CYRIL in the clinic, including further hardware and software developments. The chapter ends with a final concluding section highlighting the major contribution of the research (section 9.3).

9.1 Thesis Summary

The main motivation behind this thesis was the absence of a compact portable and cost-effective instrument that can non-invasively measure, not only tissue oxygenation but also oxygen metabolism at bed/cot side. This is specifically important for monitoring central nervous system (CNS) due to its high energy demands and high metabolic rate. Pathologies and injuries to the CNS tissues because of metabolic dysfunction is most of the times irreversible because generally neurones in the central nervous system cannot repair or renew.

It was discussed in chapter 2 (section 2.8.2) that even though the optical measurement of MRO_2 (metabolic rate of oxygen), as a reliable marker for the evaluation of oxygen metabolism in tissue, offers a non-invasive useful way to understand tissue oxygen delivery and uptake, it fails to provide a direct measurement of tissue energetics at cellular level and simply relies on blood oxygenation measurements.

Broadband-NIRS and the measurement of oxidised-cytochrome c oxidase (oxCCO) is proposed in this thesis as a solution for a bedside mitochondria-specific marker for CNS tissue metabolism in a diverse range of conditions with a mutual devastating outcome, which is permanent damage to the tissue due to impaired aerobic metabolism. However, despite its great potential as a simple non-invasive and cost-effective technique for in-vivo measurements at bedside, broadband-NIRS has remained mostly as a research tool rather than a clinical system almost after 40 years since its first introduction [1].

In this thesis, I tried to address some of the hindering factors for broadband-NIRS being established as a clinical tool, which are summarised below:

- Lack of clear understanding about the relationship between oxCCO measured with broadband-NIRS to other metabolic markers for brain injury that are measured with gold standard techniques, such as MRI/MRS or PET.
- Bulkiness of current broadband-NIRS systems and complex daily calibrations while easy transportation and application are two important features of a bedside clinical system in demanding environments such as intensive care unit (ICU) or accident and emergency (A&E),
- Lack of extensive research on other CNS tissues. Unlike MRS and PET that are applicable to a broad range of tissue metabolism measurements, most research in the broadband NIRS and the measurement of oxCCO as a marker for metabolism has been extensively focused on brain (due to its high importance) and to a small extent on muscle studies.

To tackle these limiting factors, the following objectives were met throughout this thesis and are discussed in the subchapters below.

9.1.1 Understanding the Physiological Information that Δ[oxCCO] Offers, through its Relationship with ^{31}P-MRS Metabolic Markers for Brain Injury

The relationship between the measurement of oxCCO produced by UCL1 (the first broadband system developed at UCL in 1995) was investigated with phosphorus(^{31}P)- MRS markers for brain injury severity in the preclinical study of neonatal hypoxia-ischaemia (HI) at the UCL institute of Neurology in chapter 4. In this study, the HI insult protocol was developed and controlled based on ^{31}P-MRS measurements of NTP/epp, which is a direct measure for brain ATP levels, PCr/epp and Pi/epp (explained in chapter 4). The correlation between UCL1-measured Δ[HbT], blood volume measure, Δ[HbDiff], blood oxygenation measure, and Δ[oxCCO], oxidative metabolism measure, with the MRS markers for HI severity and recovery was investigated through the recovery fraction algorithm (n=32). A highly significant strong linear correlation was observed between Δ[oxCCO] recovery fraction with all the MRS markers (NTP/epp, PCr/epp Pi/epp) for injury severity during HI and up to 1-hour recovery. There was only a mild significant association between the recovery fraction of Δ[HbDiff], an indicator of ischaemia, with the MRS markers for HI injury (NTP/epp, PCr/epp, Pi/epp) and no correlation was seen between

the recovery fraction of [HbT] with any of the MRS markers. The recovery fraction algorithm also provided a quantifiable measure for Δ[oxCCO] signal to distinguish between the poor and good outcomes following the primary injury (71% threshold with 100% sensitivity and specificity). Our results suggested that the broadband NIRS measurement of Δ[oxCCO] is a reliable indicator of mitochondrial metabolism and can be used as a cheap alternative, non-invasive and pod side technique to ^{31}P-MRS, to monitor the HI insult in piglets' brain in the preclinical study of neonatal hypoxia-ischaemia.

9.1.2 Development of a Miniature Broadband-NIRS System Based on Easily Sourced Components

A portable broadband-NIRS system called mini-CYRIL was developed based on cost-effective miniature off-the-shelf light source and spectrometers by Ocean Optics, USA (chapter 5).

Hardware: The main challenge with miniaturisation of broadband-NIRS systems is the need for having large core diameter optical fibres to maximise the contact area with the tissue under examination and with high numerical aperture to collect highly diffused light from the tissue surface. This essential requirement is incompatible with the small throughput design of most miniature spectrometers (F/4), such as highly sensitive QE65. In this thesis, several approaches were considered to tackle the throughput problem when using miniature spectrometers.

- The first approach was f-matching using miniature collimating and focusing lenses, which resulted in 180% signal enhancement through a tissue like phantom. The main limitation with this technique was its complications and instability, which rejects one of the main requirements for a clinical device, which is being easy to use. The total enhancement in the signal was also not comparable to the ones produced by standard broadband-NIRS units such as UCL1.
- The next approach was modifying detector fibre's geometry (with smaller NA), so that it mimicked the entrance slit of the spectrometer that would allow most of the collected light through while maintaining the spectral resolution.

Because of using the modified fibre geometry, there was ~295% increase in the peak intensity. The limitation with this technique was the high cost of the modified geometry optical fibre with NA=0.37 (nearly 10 times higher than the standard (NA=0.57) circular arrangement). Furthermore, modified fibre geometry as also proposed by other groups [2], [3], was only beneficial if there was minimum mismatch between the detector fibre and spectrometer's NA hence we were limited to using 0.37 detector fibre which led to further photon loss at tissue surface.

- The final approach was using a miniature spectrometer with a less sensitive CCD (with smaller quantum efficiency in the near-infrared and without thermoelectric cooling) but larger throughput (F/2) optical bench. The spectral data generated by Ventana spectrometer had 7 times higher peak count than QE65-pro with a circularly arranged optical fibre and around twofold increase compared to when the slit-shaped fibre was used. The percentage increase across all wavelengths using Ventana spectrometer (0.57 NA fibre) was 665 ± 146 % compared to using QE65-pro with 0.57 NA fibre, and 68 ± 22% compared to QE65-pro with modified 0.37 NA detector fibre. Ventana spectrometer is more cost effective than QE65-pro and the only limitation was the absence of integrated thermoelectric cooling, which led to large accumulative dark noise varying over time. Therefore, even subtracting the dark count from the measured intensity data leads to erroneous concentration change measurement. The retrofit cooling upgrade that was done with the help of manufacturers (Wasatch Photonics, USA) could consistently maintain the CCD temperature at 10 degrees below the ambient, during long hours measurement (>24 hrs), which resolved the dark count accumulation problem.

Mini-CYRIL hardware was finalised in two versions with the same light source (HL-2000-HP) and two spectrometers for exposed tissue applications (QE65-pro) and Ventana VIS-NIR with cooling upgrade for brain measurements and for source-detector separation greater than 4 cm.

Software: Mini-CYRIl has two software version which allow for real-time data collection, processing and saving in MATLAB. The earlier version was developed for real-time measurement of change in oxygenated and deoxygenated haemoglobin as

well as cytochrome-c-oxidase through a fixed pathlength estimation (using tissue specific DPF, reported in the literature and source-detector separation).

Version 2, has an additional feature which enables real-time estimation of changes in the differential pathlength using the second differential spectroscopy technique which was proposed by Matcher et al [4].

Version 2.1. has a modified display in MATLAB which improves data processing time and offers additional features such as calculating the area under the curve (AUTC) and recovery fraction (RF) of oxCCO signal which can be used in monitoring the HI insult.

9.1.3 Validation of the Miniature Broadband-NIRS System (Mini-CYRIL) in CNS Tissue Oxygenation and Metabolism Measurement

Mini-CYRIL primarily was assessed for stability and software performance using phantom studies and cuff-occlusion measurements and the changes in the concentration of HHb and HbO_2 and oxCCO during arterial occlusion was comparable to what was reported in similar studies.

After preliminary testing, both versions of mini-CYRIL were taken to various preclinical settings (discussed below) for evaluation and further investigation of the physiological information that the Δ[oxCCO] can provide in a range of CNS disorders.

9.1.3.1 Preclinical Study of Neonatal Hypoxia Ischaemia

Mini-CYRIL2's performance was evaluated and compared with the performance of UCL1 as a standard broadband-NIRS system, in the preclinical study of HI. Mini-CYRIL2 was capable to collect high intensity transmission data through piglets' brain for optode separations greater than 4 cm. The optical signals recorded on piglets during HI and recovery were analysed for crosstalk between the signals through residual analysis and the oxCCO signal was found to behave independently to the haemoglobin signals which is significant as there is historical controversy over its independence. In addition, using broadband spectra to solve only for haemoglobin signals without oxCCO component showed to be inaccurate.

Realtime pathlength analysis showed that despite the same optode spacing, the real-time pathlength among subjects is considerably dispersed and therefore using a fixed DPF (as most broadband-NIRS systems do), could lead to under/overestimation

of the concentration of chromophores. In a group of 10 piglets, in average the mean increase in [HHb] and decrease in [HbO_2] during HI was more than 70% and in [oxCCO] around 50% greater when real-time pathlength was estimated using the absolute attenuation measurement compared to when a fixed pathlength was used. Another limitation of using a fixed pathlength in the preclinical study of HI, is the drop (~20%) in the differential pathlength in most of the piglets at nadir HI that is unaccounted for when using a fixed DPF, which leads to inaccurate quantification of change in the concentration of chromophores. Therefore, operating mini-CYRIL in real-time pathlength estimation mode is crucial in the preclinical study of HI, since the magnitude of change in [oxCCO] is used to monitor and direct the insult.

The limitation with operating mini-CYRIL in real-time pathlength estimation mode, is that failing to record a good reference spectrum (a smooth spectrum across all wavelengths with the highest possible number of counts before the CCD saturates) may result in poor estimation of pathlength, specifically when there is a significant rise in the transmitted intensity through piglet's brain, which could result in noisy or erroneous concentration data.

9.1.3.2 Preclinical Study of Multiple Sclerosis

Mini-CYRIL1 was used for the first time to investigate the role of hypoxia and mitochondrial function in neurological deficits caused by inflammation in the spinal cord of rats induced with EAE (experimental autoimmune encephalomyelitis). The measured concentrations were analysed for cross-talk between the signals through residual analysis and the oxCCO signal was found to behave independently to the haemoglobin signals. The group results (EAE (n=11) and Control (n=9)) from transient inspiratory hyperoxia demonstrated a highly significant increase in haemoglobin oxygenation ($\Delta[HbDiff]_{EAE\text{-}Control}$=+21.53) and oxidative metabolism ($[oxCCO]_{EAE\text{-}Control}$=+ 2.22) in EAE-induced rats compared to control group, while the larger increase in spinal cord total haemoglobin concentration (blood volume, $[\Delta HbT]_{EAE\text{-}Control}$= + 4.20) was not significant.

The nature of relationship between broadband-NIRS measurements of oxygenation and metabolism provided by mini-CYRIL with the disease severity and duration in the EAE-induced rats was further investigated. A strong quadratic association was observed between the change in the oxidation of cytochrome c oxidase

with the total functional deficit score (as a measure for disease severity and duration) in all the rats. This finding could suggest that mitochondrial function might be inhibited by tissue hypoxia at early stages of the disease, as demonstrated through biochemical and invasive tissue oxygen measurement studies. Therefore, an increase in systemic oxygenation will enhance the mitochondrial respiration (as measured by Δ[oxCCO]). At the later stages of the disease however, as the deficit severity and duration progress, the increase in systemic oxygenation cannot further boost mitochondrial metabolism, which could be due to the impaired electron transport chain (ETC) and oxidative metabolism as prolonged hypoxia leads to irreversible damage to the cells.

The main limitation in this study was the experimental setup due to the size of the spinal cord, which was very narrow and the large vein in the middle should have been avoided. Therefore, we were limited to using submillimetre core probes (0.5 mm) leading to a significantly small number of photons collected and reaching the CCD (even at an integration time of 10 seconds), which affected the quality of the concentration data.

9.1.3.3 Retina of Aged Rats

Mini-CYRIL1 was used for the first time to investigate LLLT (low-level light therapy) in the retina of aged rats using transient 670 nm LED exposure. AMD (age-related macular degeneration) is a retinal condition which from the early stages is associated with aggressive inflammation that leads to loss of central vision in old people. However, the use of low power 670 nm has been shown to improve mitochondrial respiration and ATP production. In this study, mini-CYRIL1's measurement of Δ[oxCCO], as a key enzyme in photobiomdulation and mitochondrial respiration (with strong correlation with ATP production as measured by MRS (NTP/epp) in chapter 4), demonstrated to provide a valuable potential predictive marker in aging and AMD.

Data were collected from 9 rats that were treated with 5-minute low power 670 nm exposure, as well 4 others that had no exposure or were exposed to 5-min of 420 nm LED that has been shown to inhibit mitochondrial function (so an increase in ATP is not expected). The group data analysis demonstrated a highly significant progressive increase in the Δ[oxCCO] signal 5 minutes after 670 nm LED illumination for up to 1

hour, which was followed by a delayed significant rise in Δ[HbT] signal while no significant change was observed in the Δ[HbDiff] signal. The delayed increase in total haemoglobin concentration [HbT] following the 670 nm exposure and the rise in oxidised CCO are indicative of an increase in retinal blood volume due to higher consumption and accordingly higher blood demand, but also possibly vasodilation. After approximately 1 h, Δ [oxCCO] declined gradually but was still significantly greater than baseline (n=6). Changes in response to 420 nm LED resulted in a non-significant decline in [oxCCO] that could be due to the small number of subjects (n=4) and there was only a very small insignificant positive drift when no light was present (n=4).

One of the limitations with this study was the impossibility to extend the monitoring period in rats beyond 2 hours (to investigate longer term changes) because of the combined influence of age and general anesthesia, which resulted in physiological decline that would affect our results. Other limitation is we assumed the detected back-reflected light was purely attenuated by the retina tissue and its cellular content. However, further computational modellings of light diffusion through the eye and simulations are required to confirm the exact origin of the signal.

9.2 Future Work

In this section, further development of the system (hardware and software) and suggestions for subsequent work focusing on in-field application is discussed.

9.2.1 Hardware Upgrade

9.2.1.1 Improving the Portability

To enhance the portability of mini-CYRIL, the miniature light source and spectrometer can be housed in a small ventilated aluminium enclosure as seen in Figure 9.129. This upgrade makes mini-CYRIL more portable and easily deployable in the clinical environment.

Figure 9.129: A possible example of a ventilated aluminium enclosure that can house mini-CYRIL's light source and spectrometer. External dimension 299 x 520 x 300 mm. Image taken from RS Components UK - http://uk.rs-online.com/web/p/rack-fitting-cases-enclosures/4549587/

9.2.1.2 Enhancing the Number of Channels

Currently, mini-CYRIL is a single channel system with one source and one detector fibre. It is however, possible to increase the number of channels by using more miniature spectrometers which enable simultaneous measurement over different regions of the brain or other parts of the CNS. The feasibility of a two-channel mini-CYRIL was investigated in the study of retina photobiomodulation using 670 nm LED (Chapter 8). As seen in Figure 9.130, the source fibre was bifurcated to illuminate both eyes and two identical detector fibres transferred the light reflected from the retina to QE65-pro and Ventana spectrometers. The software was also modified to collect and process the intensity data simultaneously from both spectrometers.

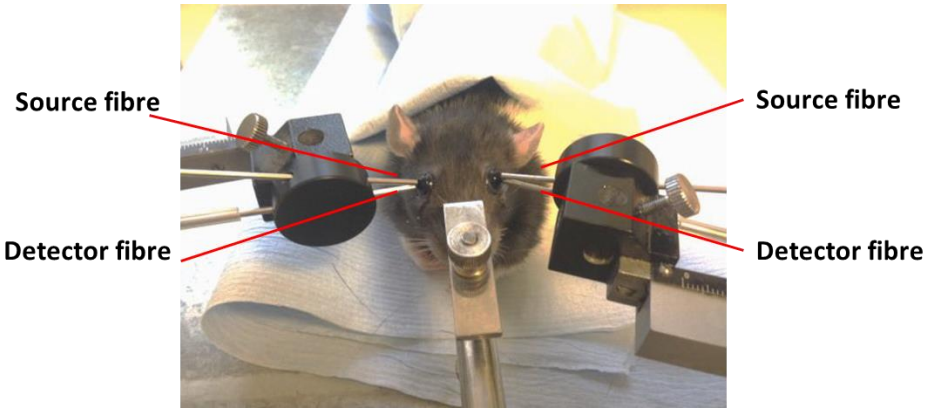

Figure 9.130: Experimental setup during 2-channel measurement on rat's retina using mini-CYRIL. The source fibre was bifurcated so that both eyes could be illuminated simultaneously.

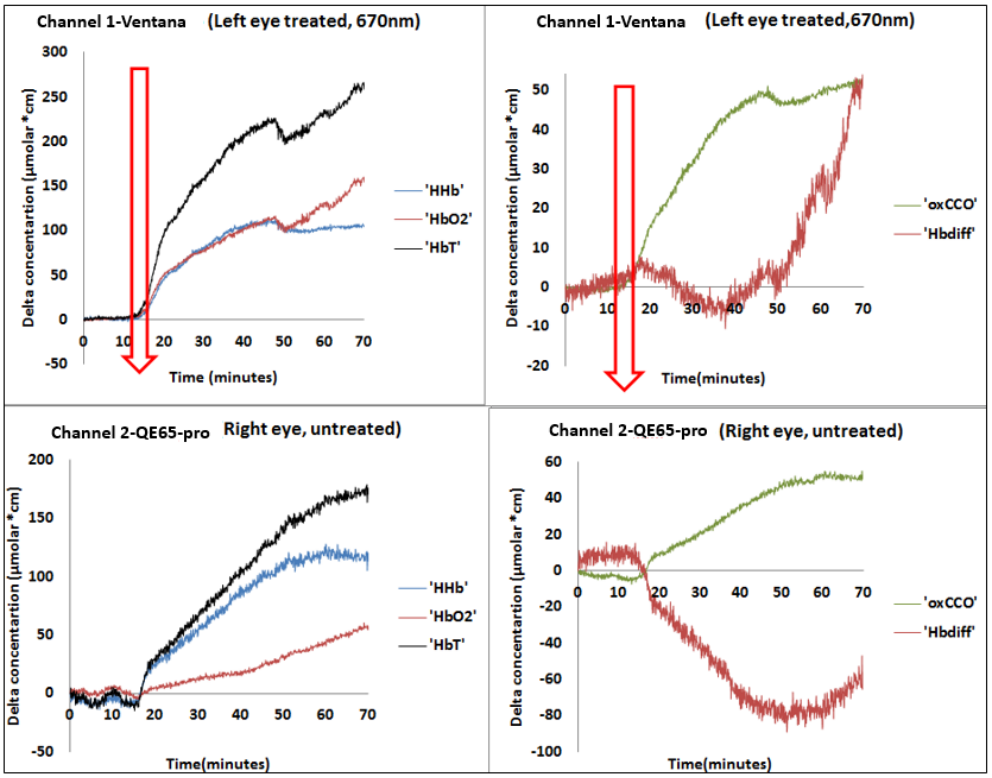

Figure 9.131: Changes in concentration of HHb],[HbO_2], [HbT], [oxCCO] and [HbDiff] in both eyes while one (the left eye) was being treated with 670 nm for 5 minutes.

Figure 9.131 illustrates simultaneous changes in [HHb], [HbO_2], [oxCCO], [HbT] and [HbDiff] measured in both eyes after one eye (left eye in this example) was treated (exposed to 670 nm for 5 minutes). Mini-CYRIL's two-channel measurement demonstrates a delayed increase in oxy- and deoxy- haemoglobin as well as cytochrome-c-oxidase in the untreated eye (no exposure). This finding might be of interest for further investigations regarding the mechanism of effect of 670 nm but does not fit in the scope of this thesis. The data was only presented here to demonstrate the feasibility of developing multichannel mini-CYRIL systems with further modifications.

9.2.1.3 Customised Miniature Spectrometer with Larger Throughput and Smaller Footprint

Currently the large bandwidth of the Ventana spectrometer is not fully used in the preclinical study of HI, since the change in concentrations are estimated based on light attenuations between 780-900 nm. Therefore, following discussions with

Wasatch Photonics, a new miniature solution has been proposed (see Figure 9.133) with larger throughput design (f/1.3) and custom grating (780-900 nm) providing 3 nm spectral resolution with slit width of 200 μm, as well as improved CCD characteristics in the NIR with retrofit cooling, at a slightly higher cost (~£3000). Comparison between the CCD that was used in the Ventana unit with the CCD used in the new customised module (mini-CYRIL3) in Figure 9.132 shows that there will be at least 10% enhanced quantum efficiency in the NIR using mini-CYRIL3, based on the customised spectrometer.

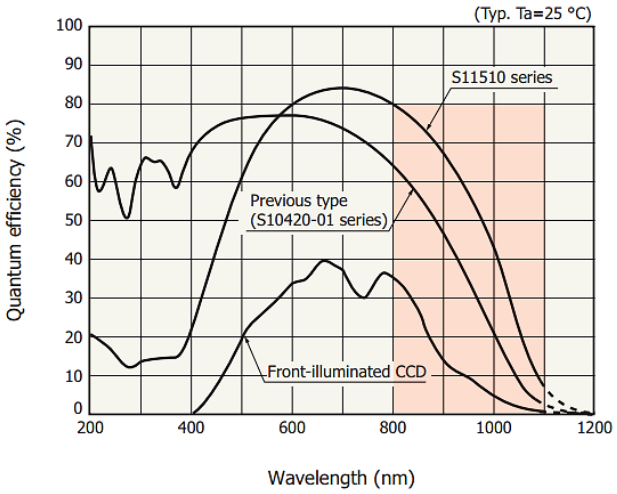

Figure 9.132: The spectral response (quantum efficiency vs wavelength) from the CCD used in Ventana spectrometer S10420-01 and S11510 series having approximately 10% higher quantum quantum efficiency in the NIR. http://www.hamamatsu.com/resources/pdf/ssd/s11510_series_kmpd1126e.pdf

Furthermore, the smaller optical bench of mini-CYRIL3 (f/1.3) compared to mini-CYRIL2's optical bench (f/2), provides a significantly higher throughput considering that throughput is inversely proportional to the square of f/# (Chapter 5, section 5.1.6). Therefore, there will at least be 130% increase in the system's throughput which is highly significant.

Figure 9.133: New modified spectrometer for mini-CYRI3 developed by Wasatch Photonics with enhanced characteristics for head transmission mode studies

9.2.2 Software Upgrade

9.2.2.1 Graphical User Interface

Despite being successfully used by members of the clinical team and in general non-physicists, the mini-CYRIL user interface could be improved to be more user friendly. This include designing graphical user interface in MATLAB with push buttons to start, stop and save the acquisition and perform other tasks such as start/stop calculating the recovery fraction or area under the curve of [oxCCO], instead of having to press certain characters on the keyboard. Furthermore, most commercial NIRS systems do not display the raw optical data which might be confusing to non-physicists. Instead, they only display the calculated concentration data which makes the instrument easier to use. A step towards reducing the complexity, especially for use in the hospital, could be developing a clinical version of the software which includes warnings to alert the user if the optical intensity spectrum is too low, and ask the user to re-position the optical fibres to make a better contact, when necessary.

Finally, the MATLAB program can be removed from the MATLAB environment and run as a standalone executable file, which makes the software easier to use and easier to transfer to different devices.

9.2.2.2 Realtime Absolute Haemoglobin Measurement

Other than calculating the real-time changes in pathlength, the raw absolute attenuation provides more information about the chromophores within the tissue. For instance, the absolute concentration of haemoglobin can also be calculated using the second differential spectroscopy method that was proposed by Matcher and Cooper in

1994 [15]. In this technique, the relative concentration of HHb to tissue water is determined by fitting of the spectral features of the two chromophores in the 710 nm and 840 nm range of the NIR spectrum. Having a large bandwidth (430-1100 nm), mini-CYRIL2, is perfectly capable of providing absolute HHb measurement without further modification.

9.2.3 Mini-CYRIL in Clinical Applications

Currently the CYRIL system developed in Multimodal Spectroscopy Group in 2014 [16] is used at the UCL Hospital to monitor brain tissue physiology in infants following neonatal hypoxic ischaemic injury. Although CYRIL was specifically built to enhance sensitivity and spectral resolution, it is very large and bulky and unsuitable for rapid deployment in a hospital clinic. With much smaller footprint, mini-CYRIL2, could fit directly behind the cot and this would make the broadband-NIRS studies much easier and more acceptable for the clinical team. Figure 9.134 shows CYRIL and mini-CYRIL2 next to a model baby for size comparison. Following mini-CYRIL2's hardware upgrade (being housed in an aluminium enclosure for enhanced portability, section 9.2.1.1 Improving the Portability), it will be easily deployed in the clinical environment. Furthermore, mini-CYRIL2 has an additional useful feature compared to the CYRIL system, and that is real-time estimation of optical pathlength during the measurement. Not only does this feature improve the concentration measurement accuracy as discussed in chapter 6 (section 6.5), but it also accounts for changes in pathlength which is very important especially in babies with changing pathophysiology which may change the nature of the anatomy (e.g. through swelling or oedema) during the measurement period [17].

Another valuable feature that can be integrated in mini-CYRIL is the absolute measurement of oxCCO, as it would allow easier comparison between patients or volunteers and give a better understanding of the state of tissue metabolism. Resolving changes in the oxidized concentration with respect to the reduced con- centration of CCO is challenging and the UCL group is working toward to do this, with both new hardware and algorithm.

Figure 9.134: (a) CYRIL doing a 2-channel reflectance measurement on baby's frontal cortex ; white light from the Oriel fibre illuminator (Newport) is filtered and sent to the head via two source fibres and the reflected light is collected by 8 detectors and focused on to the slit of LS-785 spectrograph(Princeton Instruments) . (b) Miniature system doing a one channel reflectance measurement on baby's frontal cortex; Wight light from HL2000 miniature light source (Ocean Optics) is filtered and sent to the frontal cortex via an optical fibre and the reflected light is collected and focused onto Ventana's slit (Ocean Optics) through an identical detector fibre. Image produced for [18].

9.3 Conclusion

This thesis described the development of a novel miniature broadband-NIRS system based on easily sourced components, called mini-CYRIL, with a specific focus on understanding the physiological information that mini-CYRIL and specifically the Δ[oxCCO] measurement can provide as a potential marker for clinicians and neuroscientists in a various range of CNS disorders, including novel applications in the field of broadband-NIRS.

Unlike current broadband-NIRS systems, Mini-CYRIL can be easily utilised by clinicians/non-specialists since it does not require extensive calibrations and due to its compactness and size it can be easily integrated in demanding preclinical and clinical settings. Mini-CYRIL also enables real-time measurement of optical pathlength through brain which is considered constant in all the commercial NIRS and broadband-NIRS systems. This feature improves the estimation of chromophore concentration through accounting for real-time changes in pathlength, which is

specifically important in monitoring injuries with changing pathophysiology that may change the nature of anatomy during the measurement period.

Mini-CYRIL's performance was validated in the preclinical study of neonatal hypoxia-ischaemia (HI) and was used to make transmission mode NIRS measurement through piglets' brain. The measurements of nadir and Area Under The Curve of Δ[oxCCO] during HI and recovery proved to be good indicators of HI insult severity and the real-time measurement of optical pathlength during the experiment significantly enhanced the measurement accuracy.

In the preclinical study of Multiple Sclerosis, mini-CYRIL was used to investigate the role of hypoxia in neuroinflammation and degeneration in the spinal cord of rats induced with Experimental Autoimmune Encephalomyelitis. The results from MS studies suggested that Δ[oxCCO], an indicator of mitochondrial oxygen metabolism, can be upregulated by an increase in oxygen delivery in mild to moderate EAE-induced rats.

Finally, mini-CYRIL was used to monitor changes in retinal respiration of aged rats in real time during and after photobiomodulation using 670 nm LED. It was demonstrated that 670 nm increases the redox state of mitochondria and the measurement of Δ[oxCCO] can be potentially used as a predictive marker in the aging retina and Age related Macular Degeneration.

Bibliography

[1] F. F. F. Jobsis, “Noninvasive, Infrared Monitoring of Cerebral and Myocardial Oxygen Sufficiency and Circulatory Parameters,” *Science (80-.).*, vol. 198, no. 4323, pp. 1264–1267, 1977.

[2] E. Wright, K. St. Lawrence, and M. Diop, “Conversion of a low cost off-the-shelf spectrometer into a suitable instrument for deep tissue spectroscopy,” *Proc. SPIE*, vol. 8573, p. 85730V, 2013.

[3] M. Diop, E. Wright, V. Toronov, T.-Y. Lee, and K. St Lawrence, “Improved light collection and wavelet de-noising enable quantification of cerebral blood flow and oxygen metabolism by a low-cost, off-the-shelf spectrometer.,” *J. Biomed. Opt.*, vol. 19, no. 5, p. 57007, 2014.

[4] S. J. Matcher, M. Cope, and D. T. Delpy, “Use of the water absorption spectrum to quantify tissue chromophore concentration changes in near-infrared spectroscopy.,” *Phys. Med. Biol.*, vol. 39, no. 1, pp. 177–96, 1994.

[5] A. D. Edwards, P. Brocklehurst, A. J. Gunn, H. Halliday, E. Juszczak, M. Levene, B. Strohm, M. Thoresen, A. Whitelaw, and D. Azzopardi, “Neurological outcomes at 18 months of age after moderate hypothermia for perinatal hypoxic ischaemic encephalopathy: synthesis and meta-analysis of trial data,” *Bmj*, vol. 340, p. c363, 2010.

[6] C. J. Bauer, “Investigating Brain Metabolism during Hypothermia in a Preclinical Model of Birth Asphyxia : A Broadband NIRS Study,” no. August, 2017.

[7] P. P. Drury, L. Bennet, and A. J. Gunn, “Mechanisms of hypothermic neuroprotection,” *Semin. Fetal Neonatal Med.*, vol. 15, no. 5, pp. 287–292, 2010.

[8] S. A. McLellan and T. S. Walsh, “Oxygen delivery and haemoglobin,” *Contin. Educ. Anaesthesia, Crit. Care Pain*, vol. 4, no. 4, pp. 123–126, 2004.

[9] M. F. Siddiqui, S. Lloyd-Fox, P. Kaynezhad, I. Tachtsidis, M. H. Johnson, and C. E. Elwell, “Non-invasive measurement of a metabolic marker of infant brain function,” *Sci. Rep.*, vol. 7, no. 1, p. 1330, 2017.

[10] C. Kolyva, A. Ghosh, I. Tachtsidis, D. Highton, C. E. Cooper, M. Smith, and C. E. Elwell, "Cytochrome c oxidase response to changes in cerebral oxygen delivery in the adult brain shows higher brain-specificity than haemoglobin," *Neuroimage*, vol. 85, pp. 234–244, Jan. 2014.

[11] I. de Roever, G. Bale, R. J. Cooper, and I. Tachtsidis, "Cytochrome-C-Oxidase Exhibits Higher Brain-Specificity than Haemoglobin in Functional Activation," in *Biomedical Optics 2016*, 2016, p. BTh4D.4.

[12] I. de Roever, G. Bale, R. J. Cooper, and I. Tachtsidis, "Functional NIRS Measurement of Cytochrome-C-Oxidase Demonstrates a More Brain-Specific Marker of Frontal Lobe Activation Compared to the Haemoglobins," Springer, Cham, 2017, pp. 141–147.

[13] M. Saka, J. Berwick, and M. Jones, "Linear superposition of sensory-evoked and ongoing cortical hemodynamics.," *Front. Neuroenergetics*, vol. 2, no. August, pp. 1–13, 2010.

[14] P. Zaramella, F. Freato, A. Amigoni, S. Salvadori, P. Marangoni, A. Suppiej, A. Suppjei, B. Schiavo, and L. Chiandetti, "Brain auditory activation measured by near-infrared spectroscopy (NIRS) in neonates.," *Pediatr. Res.*, vol. 49, no. 2, pp. 213–9, 2001.

[15] S. J. Matcher and C. E. Cooper, "Absolute quantification of deoxyhaemoglobin concentration in tissue near infrared spectroscopy.," *Phys. Med. Biol.*, vol. 39, no. 8, pp. 1295–312, Aug. 1994.

[16] G. Bale, S. Mitra, J. Meek, N. Robertson, and I. Tachtsidis, "A new broadband near-infrared spectroscopy system for in-vivo measurements of cerebral cytochrome-c-oxidase changes in neonatal brain injury.," *Biomed. Opt. Express*, vol. 5, no. 10, pp. 3450–66, 2014.

[17] G. Bale, "Development of Optical Instrumentation and Methods to Monitor Brain Oxygen Metabolism : Application to Neonatal Birth Asphyxia," 2016.

[18] P. Kaynezhad, I. De Roever, G. Bale, and I. Tachtsidis, "Optical monitoring of neonatal brain injury: towards the development of compact clinical systems," *Electro Optics*, London, pp. 18–19, Mar-2016.